TÉCNICO LISBOA

UNIVERSIDADE DE LISBOA
INSTITUTO SUPERIOR TÉCNICO



Shadows and gravitational lensing of Black Holes interacting with fundamental fields

Pedro Vieira Pinto da Cunha

Supervisor:	Doctor Vítor Manuel dos Santos Cardoso
Co-Supervisor:	Doctor Carlos Alberto Ruivo Herdeiro

Thesis approved in public session to obtain the PhD Degree in

Physics

Jury final classification: Pass with Distinction and Honour

2019

TÉCNICO LISBOA

UNIVERSIDADE DE LISBOA
INSTITUTO SUPERIOR TÉCNICO

Shadows and gravitational lensing of Black Holes interacting with fundamental fields

Pedro Vieira Pinto da Cunha

Supervisor: Doctor Vítor Manuel dos Santos Cardoso
Co-Supervisor: Doctor Carlos Alberto Ruivo Herdeiro

Thesis approved in public session to obtain the PhD Degree in

Physics

Jury final classification: Pass with Distinction and Honour

Jury

Chairperson: Doctor José Pizarro de Sande e Lemos, Instituto Superior Técnico, Universidade de Lisboa

Members of the Committee:

Doctor José António Maciel Natário, Instituto Superior Técnico, Universidade de Lisboa

Doctor Carlos Alberto Ruivo Herdeiro, Instituto Superior Técnico, Universidade de Lisboa

Doctor Volker Walter Horst Perlick, Center of Applied Space Technology and Microgravity (ZARM), Universität Bremen, Germany

Doctor Frédéric Henri Jean Vincent, Laboratoire d'Études Spatiales et d'Instrumentation en Astrophysique, Observatoire de Paris, France

Funding Institutions

Grant PD/BD/114071/2015 from Fundação para a Ciência e Tecnologia (FCT).

2019

Para os meus pais,

Acknowledgments

I would like to thank the support of my supervisors Prof. Vítor Cardoso and Prof. Carlos Herdeiro. I am greatly indebted to Prof. Carlos Herdeiro for his exceptional support, advice, and mentorship along these last years, and in particular I would like to thank him for all the enriching and stimulating discussions that allowed me to grow both as researcher and as a person. It has been an honour to have the opportunity to work with him.

I would like to thank the support of my PhD Grant No. PD/BD/114071/2015 under the FCT-IDPASC Portugal Ph.D. program. I am grateful for the support of the Calouste Gulbenkian Foundation under the Stimulus for Research Program 2015. This work was also partly supported by the Fundação para a Ciência e a Tecnologia (FCT) Project No. UID/MAT/04106/2019 and UID/MAT/04106/2013 (CIDMA), and also the FCT funded project PTDC/FIS- OUT/28407/2017. This work has further been supported by the European Union's Horizon 2020 research and innovation (RISE) programmes H2020-MSCA-RISE-2015 Grant No. StronGrHEP-690904 and H2020-MSCA-RISE-2017 Grant No. FunFiCO-777740. I would also like to acknowledge networking support by the COST Action CA16104. Computations were partly performed at the cluster "Blafis", "Argus" and "Baltasar-Sete-Sóis".

I would like to acknowledge the support of Instituto Superior Técnico (IST), the GRIT and CENTRA groups and the Physics Department of IST. I would also like to acknowledge the University of Aveiro (UA) as one of my affiliations, and thank the support of UA, CIDMA and the UA's Physics Department. In particular, I would like to thank the Gr@v group at UA and all its members for providing a wonderful and stimulating working environment.

I would like to thank the University of Mississippi, Johns Hopkins University, the Perimeter Institute for Theoretical Physics, Kindai University, the Yukawa Institute, Universidade Federal Pará and Universidad Nacional Autónoma de México for their hospitality during my visit to these institutions. I would equally like to thank the hospitality

of my hosts and their groups during these visits: Emanuele Berti, Luis Lehner, Akihiro Ishibashi, Juan Carlos Degollado and Luís Crispino. I would specially like to thank Luís Crispino, Akihiro Ishibashi and Juan Carlos Degollado for particularly unforgettable experiences. I am grateful for all the fruitful collaborations (not by order) that I had over these last years, namely with Carlos Herdeiro, Eugen Radu, Jai Grover, Alex Wittig, Emanuele Berti, José Font, Nicolas Sanchis-Gual, Miguel Zilhão, Maria Rodriguez, Helgi Rúnarsson, and also stimulating discussions with Luís Crispino, Volker Perlick, Juan Carlos Degollado, Jorge Delgado, Caio Macedo, Carolina Benone, Miguel Ferreira, Filip Hejda, João Rosa, António Morais and Luís Ventura. I naturally apologize to anyone that I might have missed.

On a more personal note, I would like to thank the support of my family, my cousin Rita, and in particular both my parents and my fantastic sister Susana. This work would have not been possible without them. I wish to thank my girlfriend Joana for all her kindness, support, and understanding during some of the more tough times. She can always make my day! I would like to pay tribute and dedicate a special word of gratitude to my late grandparents, who helped me so very much. This thesis is also for them. I wish to thank my friends, and in particular Maurício Soares and Tiago Rebelo for their enduring friendship, which I deeply cherish.

Resumo

A sombra de um buraco negro (BN) é provocada pelo efeito de lente gravitacional forte, e a partir desta é possível extraír algumas propriedades do espaço-tempo perto do BN. A sombra dos candidatos a BN supermassivos M87* e Sagitário A* estão agora ao alcance da Interferometria de Base Muito Longa em comprimentos de onda sub-milimétricos. É portanto oportuno analisar as diferentes previsões para a sombra em diversos modelos. Deste modo, foi analisado o efeito de lente gravitacional em redor de estrelas de Bosões/Proca e BNs de Kerr com cabelo escalar/Proca, com algumas soluções exibindo padrões caóticos. Para os BNs padrão na Relatividade Geral, assim como para outros objetos ultracompactos (com ou sem horizonte de eventos), são admitidas órbitas planares de fotões circulares. Estes Anéis de Luz (ALs) determinam várias propriedades do espaço-tempo. Em espaços-tempos estacionários e axi-simétricos genéricos também podem existir órbitas de fotões não-planares, independentemente das propriedades de integrabilidade do movimento das geodésicas. Estas Órbitas Fundamentais de Fotões (OFFs) são a generalização natural dos ALs para além da simetria esférica, que ocupam um papel central na análise de efeitos gravitacionais fortes, nomeadamente nas sombras de BNs. Nesta tese, modelos específicos são considerados para ilustrar como os OFFs podem ser úteis para compreender alguns efeitos gravitacionais não triviais. Isto é ilustrado para o caso de BNs de Kerr com cabelo de Proca, para os quais existem sombras qualitativamente novas com uma borda em cunha; tal pode ser compreendido devido à interação entre OFFs estáveis e instáveis. É também possível mostrar, através de um argumento topológico, que objetos sem horizonte que sejam fisicamente plausíveis e dinamicamente razoáveis com um AL instável, também deverão possuir um AL estável adicional. Curiosamente, tem sido argumentado que os AL estáveis desencadeiam, genericamente, instabilidades não-lineares no espaço-tempo. Como consequência, este resultado implica que objectos razoáveis que poderiam imitar um BN não são alternativas observacionais viáveis aos BNs, sempre que essas instabilidades ocorrem em escalas de tempo astrofisicamente pequenas.

Keywords: Relatividade Geral, Buracos Negros, Sombras, Lente Gravitacional, Campos Fundamentais

Abstract

The shadow of a Black hole (BH) is due to the strong gravitational lensing in the vicinity of the black hole. Through this lensing, some properties of the spacetime can be found. The shadow of the supermassive BH candidates M87* and Sagittarius A* are now within reach of Very Long Baseline Interferometry at sub-millimeter wavelengths, and it is hence timely to analyse the shadow predictions within different models. The lensing of light around Boson/Proca stars and Kerr black holes with scalar/Proca hair is analysed, with some solutions exhibiting chaotic patterns. For the standard BHs in General Relativity, as well as other ultra compact objects (with or without an event horizon) planar circular photon orbits are admitted. These Light Rings (LRs) determine several spacetime properties. In generic stationary, axi-symmetric spacetimes, non-planar bound photon orbits may also exist, regardless of the integrability properties of the photon motion. These Fundamental Photon Orbits (FPOs) are the natural generalisation of LRs beyond spherical symmetry and should generalise the LRs pivotal role in the theoretical analysis of strong gravitational lensing effects, and of BH shadows in particular. In this work, specific models are considered to illustrate how FPOs can be useful in order to understand some non-trivial gravitational lensing effects. We illustrate this for the case of Kerr BHs with Proca hair, wherein, moreover, qualitatively novel shadows with a cuspy edge exist, a feature that can be understood from the interplay between stable and unstable FPOs. One can also shown, via a topological argument, that for physically and dynamically reasonable horizonless objects with an unstable LR, an additional stable LR must also be present. Intriguingly, stable LRs have been argued to trigger, generically, nonlinear spacetime instabilities. As a consequence, this result implies that reasonable, smooth BH mimickers are not viable as observational alternatives to BHs, whenever these instabilities occur on astrophysically short time scales.

Keywords: General Relativity, Black Holes, Shadows, Gravitational Lensing, Fundamental Fields

Contents

Acknowledgments v

Resumo vii

Abstract ix

Glossary xv

Overview 1

1 Introduction **7**

1.1 The Kerr Space-time 10

1.2 Local observer basis 13

1.2.1 Image coordinates 15

1.3 Analytical form of the Kerr shadow 17

1.3.1 Shadow as a function $y(x)$ 18

1.4 Numerical Kerr shadow 21

1.5 Light rings (LRs) and Fundamental Photon Orbits (FPOs) 24

1.5.1 Shadow sketch 27

1.5.2 Effective potentials 28

1.5.3 Topological charge of a LR 31

1.6 Non-Kerr shadows in GR 34

1.6.1 Shadow cusp 37

1.7 Lensing by a horizonless UCO 40

1.8 Non-Kerr shadows in alternative gravity theories 42

2 BHs with scalar hair **47**

2.1 Boson Stars and KBHsSH 49

2.2 Effective potentials contour plots . . . 55
2.3 The effective potentials in Kerr . . . 60
2.3.1 Pocket formation, chaos and turning points . . . 62
2.4 Quasi-bound orbit in $(r, \dot{r})$ phase space . . . 67
2.5 Acceleration field $\mathcal{F}_r$ . . . 69
2.6 Physical conditions for Light Rings . . . 71
2.7 Gallery of Images . . . 75
2.7.1 Rotating boson stars . . . 76
2.7.2 Kerr BHs with scalar hair . . . 78

3 Kerr BHs with Proca hair **93**
3.1 Proca stars and KBHsPH . . . 94
3.2 Lensing by rotating Proca stars . . . 96
3.3 Shadows of Kerr BHs with Proca hair . . . 98
3.3.1 Classification of FPOs . . . 98
3.3.2 Stability of FPOs . . . 103
3.3.3 Kerr (and Kerr-like) FPOs . . . 105
3.3.4 Non-Kerr FPOs . . . 106

4 Black Hole mimickers **111**
4.1 Ultra-compact bosonic stars . . . 113
4.1.1 Lensing of Ultra-Compact Bosonic Stars . . . 117
4.2 Light Ring stability in UCOs . . . 122
4.2.1 LRs come in pairs . . . 125
4.2.2 LRs in Spherical Symmetry . . . 127
4.2.3 LRs in Axisymmetry . . . 127
4.3 Spacetime instability and stable trapping . . . 132
4.4 Topological charges via contour integrals . . . 137
4.4.1 Non-degenerate critical points . . . 141
4.4.2 Application of contour integrals to UCOs . . . 144

5 BHs beyond General Relativity **147**

5.1 The EdGB model and solutions 150

5.1.1 The static EdGB black holes 151

5.1.2 The spinning EdGB black holes 153

5.2 Shadows of EdGB BHs 154

5.2.1 Shadows of rotating EdGB BHs 156

5.2.2 Shadows of static EdGB BHs 160

6 The Road ahead **165**

Bibliography **167**

A Connection to integrations in the Complex plane **195**

B Horizonless UCOs with non-trivial topology **199**

C List of publications **201**

Glossary

ADM	Arnowitt-Deser-Misner
BH	Black Hole
BS	Boson Stars
EHT	Event Horizon Telescope
EdGB	Einstein-dilaton-Gauss-Bonnet
FPOs	Fundamental Photon Orbits
GR	General Relativity
GWs	Gravitational Waves
HBH	Hairy Black Hole
KBHsPH	Kerr BHs with Proca hair
KBHsSH	Kerr BHs with scalar hair
LIGO	Laser Interferometer GW Observatory
LR	Light Ring
PS	Proca Stars
RBS	Rotating Boson Stars
RPS	Rotating Proca Stars
UCO	Ultra-Compact Object

Overview

The true nature of Black Hole (**BH**) candidates that populate the cosmos remains elusive. The question of whether they are described by the paradigmatic Kerr BHs of General Relativity (**GR**), or instead by some other alternative compact objects, is not completely settled.

With the advent of new observation channels, namely through the Laser Interferometer Gravitational-Wave Observatory (**LIGO**) and the Event Horizon Telescope (**EHT**), directly probing BH candidates is now finally within reach. Such ongoing observations might help us answer the pressing question:
What is the correct description of astrophysical BHs?

In particular, are these objects described by (if any):

- the paradigmatic Kerr BH of GR?
- a BH solution of GR in equilibrium with a (fundamental) matter field?
- an ultra-compact object without an horizon, *i.e.* a BH mimicker?
- a BH solution in an alternative theory of gravity?

In this quest to address these questions, scientific open mindedness requires one to consider a diverse range of models, within and outside GR, and how their predictions impact on observational channels. The analysis of null geodesics in particular plays a special role, since they describe how electromagnetic and Gravitational Waves (**GWs**) behave at high frequencies. The work here presented has primarily focused on the electromagnetic channel, and with particular emphasis on a direct observable: the *shadow* of BHs.

Since BHs are not a source of radiation and are completely absorbent (at least classically), their manifestation in the observer's sky can be expected to be a sharp decrease in luminosity, contrasting with some background light. It is then quite fitting to name the image of a BH as its *shadow*: it embodies an absence of radiation. Since the shadow outline is determined by the strong gravitational lensing of light rays, the shadow can be regarded as a window to the strong gravity environment surrounding the BH.

A special class of orbits

Due to its strong gravity, it is well known that the Kerr spacetime possesses closed circular photon orbits (or **Light Rings**). These orbits are of paramount importance to determine the edge of the BH *shadow* (virtually the BH's "snapshot"), which is a direct observable targeted of the EHT collaboration. Indeed, EHT's recent (April 10^{th} 2019) public release of the first image ever of a BH candidate [1, 2, 3], consistent with a BH shadow, makes this work a quite timely topic.

Surprisingly, Light Rings (**LRs**) can also play a major role in the GW channel. For instance, the GW ringdown detected by LIGO [4, 5, 6, 7, 8], emitted after the merger of a BH binary, displays the signature of the LR orbit rather than the existence of an horizon [9]. In addition, LRs also display a connection to the BH's quasinormal modes of the BH remnant.

As discussed in this work, we can further associate a topological charge to each LR orbit. As is commonly the case when using topological tools, these charges can be useful to generate qualitative results, like existence theorems, as opposed to more quantitative measures. In particular, we discuss a general argument to analyse the LR structure around horizonless Ultra-Compact Objects, within fairly generic and reasonable assumptions [10].

LRs can be generalized into a more fundamental class, dubbed *Fundamental Photon Orbits* (**FPOs**), for stationary spacetimes with rotation [11]. Although FPOs operate as

a direct probe of the strong gravity regime, and despite their relevance for observations, a thorough analysis of FPOs in non-integrable spacetimes has remained largely unexplored by the community (unlike in Kerr). This opens an interesting window of opportunity to analyse of FPOs in a different range of spacetime models. One of the simplest such models are BHs interacting with matter fields.

BHs with a matter field within GR

The Kerr BH has a special status within GR, mainly due to a series of uniqueness theorems that establish the Kerr spacetime as the physical stationary BH solution in vacuum. Although the Kerr shadow is known analytically, it is fundamental to consider different BH models (namely outside vacuum), in order to understand how shadows can be different from Kerr's. In this respect, a particularly interesting starting point is a class of BHs in equilibrium with a massive fundamental field: *Kerr BHs with bosonic hair* [12, 13, 14, 15, 16]. This is the topic of Chapters 2 and 3.

These hairy BHs are exact GR solutions with a reasonable matter content (*e.g.* scalar or Proca field), that interpolate between (vacuum) Kerr and horizonless self-gravitating configurations (Boson/Proca stars) [17, 18, 19, 20, 21, 22]; in addition, these fields can work as a proxy for dark matter. Hairy BHs can exhibit various intriguing properties, including shadows that can differ significantly from the Kerr prediction [23, 24]. In contrast, it is quite challenging to find well defined models that lead to such large shadow deviations from the Kerr case (even outside GR).

As a consequence, hairy BHs are an ideal test bed to have a deeper understanding of FPOs. For instance, these orbits are pivotal when attempting to understand non-trivial features both at the level of the BH shadow and at the level of strong gravitational lensing [11, 25]. Although a subset of FPOs also exist in the Kerr case, Kerr BHs with bosonic hair can allow for a much richer structure.

BH mimickers

As was previously remarked, the initial part of the ringdown signal of BH candidates detected by LIGO has actually the signature of an unstable LR, rather than an horizon. As a consequence, an ultra-compact object with no horizon but with an unstable LR could in principle mimic LIGO's (initial) ringdown signal. However, would these (speculative) BH mimickers be viable candidates? This is the topic of Chapter 4.

For instance, as reasonable alternative to BHs, these objects should:

- Arise in a consistent and well motivated (effective field) theory of gravity.
- Have a dynamical formation mechanism
- Be (sufficiently) stable, *i.e.* posses a lifetime relevant for astrophysical applications.

Related to this last point, we introduce a simple argument, based on the topological LR charge, for a possible instability of such alternative objects; one can shown that for physically and dynamically reasonable horizonless objects with an unstable LR, an additional *stable* LR must also be present. Intriguingly, stable LRs have been argued to trigger, generically, nonlinear spacetime instabilities [10, 26, 27], see Section 4.2. This can be understood intuitively as a successive buildup of trapped radiation around the stable LR, eventually leading to a back-reaction on the spacetime, and ultimately inducing an instability on the compact object. As a consequence, this result implies that reasonable, smooth BH mimickers are not viable as observational alternatives to BHs, whenever these instabilities occur on astrophysically short time scales.

BHs in an alternative gravity theory

There are strong theoretical motivations to search for alternative theories to Einstein's GR (*e.g.* non-renormalizability and curvature singularities). Higher order curvature corrections can be included, often leading to field equations with higher order derivatives

and typically resulting in unphysical run-away modes [28].

Nevertheless, this can be prevented by a cleaver combination of higher curvature terms, such as the *Gauss-Bonnet* combination [29]. Despite leading to a topological constant in GR, this term can contribute via a coupling to a dynamical scalar field (dilaton). This gives rise to a new gravity model: *Einstein-dilaton-Gauss-Bonnet* (**EdGB**), which also occurs naturally as the low energy limit of string theory. This is the topic of Chapter 5.

The Gauss-Bonnet term can be interpreted as an *effective* energy momentum-tensor within plain GR, hence representing some type of *exotic matter* that can violate energy conditions. One could expect that the distribution of this exotic matter around a EdGB BH would lead to some type of sharp signature at the level of the shadow. However, rather surprisingly, this does not appear to be the case [30]. The main reason for this result appears to be the small variation of the FPO structure with respect to Kerr. Since most of the non-trivial physics exists just outside the horizon, but still enclosed by the FPO structure, any potential new signature from the Gauss-Bonnet term appears to be *hidden* by the BH shadow. This particular model illustrates the fact that new theories of gravity need to significantly modify the FPO structure in order to generate sharp signatures at the level of shadow observations [31].

Pubished work

The research presented in this thesis is not substantially the same as any that I have submitted for a degree, diploma or other qualification at any other university; no part of it has already been or is concurrently submitted for any such degree, diploma or other qualification. Most of the chapters of this thesis have been published. The work presented in Chapter 1 is mostly based in [32, 31]. The work presented in Chapter 2 is mostly based in [24]. The images presented in this Chapter were produced with two independent codes: Pyhole, developed by J. Grover and A. Witting, and another ray-tracing code developed

during my PhD. The work presented in Chapter 3 is mostly based in [11]. The work presented in Chapter 4 is mostly based in [25]. The work presented in Chapter 5 is mostly based in [30]. Further publications written during the development of the PhD are not discussed here. The full list of publications published during the PhD can be found in Appendix C.

Chapter 1

Introduction

One of the extraordinary predictions of General Relativity (GR) was the bending of light rays due to the spacetime curvature, creating a net effect not too dissimilar from that of a lens [33, 34, 35, 36]. Although the measurement of the bending of light was itself instrumental in establishing GR as a physical theory of the Universe, the prospects of a direct observation of a gravitational lens was considered unlikely at the time of Einstein.

The discovery of quasars in the 1960s [37] brought major advancements to the field of gravitational lensing. Since these sources are both very distant and bright, they are ideal to observe lensing effects if their line of sight is crossed by a massive object (typically a galaxy). In 1979 the first lensing effect of a distant quasar was recorded [38], with similar discoveries being made thereafter [39]. However, some of the largest lensing effects that have been presently observed in astrophysical objects are only of the order of a few tens of arc seconds (see *e.g.* [40]).

By contrast, Ultra-Compact Objects (UCOs) can cause much more extreme local deflections of light. These objects (by definition) possess *light rings* (LRs) and can bend light by an *arbitrarily large angle* (see Section 1.5). LRs are circular photon orbits, an extreme form of light bending with distinct phenomenological signatures in both the electromagnetic and gravitational waves channels.

In the gravitational waves channel, the first events detected by LIGO [4, 5, 6, 7, 8] actually support the existence of LRs (and hence of UCOs), as the post-merger part of the signal (the ringdown) does not carry the direct signature of an event horizon, but rather that of a LR [9]. Notice that black holes (BHs) fall within the UCO definition: they are UCOs with a horizon. However, there are other compact objects with a LR that could potentially mimic the observed signal. These *horizonless* UCOs are a far more speculative class of objects, which has been widely discussed in the literature for decades.

They are motivated by both classical and quantum conceptual issues related to the existence of an event horizon and of a curvature singularity, whose existence in General Relativity follows from Penrose's singularity theorem, if matter obeys the null energy condition [41, 42]. Horizonless UCOs recently attracted renewed interest precisely because of the LIGO detections. However, most of these objects lack a (known) dynamical formation mechanism and, as shown recently in [10], physically reasonable horizonless UCOs have potential stability issues. This argument relies on the existence of stable LRs and is briefly discussed in section 1.5.3. In addition, the gravitational lensing of a particular horizonless UCO model is analysed in section 1.7. These topics are covered in more detail in Chapter 4.

In the electromagnetic channel, LRs and *Fundamental Photon Orbits* (FPOs) (which generalize the latter, see Section 1.5) are also closely connected to an important observable that is being targeted by the Event Horizon Telescope: the BH *shadow* [43]. Simply, the shadow of a BH in a given observation frame is the set of directions in the local sky that would receive light from the event horizon; since the latter is not a source of radiation (at least classically) the shadow actually corresponds to a lack of radiation [44, 45]. This concept is hence associated with the BH's light absorption cross-section at high frequencies, if the light rays were traced back in time. In particular, the high frequency limit with no polarization is implicitly assumed throughout most of the paper, with light rays simply following null geodesics.

One should not expect astrophysical BHs to exist in total vacuum, but rather surrounded by an accretion disk and ionized matter. Hence, the motion of light rays affected by the presence of a plasma could also be taken into consideration, as the latter might lead to some observable effects. This topic has been extensively analysed in the literature, *e.g.* see [46, 47, 48, 49, 50, 51, 52]; however, it will not be pursued here.

The shadow outline in the sky depends on the gravitational lensing of nearby radiation, thus bearing the fingerprint of the geometry around the BH [53, 31]. This builds a particularly exciting prospect for the use of very large baseline interferometry (VLBI) techniques to resolve the angular scale of the event horizon and corresponding shadow of supermassive BH candidates. Indeed, on the 10^{th} of April 2019 the Event Horizon Telescope (EHT) collaboration released an image of the distant BH candidate M87* obtained with horizon scale resolution using VLBI techniques [1, 2, 3]. Remarkably, the observed image is consistent with a Kerr BH shadow. Besides M87*, the supermassive BH candidate Sagittarius A* in our galaxy center also appears to be a promising target for the EHT, which makes this work a quite timely topic. Shadow observations probe the spacetime geometry in the vicinity of the horizon, at least as close as the LR orbits, and consequently would test possible deviations to the expected BH geometry (*i.e.* the Kerr geometry) in this crucial region [43].

In special cases for which the geodesic motion is integrable (*e.g.* Kerr), it is possible to have an analytical closed form for the shadow edge (see Section 1.3). However, generically this is not possible and one has to resort to numerical methods. For the latter case, the evolution of light rays is performed numerically by solving the null geodesics equation, with the general form given by [54, 55]:

$$\ddot{x}^{\mu} + \Gamma^{\mu}_{\alpha\beta}\, \dot{x}^{\alpha} \dot{x}^{\beta} = 0, \tag{1.1}$$

where the (dot) derivative is taken with respect to an affine parameter and $\Gamma^{\mu}_{\alpha\beta}$ are the Christoffel symbols. This comprises four second order differential equations, although the existence of spacetime symmetries allows some of the four equations to be simplified to

first order. Numerically, instead of evolving the light rays directly from a light source and detect the ones that reach the observer, the most efficient procedure actually requires the propagation of light rays from the observer backward in time and identify their origin [56], a method named *backwards ray-tracing*.

The Kerr space-time [57] is, according to the uniqueness theorems [58, 59, 60], the *only* stationary, regular, asymptotically flat BH solution of *vacuum* General Relativity. As such, it is thought to describe the endpoint of gravitational collapse when (essentially) all matter has either fallen to the BH or been scattered towards infinity. As a consequence, all observational data of BH candidates are primarily compared with the predictions from the Kerr spacetime. It is then rewarding to start with a brief review of the Kerr case, before discussing any possible deviations from the latter. Throughout this thesis, unless otherwise mentioned, natural units $c = G = \hbar = 1$ are assumed.

1.1 The Kerr Space-time

In Boyer-Lindquist coordinates $\{t, r, \theta, \varphi\}$ the Kerr metric is given by [57, 54, 55]:

$$ds^2 = -\left(1 - \frac{2Mr}{\rho^2}\right) dt^2 - \left(\frac{4Mar\sin^2\theta}{\rho^2}\right) dt d\varphi + \left(\frac{\rho^2}{\Delta}\right) dr^2 + \rho^2 d\theta^2 + \\ + \sin^2\theta \left(r^2 + a^2 + \frac{2Mra^2\sin^2\theta}{\rho^2}\right) d\varphi^2, \tag{1.2}$$

where $\rho^2 = r^2 + a^2\cos^2\theta$ and $\Delta = r^2 - 2Mr + a^2$. This metric depends only on two parameters: the Arnowitt-Deser-Misner (ADM) mass M of the BH and the rotation parameter $a \in [-M, M]$; the latter is proportional to the total[1] angular momentum $J = Ma$. By setting $a = 0$ we recover the well-known Schwarzschild metric. The Kerr spacetime is asymptotically flat, *i.e.* in the limit $r/M \gg 1$ one recovers Minkwoski spacetime is standard spherical coordinates. Moreover, it is stationary and axially-symmetric, with both symmetries defined in terms of the two Killing vectors $\boldsymbol{\zeta} = \partial_t$ and $\boldsymbol{\xi} = \partial_\varphi$. The isometric mapping defined by the integral curves of $\boldsymbol{\xi}$ has a set of fixed points ($\boldsymbol{\xi} = 0$),

[1] More precisely, J is the Komar angular momentum at spatial infinity [61].

which defines the rotation axis [62], the latter being localized at $\theta = \{0, \pi\}$. In addition to these Killing symmetries, the metric is invariant under the discrete transformation $\{t, \varphi\} \to -\{t, \varphi\}$ (*i.e.* circularity), and possesses a $\mathbb{Z}_2$ reflection symmetry with respect to the surface $\theta = \pi/2$ (the equatorial plane).

The condition $\Delta = 0$ determines the location of two horizons, with the outermost one at the radial coordinate $r_+ = M + \sqrt{M^2 - a^2}$. It then follows that $a^2 \leqslant M^2$ must hold in order for the Kerr metric to describe a BH, with the equality applying in the *extremal* case. We will mainly focus on the region outside the outermost horizon: $r \in [r_+, +\infty[$, $t \in]-\infty, +\infty[$, $\theta \in [0, \pi]$ and $\varphi \in [0, 2\pi[$. This region does not cover the maximal analytical extension of the Kerr spacetime [55].

Admirably, geodesics are fully separable in the Kerr space-time. Using the Hamilton-Jacobi formalism [63] it is possible to write the geodesic equations in Kerr space-time as four first-order differential equations[2]:

$$\rho^2 \dot{r} = \pm\sqrt{\mathcal{R}}, \qquad \text{with} \qquad \mathcal{R} \equiv \Big[E(r^2 + a^2) - aL\Big]^2 - \Delta[Q + (aE - L)^2 + m_o^2 r^2], \tag{1.3a}$$

$$\rho^2 \dot{\theta} = \pm\sqrt{\Theta}, \qquad \text{with} \qquad \Theta = Q - \cos^2\theta \left(a^2(m_o^2 - E^2) + \frac{L^2}{\sin^2\theta}\right). \tag{1.3b}$$

$$\rho^2 \dot{t} = \frac{E}{\Delta}[(r^2 + a^2)^2 - a^2 \Delta \sin^2\theta] - \frac{2Mar}{\Delta} L. \tag{1.3c}$$

$$\rho^2 \dot{\varphi} = \frac{2MaEr}{\Delta} + L\frac{(\Delta - a^2 \sin^2\theta)}{\Delta \sin^2\theta}. \tag{1.3d}$$

This simplification is possible due to the existence of four constants of motion $\{E, L, m_o, Q\}$ [63]. The constants $\{E, L\}$ are a result of the Killing symmetries $\{\boldsymbol{\zeta}, \boldsymbol{\xi}\}$, and they can be interpreted as the particle's energy and angular momentum respectively[3]. The remaining constants $\{m_o, Q\}$ can both be related to the existence of Killing tensors [65]. The particle's rest mass m_o (which is zero for a null geodesic) is associated to the metric tensor itself, which is a *trivial* Killing tensor. However, the Carter constant Q, named after

[2] $\dot{x}^\mu$ denotes derivative with respect to an affine parameter.

[3] Here the affine parameter λ is defined via the particle's proper time τ by $d\tau = m_o d\lambda$ [64].

Brandon Carter [63], is determined by a *non-trivial* Killing tensor, and is thus a hidden symmetry of the Kerr spacetime.

For null geodesics, the motion dynamics is expressed with just two independent impact parameters:

$$\eta \equiv \frac{L}{E}, \qquad \chi \equiv \frac{Q}{E^2}.$$

Kerr is endowed with null geodesics that live, in Boyer-Lindquist coordinates, on surfaces with a constant radial coordinate r, having conveniently been dubbed "spherical photon orbits" in the literature [66]. These orbits can be computed via (1.3a), by imposing $\mathcal{R} = 0$ and $d\mathcal{R}/dr = 0$. Notice that while these orbits do lie on surfaces with spherical topology, the geometry is (generically) not spherical. Spherical photon orbits also describe a symmetric motion with respect to the equatorial plane (the surface with $\mathbb{Z}_2$ reflection symmetry) in terms of the Boyer-Lindquist θ coordinate, reaching a maximum latitude with respect to the symmetry axis. The turning point value θ_* in a given spherical orbit is given by:

$$a^2 \cos^4\theta_* + [\chi + \eta^2 - a^2]\cos^2\theta_* - \chi = 0. \tag{1.4}$$

In addition, for a given spherical photon orbit at radius r, the corresponding impact parameters must satisfy [66, 64]:

$$\eta = \frac{r^3 + a^2 r + M a^2 - 3Mr^2}{a(M-r)}, \tag{1.5}$$

$$\chi = \frac{r^2}{r^2 - a^2}(3r^2 + a^2 - \eta^2) \geqslant 0, \tag{1.6}$$

where $r \in [r_1, r_2]$. These are defined as the roots[67, 44] of η:

$$r_1 = 2M\left\{1 + \cos\left(\frac{2}{3}\arccos\left[-\frac{|a|}{M}\right]\right)\right\}, \quad r_2 = 2M\left\{1 + \cos\left(\frac{2}{3}\arccos\left[\frac{|a|}{M}\right]\right)\right\}. \tag{1.7}$$

The edge of the Kerr shadow will be the locus of points in the observer's local sky associated to geodesics that barely skim these spherical photon orbits, and hence have the correct values of the impact parameters $\{\chi, \eta\}$. In order to explicitly compute the

shadow, let us construct a local observer frame [32].

1.2 Local observer basis

In order to keep the discussion more general, in this section we assume a more generic spacetime of a central compact object that is stationary and axially symmetric, and thus having two Killing vector fields $\{\boldsymbol{\zeta},\boldsymbol{\xi}\}$. Additionally, we also assume circularity and asymptotic flatness. We keep a similar coordinate notation from the Kerr case $\{t, r, \theta, \varphi\}$, with a spherical-like flavour. In particular, t and φ are each adapted to the corresponding Killing vector as before, and by making a gauge choice we set the coordinates $\{r, \theta\}$ to be orthogonal, *i.e.* $g_{r\theta} = 0$, and we also set $g_{rr} > 0$ and $g_{\theta\theta} > 0$.

The observer basis $\{\hat{e}_{(t)}, \hat{e}_{(r)}, \hat{e}_{(\theta)}, \hat{e}_{(\varphi)}\}$ can be expanded in the coordinate basis $\{\partial_t, \partial_r, \partial_\theta, \partial_\varphi\}$. This decomposition is not unique, allowing for spatial rotations and Lorentz boosts. A possible choice is given by:

$$\hat{e}_{(\theta)} = A^\theta \partial_\theta, \qquad \hat{e}_{(r)} = A^r \partial_r, \tag{1.8}$$

$$\hat{e}_{(\varphi)} = A^\varphi \partial_\varphi, \qquad \hat{e}_{(t)} = \gamma \left(\partial_t + \omega\, \partial_\varphi\right), \tag{1.9}$$

where $\{\omega, \gamma, A^r, A^\theta, A^\varphi\}$ are real coefficients. This particular choice is connected to a reference frame with zero axial angular momentum in relation to spatial infinity, and hence it is sometimes called the ZAMO reference frame, standing for *Zero Angular Momentum Observers* [55]. We remark that an observer at rest in this frame moves with respect to the coordinate system, as a consequence of frame-dragging[4]. The observer basis has a Minkowski normalization:

$$1 = \hat{e}_{(\theta)} \cdot \hat{e}_{(\theta)}, \qquad 1 = \hat{e}_{(\varphi)} \cdot \hat{e}_{(\varphi)}, \tag{1.10}$$

$$1 = \hat{e}_{(r)} \cdot \hat{e}_{(r)}, \qquad -1 = \hat{e}_{(t)} \cdot \hat{e}_{(t)}. \tag{1.11}$$

[4]This dragging effect is connected to a non-zero cross-term $g_{t\varphi}$ in the metric.

We also require that $0 = \hat{e}_{(t)} \cdot \hat{e}_{(\varphi)}$. Using these conditions we obtain:

$$A^{\theta} = \frac{1}{\sqrt{g_{\theta\theta}}}, \qquad A^{r} = \frac{1}{\sqrt{g_{rr}}}, \qquad A^{\varphi} = \frac{1}{\sqrt{g_{\varphi\varphi}}}, \tag{1.12}$$

where the sign of the square roots was chosen positive so that at spatial infinity we have the standard orthogonal basis in spherical coordinates. Similarly we get [53, 44]:

$$\omega = -\frac{g_{t\varphi}}{g_{\varphi\varphi}}, \qquad \gamma = \sqrt{\frac{g_{\varphi\varphi}}{g_{t\varphi}^2 - g_{tt}g_{\varphi\varphi}}}. \tag{1.13}$$

A local measurement of a particle's property is performed by an observer at a given frame in the same position as that particle. Thus, the locally measured energy $p^{(t)}$ of a photon is given by the projection of its 4-momentum[5] p^{μ} onto $\hat{e}_{(t)}$ [44]:

$$p^{(t)} = -(\hat{e}^{\mu}_{(t)}\, p_{\mu}) = -\gamma(p_t + \omega p_{\varphi}). \tag{1.14}$$

The minus sign is a consequence of the time-like normalization $\hat{e}_{(t)} \cdot \hat{e}_{(t)} = -1$. The quantities $E \equiv -p_t$ and $p_{\varphi} \equiv L$ are conserved due to the associated Killing vectors, and they turn out to be respectively the photon's energy and angular momentum relative to a static observer at spatial infinity[6] [44] .

The locally measured linear momentum of the photon in all three spatial directions is obtained similarly, and so we obtain overall:

$$\boxed{p^{(t)} = \gamma\left(E - \omega L\right),} \qquad \boxed{p^{(\theta)} = \hat{e}^{\mu}_{(\theta)}\, p_{\mu} = \frac{1}{\sqrt{g_{\theta\theta}}} p_{\theta},} \tag{1.15}$$

$$\boxed{p^{(\varphi)} = \hat{e}^{\mu}_{(\varphi)}\, p_{\mu} = \frac{1}{\sqrt{g_{\varphi\varphi}}} L,} \qquad \boxed{p^{(r)} = \hat{e}^{\mu}_{(r)}\, p_{\mu} = \frac{1}{\sqrt{g_{rr}}} p_{r}.} \tag{1.16}$$

A photon with zero angular momentum ($L = 0$) is observed in the ZAMO frame with no momentum component in the $\hat{e}_{(\varphi)}$ direction. This is due to the fact that an observer at rest at ZAMO also has zero angular momentum with respect to infinity, as was previously stated.

[5] We remark that with our choice for the affine parameter, $p^{\mu} = \dot{x}^{\mu}$.

[6] This statement can be justified in the limit $r \to \infty$, which leads to $p^{(t)} = E$ and to $p^{(\varphi)} r \sin\theta = L$.

1.2.1 Image coordinates

Consider the projection of photons detected in an observation image, corresponding to the optical perspective of an observer, which could be taken as a camera. The image coordinates (x, y) assigned to each photon in this image are its impact parameters [53] and they are a function of the respective observation angles (α, β) (see Fig. 1.1).

The solid angle that a given object occupies in the observer's sky is a well defined concept and it depends strongly on how far the the object is from the observer. However, there are different measures that can be used for this "distance" in a curved space-time. Using the proper distance can have certain disadvantages: it is anon-local (integrated) quantity that can diverge (*e.g.* the extremal Kerr case) [44]. For this reason we shall take the *perimetral radius* as a measure for the distance. Given a circumference at the equator ($\theta = \pi/2$) with constant radial coordinate r, its perimeter $\mathcal{P}$ is obtained by:

$$\mathcal{P} = \int_0^{2\pi} \sqrt{g_{\varphi\varphi}}\, d\varphi = 2\pi\sqrt{g_{\varphi\varphi}}. \tag{1.17}$$

Since there is no dependence on the coordinate φ the integration is trivial. The *perimetral radius* (or circumferential radius) $\tilde{r}$ is then defined as:

$$\tilde{r} \equiv \frac{\mathcal{P}}{2\pi} = \sqrt{g_{\varphi\varphi}}. \tag{1.18}$$

This quantity is a possible choice as a measure of the distance to the compact object, *e.g.* a BH. For instance, one can expect the observation angles (α, β) that capture the object's image to have a $1/\tilde{r}$ dependence as the observer approaches spatial infinity. Hence, a set of *image coordinates* (x, y), which can be regarded as a set of impact parameters, can be naturally defined as [32, 53, 44]:

$$x \equiv -\tilde{r}\beta \qquad \text{and} \qquad y \equiv \tilde{r}\alpha, \tag{1.19}$$

where the perimetral radius $\tilde{r}$ is computed at the position of the observer. The minus sign in the x definition comes from the sign convention for β (see Fig. 1.1). Notice

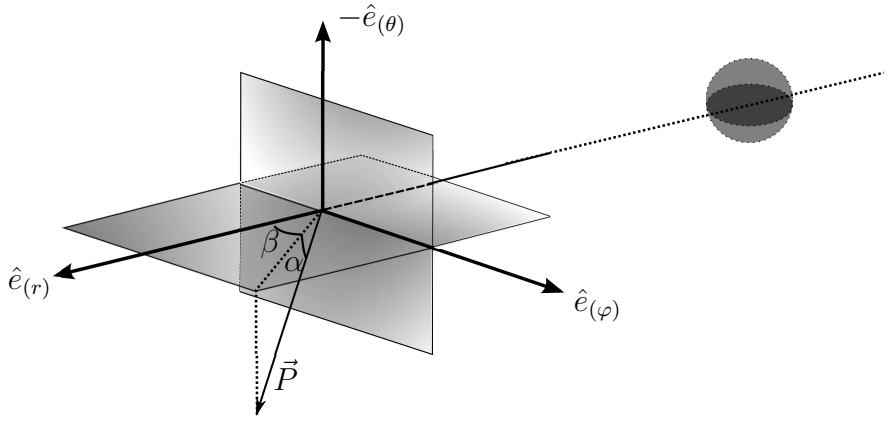


Figure 1.1: Perspective drawing of the geometric projection of the photon's linear momentum $\vec{P}$ in the observer's frame $\{\hat{e}_{(r)}, \hat{e}_{(\theta)}, \hat{e}_{(\varphi)}\}$. The observation angles α, β were drawn as positive. The planes associated with the angles α and β are perpendicular between themselves and the 3-vector $\vec{P}$ is in the same plane as α. The vectors $\hat{e}_{(\varphi)}, \hat{e}_{(r)}$ and also co-planar with β. The BH is represented by the grey sphere in the image. Adapted from [32].

the observation angles (α, β) are both zero in the direction pointing to the center of the compact object, in the observer's frame. The 3-vector $\vec{P}$ in Fig. 1.1 is the photon's linear momentum with components $p^{(r)}, p^{(\theta)}$ and $p^{(\varphi)}$ in the orthonormal basis $\{\hat{e}_{(r)}, \hat{e}_{(\theta)}, \hat{e}_{(\varphi)}\}$. We then have:

$$|\vec{P}|^2 = \left[p^{(r)}\right]^2 + \left[p^{(\theta)}\right]^2 + \left[p^{(\varphi)}\right]^2. \tag{1.20}$$

Moreover, attending to the geometry of the photon's detection (see Fig. 1.1), we obtain:

$$p^{(\varphi)} = |\vec{P}| \sin\beta \, \cos\alpha, \tag{1.21a}$$

$$p^{(\theta)} = |\vec{P}| \sin\alpha, \tag{1.21b}$$

$$p^{(r)} = |\vec{P}| \cos\beta \, \cos\alpha. \tag{1.21c}$$

Since the photon has zero mass $|\vec{P}| = p^{(t)}$. The angular coordinates (α, β) (see Fig. 1.1) of a point in the observer's local sky define the direction of the associated light ray and establishes its initial conditions. Combining the 4-momentum projections (1.15 - 1.16) and the linear momentum $\vec{P}$ decomposition (1.21), we obtain:

$$p_\theta = |\vec{P}|\sqrt{g_{\theta\theta}}\sin\alpha, \qquad L = |\vec{P}|\sqrt{g_{\varphi\varphi}}\sin\beta\,\cos\alpha, \tag{1.22a}$$

$$p_r = |\vec{P}|\sqrt{g_{rr}}\cos\beta\,\cos\alpha, \qquad E = |\vec{P}|\left(\frac{1}{\gamma} + \omega\sqrt{g_{\varphi\varphi}}\sin\beta\,\cos\alpha\right). \tag{1.22b}$$

Curiously the value of $|\vec{P}|$ is redundant for the geodesic trajectory since its variation leads to a simple rescaling of the affine parameter. In fact, $|\vec{P}|$ only establishes the photon's frequency and does not influence the trajectory itself. For this reason this value can be set to unity for simplicity.

Now having constructed an observation frame, we can compute the Kerr shadow edge as seen by a ZAMO observer in the Kerr spacetime.

1.3 Analytical form of the Kerr shadow

The shadow's edge of a Kerr BH can be calculated in an analytical closed form. In the following calculation the observer is at a ZAMO frame at radial coordinate r_o and latitude coordinate θ_o. Starting from (1.21) and solving for the observation angles (α, β) we obtain:

$$\tan\beta = \frac{p^{(\varphi)}}{p^{(r)}}, \qquad \sin\alpha = \frac{p^{(\theta)}}{p^{(t)}}. \tag{1.23}$$

For an observer facing the BH, photons coming from the shadow edge have $p^{(r)} \geq 0$, and so we have $p^{(r)} \geq 0 \implies \cos\beta \geq 0$. Since the domain of α is $[-\pi/2, \pi/2]$ we obtain:

$$\beta = \arctan\left[\frac{p^{(\varphi)}}{p^{(r)}}\right], \qquad \alpha = \arcsin\left[\frac{p^{(\theta)}}{p^{(t)}}\right]. \tag{1.24}$$

Combination of (1.15), (1.16) and (1.3) yields:

$$p^{(\theta)} = \pm\frac{\sqrt{\Theta}}{\sqrt{g_{\theta\theta}}}, \qquad p^{(\varphi)} = \frac{L}{\sqrt{g_{\varphi\varphi}}}, \tag{1.25a}$$

$$p^{(r)} = \frac{\sqrt{R}}{\Delta\sqrt{g_{rr}}}, \qquad p^{(t)} = \gamma\left(E - \omega L\right). \tag{1.25b}$$

Using the definition of the impact parameters $\eta \equiv L/E$ and $\chi \equiv Q/E^2$, and of the coordinates (x, y):

$$y = \tilde{r}\arcsin\left[\frac{\pm 1}{\gamma(1-\eta\omega)}\frac{\sqrt{\chi + a^2\cos^2\theta_o - \eta^2/\tan^2\theta_o}}{\sqrt{r_o^2 + a^2\cos^2\theta_o}}\right], \tag{1.26}$$

$$x = -\tilde{r}\arctan\left[\frac{\eta\sqrt{\rho^2\Delta}}{\sqrt{g_{\varphi\varphi}}\sqrt{r_o^4 + (a^2 - \chi - \eta^2)r_o^2 + 2mr_o[\chi + (a-\eta)^2] - \chi a^2}}\right], \tag{1.27}$$

where all metric functions are computed at the observer's position. The impact parameters $\{\eta, \chi\}$ of the previous expressions are defined in terms of the coordinate radius r of the spherical photon orbits via equations (1.5) and (1.6). The rim of the shadow's edge in the (x, y) observation image is then defined *parametrically*, as r changes in the interval $r \in [r_1, r_2]$. An example is displayed in Fig. 1.2.

For a static observer in the asymptotically flat limit (*i.e.* spatial infinity), the previous expression simplifies considerably, in which case the coordinates (x, y) of the Kerr BH shadow edge, are provided by [44]:

$$x = -\eta/\sin\theta_o, \qquad y = \pm\sqrt{\chi + a^2\cos^2\theta_o - \eta^2/\tan^2\theta_o} \tag{1.28}$$

As before, the shadow is here also defined as a parametric curve, with a dependence on the spherical orbit radius r. The analytical solution for the Kerr shadow appears usually in this way. However, is it possible to write the function $y(x)$ explicitly?

1.3.1 Shadow as a function $y(x)$

For an observer at infinity, η is trivially obtained from x, see equation (1.28). Also, given η and r, the value of χ can be obtained directly from eq. (1.6). The non-trivial step is

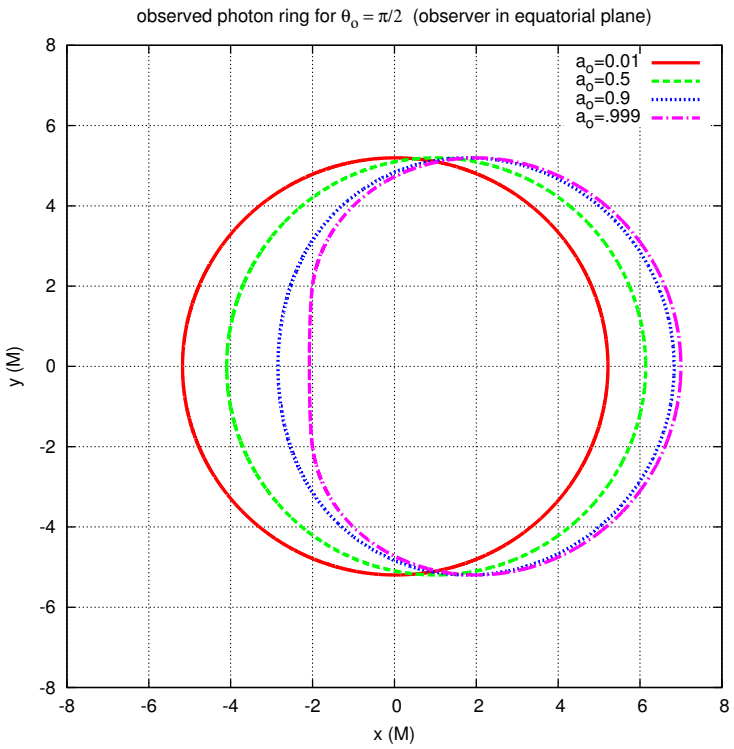


Figure 1.2: Representation of the Kerr shadow rim from the analytical solution, as observed from very large distances ($r_o \gg M$) in the equatorial plane of the BH ($\theta_o = \pi/2$). Different values of the dimensionless rotation parameter $a_o = a/M$ are displayed. Notice that for $a_o \simeq 0$ we have almost a circle due to the symmetry of the Schwarzschild solution and for $a_o \simeq 1$ we have a D-like shape due to frame-dragging. Adapted from [32].

only to obtain r given η. In other words, starting from eq. (1.5), one has to find the root of the following expression:

$$r^3 - 3Mr^2 + a(a+\eta)r + Ma(a-\eta) = 0. \tag{1.29}$$

Defining $\mathcal{A} \equiv M^2 - \frac{1}{3}a(\eta + a)$ and $\mathcal{B} \equiv M(M^2 - a^2)\,|\mathcal{A}|^{-3/2}$, together with Viéte's trigonometric trick [68, 69], one can write the exact (real) solution [31]:

$$
\begin{aligned}
&\mathcal{A} > 0, \quad \mathcal{B} \leqslant 1 : && r = M + 2\sqrt{\mathcal{A}}\cos\left(\frac{1}{3}\arccos\mathcal{B}\right) \\
&\mathcal{A} \geqslant 0, \quad \mathcal{B} > 1 : && r = M + 2\sqrt{\mathcal{A}}\cosh\left(\frac{1}{3}\log\left[\sqrt{\mathcal{B}^2 - 1} + \mathcal{B}\right]\right) \\
&\qquad\quad \mathcal{A} < 0 : && r = M - 2\sqrt{|\mathcal{A}|}\sinh\left(\frac{1}{3}\log\left[\sqrt{1 + \mathcal{B}^2} - \mathcal{B}\right]\right)
\end{aligned}
$$

Hence, given x one can compute r and then χ and y. Notice that each of these branches can describe a different section of the same shadow edge (see Fig. 1.3). This result is consistent with [70], since $y(2a) = 3\sqrt{3}\,M$ for $\theta_o = \pi/2$.

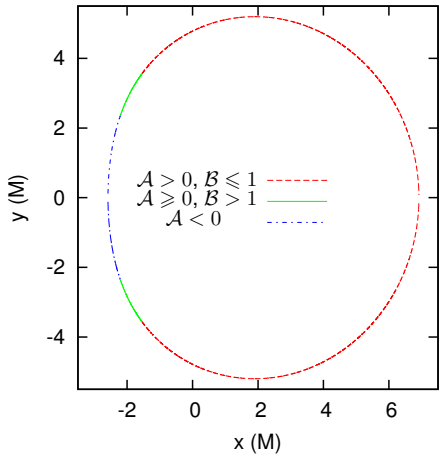


Figure 1.3: Kerr shadow edge function $y(x)$ for $a/M = 0.95$. All three branches are necessary to cover the entire edge. The observer is at infinity and in the equatorial plane ($\theta_o = \pi/2$). The axis are in M units. Adapted from [31].

In the extremal limit ($a/M = 1$), it is possible to simplify this expression even further. Still for a far away observer in the equatorial plane ($\theta_o = \pi/2$), the Kerr shadow shape $y(x)$ is given by [31]:

$$
y(x) = \pm\sqrt{11 + 2x - x^2 + 8\sqrt{2 + x}}, \qquad \text{with} \quad x \in]-2\,,\,7].
$$

Remarkably, the shadow area $\mathcal{A}$ can also be explicitly computed:

$$\mathcal{A} = \int_{-2}^{7} 2\, y(x)\, dx = 15\sqrt{3} + 16\pi.$$

Despite the existence of an analytical solution, the Kerr shadow can be obtained numerically as a cross-check. This is discussed in the next section.

1.4 Numerical Kerr shadow

In the optical channel, the gravitational lensing can strongly modify how an observer perceives its *local sky*. The latter should be interpreted as a set of light receiving directions at the location of the observer, being part of the local null tangent space (see also the review [71]). One can make a correspondence between the local sky and a closed S^2 manifold O, parameterized by two observation angles (say $\{\alpha, \beta\}$ in section 1.2). By placing a light emitting far-away sphere $\mathcal{N}$, surrounding the observer and the BH, some of the light rays will be received in the local sky O, forming a map $\mathcal{I} : O \to \mathcal{N}$, *i.e.* from $S^2 \to S^2$. However, if a BH is present, some points in O are actually not mapped to $\mathcal{N}$, as they correspond to light rays that would have originated from the BH. This set of points forms the BH *shadow* (see Fig. 1.4).

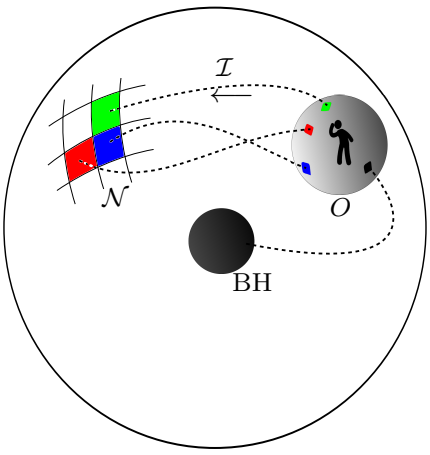


Figure 1.4: Schematics of the observational setup. An observer has a local sky O, forming a map either to the BH or to the sphere $\mathcal{N}$ surrounding them both. Adapted from [31].

In order to represent the map $\mathcal{I}$, and following the setup in [72, 24, 23], one first attributes a color to each point in $\mathcal{N}$ according to a regular pattern, say colored quadrants with a grid. Then for each point in O that is not part of the shadow one can compute the color in $\mathcal{N}$ as provided by the map $\mathcal{I}$. The shadow is simply represented in black.

Using the observer frame constructed in section 1.2, comparable sections of O are projected into $\mathbb{R}^2$ *observational images* in Fig. 1.5, not unlike the Cartesian-like plane in Fig. 1.3. In particular, the image's x and y-axis represent respectively the azimuthal and latitude coordinates of the local sky O, with the origin pointing to the center of the sphere $\mathcal{N}$, where the BH can lie.

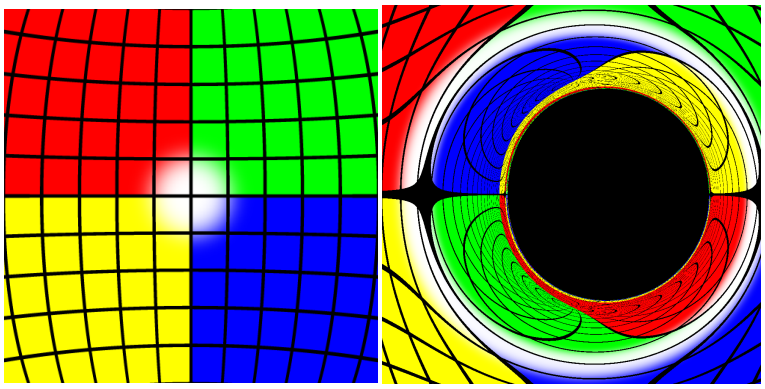


Figure 1.5: (*Left*) Observational images in O for: flat spacetime; (*right*): a Kerr BH with $a/M \simeq 0.82$. The observer is set on the equatorial plane. Adapted from [23].

The left image in Fig. 1.5 displays the observational image in flat spacetime. Since the light rays are not affected by the gravitational field in this case, this image is quite representative of the color pattern in $\mathcal{N}$ that is directly on the line of sight of the observer. In particular, notice that the white dot is in the image center.

By placing a Kerr BH in the center of the sphere $\mathcal{N}$ and considering an observer in similar observation conditions (see right image of Fig. 1.5), the white dot is now stretched into a white circle, known as an *Einstein-ring*. Inside the latter one can recognize the Kerr shadow with $a/M \simeq 0.82$, and although it might be unclear from the image, the entire sphere $\mathcal{N}$ is mapped an infinite number of times in-between the Einstein ring and

the shadow edge.

We remark that there is a subtle point in what can be regarded as *similar observation conditions*. For instance, take two different spacetimes with distinct geometries (say two Kerr BHs with different spin a). Naively placing the observer at the same radial coordinate r in both spacetimes might be geometrically meaningless, since the coordinate chart will in general have different meanings for each spacetime manifold. Thus at this point it is necessary to introduce a *criteria* for what is considered a *similar observation*.

We now define two observers in the equatorial plane to be in similar observation conditions if the perimetral radius $\tilde{r}$ is the same for both observers (see (1.18)). This implies

$$\sqrt{g_{\varphi\varphi}{}^{(1)}} = \sqrt{g_{\varphi\varphi}{}^{(2)}}, \tag{1.30}$$

where each superscript (1) and (2) labels the respective space-time. This criteria has a well defined geometrical meaning, since it is anchored on the proper distance along integral curves of the azimuthal Killing vector $\boldsymbol{\xi}$, and the $\mathbb{Z}_2$ reflection symmetry of the equatorial plane.

As an example, a point on the Kerr spacetime with a radial coordinate r and $\theta = \pi/2$ has a perimetral distance:

$$\tilde{r} = \sqrt{r^2 + a^2 + \frac{2Ma^2}{r}}. \tag{1.31}$$

The inversion of this equation leads to:

$$r = 2\sqrt{\frac{\tilde{r}^2 - a^2}{3}} \cos\left(\frac{1}{3}\arccos\left[\frac{3a^2M}{a^2 - \tilde{r}^2}\sqrt{\frac{3}{\tilde{r}^2 - a^2}}\right]\right). \tag{1.32}$$

So, given a radius $\tilde{r}$ in flat space, we can compute the equivalent radial coordinate r in Kerr space-time with a similar observation condition. We remark that in practice, the difference $(\tilde{r} - r)$ will quite small compared with $\tilde{r}$, unless the Kerr observer is very close to the BH. For example, for $a = 0.999M$ we have $\tilde{r} = 15M \implies r \simeq 14.96M$. For sim-

plicity, most observational images are generated with an observer at $\tilde{r} = 15M$, whereas $\mathcal{N}$ is placed at $\tilde{r} = 30M$.

1.5 Light rings (LRs) and Fundamental Photon Orbits (FPOs)

LRs are a special class of null geodesics, hereafter defined for spacetimes that possess (at least) two commuting Killing vectors $\boldsymbol{\zeta}, \boldsymbol{\xi}$, with $[\boldsymbol{\zeta}, \boldsymbol{\xi}] = 0$; these are associated respectively to stationarity and axial-symmetry of the spacetime, and are expressed in the symmetry adapted coordinates t, φ as $\boldsymbol{\zeta} = \partial_t$, $\boldsymbol{\xi} = \partial_\varphi$. Any null vector tangent to a LR is spanned by a combination of $\boldsymbol{\zeta}$, $\boldsymbol{\xi}$, and it thus geometrically anchored to these symmetries. As a curious particular case, *static* LRs are possible in some spacetimes; an example occurs at the onset of formation of an ergotorus [73]. For a static LR $\boldsymbol{\zeta}$ *alone* is always tangent to the LR orbit.

LRs can be classified according to their dynamical stability under perturbations. *Unstable* LRs play an important role in strong gravitational lensing and in the formation of BH shadows. For instance, in the paradigmatic Kerr BH of GR all the LRs are unstable. Their existence allows light to encircle the BH any number of times before being either scattered back to infinity or plunged into the BH, embodying a scattering threshold. In particular, from an observation perspective, LRs contribute to the boundary of the Kerr shadow. However, we remark that (in general) LRs are not necessarily connected to a shadow edge, namely if multiple unstable LRs are available, or if horizonless UCOs are considered [24, 25].

In contrast to the previous case, *stable* LRs if perturbed can revolve closely to the equilibrium trajectory. Although not as common as their unstable relatives, there are multiple examples in the literature which feature stable LRs, *e.g.* Boson and Proca stars, Kerr BHs with bosonic hair (see Chapters 2 – 4) and even wormholes [24, 25, 9]. One can

anticipate that if the spacetime is perturbed, different modes can accumulate and build-up close to a stable LR position, eventually leading to a back-reaction on the spacetime. This intuition was reinforced in a paper by Keir [26], in which the existence of a stable LR sets a decay limit for linear waves, being highly suggestive of a non-linear instability (see Section 4.3). In fact, as discussed in Section 1.5.3, horizonless UCOs that are physically reasonable (*e.g.* smooth, topologically trivial), must have a *stable* LR and are hence prone to non-linear instabilities [10].

Despite the close connection between LRs and the shadow edge, the former do not entirely determine the latter. Consider again the Kerr case, wherein geodesic motion is Liouville integrable and separates in Boyer-Lindquist coordinates $(t, r_{BL}, \theta, \varphi)$ [63]. For such coordinates, orbits with a constant r_{BL} exist, known in the literature as *spherical orbits* [66] (see Section 1.1). The subset restricted to the equatorial plane, *i.e.* the surface of $\mathbb{Z}_2$ reflection invariance, are two LRs with co(counter)-rotation with respect to the BH. These LRs coincide in the Schwarzschild limit at $r_{BL} = 3M$, where M is the Arnowitt-Deser-Misner (ADM) mass [74, 75]. The set of spherical orbits completely determines the edge of the Kerr shadow, embodying a scattering threshold similar to LRs.

From the viewpoint of an observer which sees the Kerr BH lit by a distant (background) celestial sphere, an increasingly larger number of copies of the whole celestial sphere accumulate as we approach an edge in the observer's sky. This edge, parameterized by observation angles, sets the boundary of the Kerr shadow, with each point of the boundary associated to a particular spherical orbit, see Section 3.3.3. We remark that the LRs only determine two points of the shadow edge, if the observer is on the equatorial plane.

As it is apparent from section 1.1, a vector tangent to a spherical orbit is not (generically) spanned by $\boldsymbol{\zeta}$, $\boldsymbol{\xi}$, in contrast to LRs. Hence, despite being the natural generalisations of the latter, spherical orbits are intrinsically a different identity. Moreover, orbital analogues of the spherical orbits can exist for spacetimes other than Kerr, even if the geodesic

motion is not integrable (see also [76]). Following previous work [11, 77], these orbital generalisations will be designated as *Fundamental Photon Orbits* (FPOs).

Similarly to LRs and Kerr's spherical orbits, FPOs are defined for spacetimes with the Killing vectors $\boldsymbol{\zeta}$, $\boldsymbol{\xi}$, although they have a more complicated formulation. In particular, notice that Kerr spherical orbits were defined in terms of a "constant radius" in Boyer-Lindquist coordinates, which is not an invariant statement. Moreover, a similar criteria in spacetimes for which separability is unknown is meaningless, since $r_{BL} = const.$ is not preserved by mixing r_{BL} and θ, and no basic property favors a particular coordinate chart.

Nevertheless, for generic stationary and axisymmetric spacetimes, one can define FPOs as follows [11]:

Definition: let $s(\lambda) : \mathbb{R} \to \mathcal{M}$ be an affinely parameterised null geodesic, mapping the real line to the space-time manifold $\mathcal{M}$. $s(\lambda)$ is a FPO if it is restricted to a compact spatial region – it is a bound state – and if there is a value $T > 0$ for which $s(\lambda) = s(\lambda + T), \forall\, \lambda \in \mathbb{R}$, up to isometries.

In short, this definition simply requires that an FPO is periodic on the coordinates (r, θ), by the coordinate notation used, as (t, φ) are connected to Killing vectors.

To summarise, FPOs in Kerr are provided by spherical photon orbits, which include LRs as a susbset. All FPOs in Kerr are unstable outside the horizon, but more generically FPOs can also be *stable*, potentially leading to non-trivial spacetime instabilities by analogy with the stable LRs. As discussed in [11], FPOs can also be paramount in understanding the detailed structure of more generic BH shadows. For instance, consider section 1.6, wherein the interaction between different unstable FPOs can give rise to non-trivial effects at the level of the shadow edge, namely a cusp (see also Chapter 3).

1.5.1 Shadow sketch

As an application of the FPO concept, consider the Schwarzschild case by setting $a = 0$ for the Kerr metric. Combining equations (1.4)-(1.6) we have:

$$\chi + \eta^2 = 3r^2, \qquad (\chi + \eta^2)\cos^2\theta_* = \chi,$$

whereas from (1.29) one concludes that $r = 3M$ for all FPOs. For the sake of simplicity, consider a far away observer on the equatorial plane ($\theta_o = \pi/2$), leading to a y shadow coordinate of

$$y = \pm\sqrt{3}\, r\cos\theta_*.$$

Due to spherical symmetry, $r\sin\theta_* = \sqrt{g_{\varphi\varphi}(r,\theta_*)}$, and the expression for y can be re-written in the form:

$$y = \pm\sqrt{3}\,\sqrt{g_{\varphi\varphi}(r,\pi/2) - g_{\varphi\varphi}(r,\theta_*)}. \tag{1.33}$$

This is an exact result for Schwarzschild. One can however develop an approximate method to obtain a shadow for other BHs, knowing only the (multiple) radii r at which FPOs occur, their turning points in "latitude" and also their impact parameters η. We critically assume that the contribution of each FPO to the shadow is similar to that of a Schwarzschild spherical orbit in the *same location*.

Using $x = -\eta$ and equation (1.33), we can make a naive prediction for the shadow shape. In particular, we can retry to obtain the Kerr shadow and compare the result with the exact solution (see Fig. 2.8). For $a = 0$ the approximation is identical to Schwarzschild, since it is the foundation for the method itself. For the almost extremal case $a \simeq 0.999\,M$ there is not a perfect agreement, but the approximation still manages to capture the main features of the correct shadow, in particular the D shape and the horizontal shift. For such a naive calculation, born from spherical symmetry, it is quite surprising. We further remark that this method can be applied with interesting results even for spacetimes that deviate strongly from Kerr, and in which a Carter-like constant is not known, such as Black Holes with scalar hair [13, 12].

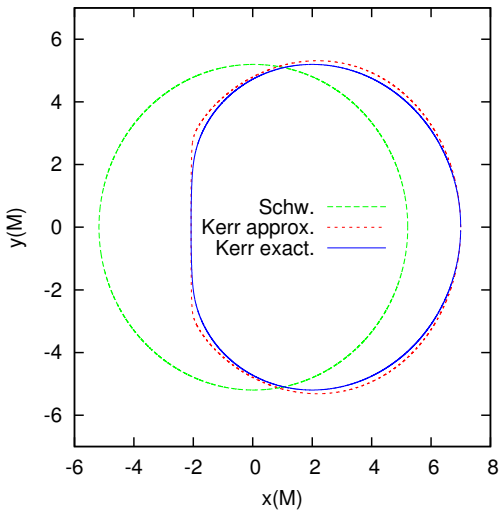


Figure 1.6: Shadow of a Schwarzschild BH and a Kerr BH with $a/M = 0.999$, together with its approximation. The observer is a at infinity in the equatorial plane. The axis are in M units. Adapted from [31].

1.5.2 Effective potentials

The LR structure of a given spacetime can be analysed even if the the geodesic motion is not fully integrable. The introduction of effective potentials will be particularly useful for that purpose.

Consider a 4-dimensional metric, stationary and axially symmetric, written in quasi-isotropic coordinates (t, r, θ, φ) [24, 10]. The coordinates t, φ are connected respectively to the commuting azimuthal and stationarity Killing vectors $\boldsymbol{\zeta}$, $\boldsymbol{\xi}$, with the metric being invariant under the simultaneous reflection $t \to -t$ and $\varphi \to -\varphi$. No reflection symmetry $\mathbb{Z}_2$ will be required in this section on the equatorial plane $\theta = \pi/2$, and a gauge condition is chosen in order to have $g_{r\theta} = 0$, with both $g_{rr} > 0$, $g_{\theta\theta} > 0$. In order to prevent closed time-like curves we further require $g_{\varphi\varphi} > 0$. Unless otherwise specified, no assumptions are made on the field equations, with the results applying to any metric theory of gravity in which photons follow null geodesics.

The Hamiltonian $\mathcal{H} = \frac{1}{2} g^{\mu\nu} p_\mu p_\nu = 0$ determines the null geodesic flow, where p_μ denotes the photon's four-momentum. The Killing vectors $\boldsymbol{\zeta}$, $\boldsymbol{\xi}$ yield the constants of

geodesic motion $E \equiv -p_t$ and $L \equiv p_\varphi$, respectively interpreted as the photon's energy and angular momentum at infinity.

The Hamiltonian can be split into a sum of two parts: a potential term, $V(r,\theta) \leqslant 0$ and a kinetic term, $K \geqslant 0$: $2\mathcal{H} = K + V = 0$, where

$$K \equiv g^{rr} {p_r}^2 + g^{\theta\theta} {p_\theta}^2$$

$$V = -\frac{1}{D}\left(E^2 g_{\varphi\varphi} + 2E\, L g_{t\varphi} + L^2 g_{tt}\right), \tag{1.34}$$

where $D \equiv g_{t\varphi}^2 - g_{tt} g_{\varphi\varphi} > 0$. Since the LR's tangent vector is spanned by $\boldsymbol{\zeta}$, $\boldsymbol{\xi}$, then at a LR $p_r = p_\theta = \dot{p}_\mu = 0$, where the dot denotes a derivative with respect to an affine parameter. These equalities can be stated in terms of V alone. In particular, notice that from $\mathcal{H} = 0$ we can write:

$$V = 0 \quad \Leftrightarrow \quad K = 0 \quad \Leftrightarrow \quad p_r = p_\theta = 0.$$

Moreover, Hamilton's equations yield:

$$\dot{p}_\mu = -\left(\partial_\mu g^{rr} p_r^2 + \partial_\mu g^{\theta\theta} p_\theta^2 + \partial_\mu V\right)/2.$$

Combining these relations, one can then conclude that at a LR:

$$V = \nabla V = 0\,. \tag{1.35}$$

The potential V has however the disadvantage of depending on the photon parameters (E, L). Below, an alternative potential is constructed that does not have this issue [24, 11].

One should first realise that $L \neq 0$ at a LR. Indeed, consider by *reductio ad absurdum* that $L = 0$ and $E \neq 0$; then by eq. (1.34) $V \neq 0$, and the LR requirement is violated by eq. (1.35). We could also consider the case for which both $E = L = 0$; however this is also not possible, since the energy of a physical photon must be positive for a local observer,

yielding $E > -L\, g_{t\varphi}/g_{\varphi\varphi}$ [24] (see also Section 2.6).

Since $L \neq 0$ at a LR, it is useful to define the (inverse) impact parameter $\sigma \equiv E/L$. With this parameter, V can be factorized as $V = -L^2 g_{\varphi\varphi}(\sigma - H_+)(\sigma - H_-)/D$, where we have introduced the 2D-potential functions $H_\pm$:

$$H_\pm(r,\theta) \equiv \frac{-g_{t\varphi} \pm \sqrt{D}}{g_{\varphi\varphi}}.$$

In contrast to V, these potentials are independent on the parameter σ, and only depend on the metric elements. Additionally, the condition $V = 0$ implies one of the mutually exclusive conditions $\sigma = H_+$ or $\sigma = H_-$ to be true, since $H_\pm - H_\mp = \pm 2\sqrt{D}/g_{\varphi\varphi} \neq 0$. We remark however, that $\sigma = H_\pm(r,\theta)$ is not actually a constraint on $H_\pm$, but it rather determines the required σ in order to have $V = 0$, given (r,θ).

The LR conditions (1.35) in terms of $H_\pm$ are simply transcribed into the single equation $\nabla H_\pm = 0$. In other words, a LR is a *critical point* of the potential $H_\pm$, with the value of the latter only determining the LR impact parameter σ.

The stability of a LR can be inferred by the second derivatives of the potentials. In particular, a LR is stable (unstable) along a coordinate x^μ if $\partial_\mu^2 V$ is positive (negative). In terms of $H_\pm$, at a LR this is translated into:

$$\partial_\mu^2 V = \pm \left(\frac{2L^2}{\sqrt{D}}\right) \partial_\mu^2 H_\pm,$$

i.e. the signs of $\partial_\mu^2 V$ and $\pm\partial_\mu^2 H_\pm$ coincide. The two eigenvectors of the Hessian matrix of $H_\pm$ determine if the LR is a local extremum (saddle point) if both directions have equal (different) stability. In particular, if both directions are stable, then the LR is stable, whereas the latter is unstable if at least one direction is unstable.

1.5.3 Topological charge of a LR

For a continuous family of spacetimes with the Killing vectors $\boldsymbol{\zeta}$,$\boldsymbol{\xi}$, such as *e.g.* Boson or Proca stars [21, 20, 19], the number of LRs is not a constant (see [24, 73]). However there is still a LR related topological quantity that is preserved [10].

Consider the stationary and axially-symmetric spacetimes of section 1.5.2 and a compact and simply connected region X on the (r,θ) plane for which the metric is *smooth*[7]. One can define a map $f:(r,\theta)\to\nabla H_{\pm}$, which maps each point of X with coordinates (r,θ) to a 2D space $Y_{\pm}$ parameterised by the components $\partial^i H_{\pm}$, $i\in\{r,\theta\}$. In particular, a critical point of $\nabla H_{\pm}$ (*i.e.* a LR) is mapped to the origin of $Y_{\pm}$.

Fixing the boundary contribution, one can then compute a topological quantity w, called the *Brouwer degree* of the map, that is preserved under continuous deformations of the map (*i.e.* homotopies) [78, 79]. If $\nabla H_{\pm}=0$ is a regular value of the map, then w can be computed as:

$$w=\sum_k \text{sign}(J_k), \qquad J_k=\det(\partial_i\partial^j H_{\pm})_k,$$

where the sum is over the k^{th} (non-degenerate) LR within the region X. In short, one assigns a topological charge $w_k=\pm 1$ to each LR according to the sign of J_k, *i.e.* the Jacobian of the map at the LR location. The limit case in which two LRs with opposite "charges" exist at the same location (r,θ) corresponds to a *degenerate*[8] LR. Due to its topological character, continuous deformations of the metric (and hence of the potentials $H_{\pm}$) leave the total w preserved. This implies in particular that new LRs are *created in pairs*, with one LR endowed with a $+1$ charge and the other one with a -1 (see Fig. 1.7 for an illustration).

A smooth sequence of solutions within a continuous family of spacetimes can be regarded as a metric deformation, with the assumed symmetries preserved at each stage.

[7] Actually it needs to be at least 2^{nd} order differentiable; for simplicity we enforce smoothness, which is a stronger condition, see Section 4.2.

[8] Unless stated otherwise, the LRs under consideration are non-degenerate. See [80] for a discussion of the degenerate case.

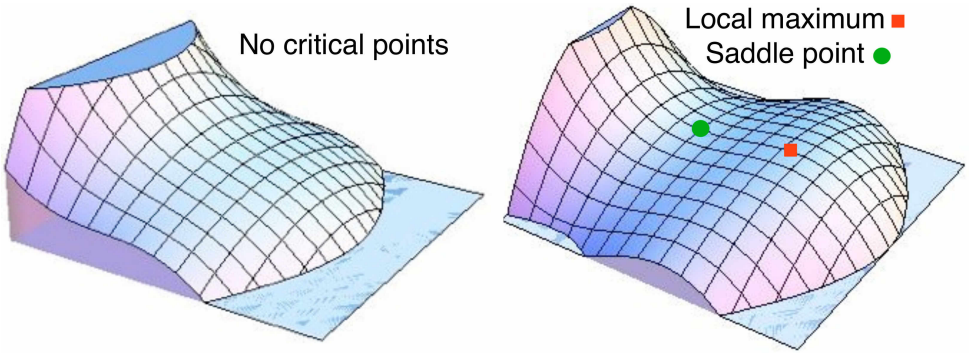


Figure 1.7: Conservation of the Brouwer degree under a continuous deformation of a 2D map $(x, y) \to \nabla H$. We have chosen the illustrative potential $H(x, y) = x(x^2 - a) - (1 + x^2)y^2$, where a is a *local* deformation parameter that does not affect the asymptotic behavior of the map. Left panel: $a = -2$; there are no critical points and the Brouwer degree is zero. Right panel: $a = 1$; there are two critical points, namely one local maximum ($w = +1$) and one saddle point ($w = -1$), with the Brouwer degree still being zero. Adapted from [10].

However, we remark that, even if a family of solutions is not present, a similar topological argument can still exist.

For instance, starting from an approximately flat spacetime, consider an horizonless smooth object that is formed from an incomplete gravitational collapse. Astrophysically, it is reasonable that this final equilibrium state is well described as being stationary, axially-symmetric and asymptotically flat. Moreover, assuming causality, the final state must also be topologically trivial, according to a celebrated theorem by Geroch [81].

In clear contrast to the endpoint states, any intermediate stage of the dynamical collapse is in general neither stationary nor axially-symmetric, unless the collapse process is adiabatic-like. Nevertheless, one can still smoothly deform the endpoint states into each other, via a sequence of *off-shell* spacetimes that possess the Killing vectors $\boldsymbol{\zeta}$,$\boldsymbol{\xi}$. The actual deformation process is irrelevant, being its *existence* that leads to the conclusion that the total w in both the final and initial stages are the same. Since there are no LRs for the initially flat spacetime, w must vanish in both endpoints of the collapse. If our final object has a (non-degenerate) LR (*i.e.* it is an UCO), then it must possess at least another LR, with a symmetric charge.

Furthermore, the stability of each LR can be related to its topological charge. In particular, the analysis of the Jacobian $J = \det(\partial_i \partial^j H_\pm)$ leads to the conclusion that a local maximum (or minimum) of $H_\pm$ has $w = +1$, whereas a saddle point of $H_\pm$ has $w = -1$. Similarly, an identical statement in terms of the potential V can also be performed, leading to three types of LRs:

(a): saddle point of $V \longrightarrow$ unstable LR with $w = -1$

(b): local minimum of $V \longrightarrow$ stable LR with $w = +1$

(c): local maximum of $V \longrightarrow$ unstable LR with $w = +1$

The LRs (a) exist on several spacetimes, namely for the Kerr and Schwarzschild solutions. Moreover, the ringdown signal of the first LIGO events possess the signature of this LR type, as discussed in [9].

Several spacetimes in the literature also feature LRs of the second category (b), with Proca/Boson stars [24, 73, 25] or the Majumdar-Papapetrou di-hole system [77] as possible examples. As was previously discussed, these LRs are expected to operate as a radiation trap, leading to a pile up of energy and to an eventual backreaction on the spacetime, possibly triggering a non-linear instability [26] (see Section 4.3).

Surprisingly, LRs of the last type (c) are not very frequent. In fact, I am not aware of any literature model featuring this type of LR. Moreover, one can show that the existence of these LRs actually implies a violation of the *Null Energy Condition* (NEC), reason why we shall designate these LRs as *exotic* (see details in Section 4.2.3). The NEC plays a pivotal role in GR, namely being a critical assumption of Penrose's singularity theorem [41, 42]. Furthermore, the NEC is often considered to be a robust assumption for a healthy theory of gravity, although there can be exceptions [82].

Assuming Einstein's field equations in geometrized units $G^{\mu\nu} = 8\pi T^{\mu\nu}$, the NEC states that $T^{\mu\nu} p_\mu \, p_\nu \geqslant 0$, where $T^{\mu\nu}$ is the energy-momentum tensor and p_μ is a null vector.

Then one can show (see [10] and Chapter 4) that if p_μ is the LR's four-momentum:

$$T^{\mu\nu}p_\mu p_\nu = \frac{1}{16\pi}\partial_i\partial^i V, \tag{1.36}$$

which is negative if the LR corresponds to a maximum of V. Hence exotic LRs require a violation of the NEC. However, the converse is not necessarily true, as the NEC can be violated at some point other than the location of the LR. In short:

$$\text{Exotic LR} \implies \text{NEC violation}$$

$$\text{NEC violation} \not\Longrightarrow \text{Exotic LR}$$

A similar formulation can hold even in alternative theories of gravity, as long as the field equations can be rewritten as GR with an *effective* energy-momentum tensor, with the NEC now being stated in terms of that tensor. From eq. (1.36), one can further conclude that stable LRs are not possible in vacuum, which is consistent with [83].

In conclusion, if the NEC is enforced, a smooth horizonless UCO that could be a BH mimicker must also possess a stable LR. The latter is then expected to induce a spacetime instability, which possibly creates an issue for these alternative LIGO candidates.

As a final remark, let us mention that if similar topological quantities could be defined for generic FPO families, they could be a powerful tool in the analysis of lensing properties.

1.6 Non-Kerr shadows in GR

Due to the uniqueness theorems, the Kerr spacetime is the only physical BH solution in GR, for *vacuum*. However, when considering matter fields, other BH solutions with possible astrophysical relevance can be found. In particular, scalar and Proca fields are some of the simplest matter models one can consider, giving rise to non-trivial BH solutions coupled to these fields. Among these models, *Kerr BHs with bosonic hair* have gathered attention recently, being both physically reasonable and minimally coupled to 4D grav-

ity [12, 13, 16, 11]. These BHs are fully non-linear solutions of Einstein's gravity with a complex massive scalar (or Proca) field, moreover being stationary, axially-symmetric, asymptotically flat and $\mathbb{Z}_2$ symmetric. These solutions exist within GR (and cousin solutions may exist in alternative theories of gravity), they are regular on and outside the horizon, they satisfy all the energy conditions and have no clear pathologies outside the horizon (*e.g.* close timelike curves or conical singularities). Moreover, Kerr BHs with Proca hair have recently been shown to form dynamically as the endpoint of the superradiant instability, and can thus have a well motivated formation channel [84, 15].

Kerr BHs with bosonic hair exist within a continuous family of solutions, interpolating between (vacuum) Kerr with a test field [85, 86] and the corresponding solitonic limit, namely Boson/Proca stars, which do not possess an event horizon. These hairy BHs can possess a surprisingly rich LR and FPO structure, the interplay of which can lead in some cases to unusual effects at the level of the BH shadow and gravitational lensing. We remark that we assume both the scalar and Proca fields to be completely *transparent* to radiation, interacting with light rays only gravitationally.

As previously mentioned, Kerr BHs with bosonic hair have (vacuum) Kerr as one of the endpoints, and so the lensing and shadow might be indistinguishable from the latter. However, if the scalar/Proca field contains a significant fraction[9] of the total ADM mass, the observational image can be quite different.

Consider for instance the bottom row of Fig. 1.8, wherein the leftmost image displays the shadow of a Kerr BH with scalar hair that is still very Kerr-like, with the lensing removed for clarity. In particular, we remark that the shadow has a slightly different shape (it is more squared) and it is also smaller than a comparable[10] Kerr shadow (see [24, 23] for more details). Nevertheless, the FPO structure is still very similar to Kerr.

However, as displayed in the rightmost image of the bottom row in Fig. 1.8, the shadow

[9] The mass of the central BH can be determined via Komar integrals.
[10] A comparable Kerr BH has the same ADM mass and angular momentum.

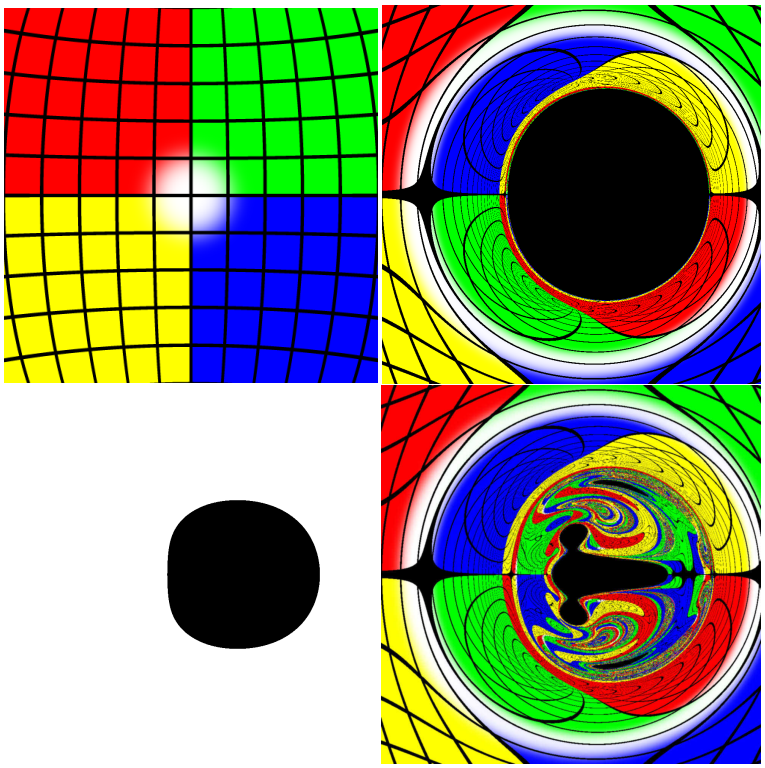


Figure 1.8: (From left to right) Observational images in O for *(top row):* flat spacetime; Kerr BH with $a/M \simeq 0.82$; *(bottom row):* Kerr-like hairy BH; hairy BH with radical deviations, respectively conf. II and III of Chapter 2. Adapted from [23].

of Kerr BHs with scalar hair can be radically different from the Kerr case, both in terms of size, shape and topology [23]. Moreover, the lensing enveloping this hammer-like shadow also displays chaotic-like structures, with the latter being connected to the existence of radiation pockets [24, 77]. The FPO structure of this solution is strikingly different from the Kerr case, which is actually the main reason for these significant differences (for instance, there are four LRs, see Chapter 2). This hairy BH has almost all of the mass and angular momentum stored in the scalar field, heuristically corresponding to a tiny BH inside a rotating Boson star [23]. Similarly, the FPO structure can also be heuristically regarded as the combination of a Boson Star's FPOs and the FPOs of a central BH. As an illustration of this complex arrangement, notice that there is a circular *ghost shadow edge*, with a Kerr-like profile, surrounding the turbulent part of the image. This is a consequence of a FPO that is not actually responsible for the edge of a shadow, although its lensing signature is still present.

1.6.1 Shadow cusp

In order to illustrate the importance and non-trivial role that FPOs can have at the level of the shadow, consider the leftmost image of Fig. 1.9, displaying the shadow of a Kerr BH with Proca hair. In sharp contrast to the previous solutions, the edge of this shadow has a *cusp* and it is thus non-smooth (albeit continuous) [11]. Surprisingly, this feature can be understood as a consequence of a sharp transition between the FPOs responsible for the shadow edge (see Chapter 3).

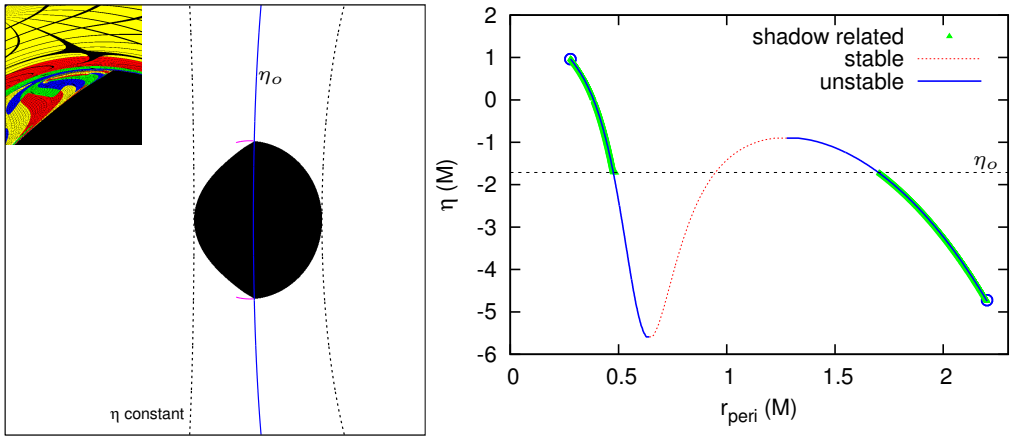


Figure 1.9: *Left:* Shadow of a hairy BH with a cusp. The blue line is the set of points with constant η_o. The inset shows the lensing of a ghost shadow edge (pink curve). *Right:* η as a function of the perimetral radius r_{peri} for a continuous FPO family. Notice the branch transition for FPOs related to the shadow edge. Adapted from [11].

As the geodesic motion is not known to be separable, FPOs in this solution generically exist on a surface with non constant r and with non-trivial motion in θ. Additionally, the FPOs relevant for the shadow have a $\mathbb{Z}_2$ reflection symmetry with respect to the equatorial plane ($\theta = \pi/2$), and each individual FPO intersects this plane at a single radial coordinate r.

Using this property, we can use the intersection radius as a label for each individual

FPO. In particular, the perimetral radius $r_{peri} \equiv \sqrt{g_{\varphi\varphi}}\big|_{\theta=\pi/2}$, computed at each intersection point, is an invariant quantity related to the $\mathbb{Z}_2$ symmetry and to the Killing vector $\boldsymbol{\xi} = \partial_\varphi$. On the right of Fig. 1.9 the impact parameter $\eta \equiv L/E$ of a continuous FPO family is represented as a function of r_{peri}.

There are three main branches within this FPO family, two unstable and one stable, with the endpoints being unstable LRs with opposite rotation. A similar FPO diagram also exists for Kerr, although for the latter the intermediate stable branch does not exist, and the FPO $\eta(r_{peri})$ curve has no backbendings.

The thick green line in the right image represents the FPOs that are actually responsible for the shadow edge. There is a sudden transition between the two unstable branches, as marked by the dashed black line for $\eta_o \simeq -1.7M$. This transition coincides with the cusp, as illustrated by the $\eta_o = const.$ blue line in the left of Fig. 1.9. Also for the latter, two dotted black lines with constant η are represented with the impact parameter of both LRs, each intersecting the shadow at a single point.

Still, one can wonder what is the role of the FPOs that are unrelated to the shadow edge. Curiously, these *bare* FPOs that have $\eta < \eta_o$ produce no observable effect, as they are *cloaked* by the shadow being created by FPOs with larger r_{peri}. However, (unstable)[11] bare FPOs with $\eta > \eta_o$ produce a ghost shadow edge, noticeable at the level of the lensing. This is displayed by the pink eyelashes sprouting from the cusp, on the left of Fig. 1.9.

Similar results have also been reported in [87] for a Konoplya-Zhidenko rotating BH, wherein a transition between spherical orbits leads to a cusp at the level of the shadow. However, in contrast with Kerr BHs with bosonic hair, the geodesic motion is separable in that spacetime.

As a concluding remark, and in order to illustrate the stability properties of FPOs, consider in Fig. 1.10 two examples of the latter, dubbed A and B. These are displayed

[11] Stable FPOs can also contribute to the lensing despite not producing a sharp signature.

as blue lines in the figure, together with their perturbed versions in red, to further illustrate their stability. The x-axis display the radial coordinates r shifted by $\tilde{r}$, which is respectively the radius at which each FPO intersects the equatorial plane.

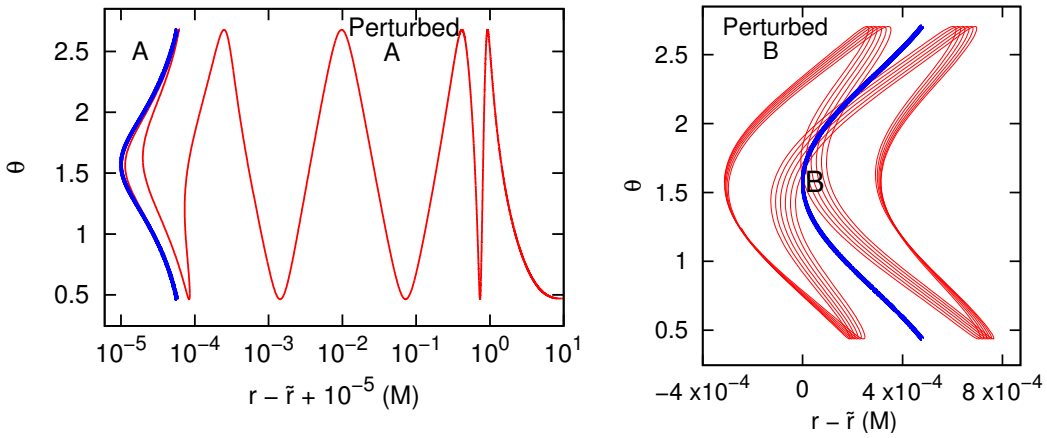


Figure 1.10: Projection of two FPOs (A and B) on the (r, θ) plane (blue lines). Illustrative perturbations of these orbits are displayed in red, suggesting that B (A) is stable (unstable). Adapted from [31, 11].

The FPO A is represented in the left of Fig. 1.10, wherein the x-axis has an additional *ad-hoc* radial shift of 10^{-5} (notice that the latter is necessary in order to keep all of A visible under the use of a logarithmic scale). The perturbed A orbit is clearly unstable, with the deviation increasing several orders of magnitude in the course of a few oscillations.

In contrast to the latter, the FPO B in the right of Fig. 1.10 appears to be stable, as suggested by its perturbed version. Indeed, the perturbed B orbit never deviates significantly from B, simply revolving around the latter as if it was an equilibrium point. We remark that a more precise measure of stability can be made in terms of the Poincaré section of these orbits on the equatorial plane, leading to the same conclusion [11, 88] (see Chapter 3).

It is also relevant to mention that the displayed FPOs (in blue) have motion in all coordinates, and in particular these FPOs do not exist at a single r for the chosen coordinate chart. We further stress that a pure FPO is periodic in the (r, θ) plane, *i.e.* both

A and B are always projected to the respective blue lines in the figure, never leaving the latter.

1.7 Lensing by a horizonless UCO

As previously discussed in section 1.6, FPOs can produce sharp effects on the observational image without being connected to the edge of a shadow. This idea will be further reinforced in this section by analysing the gravitational lensing of a particular horizonless UCO: a static Proca star with spherical symmetry [22, 25], containing a LR pair with opposite stability.

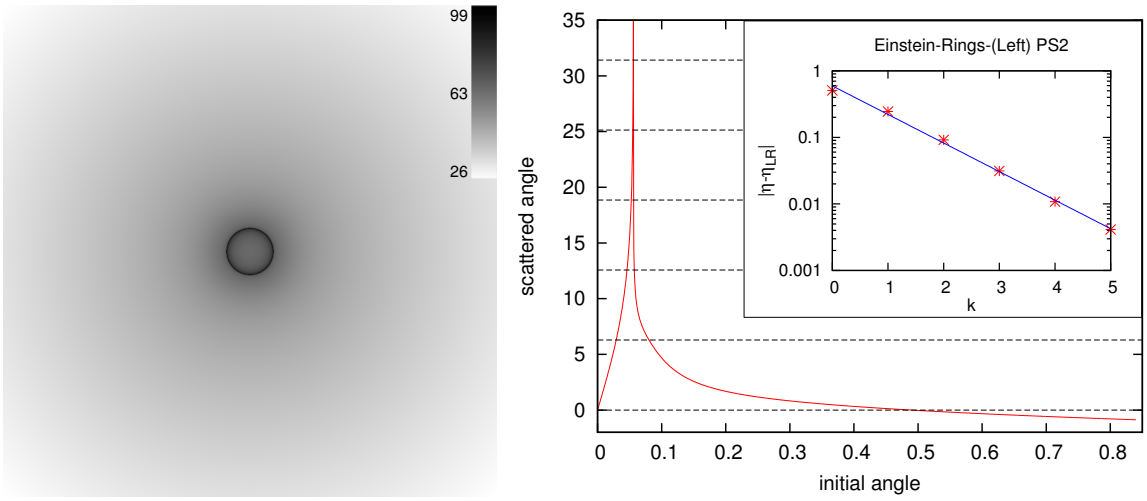


Figure 1.11: *Left:* time delay map (t in M units) for a static spherically symmetric Proca star. The darker annular region is a signature of the unstable LR. *Right:* scattered angle as a function of the initial angle; the inset illustrates how well the logarithmic divergence approximates the position of the Einstein rings in the image. Adapted from [25].

Consider the left of Fig. 1.11, displaying the geodesic *time delay* of the Proca star observational image [25]. This time delay map is similar to the images in Fig. 1.8, although the grey levels now represent the variation of the time coordinate t between $\mathcal{N}$ and O (see Fig. 1.4). This representation sharply reveals an annular region in the sky for which photon motion is much more time consuming. Not too surprisingly, this region is

connected to an (unstable)[12] LR orbit.

Although there is no event horizon present, and hence no shadow, the attentive reader might notice an uncanny resemblance to a shadow, which is not a coincidence. This particular Proca star has a high density core, leading to a very large redshift of any radiation emitted close to the star's center. In this regard, this configuration is closely related to the concept of a *frozen star* [89], the latter being the shadowy afterglow of a star collapsing into a BH, as seen by a faraway observer (see also [90]). Indeed, as discussed in [25], the fully dynamical evolution of this Proca star quickly leads to a gravitational collapse into a Schwarzschild BH, as this spacetime is plagued with several instabilities (the stable LR might contribute to this). However, despite the resemblance, the angular size of the (final) BH shadow is larger than the (initial) star's annular region, as most of the Proca field mass exists outside the star's unstable LR.

Since this Proca star is spherically symmetric, the gravitational lensing can be fully described by a 1D scattering process on the equatorial plane. In particular, the initial angle is provided by the (angular) distance with respect to the observational image center (*i.e.* in O), whereas the scattered angle is the final angle on $\mathcal{N}$, with its origin on the point that would be directly in front of the observer in flat spacetime.

The plot on the right of Fig. 1.11 displays the scattering angle, as a function of the initial angle, with the scattering divergence being a clear signature of the unstable LR. Curiously, the scattering profile for the Schwarzschild BH is quite similar, except for the left part of the peak which would be replaced by the Schwarzschild shadow.

Due to symmetry, if the scattered angle is a multiple of π, then there are points in O along a ring that are mapped to a single point in $\mathcal{N}$, forming a caustic (see also [71]). These rings, commonly known as *Einstein rings*, already appeared in Fig. 1.8, with the large white circle being the clearest example. The latter is the lensing of the white point

[12]The stable LR does not have such a clear lensing signature.

in $\mathcal{N}$ that would be directly in front of the observer in flat spacetime. Hence, any scattering angle multiple of 2π would lead to such a white circle in O. However, a scattering angle of an *odd* multiple of π also leads to an Einstein ring, although it corresponds to the lensing of the point in $\mathcal{N}$ that would be directly *behind* the observer. With no loss in generality, we shall focus on the first case.

Due to the LR scattering singularity, there is an infinite number of Einstein rings in the image that pile-up close to the LR edge. This LR feature is manifested when representing multiples of 2π on the right of Fig. 1.11 using horizontal lines. Moreover, since this divergence of the scattering angle close to the LR is logarithmic, one can write the impact parameter of the k^{th} Einstein ring, corresponding to a scattering angle of $2\pi k$, as:

$$\eta_{ER}^{(k)} \simeq \eta_{LR} + be^{-2\pi k/a},$$

where η_{LR} is the impact parameter of the (unstable) LR and $\{a, b\}$ are constants [91]. We remark that, despite not being an angle, the impact parameter $\eta \equiv L/E$ can be used to parametrize the initial angle in O (*e.g.* see Fig. 1.9). In the inset of the right image of Fig. 1.11, the numerical values of $|\eta_{ER} - \eta_{LR}|$ are represented as red points, together with the best fit (in blue) to the logarithmic approximation above, showing a good approximation even for the lowest k orders.

1.8 Non-Kerr shadows in alternative gravity theories

The discussion in the previous sections only considered spacetimes within GR. However, there are strong theoretical motivations (*e.g.* non-renormalizability and curvature singularities) to search for alternative theories to Einstein's GR [30]. Higher order curvature corrections can be included in the action as a simple GR generalization, often leading to field equations with higher order derivatives. Due to covariance, this also leads to time derivatives higher than second order, resulting in unphysical run-away modes (Ostrogradsky instabilities [28]).

Nevertheless, by a cleaver combination of higher curvature terms in the Lagrangian, it is still possible to obtain field equations that are at most second order. In particular, Lovelock [29] established that in vacuum gravity the most general such combination is provided by the Euler densities $\mathcal{E}_n$, with the latter being scalar polynomial arrangements of the curvature tensor of order n. In particular for $D = 4$ dimensions, the most general (vacuum) Lovelock theory is a linear combination of $\mathcal{E}_0$ and $\mathcal{E}_1$, simply corresponding to GR with a cosmological constant. Euler densities of higher order, such as the *Gauss-Bonnet* combination $\mathcal{E}_2$, are topological constants in $D = 4$, thus not leading to any dynamical contribution when applying the variational method. Nevertheless, by simply coupling $\mathcal{E}_2$ to a dynamical scalar field, the 2^{nd} Euler density can generate a non-trivial effect, giving rise to a new theory.

The latter model, known in the literature as *Einstein-dilaton-Gauss-Bonnet* (EdGB), occurs naturally as the low energy limit of string theory [92] and can also be regarded as an effective description of higher curvature corrections. BHs can be found within the EdGB theory, both in the static [93, 94, 95, 96, 97, 98, 99] and rotating case [100, 101, 102, 103, 104, 105]. These BH solutions can moreover be perturbatively stable, asymptotically flat and regular, possessing a dilatonic field as a form of non-independent *hair* [30, 14].

We further remark that the Gauss-Bonnet term can be interpreted as an *effective* energy momentum-tensor within plain GR, hence representing some type of *exotic matter* that can violate energy conditions [30, 14]. One could expect that the distribution of this exotic matter around a EdGB BH would lead to some type of sharp signature at the level of the shadow. However, rather surprisingly, this does not appear to be the case. To illustrate this point, consider Fig. 1.12, wherein the shadow of a rotating EdGB BH is compared with the corresponding Kerr shadow, with the same global ADM quantities. The difference in the shadow size is almost imperceptible (around $\simeq 1.4\%$), with the latter being a representative case of most of the EdGB solution space. The main reason for this result appears to be the small variation of the FPO structure with respect to Kerr. Since most of the non-trivial physics exists just outside the horizon, but still enclosed by the

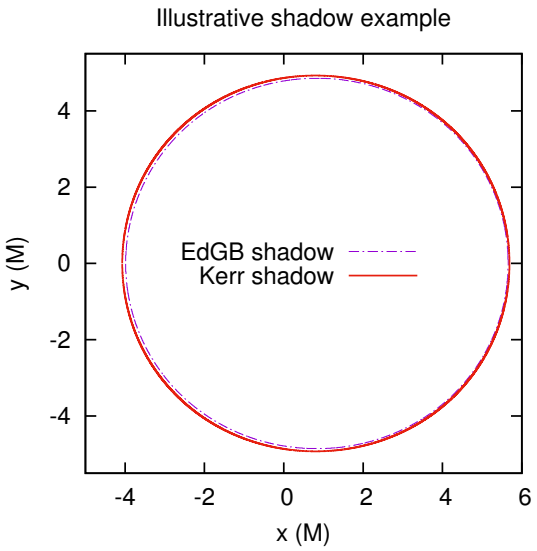


Figure 1.12: Shadow of a representative rotating EdGB BH and its comparable Kerr BH ($a/M \simeq 0.41$). Adapted from [30].

FPO structure, any potential new signature from the Gauss-Bonnet term appears to be *hidden* by the BH shadow.

This particular model illustrates the fact that new theories of gravity need to significantly modify the LR and FPO structure of the Kerr BH in order to generate a sharp signature at the level of the shadow. More details in Chapter 5.

Remarks

Almost 100 years ago, Eddington's observation of light deflection by the sun – *weak gravitational lensing* – played a key role in establishing GR as a physical model of the Universe. With the advent of new observation channels, namely the Event Horizon Telescope, the detection of *strong gravitational lensing* is finally within reach. This prospect has led to a renewed interest, in the XXIst century, on what is a standard problem in GR: the motion of light around compact objects and in particular the computation of the shadows of BHs. There is already a vast recent literature studying these problems in many different models, see *e.g.* [106, 107, 108, 109, 110, 111, 112, 113, 114, 115, 116, 117, 118, 119, 120, 121,

122, 123, 124, 125, 126, 127, 128, 129, 130, 131, 132, 133, 134, 135, 136, 137, 77, 83, 138, 23, 139, 140, 141, 142, 32, 143, 144, 145, 146, 147, 148, 149, 150, 87, 151, 152, 153, 154, 155, 156, 157]. For *ultra* compact objects (UCOs), Light Rings (LRs) and Fundamental Photon Orbits (FPOs) have a pivotal role in the theoretical analysis of these effects, and of BH shadows in particular. This introduction aims to be a brief overview and reflection on some of these concepts, substantiated by sharp examples, before discussing them in more detail in the following chapters.

Chapter 2

BHs with scalar hair

A set of influential theorems that became known as the *uniqueness theorems*, establish that stationary and regular BHs in vacuum GR that are asymptotically flat must be described by the Kerr metric (or Kerr-Newman if electric charge is present, which will not be considered) [12, 58, 59, 60]. A direct consequence of these theorems is that BHs in vacuum are completely described by their total mass M and angular momentum J. This implies that two BHs in vacuum with the same M and J are *identical*, which comes in sharp contrast with more familiar objects, *e.g.* our Sun, that cannot be fully characterised with only two quantities. During the formation of a BH, any residual information other than the mass and spin of the original system must then be radiated away or hidden within the horizon [158].

These theorems have inspired the *conjecture* that the dynamical endpoint of gravitational collapse in the presence of any type of matter-energy configuration must be described by the Kerr metric [14], which is a much stronger statement. This idea was captured in John Wheeler's mantra "BHs have no hair", where the *hair* is a metaphor for additional parameters that are required to fully describe the spacetime that can be associated to matter fields outside the horizon [14]. From of all the possible descriptions of matter, scalar fields are one of the simplest, and so it is natural to search for BH solutions coupled to these fields. The discovery in 2012 of a scalar particle in the Large Hadron Collider (at CERN), identified as the Higgs boson [159, 160], further motivates

considering fundamental scalar fields in astrophysical contexts. Moreover, they can be used as a proxy for perfect fluids and dark matter [14].

In a recent letter [23], it was studied the lensing and shadows of a deformed type of Kerr BHs, known as *Kerr BHs with scalar hair* (KBHsSH) [12, 13, 161] (see also [162, 163, 14, 164, 22, 165, 166, 16, 167, 168, 169, 170, 171, 172, 173] for generalizations and physical properties) with some potential astrophysical relevance. These are solutions to Einstein's gravity minimally coupled to a simple and physically reasonable matter content: a complex, massive, free scalar field. KBHsSH interpolate between a (subset of) of vacuum Kerr BHs, when the scalar field vanishes, and horizonless, everywhere regular, gravitating scalar field configurations known as Boson Stars (BSs) [18, 21], when the horizon vanishes. For KBHsSH, the massive scalar field neither relies on non-linear matter effects nor self-interactions as means to sustain itself against gravitational collapse into the BH. Instead, KBHsSH are the non-linear generalization of scalar clouds for a back-reacting scalar field, living at the threshold of superradiant instability. These solutions evade well-known *no-hair theorems*, which can for example assume that the scalar field is real or that it shares the same symmetries as the space-time, which is not the case here [14].

The lensing of both KBHsSH and their solitonic limit [rotating boson stars (RBSs)] was observed to exhibit chaotic patterns for solutions in some region of the parameter space, as illustrated by the example in Fig. 2.1. Chaotic scattering in GR spacetimes has been observed and discussed in binary or multi-BH solutions – see, *e.g.*, [174, 175, 176, 177, 178, 179, 180, 181, 182, 77, 83, 183] – and is well known in the context of many body scattering in classical dynamics, for example the scattering of charged particles off magnetic dipoles [184] and the 3-body problem (see *e.g.* [185]). KBHsSH, or RBSs, provide an example of chaos in geodesic motion on the background of a single compact object, which moreover solves a simple and well defined matter model minimally coupled to GR.[1] Additionally, these objects possess a rich geometric structure, and may contain both multiple

[1]Chaotic geodesic motion has also been reported around BHs surrounded by disks [186, 187]. These models have some parallelism with KBHsSH, since the scalar field of the latter have a toroidal-type energy distribution, around the horizon.

light rings [23], including a stable one, as well as a structure of ergoregions [162, 167]. The purpose of this chapter is to investigate, in detail, chaotic scattering in this family of backgrounds and its interplay with the above geometric structure.

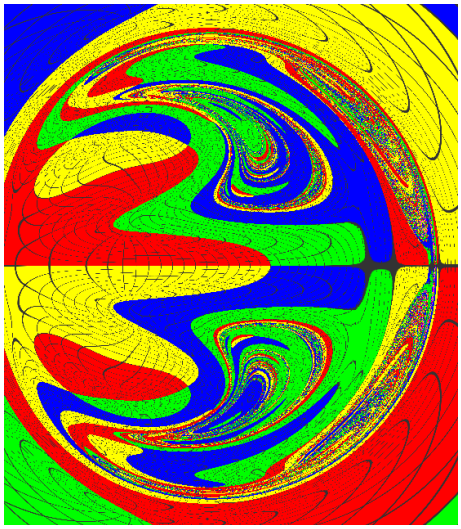


Figure 2.1: Example of a RBS exhibiting chaotic scattering, which can be clearly seen in some fringes on the right hand side (wherein neighbouring pixels present different colours). The setup for this figure is explained in [23] (see Section 2.7 below), and this image corresponds to configuration 11 therein (zoomed). Adapted from [24].

2.1 Boson Stars and KBHsSH

Consider a complex massive scalar field ϕ minimally coupled to Einstein's gravity. The action $\mathcal{S}[g_{\mu\nu}, \phi]$ is given by:

$$\mathcal{S}[g_{\mu\nu}, \phi] = \int d^4x\sqrt{-g}\left[\frac{R}{16\pi} - \nabla_\nu\phi\nabla^\nu\phi^* - \mu^2\phi^*\phi\right], \tag{2.1}$$

where g is the determinant of the metric, R is the Ricci scalar and μ is the mass of the scalar particle. Besides the Einstein field equations, the variational principle yields the massive Klein-Gordon equation for the field: $\nabla_\nu\nabla^\nu\phi = \mu^2\phi$. It is possible to find a family of BH solutions in equilibrium with the scalar field: *Kerr BHs with scalar hair* (KBHsSH) [12, 13]. This family has (a subset of) vacuum Kerr space-time and Rotating

Boson Stars (RBS) as limiting cases (see the existence space of solutions in Fig. 2.2). We further remark that KBHsSH are solutions to Einstein's gravity minimally coupled to a simple and physically reasonable matter content, which satisfies all energy conditions, and is regular on and outside the horizon. In contrast to the Kerr case, wherein the boundary of the ergoregion is topologically *spherical*, some RBS can possess ergoregions with *toroidal* topology: an ergo-torus. As a consequence, some KBHsSH can have disconnected ergoregions with different topologies: an ergo-Saturn [13].

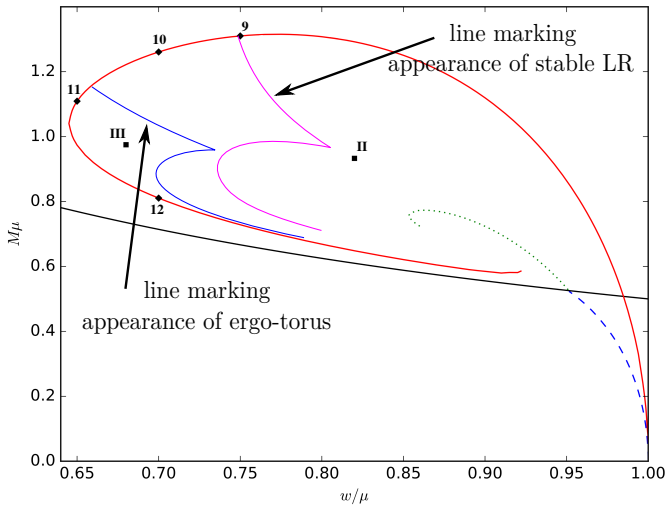


Figure 2.2: RBS solutions (solid red spiral) in a ADM mass, $M_{\rm ADM}$, *vs.* scalar field frequency w diagram. KBHsSH exist within the RBS spiral and are bounded by a subset of Kerr solutions (dashed blue line), extremal KBHsSH (dotted green line) and the RBS spiral itself. Points 9 - 12 (II - III) correspond to the BSs (KBHsSH) under discussion. Two extra lines mark the appearance of a stable light ring (LR) and an ergo-torus, always to the left of these lines. See [23, 12, 162] for more details. Adapted from [24].

In this chapter we shall take the following ansatz for the line element:

$$ds^2 = -e^{2F_0} N dt^2 + e^{2F_1}\left(\frac{dr^2}{N} + r^2 d\theta^2\right) + e^{2F_2} r^2 \sin^2\theta (d\varphi - W dt)^2 \,, \tag{2.2}$$

where $N = 1 - r_H/r$ and r_H is the radial coordinate of the horizon (for RBSs $r_H = 0$). The ansatz for the scalar field is given by:

$$\phi = \widetilde{\phi}(r,\theta) e^{i(m\varphi - wt)}, \tag{2.3}$$

where w is the field frequency and m is an integer named azimuthal harmonic index. The explicit form of the functions $\widetilde{\phi}, F_0, F_1, F_2, W$, all of them functions of (r, θ), is only known numerically (examples can be found in [188]). All elements of this family are stationary[2] and axially symmetric, with the coordinates $\{t, \varphi\}$ adapted to the corresponding Killing symmetries. In addition, these solutions satisfy the circularity condition, *i.e.* invariance under $\{t, \varphi\} \to -\{t, \varphi\}$, and are $\mathbb{Z}_2$ symmetric with respect to the equatorial plane $\theta = \pi/2$.

We remark that the existence of a Carter constant Q is a special property of Kerr, consequence of an hidden symmetry (a non-trivial Killing tensor). Since such a symmetry is not known (or expected) to exist in this case, it is not possible to reduce all the four geodesic equations to first order. The geodesic motion of a photon on a background spacetime $(\mathcal{M}, g_{\mu\nu})$, assuming minimal coupling between the (photon's) electromagnetic field and the geometry, is described by the Hamiltonian

$$\mathcal{H} \equiv \frac{1}{2} p_\mu p_\nu \, g^{\mu\nu} = 0 \ , \tag{2.4}$$

where p_μ are the 4-momentum components of the photon orbit and $g^{\mu\nu}$ is the inverse metric. For convenience we will now repeat some of the discussion in Section 1.5.2. Explicitly, the Hamiltonian takes the form

$$p_r^2 g^{rr} + p_\theta^2 g^{\theta\theta} + p_t^2 g^{tt} + p_\varphi^2 g^{\varphi\varphi} + 2\, p_t \, p_\varphi \, g^{t\varphi} = 0 \ . \tag{2.5}$$

Since the quantity

$$K \equiv p_r^2 g^{rr} + p_\theta^2 g^{\theta\theta} \geqslant 0 \ , \tag{2.6}$$

is positive definite, we can write the Hamiltonian condition in the form

$$2\mathcal{H} = K + V = 0 \ , \tag{2.7}$$

[2]The spacetime is stationary and axially-symmetric; however the full solution with ϕ is not, due to the explicit time dependence: there is a single helicoidal Killing vector [13].

and identify the problem with a mechanical system with vanishing total energy, kinetic energy K and potential energy V

$$V \equiv p_t^2 g^{tt} + p_\varphi^2 g^{\varphi\varphi} + 2\, p_t\, p_\varphi\, g^{t\varphi} \leqslant 0 \ . \tag{2.8}$$

This inequality defines the *allowed region* in the (r, θ)–space. The geodesic equations are obtained from Hamilton's equations:

$$\dot{x}^\mu = \frac{\partial \mathcal{H}}{\partial p_\mu} \ , \qquad \dot{p}_\mu = -\frac{\partial \mathcal{H}}{\partial x^\mu} \ , \tag{2.9}$$

where the dot denotes differentiation with respect to an affine parameter. In coordinates adapted to the stationarity and axi-symmetry, $\mathcal{H}$ does not depend on t and φ, and both p_t and p_φ are constants of the geodesic motion. We can then define the integrals of motion E and L which are interpreted as the photon's energy and angular momentum, as measured by an asymptotic static observer (assuming asymptotic flatness):

$$E \equiv -p_t \qquad L \equiv p_\varphi \ . \tag{2.10}$$

Inserting these terms in equation (2.8) for V we obtain

$$V = -\frac{1}{D}\left(E^2 g_{\varphi\varphi} + 2EL g_{t\varphi} + L^2 g_{tt}\right) \leqslant 0 \ , \tag{2.11}$$

where

$$D \equiv g_{t\varphi}^2 - g_{tt} g_{\varphi\varphi} = N r^2 \sin^2\theta\, e^{2(F_2+F_0)} \ , \tag{2.12}$$

which implies $D > 0$ outside the horizon. Since we are only interested in the geodesic motion outside the event horizon, and in order to introduce an explicit dependence on the *impact parameter*, η,

$$\eta \equiv \frac{L}{E} \ , \tag{2.13}$$

we define the rescaled potential energy $\widetilde{V}$, such that:

$$-\frac{D\,V}{E^2} \equiv \widetilde{V} = g_{\varphi\varphi} + 2 g_{t\varphi}\eta + g_{tt}\eta^2 \geqslant 0 \ , \tag{2.14}$$

which is a quadratic function of the impact parameter, with (r, θ)-dependent coefficients. Factorizing this function leads to *two effective potentials*, that we now address.

Two effective potentials

The rescaled potential $\widetilde{V}$ can be written in the form:

$$\widetilde{V} = g_{tt}\,(\eta - h_+)\,(\eta - h_-) \geqslant 0\ , \qquad (\text{with} \quad g_{tt} \neq 0)\ . \tag{2.15}$$

This introduces the two functions $h_\pm(r, \theta)$ which we dub the two effective potentials. Their usefulness, is connected to the observation that $h_\pm = \eta \implies \widetilde{V} = 0$. Thus, the *equipotential lines* of $h_\pm(r, \theta)$ give the boundary of the allowed region in the (r, θ)–space, for each value of η. Similar effective potentials can also be found in the literature, *e.g.* [77, 83, 189]. Since the solutions of the quadratic equation are

$$h_\pm \equiv \frac{-g_{t\varphi} \pm \sqrt{D}}{g_{tt}}\ , \tag{2.16}$$

there is a regime transition when g_{tt} changes sign, which is possible outside the event horizon when entering/exiting an ergoregion. These potentials are related to the ones defined in Section 1.5.2 by $H_\mp\, h_\pm = 1$.
For the special case $g_{tt} = 0$, we have

$$\widetilde{V} = 2g_{t\varphi}\left(\eta - \widetilde{h}\right) \geqslant 0\ , \qquad (\text{with} \quad g_{tt} = 0)\ , \tag{2.17}$$

where:

$$\widetilde{h} \equiv -\frac{g_{\varphi\varphi}}{2g_{t\varphi}}\ . \tag{2.18}$$

In the limit $g_{tt} \to 0$, one of the functions $h_\pm$ diverges and the other converges to $\widetilde{h}$.

We remark that the asymptotic limit of the effective potentials (at spatial infinity) is:

$$h_\pm \to \mp r \sin\theta\ . \tag{2.19}$$

In the following two subsections we analyse the effective potentials outside and inside

an ergoregion respectively, and in the subsequent one we examine light rings and spherical orbits.

Outside the ergoregion ($g_{tt} < 0$)

Since $g_{tt} < 0$ holds outside the ergoregion, $-g_{tt}g_{\varphi\varphi} > 0 \implies g_{t\varphi}^2 - g_{tt}g_{\varphi\varphi} > g_{t\varphi}^2 \implies \sqrt{D} > |g_{t\varphi}|$, where we assumed that $g_{\varphi\varphi} > 0$ (absence of closed timelike curves). This condition is verified for all RBSs and KBHsSH that shall be studied in this work. As a consequence, the effective potentials read:

$$h_+ = \frac{-g_{t\varphi} + \sqrt{D}}{g_{tt}} < 0 \ , \qquad h_- = \frac{-g_{t\varphi} - \sqrt{D}}{g_{tt}} > 0 \ . \tag{2.20}$$

A generic plot of $\widetilde{V}$ outside of the ergoregion can be found in Fig. 2.3 (left panel). We conclude that the boundary of the forbidden region in the phase space (r, θ) is given by the equipotential lines defined as:

$$h_+(r,\theta) = \eta, \quad \text{if } \eta < 0 \qquad \text{and} \qquad h_-(r,\theta) = \eta, \quad \text{if } \eta > 0 \ . \tag{2.21}$$

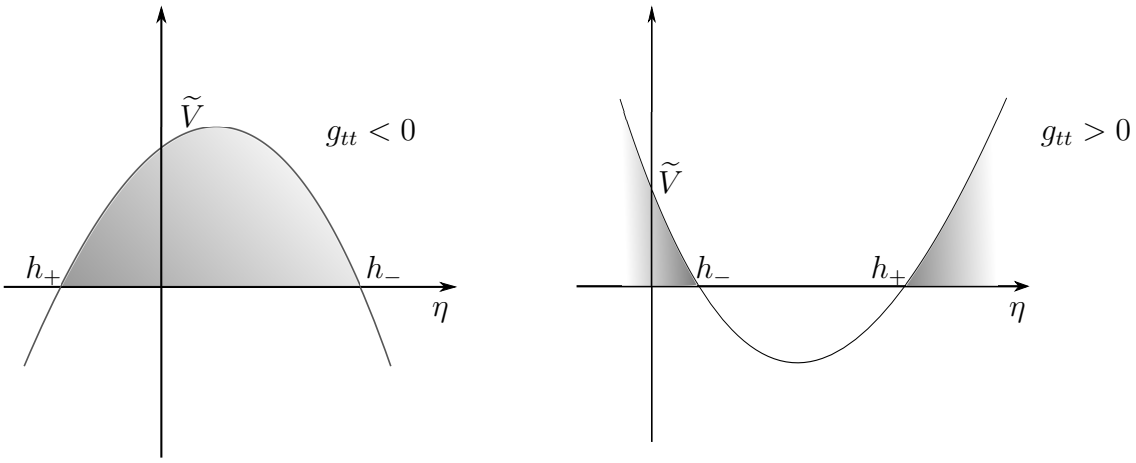


Figure 2.3: Dummy shape of the potential $\widetilde{V}$ (left panel) outside of the ergoregion, $g_{tt} < 0$; (right panel) inside of the ergoregion, $g_{tt} > 0$. The shaded region illustrates the allowed η interval. In the first case, h_+ must always be negative and h_- always positive. Due to the condition $\widetilde{V} \geqslant 0$, we have $h_+ \leqslant \eta \leqslant h_-$. In the second case, if $W > 0$ (spacetime with positive rotation), then $h_\pm$ is always positive, with $h_- < h_+$. Due to the condition $\widetilde{V} \geqslant 0$, we have $\eta \leqslant h_-$ or $h_+ \leqslant \eta$. Since $h_+ \to +\infty$ as $g_{tt} \to 0^+$ the right region is not accessible from spatial infinity. Adapted from [24].

Inside the ergoregion ($g_{tt} > 0$)

Since $g_{tt} > 0$ holds inside the ergoregion, $-g_{tt}g_{\varphi\varphi} < 0 \implies g_{t\varphi}^2 - g_{tt}g_{\varphi\varphi} < g_{t\varphi}^2 \implies \sqrt{D} < |g_{t\varphi}|$, where we again assumed that $g_{\varphi\varphi} > 0$. In this case the sign of the h-functions will depend on the sign of the function W. For the sake of simplicity we will here assume[3] that $W > 0 \implies -g_{t\varphi} > 0$. This will be the case for all configurations analysed afterwards. In such a situation:

$$h_+ = \frac{-g_{t\varphi} + \sqrt{D}}{g_{tt}} > 0 \ , \qquad h_- = \frac{-g_{t\varphi} - \sqrt{D}}{g_{tt}} > 0 \ . \tag{2.22}$$

We remark that $h_+ > h_-$ holds, regardless of the sign of W.

A generic plot of $\widetilde{V}$ inside of the ergoregion (with $W > 0$) can be found in Fig. 2.3 (right panel). Notice that as we go from the inside to the outside of the ergoregion, or in other words as we approach $g_{tt} \to 0^+$, we have that $h_+ \to +\infty$. Since the impact parameter η is a constant of motion for a given photon trajectory, the allowed region $h_+ < \eta$ is not accessible from spatial infinity: as it turns out, it corresponds to bound states with negative energy (see Section 2.6). In fact, there are stable light rings around RBSs which can be populated by photons in such a state.

A boundary to a forbidden region only exists in this case for $\eta > 0$ (if $W > 0$):

$$h_-(r,\theta) = \eta, \quad \text{(scattering state)} \qquad \text{and} \qquad h_+(r,\theta) = \eta, \quad \text{(bound state only)} \ . \tag{2.23}$$

2.2 Effective potentials contour plots

We will now exhibit contour plots of h_+ and h_- for different spacetimes, namely three RBSs and one KBHSH. The solid lines (blue) represent negative η values, whereas dashed lines (red) represent positive values of η. Although the function h_- is also relevant for defining the allowed region for some photon trajectories, the landscape of the function h_+ is richer, in particular as it leads to the appearance of a trapping region. Recalling the discussion in Sections 1.5 and 1.5.2, Light Rings (LRs) are photon orbits with $p_r = \dot{p}_r = 0$ and $p_\theta = \dot{p}_\theta = 0$. For this family of spacetimes, all LRs exist on the equatorial plane

[3]The case $W < 0$ can be obtained by a transformation $W \to -W$, $h_\pm \to -h_\mp$ and $\eta \to -\eta$.

($\theta = \pi/2 \Rightarrow p_\theta = 0$), which simplifies the analysis. We equally remark that light rings are related to extrema of $h_\pm$ (see Section 2.6). The following table summarizes the particular configurations (see Fig. 2.2) for which the $h_\pm$ contour lines are shown below:

Object	Configuration in [23]	Light rings	Ergoregions	Chaos	Fig.
RBS	9 (w=0.75 μ)	No	No	No	2.4
RBS	10 (w=0.7 μ)	1 Stable + 1 Unstable	No	Yes	2.5, 2.14
RBS	11 (w=0.65 μ)	1 Stable + 1 Unstable	Yes	Yes	2.1, 2.6, 2.15
KBHSH	III	1 Stable + 3 Unstable	Yes	Yes	2.7, 2.19 – 2.21

The value of w (in units of the scalar field mass μ), in the second column of the table, is the frequency in the scalar field ansatz, see eqs. (4) in [12], whereas the column "Chaos" refers to the occurrence of chaotic patterns in the lensing images of that configuration. In the plots below a compactified radial coordinate $R \in [0;1]$ will be used,

$$R = \frac{R^*}{1+R^*}, \qquad \text{with} \quad R^* \equiv \sqrt{r^2 - r_H^2}\ . \tag{2.24}$$

In the remainder of this chapter, configurations 9, 10 and 11 of RBSs, as well as configurations III (and also II) of KBHsSH, are the same as those considered in [23] (see Fig. 2.2). We keep this labelling here, to avoid confusion, even though we shall not discuss all configurations presented in [23].

Fig. 2.4 exhibits the effective potentials contour plots for the RBS configuration 9. This background has no ergoregion or light rings, but it is very close, in solution space, to the RBS for which light rings first appear (see Fig. 2.2). Each contour line of h_+ in Fig. 2.4 sets the boundary of the forbidden region in (r, θ) space for a given η. There is a distinct deformation of the h_+ contour lines, which will grow into a *pocket* in the following cases to be analysed. Since $\partial_r h_\pm$ is never zero on the equatorial plane there are no light rings – neither maxima, minima nor saddle points of $h_\pm$ exist. The contour plot of h_- for this configuration is very similar to the one displayed in the bottom panel of Fig. 2.6 and hence it will not be shown.

The next case, shown in Fig. 2.5, corresponds to the RBS configuration 10. It has no ergoregion but it has two light rings, one stable and one unstable. The new feature in the

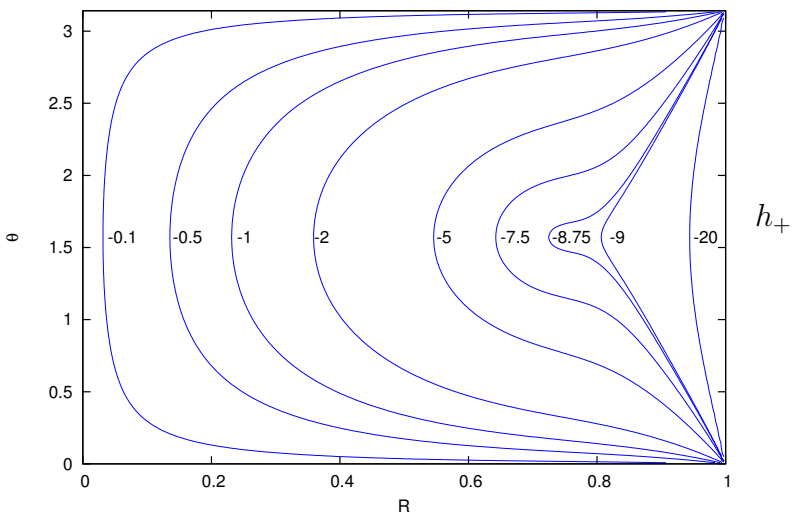


Figure 2.4: Contour plots of h_+ for the RBS configuration 9. In this and the next figures, the solid lines (blue) represent negative η values. It has no ergoregion or light rings. This configuration is very close in solution space to a RBS where light rings first appear. There is a deformation of the h_+ lines, which will grow into a *pocket* in the cases considered next. Adapted from [24].

h_+ contour lines is the existence of a *pocket* that can be closed below a certain impact parameter η, and form an allowed region which is disconnected from spatial infinity (thus leading to *bound orbits*). This can be seen in Fig. 2.5.

This disconnected region can in fact be made arbitrarily small until it becomes a single point on the equatorial plane for $\eta \simeq -11.97$ (quantities in this chapter come in $1/\mu$ units, unless otherwise stated), with $\partial_r h_+ = 0$ at that point. The latter actually corresponds to a *stable light ring* since the motion is bounded. From Fig. 2.5, we see clearly that a saddle point appears on the equatorial plane, which in that case corresponds to an *unstable light ring*, since the photon can escape due to radial perturbations, for $\eta \simeq -8.61$. The contour plot of h_- for this configuration is very similar to the one displayed in the bottom panel of Fig. 2.6 and hence it will not be shown.

In Fig. 2.6 we consider the RBS configuration 11. This background has two light rings and one ergoregion (an ergo-torus [162]). As discussed before, h_+ will diverge to $-\infty$ as the ergosurface is approached from the outside of the ergoregion. After entering the

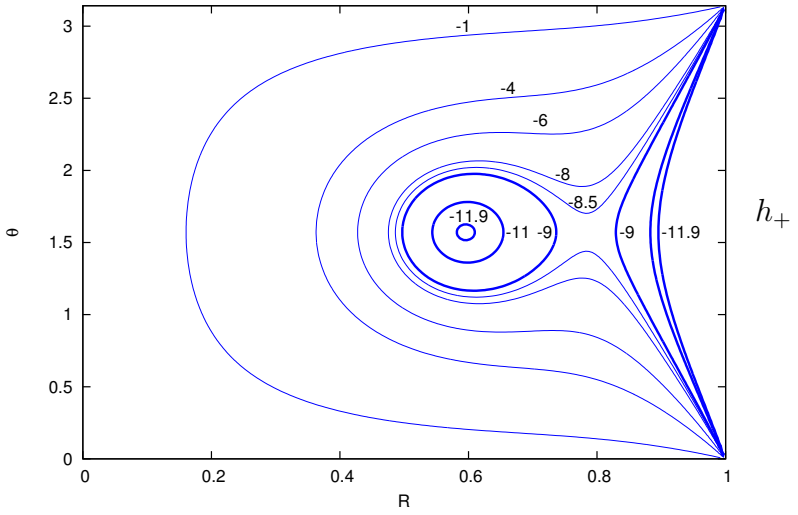


Figure 2.5: Contour plots of h_+ for the RBS configuration 10. It has no ergoregion but it has two light rings, one stable and one unstable. There is a *pocket* that can be closed below a certain impact parameter η and form an allowed region which is disconnected from spatial infinity, leading to bound orbits. Adapted from [24].

latter, h_+ will decrease from $+\infty$ to a minimum at positive η, which corresponds to a stable light ring. It turns out that such a light ring has negative energy (see Section 2.6). In Fig. 2.6 (top panel) are displayed the contour plots of h_+.

Again, blue solid lines represent negative values of η, whereas red dashed contour lines represent positive values. Notice the sharp transition of h_+ from -100 to +100, since the function diverges at the boundary of the ergoregion. Observe that the function h_- (Fig. 2.6, bottom panel) does not form a pocket; the corresponding h_- functions of the previous configurations 9 and 10 were not displayed due to the strong similarity with the RBS 11 function h_-.

The existence of a pocket in the effective potential, whose opening can be made arbitrarily small, leads to *trapped* or *quasi-bound* orbits, from which a photon might only escape after a very long time. Such trapped orbits will be exemplified in the gallery of Section 2.7.

Finally, in the top (bottom) panel of Fig. 2.7, the h_+ (h_-) contour lines are shown for the KBHSH with the *hammer*-like shadow – configuration III in [23]. This spacetime

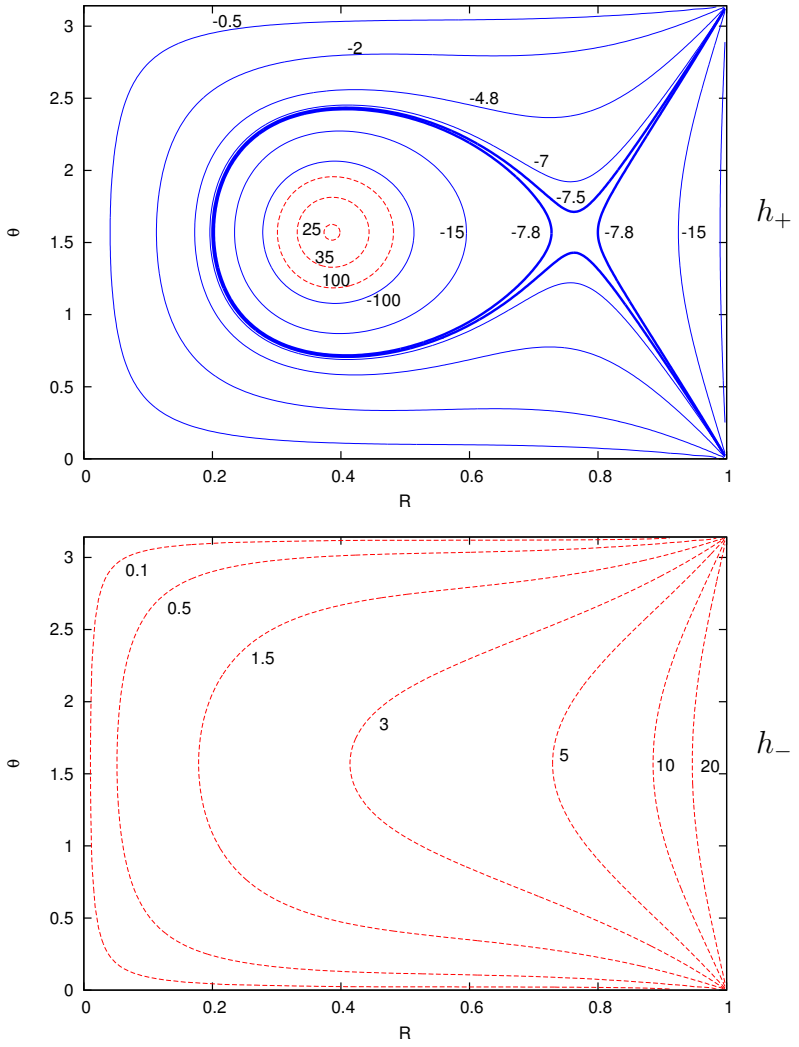


Figure 2.6: Contour plots of $h_+ = \eta$ (top panel) and h_- (bottom panel) for the RBS configuration 11, which has two light rings and an ergoregion. The positive values of h_+ set the position of the ergoregion, with the minimum corresponding to the stable light ring. The saddle point corresponds to an unstable light ring (with negative η). The function h_- has no light rings associated with it. Adapted from [24].

contains two ergoregions (Saturn-like topology [162]) and four light rings, three unstable and one stable. In Fig. 2.7 (top panel), as before, the sharp transition from negative to positive η values marks the boundary of the ergoregion. As this boundary is approached from the outside (inside) of the ergoregion, h_+ diverges to negative (positive) values. Inside the ergotorus there is a stable light ring for $R \simeq 0.3$. Clearly, there are also saddle points for $R \simeq 0.06$ and $R \simeq 0.74$ on the equatorial plane, corresponding to unstable light rings. Additionally, there is an ergoregion near the horizon (which is at $R = 0$),

amounting to a pileup of h_+ contour lines at $R \sim 0.02$ (on the equatorial plane), since h_+ diverges. Inside this ergoregion there are no light rings.

Fig. 2.7, bottom panel, shows the h_- contour plot, which reveals the existence of a saddle point at $R \simeq 0.032$ on the equatorial plane and hence an unstable light ring. Heuristically, this is the merging of the structure of both a Kerr-like BH and a RBS: a Kerr BH has an ergosphere and two unstable light rings (see Section 2.3); a RBS such as configuration 11 has an ergotorus and two light rings, one stable and the other unstable.

2.3 The effective potentials in Kerr

In this section, we will implement the $h_\pm$ framework for the Kerr spacetime. Although the analysis of geodesics is well-known for Kerr, it is typically treated by separating variables, as discussed in Section 1.1. We provide here a treatment parallel to that discussion that can be applied for solutions for which no separation of variables is known (or likely to exist).

In the Kerr case, we have two unstable light rings on the equatorial plane at radial coordinates r_1 (for co-rotating photons) and r_2 (for counter-rotating photons), in Boyer-Lindquist coordinates, given a value of the rotation parameter a such that $a/M \in [-1; 1]$ (see Section 1.1) [44, 66], with $r_1 \leqslant r_2$.

Between these radii we can have *unstable spherical orbits*, which are not restricted to the equatorial plane and for which θ oscillates between $\pi/2 \pm \psi$, where $\psi \in [0, \pi/2]$. In particular, given a radial coordinate r such that $r_1 \leqslant r \leqslant r_2$, we can have a spherical photon orbit at that position as long as we have the correct restrictions on the constants of geodesic motion. For Kerr these constants are E, L and Q, the latter being the Carter constant [44, 63]. Specifically, the relations that must be satisfied are:

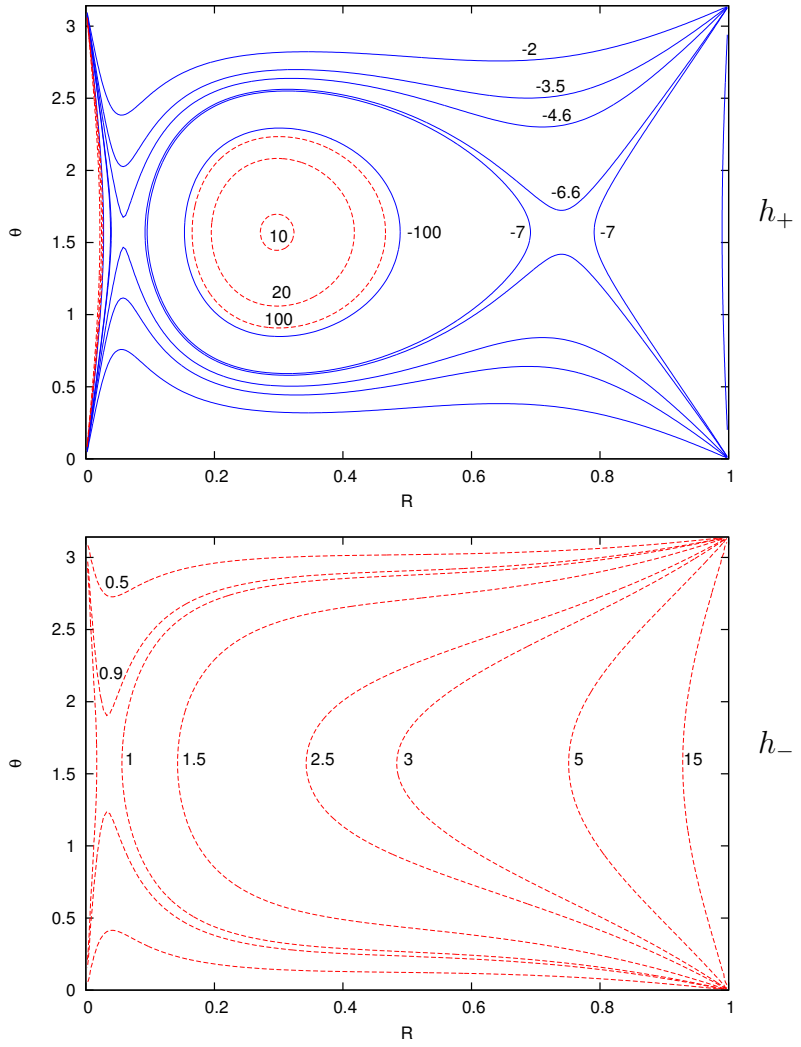


Figure 2.7: Contour plots of h_+ (top panel) and h_- (bottom panel), for the KBHSH with the *hammer*-like shadow (configuration III). This configuration contains two ergoregions (Saturn-like topology) and four light rings, three unstable and one stable. The h_+ dashed (red) lines occur within the two disconnected ergoregions, one of which is near the horizon (at $R = 0$). The function h_- in this case has a saddle point on the equatorial plane, signaling the existence of an unstable light ring (bottom panel). Adapted from [24].

$$\eta \equiv \frac{L}{E} = -\frac{r^3 - 3Mr^2 + a^2 r + Ma^2}{a(r-M)}, \qquad \chi \equiv \frac{Q}{E^2} = -\frac{r^3(r^3 - 6Mr^2 + 9M^2 r - 4a^2 M)}{a^2(r-M)^2}.$$

The first equation establishes a connection between our impact parameter η and the radial coordinate of a spherical orbit. From it, it is possible to conclude that the η required is

positive for r_1 and negative for r_2 (given $a > 0$), with the physical interpretation that r_1 is connected to a co-rotating light ring, whereas r_2 is related to a counter-rotating one (see Section 2.6) [66].
As mentioned, θ oscillates between $\pi/2 \pm \psi$, where ψ can be computed as:

$$\psi(r) = \arcsin\left\{-\sqrt{\frac{[a^2-\eta^2-\chi]+\sqrt{[a^2-\eta^2-\chi]^2+4a^2\chi}}{2a^2}}\right\}.$$

Hence given a value of r (with $r_1 \leqslant r \leqslant r_2$) one can compute $\eta(r)$ and $\chi(r)$ and obtain the respective $\psi(r)$. The curve $\pi/2 \pm \psi(r)$ in (r, θ) space is represented in Fig. 2.8 as a dotted line (black). In this figure are also represented the contour lines of the functions $h_\pm$, each with a saddle point that coincides with the position of a light ring. This is consistent with the previous discussion since the saddle point for h_+ (h_-) occurs for a negative (positive) value of η and thus corresponds to a light ring which is counter(co)-rotating. Moreover, the h_- saddle point (connected to co-rotation) occurs for a smaller radial coordinate that the h_+ saddle point (connected to counter-rotation), as expected.

Interestingly, it is clear that the curve given by $\pi/2+\psi(r)$ and $\pi/2-\psi(r)$ also satisfies the condition $\partial_r h_\pm = 0$. As such, the latter also yields spherical orbits. In particular, for $\eta = 0$ we have $\psi = \pi/2$ for both $h_\pm$. Hence there is a continuous connection between spherical orbits as we go from h_+ to h_- (or vice-versa). As a final observation, h_+ can diverge due to the existence of an ergoregion, in this case with spherical topology. As before, inside this region the h_+ contour lines are for positive η (see Section 2.3.1).

2.3.1 Pocket formation, chaos and turning points

The formation of pockets in the effective potential will lead to quasi-bound orbits, *i.e.*, orbits that stay in a confined spatial region for a long time. We shall now show that one can associate these orbits to the emergence of chaotic patterns in the lensing images, such as the one exhibited in Fig. 2.1. In order to do so, we recall that for a given photon orbit the value of the impact parameter η is a constant of motion. This value also fixes the photon's allowed spacetime region. Let us analyse the contour $\eta =$ constant in an image

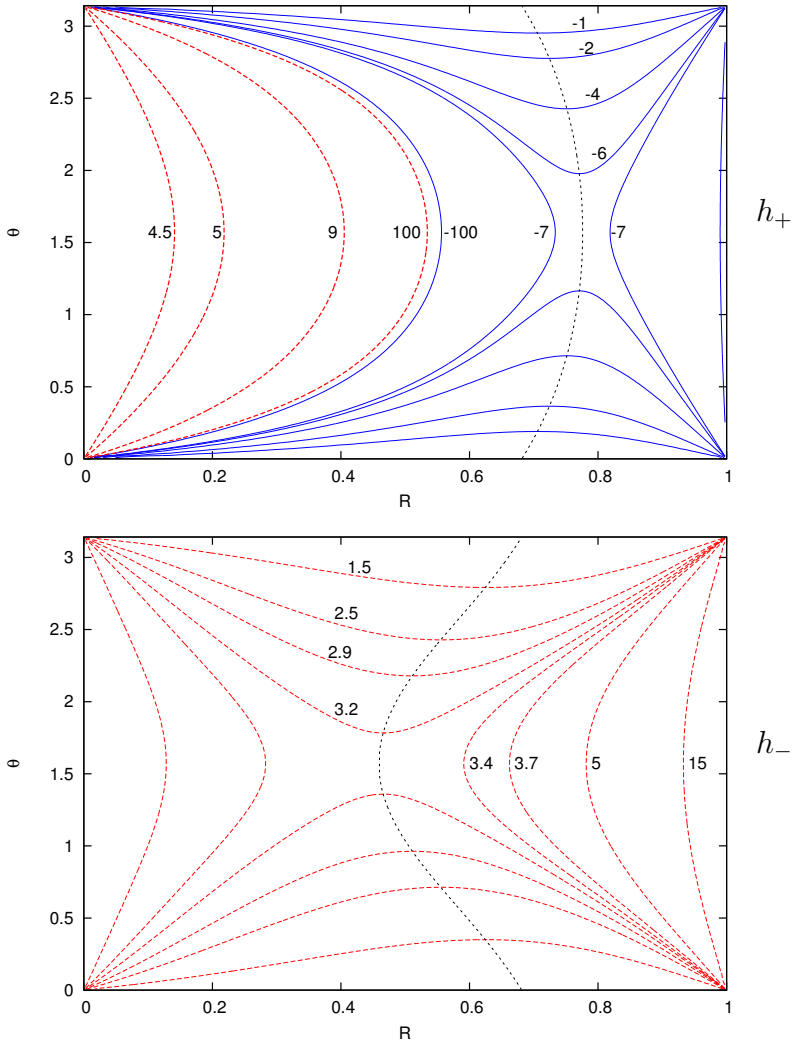


Figure 2.8: Contour plots of h_+ (top panel) and h_- (bottom panel), for the Kerr BH solution. The solid lines (blue) represent negative η values, whereas dashed lines (red) represent positive values. The dotted line (black) is given by both $\pi/2+\psi(r)$ and $\pi/2-\psi(r)$, coinciding with the condition $\partial_r h_\pm = 0$. The saddle points of $h_\pm$ are consistent with the position of the light rings, as expected. The coordinate R is computed with the same expression as before (2.24), despite r being a Boyer-Lindquist coordinate now. Adapted from [24].

containing the lensing of a RBS or a KBHSH.

In Fig. 2.9 we exhibit three contour plots of η = constant, with $\eta = -7.8$, $\eta = -7.5$ and $\eta = 0.1$, in a detail of Fig. 2.1, corresponding to the gravitational lensing of the RBS configuration 11, whose effective potentials are shown in Fig. 2.6. Observe that in the contour plot for $\eta = -7.8$ the pocket is not yet open (Fig. 2.6, top panel); correspond-

ingly, there is no chaos in the lensing image for this value of the impact parameter. For $\eta = -7.5$, on the other hand, the pocket is open and indeed the $\eta =$ constant contour line in the lensing image intersects a chaotic region. As the impact parameter becomes even larger, the pocket's opening becomes wider, explaining why the chaotic region expands to higher latitudes in the lensing image. This analysis suggests that pocket formation induces chaotic behaviour.

One may wonder, however, if the existence of a pocket is *necessary* for the occurrence of chaotic regions. It turns out that it is not. To establish this, observe that the line of constant $\eta = 0.1$ crosses a chaotic region near the edges of the figure, but there is no pocket associated with it in the h_- function (Fig. 2.6, bottom panel). Thus, there are chaotic regions with no corresponding pocket in the effective potential. One way to understand these regions is via a different "potential", *the acceleration field* $\mathcal{F}_r$. We leave the discussion of the latter to Section 2.5.

The relation between chaotic patterns on the image plane and the characteristics of the corresponding geodesic motion can be understood in a number of different ways. The manifestation of this chaos is the pixelated aspect of some image patches, which suggest that there is a sensitive dependence on initial conditions in the map between a camera pixel and a point on the celestial sphere; the map corresponding to the geodesic linking the two points. To quantify such chaoticity, one can then introduce a number of measures such as the Lyapunov exponent, entropy, the time delay function T associated to each pixel, or the number of radial turning points. In the following, we shall expand on the two last notions, as particularly well suited to measure chaoticity.

The *time delay function* is defined as the variation of the coordinate time t, in units of $1/\mu$ (with μ the mass of the scalar field), required for the geodesic emanating from a particular pixel to reach a corresponding point on the celestial sphere or fall asymptotically into the black hole. The idea behind this function is that trajectories which are semi-permanently trapped in the pocket take much longer to escape, giving initially

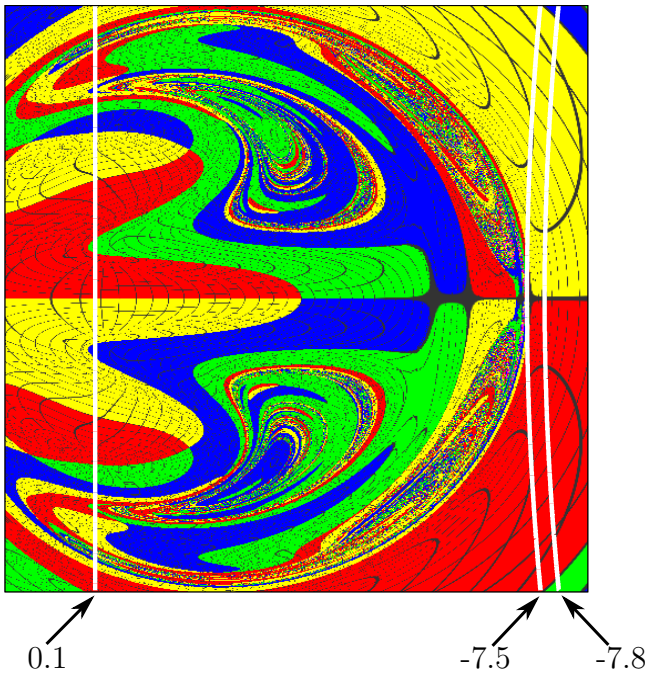


Figure 2.9: Gravitational lensing of the RBS configuration 11 (zoomed). White contour lines of constant η are shown for three values of η. Notice the transition from $\eta = -7.8$ to $\eta = -7.5$ leads in this image to an overlap with the chaotic region, whereas in the effective potential (Fig. 2.6, top panel) it is connected to the appearance of a pocket. However, the line of constant $\eta = 0.1$ crosses a chaotic region near the edges of the figure, but there is no pocket associated with it in the potential (Fig. 2.6, bottom panel). Adapted from [24].

nearby orbits more time to diverge.

In Fig. 2.10 the time delay for configuration III is portrayed as a heat map – with the corresponding scale on the right of the image – indicating the variation of the coordinate time for each trajectory to travel from the camera to the celestial sphere. The "brighter" regions on the time delay image can be seen to match the chaotic regions seen in the lensing image of this configuration – see Fig. 2.11. The *number of radial turning points*, on the other hand, is defined as the number of times that $\dot{r}$ changes sign during the light ray's trajectory. Recall that null geodesics on a Kerr spacetime have at most one radial turning point [64]; hence a violation of the latter can be interpreted as a deviation from Kerr.

On the panels to the right of Fig. 2.11 we have a representation of the number of radial

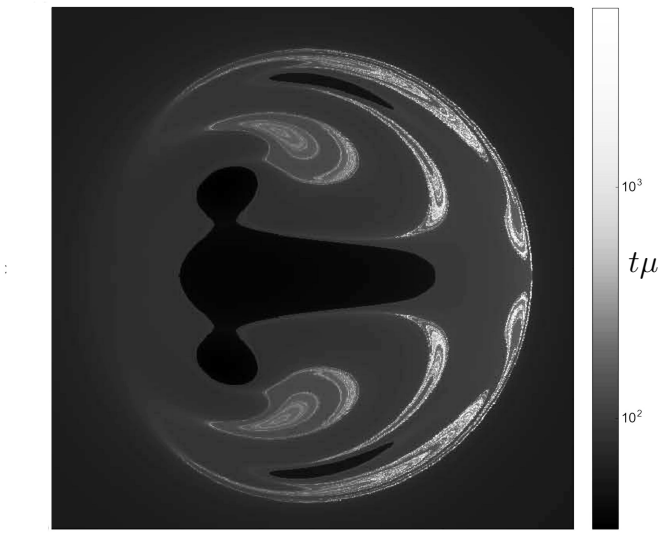


Figure 2.10: Time delay heat map associated to scattering orbits for KBHSH configuration III (zoomed). Adapted from [24].

turning points as a grey level for the RBS configuration 11 (top row) and the KBHSH III (bottom row); a larger number of turning points corresponds to a darker shade in the image, with white connected to just one turning point. The shadow of KBHSH III is represented in black in order to ease visualization – the number of turning points is actually zero in that case, both for the main shadow as well as the eyebrows[4]. On the left panels of Fig. 2.11 we have a representation of the gravitational lensing of the respective configurations; observe the correlation between the regions with a larger number of turning points (right panels) and the chaotic patterns (left panels). This suggests that having more than one radial turning point is a necessary ingredient for chaos, a feature absent in geodesic motion around a Kerr BH. Note, however, this correlation is not an equivalence: there are still some regular regions with more than one turning point.

Let us summarise the situation briefly. Chaotic patterns on the image plane correspond to trajectories that stay quasi-bound around the central object (RBS or KBHSH) and hence have a large time delay and numerous (more than one) radial turning points. Spacetimes that admit such trajectories/patterns are those that have a stable light ring

[4]Secondary shadows, disconnected from a larger one are dubbed *eyebrows* [72].

(in addition to an unstable light ring as with Kerr).

The existence of a stable light ring leads to the formation of pockets in the effective potential describing null geodesic motion; the opening of these pockets to infinity, through a narrow throat, signals the onset of a regime in which quasi-bound trajectories are possible (but not guaranteed). These pockets, while bottle-necked, have the effect of promoting quasi-bound motion. The widening of these pockets suppresses chaoticity but does not eliminate it, even when fully opened. This last feature can be understood intuitively by the effect of a stable light ring on an acceleration field, as defined in Section 2.5.

As a side note, we remark that the presence of an ergoregion is not necessary for quasi-bound motion. However the existence of an *ergo-torus* is a sufficient condition for the existence of a stable light ring [73] - this can be understood from the behaviour of the effective potential h_+ - and hence a sufficient condition for chaotic behaviour to manifest in these spacetimes.

2.4 Quasi-bound orbit in $(r, \dot{r})$ phase space

A quasi-bound orbit displays an interesting dynamics. The motion is 2-dimensional, in (r, θ). Thus, focusing, on the $(r, \dot{r})$ phase space, one can anticipate effective energy losses (gains) due to the coupling to the θ motion. This is exactly what can be observed in a neat way for some trajectories.

As an example, the plot in Fig. 2.12 (left panel) displays a trajectory in phase space $(r, \dot{r})$ for a photon that enters a trapping region in the RBS configuration 11. The orbit spans a "pear-like" curve which decreases in size, resembling the well known picture for a harmonic oscillator with friction (wherein the curve is an ellipse). Here, however, the energy is not being lost, rather it is being transferred into the θ-motion. The envelope curve in Fig. 2.12 left (the red solid line) can be computed as follows. The maximum

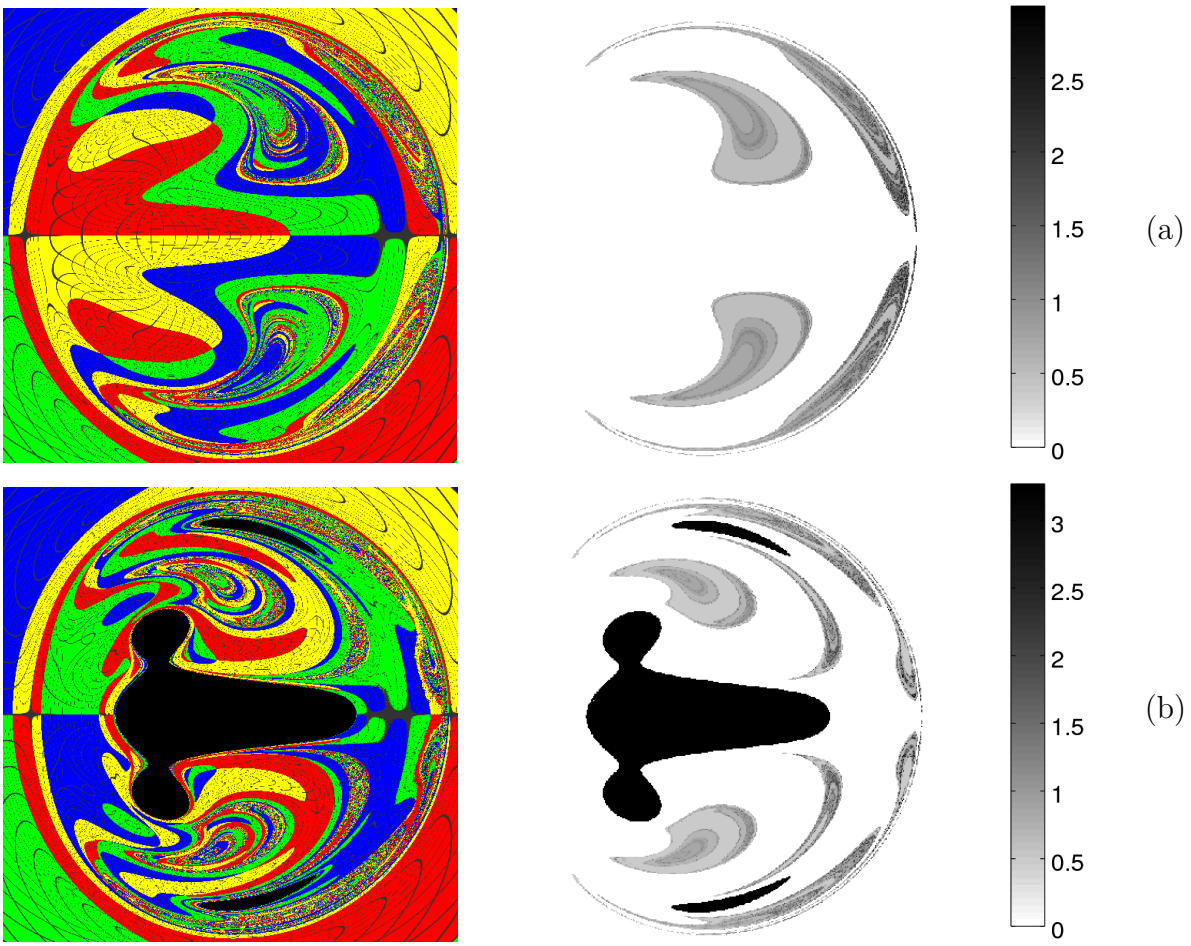


Figure 2.11: Zoomed turning point heat map (right panels) and lensed image (left panels) for the RBS 11 (row a) and the KBHSH III (row b). Clearly, there is a strong correlation between the chaotic patters (left) and the number of turning points n (right). The logarithmic scale displayed is given by $\log_{10}(n)$, with $n \geqslant 1$; the exceptional case $n = 0$ corresponds to the shadow points, shown in black. Adapted from [24].

possible value of $\dot{r}$ is obtained on the equatorial plane[5] ($\theta = \pi/2$) with $\dot{\theta} = 0$. This implies

$$\dot{r} = \sqrt{-\frac{V(r, \pi/2)}{g_{rr}}} \, . \tag{2.25}$$

This function (red solid line in Fig. 2.12 – left) describes perfectly the envelope shape.

For a given value η, the conditions $h_+ = \eta$ and $\partial_r h_+ = 0$ are satisfied in phase space by the green dot in the figure. The trajectory of the photon near that central dot is represented in Fig. 2.12 (right), displaying multiple reflections on the contour line $h_+ = \eta$.

[5]The minimum of the potential V is on the equator.

The reflection points are outside the equatorial plane and close to the condition $\partial_r h_+ = 0$, leading to little motion along the r coordinate. By analogy with the Kerr analysis (see Section 2.3), it seems likely that these points are connected to a FPO.

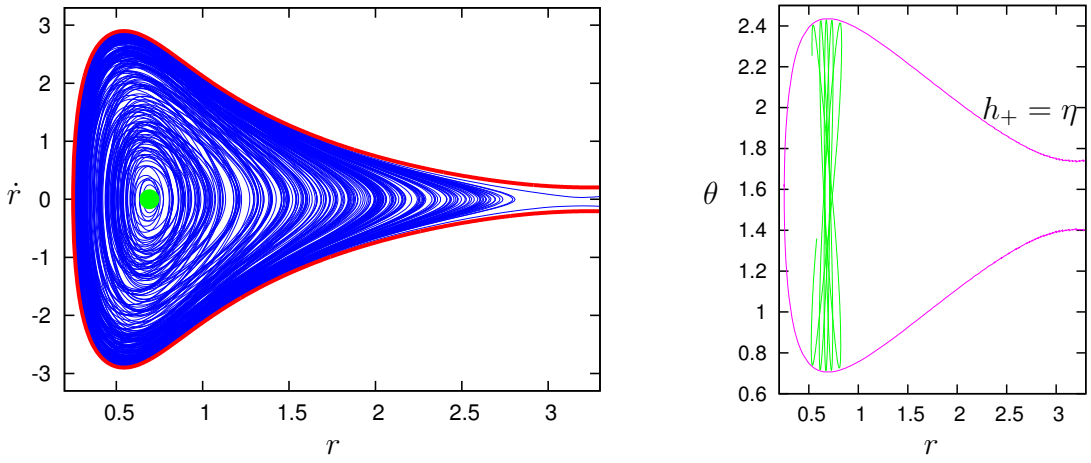


Figure 2.12: (Left panel) Phase diagram $(r, \dot{r})$ of a photon trajectory in the RBS configuration 11 with $\eta \simeq -7.46$. The red line is given by the function $\pm\sqrt{-V/g_{rr}}$ and the green dot satisfies $\partial_r h_+ = 0$ and $h_+ = \eta$; (right panel) segment of the previous trajectory equivalent to the central green dot, in (r, θ)-space. The connection to a FPO is apparent. The purple line represents the boundary of the allowed region. Adapted from [24].

2.5 Acceleration field $\mathcal{F}_r$

From one of Hamilton's equations (2.9) we obtain:

$$\dot{p}_r = -\frac{1}{2}\left(\partial_r g^{rr} p_r^2 + \partial_r g^{\theta\theta} p_\theta^2 + \partial_r V\right).$$

Setting $p_r = 0$ and solving for p_θ from $\mathcal{H} = 0$, it leads to:

$$\dot{p_r}_{[p_r=0]} = -\frac{1}{2}\left(-\frac{V}{g^{\theta\theta}}\partial_r g^{\theta\theta} + \partial_r V\right).$$

Dividing by the photon's energy at spatial infinity E, we obtain a function which only depends on (r, θ) and on the impact parameter $\eta = L/E$:

$$\mathcal{F}_r(r, \theta) \equiv -\frac{1}{2E^2}\Big(V\,\partial_r \log[g_{\theta\theta}] + \partial_r V\Big). \tag{2.26}$$

Hence, this function dubbed radial *acceleration field* returns the value of $\dot{p}_r$ of the photon when $p_r = 0$, divided by a scale factor. We remark that $g_{\theta\theta}$ is positive definite, and hence the logarithm is well defined. Now we will consider applications of the $\mathcal{F}_r$ function to some of the spacetimes.

In Fig. 2.13 are displayed the contour plots of $\mathcal{F}_r$ for the RBS configuration 11 and the Kerr case. The dashed red (solid blue) lines represent positive (negative) values of $\mathcal{F}_r$. Starting from the top left figure, for the RBS 11 with $\eta = 3$, the acceleration field only has positive values (dashed red lines) inside the allowed region. This actually implies that in this case the motion can have at most one radial turning point. For instance, if the light ray has at any given point $p_r = 0$, then $\mathcal{F}_r > 0$ implies that $\dot{p}_r > 0$, and p_r cannot become negative afterwards since there is no negative $\mathcal{F}_r$ region.

Going now to Fig. 2.13 top right we have the Kerr case with $\eta = 3.2$. The transition line from positive to negative values are the set of points such that $\mathcal{F}_r = 0$, which implies that if $p_r = 0$ at those points then $\dot{p}_r = 0$ (but $p_\theta \neq 0$ in general). This appears to be connected to a spherical orbit at that location (see Section 2.3). Notice that if $\partial_r V = 0$ at the boundary of the allowed region ($V = 0$), then $\mathcal{F}_r = 0$. Since $\partial_r V = 0 \iff \partial_r h_\pm = 0$ if $V = 0$ (see Section 2.6) then it may be possible to make a connection between $\partial_r h_\pm = 0$ and spherical orbits (see Section 2.3).

Curiously, we can also conclude that there is at most one radial turning point for the Kerr case. For instance, if during the motion $p_r = 0$ inside the red (blue) region, then the value of $\dot{p}_r$ is positive (negative) and r will start to increase (decrease). Since the sign of $\mathcal{F}_r$ will not change after this point, then the photon cannot have $p_r < 0$ ($p_r > 0$) afterwards and so the photon eventually escapes (falls into) the BH. This is consistent with the literature, as it is known that null geodesics in a Kerr spacetime have at most one radial turning point [64]. However, we note that the present approach is valid even when the geodesic equations are not fully separable and integrable, despite that not being the case for Kerr.

Continuing to Fig. 2.13 bottom left, we have the RBS configuration 11 again, now with the different impact parameter $\eta = -7.11$. In this case there are two disconnected lines for which $\mathcal{F}_r = 0$, each connected to a spherical orbit, by analogy with Kerr. Contrary to the previous cases, in this situation it is possible to have more than one turning point, since after having $p_r = 0$ the sign of $\mathcal{F}_r$ can still change. This can be traced back to the transition line $\mathcal{F}_r = 0$ that goes from positive to negative values of $\mathcal{F}_r$ as r increases, and ultimately to the existence of a stable light ring. Thus, it is possible to have a photon wobbling around that line, yielding several radial turning points (see Fig. 2.13 bottom left for an example).

Advancing to Fig. 2.13 bottom right we again have the RBS 11, now with $\eta = 0.1$. The transition line $\mathcal{F}_r = 0$ has now become closed in a loop, leading to an isolated region with $\mathcal{F}_r < 0$. As in the case before, it is possible to have more than one radial turning point. However notice that there is no pocket in this case: $\partial_r h_-$ is never zero at the boundary of the allowed region (green line). This case illustrates a situation for which chaos is possible even without a pocket (see Section 2.3.1).

2.6 Physical conditions for Light Rings

As we have seen, the existence of light rings is central to the properties of the effective potentials. In particular, the existence of stable light rings allows for pockets, which translate into spacetime quasi-trapping regions for photons. In this section we will investigate in detail the properties of the light rings for the above configurations that possess them.

Throughout this chapter, a light ring refers to a null geodesic that satisfies $p_r = p_\theta = 0$ and $\dot{p}_r = 0$ on the equatorial plane ($\theta = \pi/2$). These conditions are equivalent to $V = 0$ and $\partial_r V = 0$ (see Section 1.5.2). Using equation (2.15) and computing the derivative of

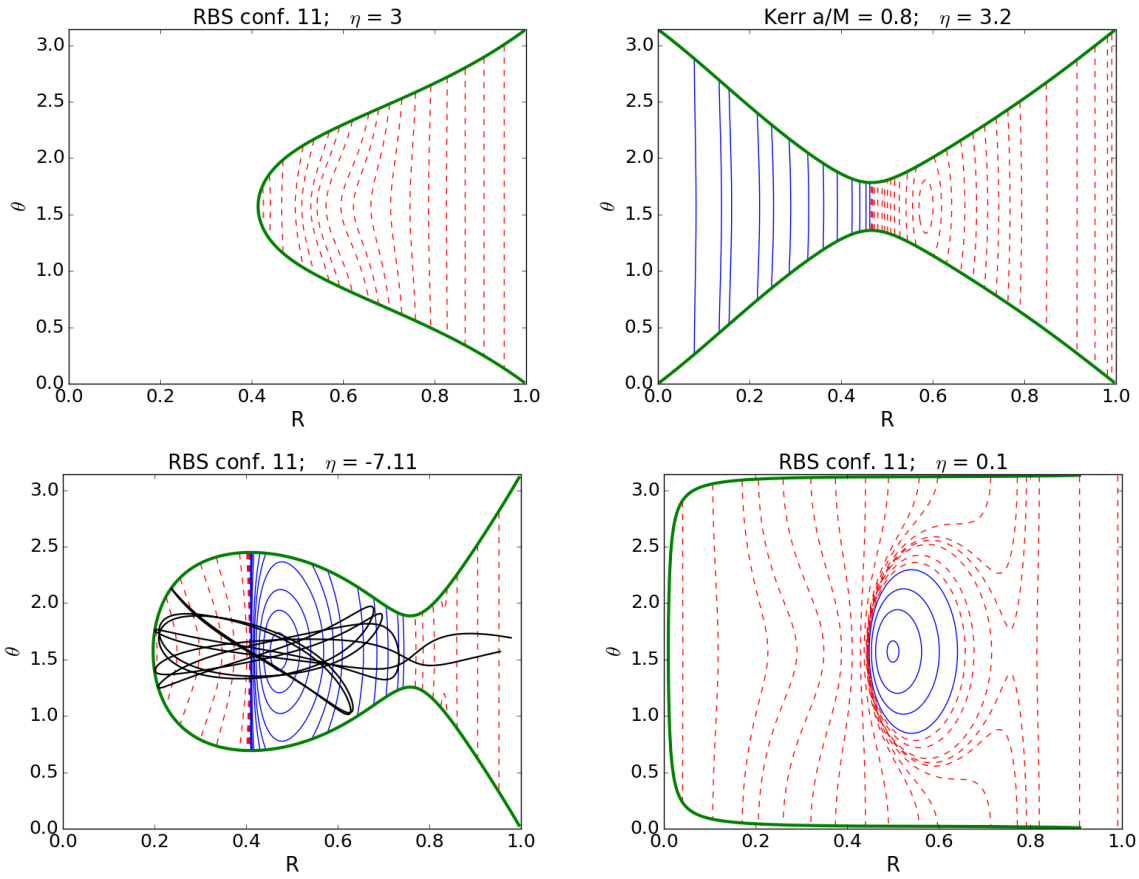


Figure 2.13: Contour lines of the acceleration field $\mathcal{F}_r$, with dashed red (solid blue) lines for positive (negative) values. All figures correspond to the RBS 11, except the top right panel which corresponds to Kerr. The thick green line sets the boundary of the allowed region. The black line on the bottom left image represents a single photon trajectory. Adapted from [24].

V with respect to r, enforcing $h_\pm = \eta \iff V = 0$ at the end, we obtain:

$$\partial_r V = \pm \left(\frac{E^2}{D} g_{tt} \right) (h_+ - h_-) \partial_r h_\pm .$$

Since $h_+ \neq h_-$ outside the horizon we conclude[6] that $\partial_r V = 0 \iff \partial_r h_\pm = 0$. Moreover, since the radial condition for stable (unstable) light rings is $\partial_r^2 V > 0 \quad (\partial_r^2 V < 0)$, by a similar calculation one can then conclude that stable (unstable) light rings satisfy $\pm \partial_r^2 h_\pm > 0, \quad (\pm \partial_r^2 h_\pm < 0)$.

Besides stability, light rings can also be categorized by their rotational direction. From

[6] We would obtain the same result even if $g_{tt} = 0$.

the geodesic equations for t and φ we have that:

$$\dot{\varphi}/E = -\frac{1}{D}\left(g_{t\varphi} + g_{tt}\eta\right) \ , \qquad \dot{t}/E = \frac{1}{D}\left(g_{\varphi\varphi} + g_{t\varphi}\eta\right) \ . \tag{2.27}$$

Their quotient yields

$$\Omega \equiv \frac{d\varphi}{dt} = -\frac{g_{t\varphi} + g_{tt}\eta}{g_{\varphi\varphi} + g_{t\varphi}\eta},$$

which describes the azimuthal rotation direction with respect to a static observer at spatial infinity. At a light ring, $V = 0$ holds $g_{\varphi\varphi} + 2g_{t\varphi}\eta + g_{tt}\eta^2 = 0$, which leads to:

$$g_{\varphi\varphi} + \eta g_{t\varphi} = -\eta\left(g_{t\varphi} + \eta g_{tt}\right) \implies \Omega = \frac{1}{\eta} \quad \text{(at a light ring)}.$$

Hence, the rotational direction of the light ring is given by sign of the impact parameter η. Additionally, at a light ring the expression for $\dot{\varphi}/E$ can be simplified using equation (2.16):

$$\dot{\varphi}/E = -\frac{1}{D}(g_{t\varphi} + g_{tt}h_{\pm}) = \mp\frac{1}{D}\sqrt{D} \implies \mp\dot{\varphi}/E > 0.$$

Since $\eta = 1/\Omega = \dot{t}/\dot{\varphi}$ and recalling sections 2.1 – 2.1:

$$g_{tt} < 0 \implies \mp h_{\pm} > 0 \implies \mp\eta > 0 \implies (\mp\eta)(\mp\dot{\varphi}/E) > 0 \implies \dot{t}/E > 0;$$
$$g_{tt} > 0 \implies h_{\pm} > 0 \implies \eta > 0 \implies \mp\dot{t}/E > 0,$$

where $g_{t\varphi} < 0$ was assumed. Hence we conclude that we can have $\dot{t}/E < 0$ at a light ring only if it is inside an ergoregion with $h_+ = \eta$. For physical photons, this actually implies that their energy is negative. Let us first detail this conclusion and then discuss its implications.

Consider a Zero Angular Momentum Observer (ZAMO) frame [55] at the position of the light ring (see Section 1.2). The locally measured energy of the photon, $p^{(t)}$, in this frame, is given by $p^{(t)} = \gamma(E - \omega L)$, which must be positive for physical photons [32]. Notice that in general $p^{(t)}$ is different from E, the latter being the photon's energy with

respect to spatial infinity. The expressions for ω and γ are given by:

$$\omega = -\frac{g_{t\varphi}}{g_{\varphi\varphi}}, \qquad \gamma = \sqrt{\frac{g_{\varphi\varphi}}{D}} \ . \tag{2.28}$$

Hence we have:

$$p^{(t)} > 0 \quad \Leftrightarrow \quad E\gamma > \gamma\omega L \quad \Leftrightarrow \quad E > -\frac{g_{t\varphi}}{g_{\varphi\varphi}} L \ . \tag{2.29}$$

We used the fact that $D > 0$ and $g_{\varphi\varphi} > 0$. The same relation is obtained if we require $\dot{t} > 0$, *i.e.*, $\dot{t} = \frac{1}{D}\left(E g_{\varphi\varphi} + L g_{t\varphi}\right) > 0$. Hence $p^{(t)} > 0 \Leftrightarrow \dot{t} > 0$. Since it is always possible to construct a ZAMO frame at the position of the light ring, we conclude that $\dot{t} > 0$ is a necessary condition for a physical photon. Then, the condition $\dot{t}/E < 0$ implies $E < 0$. Despite having a positive energy regarding a local observer, the photon has negative energy with respect to spatial infinity. Likely, the accumulation of negative energy states around this light ring is associated to an instability [26].

For the spacetime configurations already analysed, the signs of η, $\dot{t}/E$ and $\dot{\varphi}/E$ for different light rings (LR) are organized in the following table, together with other information.

Configuration in [23]	Fig.	LR	R	stability	η	g_{tt}	$\dot{t}/E$	$d\varphi/dt$
RBS 10	2.5, 2.14	h_+	0.60	stable	$-$	$-$	$+$	$-$
		h_+	0.79	unstable	$-$	$-$	$+$	$-$
RBS 11	2.1, 2.6, 2.15	h_+	0.39	stable	$+$	$+$	$-$	$+$
		h_+	0.76	unstable	$-$	$-$	$+$	$-$
KBHSH III	2.7, 2.19 – 2.21	h_-	0.03	unstable	$+$	$-$	$+$	$+$
		h_+	0.06	unstable	$-$	$-$	$+$	$-$
		h_+	0.30	stable	$+$	$+$	$-$	$+$
		h_+	0.74	unstable	$-$	$-$	$+$	$-$

The value of g_{tt} reveals whether a light ring is inside an ergoregion or not ($g_{tt} > 0$ in the former case). This occurs for two of the cases displayed. In both cases, as expected, the light ring is co-rotating, from the viewpoint of the asymptotic observer, as

appropriate for causal particles inside an ergoregion. For both these cases observe that $\dot{t}/E < 0$, which implies from the previous discussion that $E < 0$ for a physical state. We remark, however, that it is possible to have light rings inside an ergoregion with $E > 0$. Indeed, the KBHSH dubbed configuration II in [23], which is not discussed in detail here, has two unstable light rings, one of which is inside an ergoregion with $\dot{t}/E > 0 \implies E > 0$.

Throughout this chapter, light rings only exist on the equatorial plane ($\theta = \pi/2$). However we remark that they can exist outside this plane (in fact even if the latter is not present!).

2.7 Gallery of Images

In the previous section we provided various insights for the emergence of chaotic patterns in lensing images of RBSs and KBHsSH. In particular we have established that the presence of stable light rings allows for the existence of pockets in the effective potential leading to quasi-bound orbits, which are strongly correlated to the chaotic patterns. In this section we will exhibit a gallery of examples of spacetime orbits, represented together with the effective potential and the corresponding point in the lensing image, for a sample of solutions of RBSs and KBHsSH.

The setup is the same as in [23], and inspired by the construction in [72] (see Section 1.4). An observer (or camera) is placed off-centre in the spacetime and it receives light from a collection of far away sources, emitting isotropically in all directions, which we call the *celestial sphere* $\mathcal{N}$ (recall the discussion in Section 1.4). We fix $t = \varphi = 0$ for the camera's position, at some (r, θ) coordinates (r_o, θ_o). The emitting celestial sphere surrounds both the central region and the observer, being placed at a large radial coordinate.

In particular for this work, unless otherwise stated, we have placed the camera on the equatorial plane, $\theta = \pi/2$, and at a fixed radial distance specified differently for the RBS and KBHSH solutions: For RBS solutions we keep the camera at a perimetral radius of

$\tilde{r}_o = 22.5/\mu$ with μ the mass of the scalar field (taken to be 1). For KBHsSH we place the camera at a perimetral radius of $\tilde{r}_o = 15M$ where M is the ADM mass of the BH. The perimetral radius $\tilde{r}$ was defined in Section 1.2.1:

$$\tilde{r} = \frac{1}{2\pi} \oint d\varphi \sqrt{g_{\varphi\varphi}} \ , \tag{2.30}$$

where $g_{\varphi\varphi}$ is evaluated on the equatorial plane on a spacelike slice. The celestial sphere $\mathcal{N}$ is then placed at $\tilde{r} = 2\tilde{r}_o$.

To obtain an image, a scan over observation angles is performed, tracing the corresponding light rays backwards on the background, starting at the camera position and ending, heuristically, either at a point on the distant celestial sphere or at the horizon, in case there is one.

2.7.1 Rotating boson stars

As a first example, we show in Fig. 2.14 the lensing of configuration 10, as seen from the equatorial plane. In order to identify points in the image, we introduced an image coordinate system[7] (X, Y) ranging from $(-1, -1)$ at the lower left corner of the image to $(1, 1)$ at the upper right corner. We then selected three points in the lensing image, expressed as $\mathbf{1}_{10}$, $\mathbf{2}_{10}$, and $\mathbf{3}_{10}$, where the subscript denotes the configuration these points belong to. The corresponding impact parameters and their location in (X, Y) image coordinates are:

Point	η	(X, Y)
$\mathbf{1}_{10}$	-9.00	$(0.790, 0.289)$
$\mathbf{2}_{10}$	-8.50	$(0.732, 0.026)$
$\mathbf{3}_{10}$	-8.00	$(0.690, 0.189)$

Point $\mathbf{1}_{10}$ corresponds to an impact parameter for which the effective potential forms a pocket around a stable light ring (marked by a green upright triangle in the potential

[7] These coordinates are very similar to the one introduced in Section 1.2.1, albeit with an additional stereographic projection.

plot) that does not connect with the exterior region. Hence this trajectory cannot get trapped and this point belongs to a non-chaotic region in the lensing. The corresponding spacetime trajectory exhibits only weak bending around the center. In order to ease the representation of the trajectory, Cartesian-like coordinates (x, y, z) are used, defined from (r, θ, φ) as if these were standard spherical coordinates.

For point $\mathbf{2}_{10}$, the effective potential has a pocket with a small opening (a "throat") around an unstable light ring (marked by a red inverted triangle in the potential plot), connecting it to the asymptotic region. But as the corresponding orbit has small θ motion, the photon enters and exits the pocket after a single bounce off the boundary of the pocket. The corresponding point in the lensing image is at the threshold between a chaotic and non-chaotic region.

Finally, point $\mathbf{3}_{10}$ corresponds to a trajectory that gets trapped for some time in the pocket, bouncing off its boundary a few times before finding its way out. In the spacetime, the photon circles around the central region a few times, before being scattered off to infinity. In the lensing image this point appears inside a chaotic region.

In Fig. 2.15, we exhibit the lensing of configuration 11, again seen from the equatorial plane, and we have selected four points in the lensing image, denoted $\mathbf{1}_{11}$ to $\mathbf{4}_{11}$. The corresponding impact parameters and their location in (X, Y) image coordinates are:

Point	η	(X, Y)
$\mathbf{1}_{11}$	-9.00	$(0.908, 0.291)$
$\mathbf{2}_{11}$	-7.50	$(0.734, 0.029)$
$\mathbf{3}_{11}$	-7.00	$(0.685, 0.130)$
$\mathbf{4}_{11}$	-4.80	$(0.464, 0.189)$

The new qualitative feature in this configuration, with respect to the previous one, is the existence of an ergo-region. Its boundary is shown as a dashed green line in the effective potentials. Point $\mathbf{1}_{11}$ corresponds to an impact parameter for which the pocket does not connect with the asymptotic region. Its potential and spacetime orbit are similar

to those of point Point $\mathbf{1}_{10}$ (Fig. 2.14), and it is not shown here. Points $\mathbf{2}_{11}$ and $\mathbf{3}_{11}$ are also qualitatively similar to points $\mathbf{2}_{10}$ and $\mathbf{3}_{10}$ as shown in Fig. 2.14. But point $\mathbf{4}_{11}$ is qualitatively new, in the sense that the chaotic region has now extended to other disjoint parts on the lensing image.

To close the gallery on RBSs, Fig. 2.16 shows the lensing of configuration 12, seen from the equatorial plane, and three highlighted points, denoted $\mathbf{1}_{12}$, $\mathbf{2}_{12}$ and $\mathbf{3}_{12}$. The corresponding impact parameters and locations in (X, Y) coordinates of the lensing image are:

Point	η	(X, Y)
$\mathbf{1}_{12}$	-6.50	$(0.900, 0.326)$
$\mathbf{2}_{12}$	-5.50	$(0.737, 0.008)$
$\mathbf{3}_{12}$	-5.50	$(0.737, 0.044)$

The RBS 12 was not analysed in detail before, since the respective effective potential displays essentially the same features as the RBS 11. Nonetheless, the RBS configuration 12 exhibits one of the richest dynamical structures of the configurations presented here. In particular, large areas of the central region of the lensing image exhibit chaotic behaviour. The characteristics of points $\mathbf{1}_{12}$ and $\mathbf{2}_{12}$ are very similar to their counterparts in configurations 10 and 11. However, just a small perturbation of $\mathbf{2}_{12}$ leads to point $\mathbf{3}_{12}$.

It is chosen such that its impact parameter allows the photon to enter a pocket with a very small opening. At the same time, it has sufficient θ momentum for it to get trapped in the pocket for a very long time. Its orbit fills out the pocket with an almost dense covering, as well as the central spacetime region, respectively. Given sufficiently long integration time, these types of orbits tend to escape eventually.

2.7.2 Kerr BHs with scalar hair

We now turn our attention to KBHsSH, in particular configurations II and III. Similarly to the RBS 12, the KBHSH II was not discussed before since its effective potential shares

similar qualitative features as the Kerr case (see Section 2.3). Fig. 2.17 shows the lensing of configuration II, as before seen from the equatorial plane. We have selected five points in the lensing image, denoted $\mathbf{1}_{\mathrm{II}}$ to $\mathbf{5}_{\mathrm{II}}$. The corresponding impact parameters, and the location in (X, Y) image coordinates are:

Point	η	(X, Y)
$\mathbf{1}_{\mathrm{II}}$	-7.00	$(0.839, 0.343)$
$\mathbf{2}_{\mathrm{II}}$	-5.87	$(0.680, 0.000)$
$\mathbf{3}_{\mathrm{II}}$	-5.80	$(0.673, 0.087)$
$\mathbf{4}_{\mathrm{II}}$	-4.00	$(0.464, 0.292)$
$\mathbf{5}_{\mathrm{II}}$	$+1.50$	$(-0.171, 0.024)$

In Fig. 2.17 we show the effective potential and spacetime orbit for points $\mathbf{1}_{\mathrm{II}}$, $\mathbf{3}_{\mathrm{II}}$ and $\mathbf{5}_{\mathrm{II}}$, all of which are scattering states. Instead of an isolated pocket, the effective potential now has an inner allowed region connected to the BH horizon. Point $\mathbf{1}_{\mathrm{II}}$ corresponds to a state for which this inner region is not accessible from infinity.

The same holds for point $\mathbf{5}_{\mathrm{II}}$, which has an impact parameter with the opposite sign, and hence is located on the left side of the shadow. For point $\mathbf{3}_{\mathrm{II}}$, the exterior and interior allowed regions are connected, but the orbit does not fall into the BH; it bounces off at the "throat" of the potential and then escapes to infinity. In the lensing image this orbit corresponds to a region close to the shadow's edge, where smaller and smaller copies of the celestial sphere accumulate in an orderly fashion. In spacetime this orbit circles once around the BH before being scattered off to infinity.

This circling occurs in the neighbourhood of the unstable light ring. In Fig. 2.18 we instead show two orbits that are absorbed by the BH, corresponding to points $\mathbf{2}_{\mathrm{II}}$ and $\mathbf{4}_{\mathrm{II}}$ in the lensing image of Fig. 2.17. Point $\mathbf{2}_{\mathrm{II}}$ lies just barely inside the shadow along the equatorial plane. The potential is just open for this impact parameter, allowing the photon to pass through to the inner region and fall into the shadow. Point $\mathbf{4}_{\mathrm{II}}$ on the other hand lies well within the shadow and moves within a wide open effective potential.

Finally, we consider one of the richest of our backgrounds, configuration III. In Fig. 2.19, we exhibit the lensing of this configuration, seen from the equatorial plane. We selected seven points in the lensing image, denoted $\mathbf{1}_{\rm III}$ to $\mathbf{7}_{\rm III}$. The corresponding impact parameters and their locations in (X, Y) image coordinates are:

Point	η	(X, Y)
$\mathbf{1}_{\rm III}$	-7.00	$(0.806, 0.395)$
$\mathbf{2}_{\rm III}$	-6.60	$(0.735, 0.011)$
$\mathbf{3}_{\rm III}$	-4.60	$(0.504, 0.025)$
$\mathbf{4}_{\rm III}$	-3.00	$(0.337, 0.437)$
$\mathbf{5}_{\rm III}$	-3.50	$(0.394, 0.426)$
$\mathbf{6}_{\rm III}$	0.00	$(0.000, 0.260)$
$\mathbf{7}_{\rm III}$	-0.50	$(0.055, 0.265)$

In Fig. 2.19 we show the effective potential and spacetime orbit for points $\mathbf{2}_{\rm III}$, $\mathbf{3}_{\rm III}$ and $\mathbf{5}_{\rm III}$, all of which are scattering states. The orbit of point $\mathbf{1}_{\rm III}$ is similar to that of $\mathbf{1}_{\rm II}$ (Fig. 2.17), except that there are three (rather than two) disconnected regions, one of which is connected to infinity, another one to the horizon and the third is an intermediate closed pocket (as in Fig. 2.21, left panel). It is therefore not shown. The effective potential in this configuration exhibits features from both a more Kerr-like BH, such as configuration II, and a RBS with an ergoregion and light rings.

Observe the difference between points $\mathbf{3}_{\rm III}$ and $\mathbf{5}_{\rm III}$; both scatter off the innermost throat, which connects the pocket with the near-horizon region of the effective potential. But whereas point $\mathbf{3}_{\rm III}$ is the result of a single scattering, point $\mathbf{5}_{\rm III}$ also scatters off the outermost throat (which is almost nonexistent). Recall that each throat satisfies $\partial_r h_+ = 0$ at the boundary of the allowed region and is likely connected to a fundamental orbit. Moreover, notice that point $\mathbf{3}_{\rm III}$ is close to the edge of the main part of the shadow, whereas point $\mathbf{5}_{\rm III}$ is close to the edge of one of the eyebrows.

To further extrapolate these results, recall that in the familiar Schwarzschild or Kerr case, the edge of the shadow connects to a self-similar structure with infinitely many

copies of the whole celestial sphere. This is due to photons that *approximately resonate* the unstable light ring. In a spacetime endowing photon orbits with an effective potential as that in Fig. 2.19, there are several light rings. Thus, photons can approximately resonate with each of these, or, in principle any combination thereof. This creates a *hierarchy* of resonances, wherein more excited ones resonate more times, with different light rings. The plausible scenario we have just described suggests that the photons approaching the edge of the main shadow and of the eyebrows approximately resonate with different combinations of fundamental orbits.

This possibility is supported by Fig. 2.20 where we show three orbits that fall into the BH, two close to the edge of the main part of the shadow (points $\mathbf{6}_{\rm III}$ and $\mathbf{7}_{\rm III}$), and the other one close to the edge of one of the eyebrows (point $\mathbf{4}_{\rm III}$); the latter can be seen to scatter off both throats of the potential. Point $\mathbf{6}_{\rm III}$ in particular illustrates a case with zero impact parameter, that nevertheless displays a non-trivial trajectory. Clearly the effective potentials cannot describe all the dynamics.

Finally, in Fig. 2.21 we show two bound states around configuration III, for the same impact parameter as for point $\mathbf{1}_{\rm III}$. One of these bound states has non-zero θ momentum and the other one is purely planar. This illustrates that for the same values of the impact parameter there can be many different orbits, including both scattering and non-scattering states.

To close the gallery, in Fig. 2.22 we show the observation images when the metric is flat (top panels), along with configuration II (second row) and III (third and fourth rows) in [23]. For all of these the observer is placed at different polar angles, from the equator to the pole. The images of configuration II show an expected transition from the "squared" shadow shape observed along the equatorial plane to an axi-symmetric shadow when observed along the polar axis ($\theta = 0$).

A more spectacular gallery is provided by configuration III. For the latter, as we move

away from the equatorial plane the main shadow splits into (at least) two disjoint pieces, and the largest of the two eventually merges with one of the (initial) eyebrows. As we approach the polar axis, the latter structure becomes annular, whereas the other piece of the main shadow that had separated from it becomes a central eye. At the pole, we obtain a *Saturn-like shadow*, with the whole structure displaying axial symmetry, as expected.

Discussion

We have performed a detailed study of photon orbits in the background of KBHsSH and RBHs, extending and complementing the results in [23]. We now summarize some of the main results:

- For null geodesics, the Hamiltonian $\mathcal{H} = 0$ restricts the motion of the light ray and sets a forbidden region in the phase space (r, θ). The boundary of the latter can be studied in a systematic way by defining two potentials $h_{\pm}$, such that their contour lines delimit the boundary of the forbidden region for each value of the impact parameter η.

- For some configurations, this boundary forms a *pocket* that can be closed for some interval of η, giving rise to *bound* orbits. However, there is a open interval of η values that can leave an arbitrarily small entrance to the pocket, leading to *trapped* or *quasi-bound* orbits. The formation of such pockets can be traced back to the presence of a *stable light ring*, combined with at least one unstable light ring. The latter is associated to a "throat" (a pocket entrance) that connects the interior of the pocket with a different region of the allowed phase space.

- The existence of a pocket is strongly correlated to the existence of chaos in the motion of the light ray, leading to turbulent patterns in the gravitational lensed image of the configuration. However, despite inducing chaos, pockets are neither a necessary nor sufficient condition for a particular trajectory to lie in such a chaotic pattern.

- A common feature of chaotic orbits appears to be having *more than one radial turning point*, a feature which embodies a deviation from Kerr spacetime [64]. Nevertheless,

it is still possible to have several turning points for a regular scattering, and hence this is not a sufficient condition for chaos.

- The ergoregion does not appear to play a major role in this context, despite enhancing the chaotic patterns in the image.

- If an event horizon and a pocket are both present, the existence of a two throat system may be the origin of the formation of disconnected shadows for a single BH, first reported in [23] for KBHsSH.

Following the above observations, we would like to emphasize that:

- not all KBHsSH display chaotic lensing. For instance, configuration II in [23] exhibits effective potentials very similar to those of Kerr (see Section 2.3), even though the corresponding shadow is quite distinct. This also provides an example for which lack of integrability, in the sense of Liouville[8], does not imply chaos;

- an important part of our analysis in this chapter relied on numerical ray tracing. The results obtained using different ray tracing codes agree, lending them credibility. Such numerical methods, however, have issues for very long term integrations. Thus, our discussion of the chaotic patterns is mostly focused on their emergence, rather than on their precise quantitative properties, for which numerical errors may become important;

- finally, a similar analysis to that performed herein can certainly be pursued for other similar types of backgrounds, as, *e.g.* the ones discussed in [20, 22, 165, 166, 16, 172].

[8]Except for the corresponding Kerr boundary line (see Fig. 2.2), it is unlikely that any KBHsSH has a hidden constant of the motion (which exists in Kerr), and hence geodesic motion is almost certainly non-integrable in (almost) all the domain of existence.

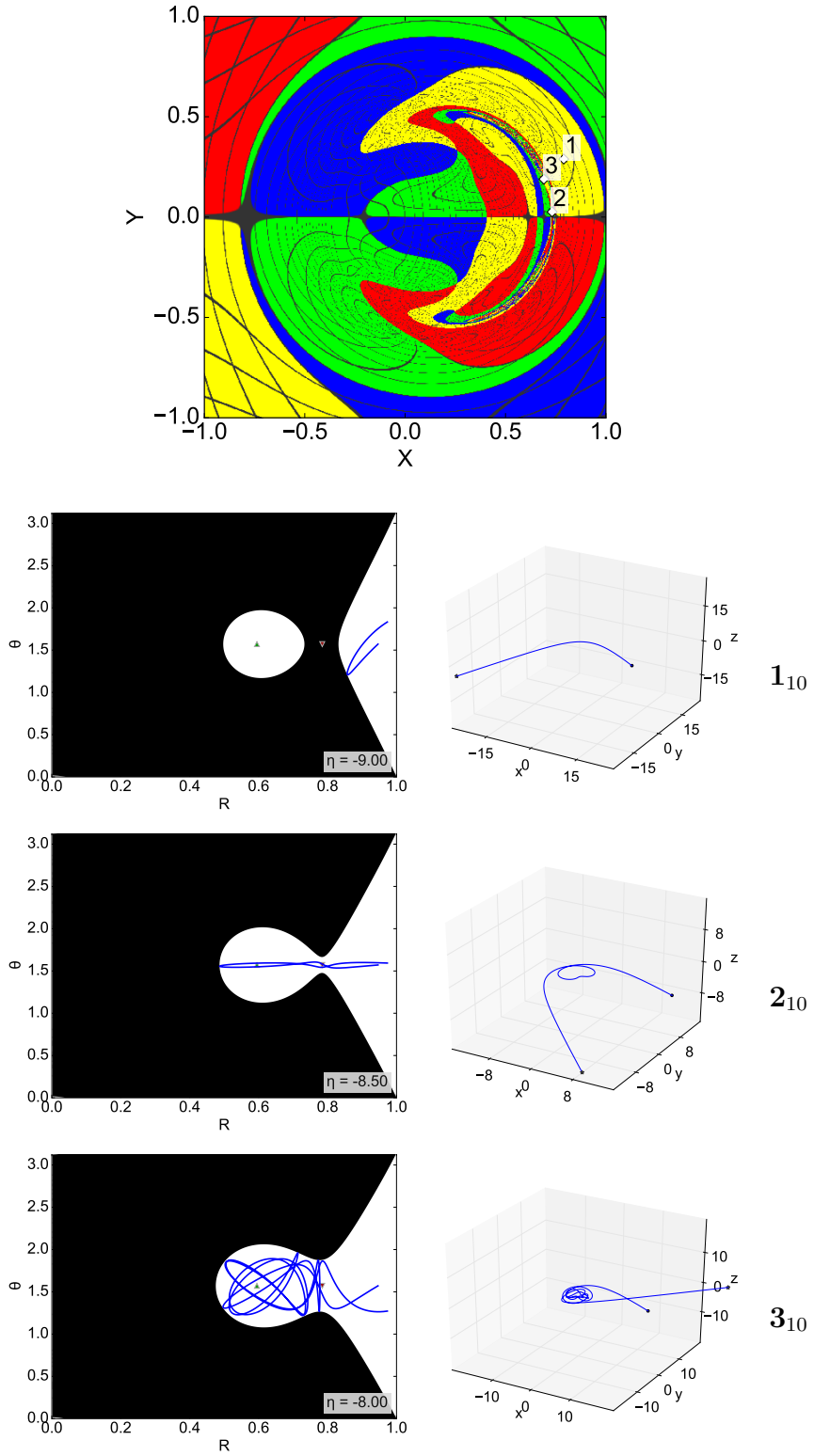


Figure 2.14: (Top) Lensing of configuration 10 with three highlighted points. Corresponding scattering orbits in the effective potential (left) and spacetime (right). Adapted from [24].

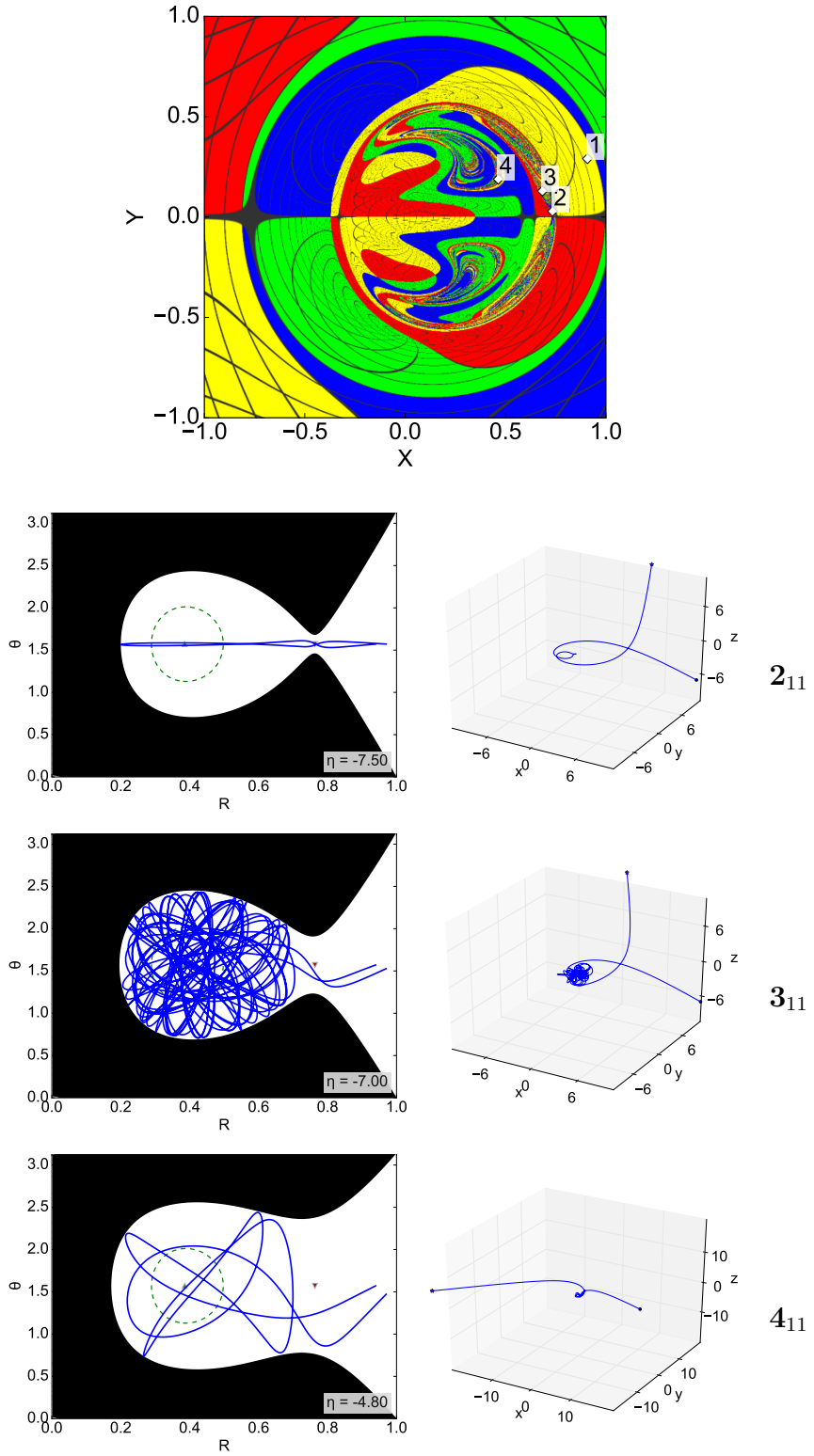


Figure 2.15: (Top) Lensing of configuration 11 with four highlighted points. Corresponding scattering orbits (except point $\mathbf{1}_{11}$) in the effective potential (left) and spacetime (right). Adapted from [24].

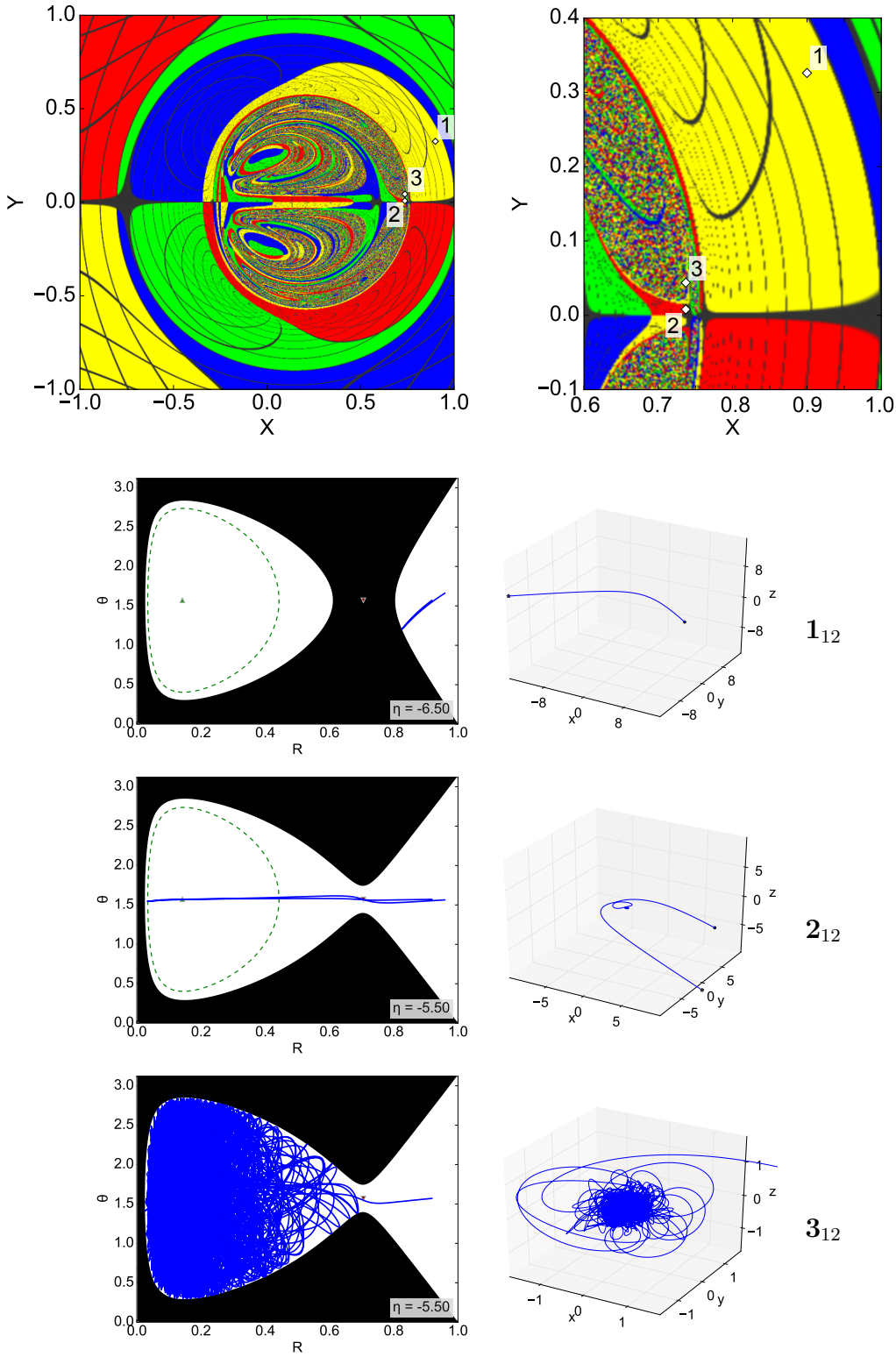


Figure 2.16: (Top) Lensing of configuration 12 with three highlighted points and enlarged image of the selected points. Corresponding scattering orbits in the effective potential (left) and spacetime (right). Adapted from [24].

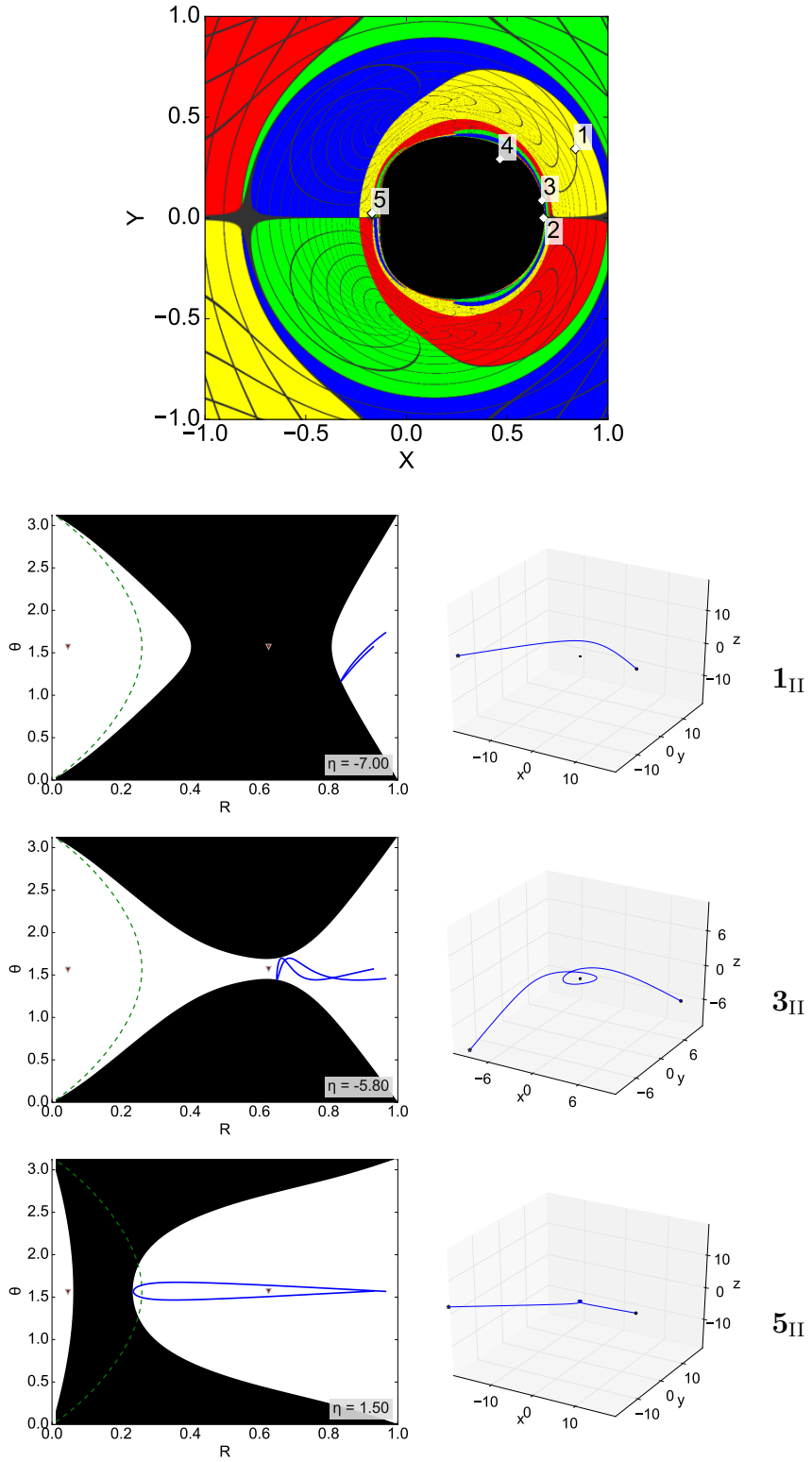


Figure 2.17: (Top) Lensing of configuration II with five highlighted points. Corresponding scattering orbits in the effective potential (left) and spacetime (right). Fig. 2.18 shows the absorption states. Adapted from [24].

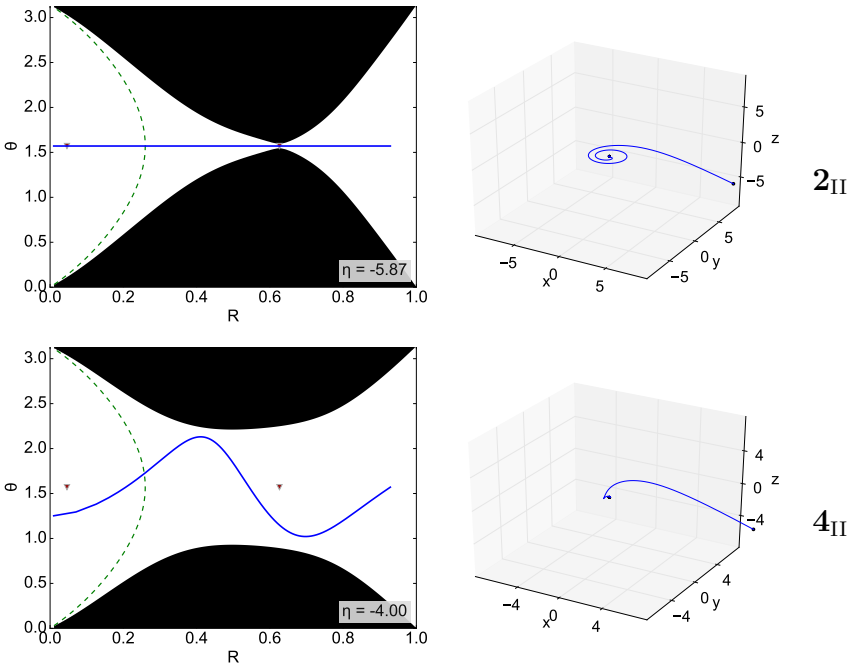


Figure 2.18: Absorption orbits in the effective potential (left) and spacetime (right), corresponding to points $\mathbf{2}_{\mathrm{II}}$ and $\mathbf{4}_{\mathrm{II}}$ in the lensing image of Fig. 2.17. Adapted from [24].

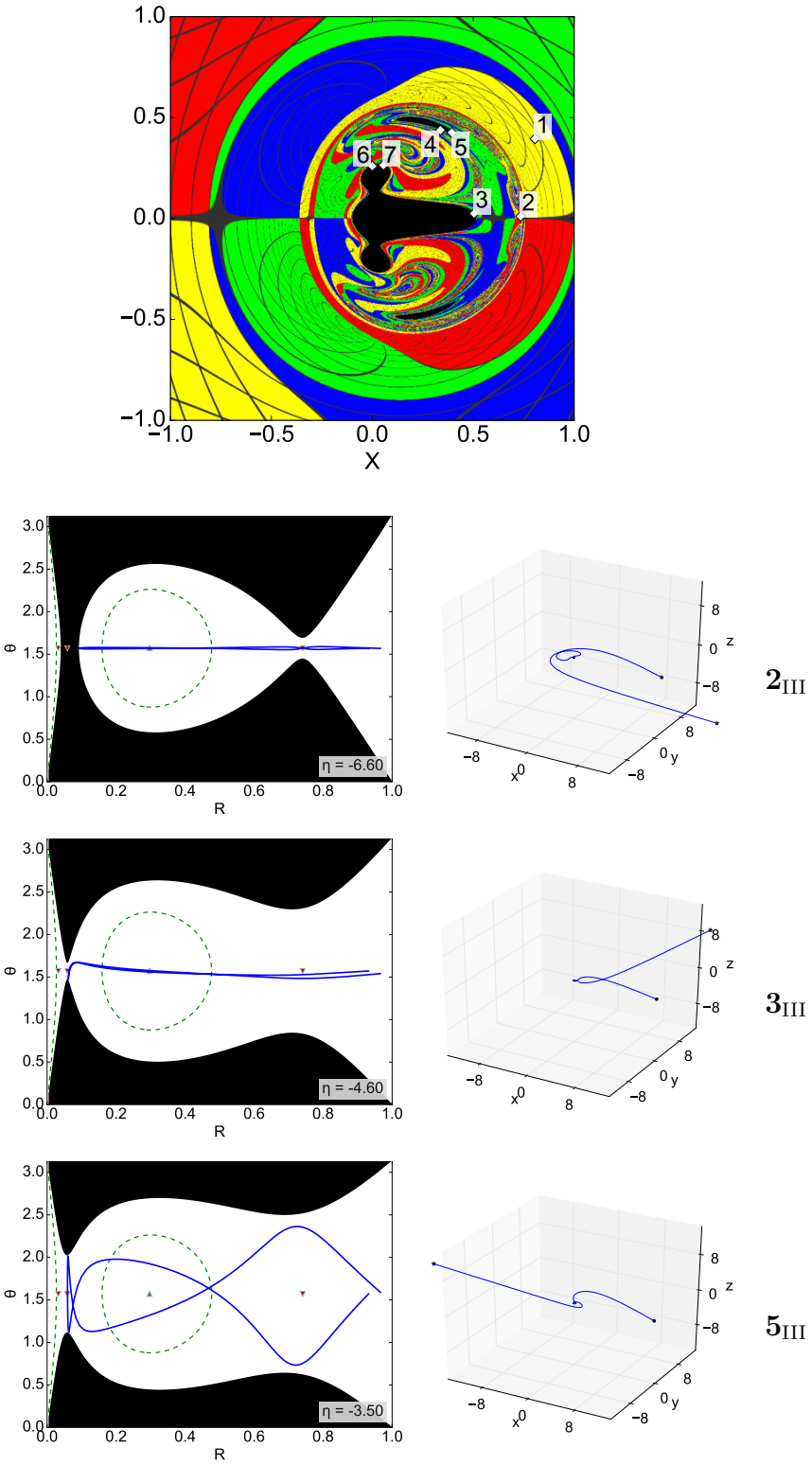


Figure 2.19: (Top) Lensing of configuration III with seven highlighted points. Orbits for points $\mathbf{2}_{\mathrm{III}}$, $\mathbf{3}_{\mathrm{III}}$ and $\mathbf{5}_{\mathrm{III}}$ in the effective potential (left) and spacetime (right). Adapted from [24].

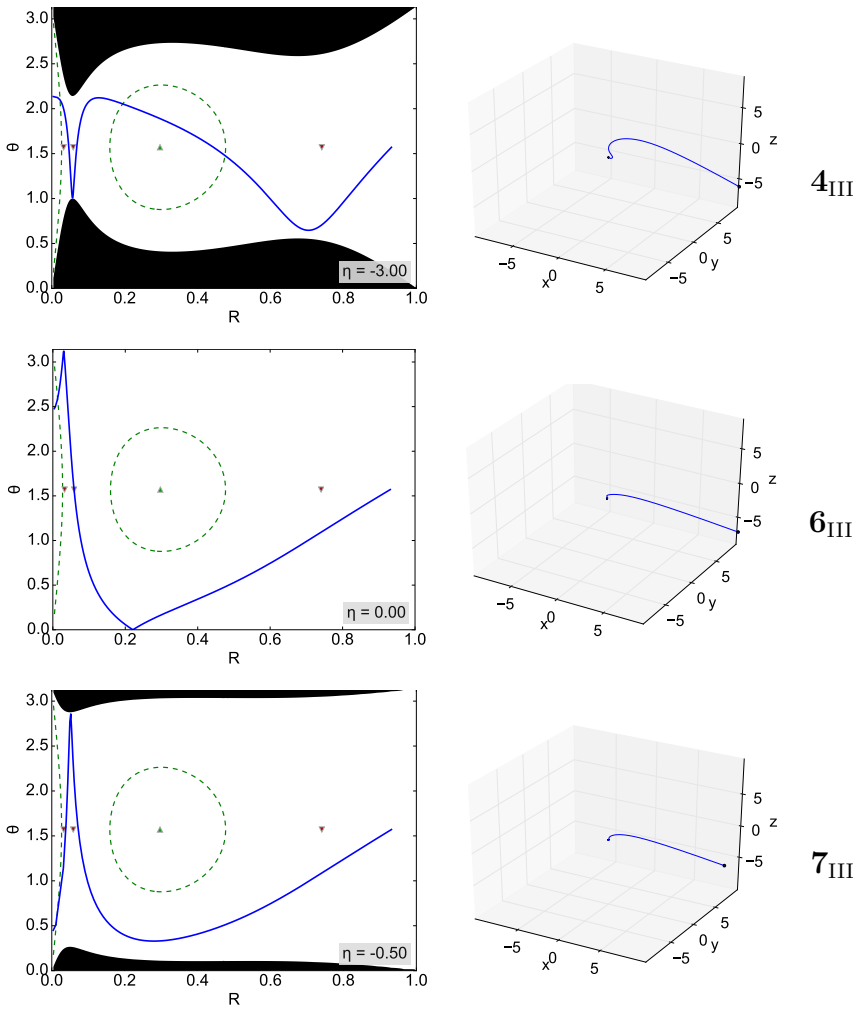


Figure 2.20: Absorption orbits in the effective potential (left) and spacetime (right), corresponding to points $\mathbf{4}_{\mathrm{III}}$, $\mathbf{6}_{\mathrm{III}}$ and $\mathbf{7}_{\mathrm{III}}$ in the lensing image of Fig. 2.19. Adapted from [24].

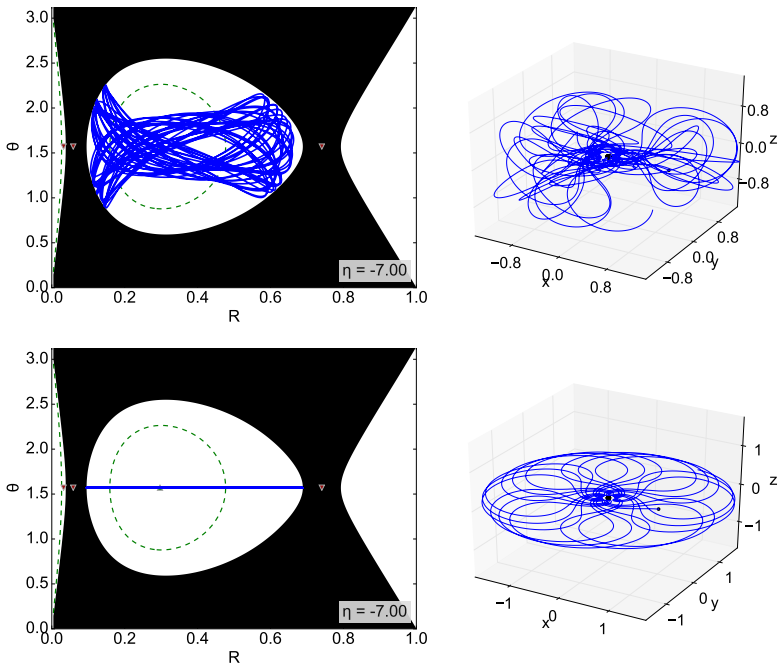


Figure 2.21: Effective potential (left) and spacetime orbits (right), of two bound orbits in configuration III ,with $\eta = -7.00$, one with θ motion and the other without. Observe that it is possible to have regular orbits even inside the pocket (bottom row). Adapted from [24].

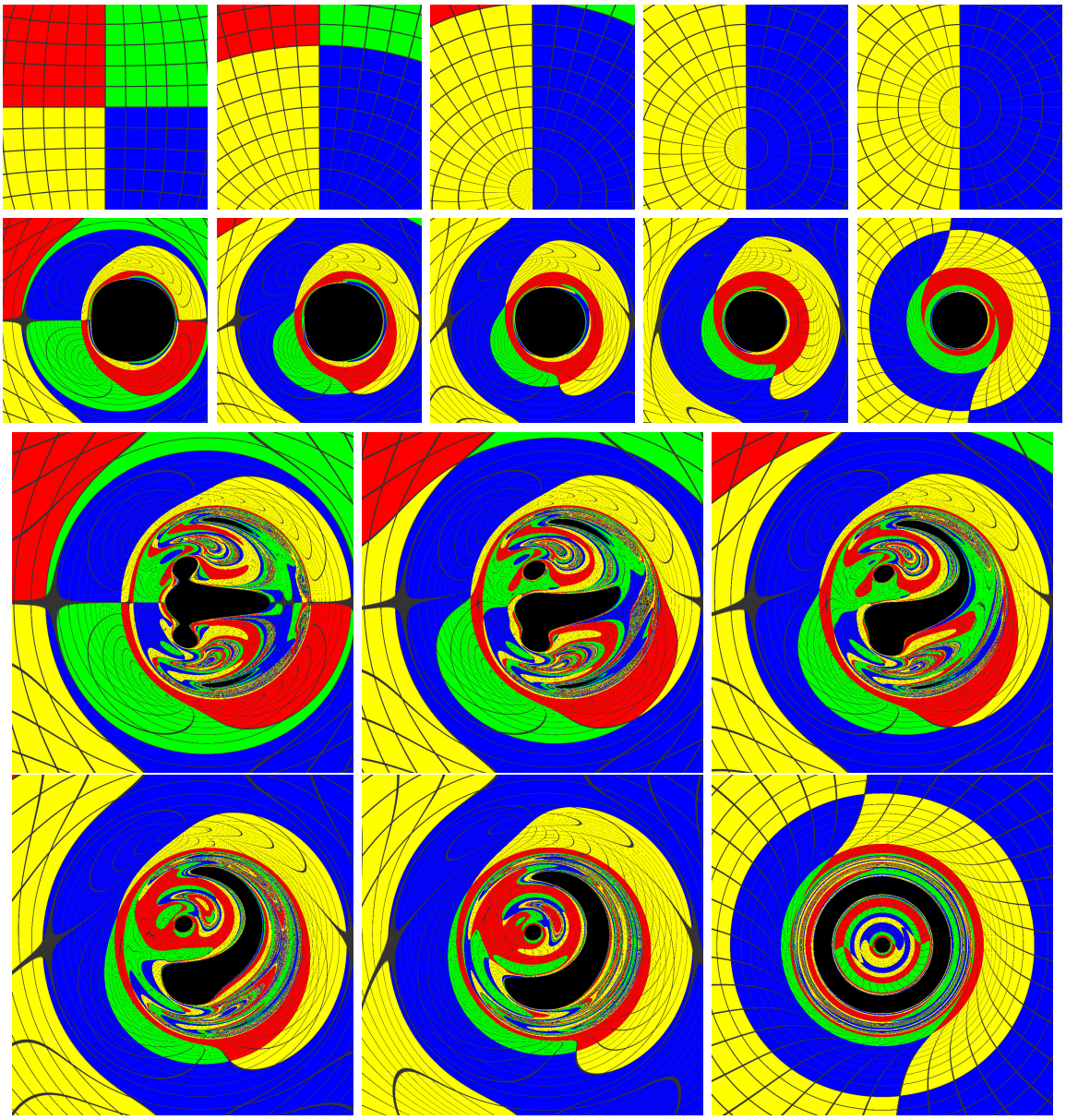


Figure 2.22: (From left to right) View from the camera of an empty space (top row) and configuration II in [23] (second row) with observer at $\theta = 90, 60, 40, 20$ and 0. (Third and bottom rows) Shadows and lensing of configuration III in [23] with observer at $\theta = 90, 80, 70, 50, 30$ and 0. (1024×1024 pixels). Adapted from [24].

Chapter 3

Kerr BHs with Proca hair

In an asymptotically flat spacetime, a wave-packet of standard electromagnetic waves never lumps under its own weight, to form a stationary configuration. In other words, Einstein-Maxwell theory does not admit gravitating solitons [190]. This fact makes Wheeler's vision of particles as classical geometric-electromagnetic field entities, (*geons*) [191], impossible in this model.

For massive, complex "photons", however, it has been recently shown that such localized, stationary lumps of energy are possible, yielding *Proca stars* [22] (PSs). These configurations can be thought of as macroscopic Bose-Einstein condensates of massive, complex, vector fields and are, in many regards, akin to the well-known (scalar) Boson Stars [18, 21] that were discussed in Chapter 2. Generalizations of (spherical) PSs have subsequently been considered including electric charge [192] or a negative cosmological constant [193].

Although well-known no go theorems exist [194, 195], stating the impossibility (under some assumptions) of endowing stationary black holes (BHs) with a non-trivial profile of a massive vector field, Kerr BHs with Proca hair (KBHsPH) were recently constructed [16]. KBHsPH reduce to rotating PSs in the limit of a vanishing horizon area and to (a particular subset) of vacuum Kerr BHs in the limit of vanishing hair. KBHsPH are actually a close cousin model of Kerr BHs with scalar hair [12, 13], a family of solutions that

also interpolate between (scalar) boson stars and a subset of (vacuum) Kerr BHs (see also Chapter 2). Both families of solutions share qualitative features, in particular the synchronization mechanism that allows them to be possible [13, 16].

As reported in a letter [23] and in its follow up paper [24], the shadows and gravitational lensing of Kerr BHs with scalar hair can be quite distinct from the paradigmatic (vacuum) Kerr case. The present Chapter aims to continue that analysis for KBHsPH, comparing the results with the scalar case. As a striking feature, KBHsPH can possess a sharp "cusp" in the shadow edge. Furthermore, we discuss the role that special photon orbits, dubbed *fundamental photon orbits* (FPOs), have in the formation of the shadow edge and how a transition between different orbital branches leads to the mentioned shadow cusp. We also make some remarks regarding the stability of FPOs using a Poincaré section.

3.1 Proca stars and KBHsPH

Consider Einstein's gravity minimally coupled to a complex Proca field $\mathcal{A}_\alpha$. In natural units the action takes the form:

$$\mathcal{S} = \int d^4x \sqrt{-g} \left[\frac{R}{16\pi} - \frac{1}{4}\mathcal{F}_{\alpha\beta}\mathcal{F}^{*\alpha\beta} - \frac{1}{2}\mu^2 \mathcal{A}_\alpha \mathcal{A}^{*\alpha} \right],$$

where $\mathcal{F}^{\alpha\beta}$ is a 2-tensor provided by $\mathcal{F} = d\mathcal{A}$. The variation with respect to $\mathcal{A}_\alpha$ leads to the Proca field equations:

$$\nabla_\alpha \mathcal{F}^{\alpha\beta} = \mu^2 \mathcal{A}^\beta,$$

where g is the determinant of the metric, R is the Ricci scalar and μ is the mass of the Proca field, in a notation similar to the one used in Chapter 2, wherein μ was the scalar field mass. As discussed in [16], it is possible to find stationary and axially-symmetric spacetime solutions (with an without horizon) that are asymptotically flat, that satisfy all energy conditions and that have a $\mathbb{Z}_2$ reflection symmetry around an equatorial plane. We consider the metric ansatz displayed in Section 2.1, with coordinates (t, r, θ, φ) [24],

whereas the Proca field ansatz takes the form:

$$\mathcal{A} = e^{i(m\varphi - wt)}\tilde{\mathcal{A}}(r,\theta),$$

where t, φ are the coordinates associated respectively to the stationary and axially-symmetric Killing vectors and $\tilde{\mathcal{A}}(r,\theta)$ is a 1-form with components depending only on the (r,θ) coordinates. The complex phase factor in the previous expression introduces an explicit t and φ dependence that cancels explicitly at the level of the energy-momentum tensor. However, the spacetime does depend on the field frequency w and on the azimuthal harmonic index m.

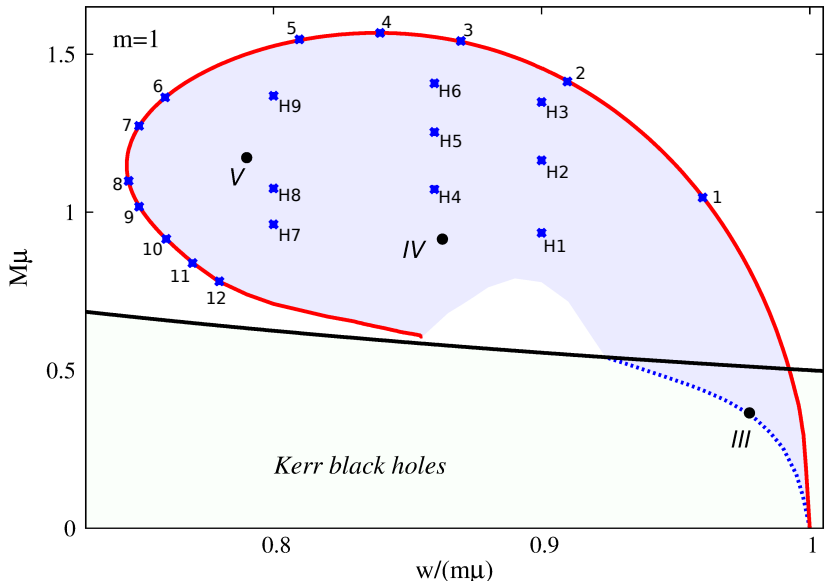


Figure 3.1: KBHsPH solutions (blue shaded region) in an ADM mass *vs.* vector field frequency diagram. The red solid line describes the family of RPSs with $m = 1$, and the blue dashed line is the Kerr existence line that can support Proca clouds. The highlighted points are configurations analysed below.

The solution space of KBHsPH[1] in a $M\mu$ *vs.* $w/(m\mu)$ diagram is displayed in Fig. 3.1, where M is the Arnowitt-Deser-Misner (ADM) mass. The solutions that are discussed in this chapter are highlighted in Fig. 3.1, with a labeling unrelated to the one used in the previous Chapter. The reader is directed to [16] for further details. The spiral curve in

[1]These solutions have one node for the temporal component of one of the Proca potentials [16]; nodeless solutions have also been found.

Fig. 3.1 represents the Rotating PS (RPS) solutions, which are continuously connected to KBHsPH if $m = 1$, but not if $m = 0$. In the next section we will start by analysing the gravitational lensing of RPSs.

3.2 Lensing by rotating Proca stars

In a nutshell, the gravitational lensing effect is a deformation of the light ray path by a gravitational field. Following [72, 23, 24], we analyse the lensing of a compact object (*e.g.* a RPS) placed in the center of a large colored sphere $\mathcal{N}$. An observer frame O is constructed (also) inside the colored sphere, at a given distance[2] from the compact object, and in the equatorial plane ($\theta = \pi/2$) (see Section 1.4). An observation image is then defined in the observer's frame as a simplified camera model, where the image parametrization is provided by the angles in the frame's local sky.

These observation images can be computed numerically by propagating null geodesics for different observation angles, starting from the observer's position and stopping when the origin of each light ray has been determined. This procedure is called *backwards ray-tracing*, since we are propagating light rays backwards in time (see Section 1.6). As previously remarked, each point in a given image sets a different initial condition for a null geodesic, with the pixel color (*e.g.* green) exhibiting the endpoint color in the surrounding colored sphere. The latter is composed of four colored quadrants with a black grid on top.

We first consider the PSs with rotation (RPS), given by the $m = 1$ spiral on Fig. 3.1. The lensed images of solutions 1 to 12 can be found in Fig. 3.2. As we move counter-clockwise along the PS spiral there is the formation of an Einstein ring and a duplication of a patch of the colored sphere. The lensing is not symmetric due to the rotation of the spacetime.

As we approach a PS that possesses a *light ring* the number of Einstein rings becomes

[2]The observer perimetral radius [23] for PSs is $\sqrt{g_{\varphi\varphi}} = 22.5\,\mu^{-1}$, and $\sqrt{g_{\varphi\varphi}} = 15M$ for BHs.

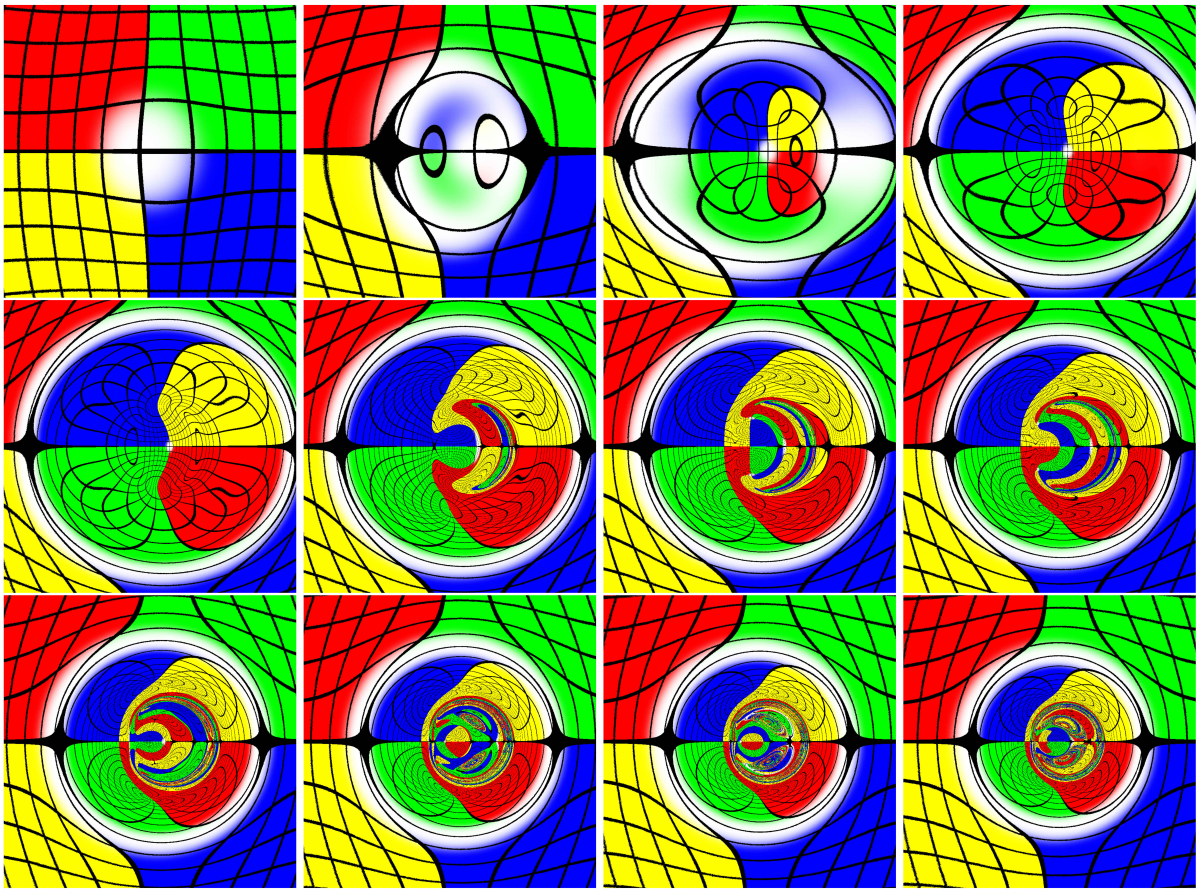


Figure 3.2: Lensing by rotating PSs with $m = 1$, from $1 \to 12$. From left to right: (top) $w_{1,2,3,4} = 0.96; 0.91; 0.87; 0.84$; (middle) $w_{5,6,7} = 0.81; 0.76; 0.75$; $w_8 = 0.746$; (bottom): $w_{9,10,11,12} = 0.75; 0.76; 0.77; 0.78$.

infinite. This is due to the fact that null geodesics very close to a light ring can revolve an arbitrarily large number of times around the PS. Light rings and their generalizations (FPOs) are analysed in Section 3.3.1. If we now move even further along the spiral chaos seems to emerge. In particular, the formation of pixelated regions in the image is a manifestation of sensitivity to initial conditions and hence an indication of chaos.

Indeed, recall that each point in the observation image determines the initial condition of a light ray. See Chapter 2 and [24] for a discussion of a similar behaviour in the scalar case. As in the case of Boson Stars (BSs), images of PSs have no shadow. However, rotating PSs are connected to KBHsPH, which (generically) have an event horizon and hence a shadow, as discussed in the next section.

3.3 Shadows of Kerr BHs with Proca hair

When obtaining the lensing of KBHsPH via backwards ray-tracing, some light rays might fall asymptotically into the BH's event horizon. Hence the lensed images of KBHsPH will display some points with a lack of luminosity[3], corresponding to the infall of geodesics into the BH. The set of all such points in the observation image forms the *shadow* of the BH. The images of the KBHsPH solutions in Fig. 3.1 are displayed in Fig. 3.3, with the circular black region in the images as the corresponding shadows. In the remainder of this chapter, configurations III, IV and IV are the same KBHsPH as those considered in [16] and that are publicly available in [196]. We keep this labelling here, to avoid confusion, even though we shall not discuss all configurations presented in [16].

In particular, solution III in the top leftmost image of Fig. 3.3 is quite close in solution space to vacuum Kerr, and shares a similar shadow with the latter. More hairy solutions however, such as $H5$, can possess shadows considerably smaller than the comparable Kerr case, while the Einstein ring structure can still be similar. Heuristically, such solutions can be regarded as small BHs surrounded by a massive Proca "cloud", where most mass resides. We would like to call the attention of the reader to solution $H8$, which displays a *cusp* in the shadow edge. This feature can be connected to special light orbits (FPOs). In the next section, an effort will be made to classify all such orbits.

3.3.1 Classification of FPOs

Light rings (LRs), *i.e.* circular photon orbits, are an extreme form of light bending by ultracompact objects (UCOs). They have distinct phenomenological signatures in both the electromagnetic and gravitational wave channels. In the former, LRs are closely connected to the *shadow* of a black hole (BH) [44, 197]. This is the absorption cross section of light at high frequencies, an observable that is being targeted by the Event Horizon Telescope [198, 199].

[3]Assuming there is no light sources in between the observer and the BH.

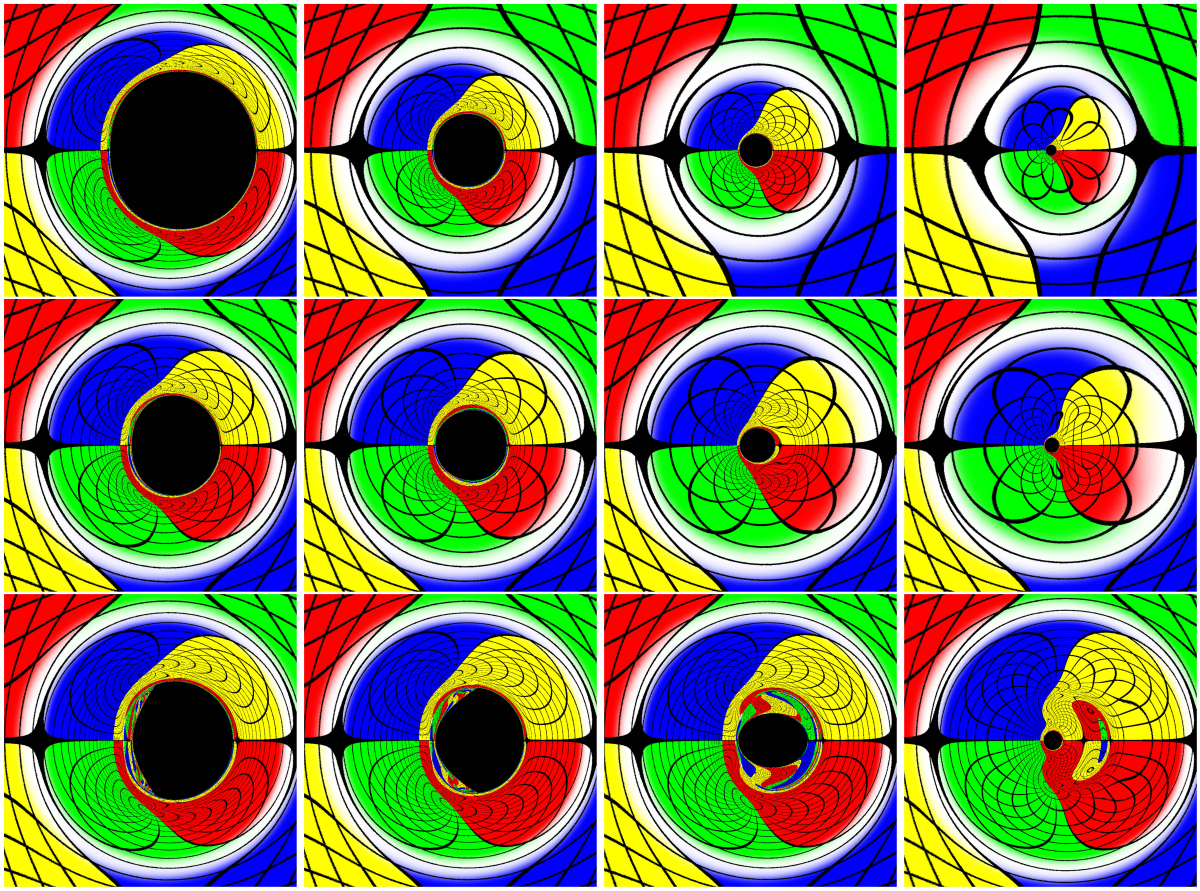


Figure 3.3: Shadows of KBHSPH with $m = 1$. From left to right: (top) III, $H1$, $H2$, $H3$; (middle) IV, $H4$, $H5$, $H6$; (bottom): $H7$, $H8$, V, $H9$.

In the gravitational wave channel, LRs determine a perturbed BH's early-time ringdown [200], corresponding to the post-merger part of the recently detected gravitational wave transients by aLIGO [4, 5]. The frequency and damping time of this early-time ringdown are set by the orbital frequency and instability time scale (Lyapunov exponent) of an (unstable) LR[4].

LRs also define other dynamical properties of UCOs. For horizonless UCOs, LRs often come in pairs, one being stable and the other unstable. The existence of a stable LR has been claimed to imply a spacetime instability [26, 27]. Finally, LRs impact on our Newtonian intuition for test particle motion: crossing (inwards) a LR swaps the perception of inwards/outwards, and reverses the centrifugal effect of angular motion [202].

[4]See also [201] for a discussion on its generality.

For spherical UCOs, bound photon orbits are always planar (*e.g.* LRs). But for an axisymmetric (and stationary) spacetime more general photon orbits are possible, that neither escape to infinity, nor fall into a BH (if the UCO is a BH). In this section, we analyse implications, and propose a classification, of this natural generalization of LRs, dubbed *fundamental photon orbits* (FPOs). In particular we argue they can trigger new spacetime instabilities and show they are paramount in understanding the detailed structure of BH shadows.

In vacuum General Relativity (GR), the only regular (on and outside an event horizon) UCO is the Kerr solution [57], wherein geodesic motion is Liouville integrable and separates in Boyer-Lindquist (BL) coordinates $(t, r_{BL}, \theta, \varphi)$ [63]. In this chart, FPOs with constant r_{BL} and motion in θ exist, known as *spherical orbits* [66] (see Section 1.1).

The subset restricted to the equatorial plane are the two LRs, one for co-rotating and one for counter-rotating photons (with respect to the BH), both converging at $r_{BL} = 3M$ in the Schwarzschild BH (mass M) limit [75]. Spherical orbits are related to the ringdown modes in BH perturbation theory [203] and completely determine the Kerr BH shadow (see Fig. 3.7). These are the most general FPOs in Kerr outside the horizon, all of them unstable. For generic stationary and axisymmetric spacetimes, we define FPOs as follows:

> *Definition:* let $s(\lambda) : \mathbb{R} \to \mathcal{M}$ be an affinely parameterised null geodesic, mapping the real line to the space-time manifold $\mathcal{M}$. $s(\lambda)$ is a FPO if it is restricted to a compact spatial region – it is a bound state – and if there is a value $T > 0$ for which $s(\lambda) = s(\lambda + T), \forall\, \lambda \in \mathbb{R}$, up to isometries.

In coordinates (t, r, θ, φ) adapted to the stationarity and axi-symmetry vector fields, $\boldsymbol{\zeta} = \partial_t$ and $\boldsymbol{\xi} = \partial_\varphi$ respectively, this definition requires periodicity only in (r, θ). Generically, LRs can be determined via the $h_\pm(r, \theta)$ or $H_\pm$ functions defined in [24, 10] and in Sections 2.1 and 1.5.2. A LR is either a saddle point or an extremum of these functions, for fixed (r, θ).

The analogue of spherical orbits in non-separable spacetimes, however, is meaningless, since $r = const.$ is not preserved by mixing r and θ, and no key property, such as separability, singles out a particular coordinate chart.

Recalling the discussion in Section 2.1, the null geodesic flow on a spacetime $(\mathcal{M}, g_{\mu\nu})$ is described by the Hamiltonian $\mathcal{H} = \frac{1}{2} g^{\mu\nu} p_\mu \, p_\nu = 0$, where p_μ is the photon's 4-momentum. Besides stationarity, axi-symmetry and asymptotic flatness, with the metric expressed in the aforementioned coordinates, we further assume a $\mathbb{Z}_2$ reflection symmetry on the equatorial plane ($\theta = \pi/2$) and metric invariance under the simultaneous reflection $t \to -t$ and $\varphi \to -\varphi$. In addition, gauge freedom is used to set $g_{r\theta} = 0$.

In terms of the first integrals of motion $p_t \equiv -E$ and $L \equiv p_\varphi$, we define a potential $V(r, \theta)$ and a kinetic term $K \geqslant 0$ [24]:

$$0 = 2\mathcal{H} = \underbrace{g^{rr} {p_r}^2 + g^{\theta\theta} {p_\theta}^2}_{K \geqslant 0} + \underbrace{g^{tt} E^2 - 2 g^{t\varphi} E \, L + g^{\varphi\varphi} L^2}_{V \leqslant 0} \ .$$

$V > 0$ defines a forbidden region in phase space. At its boundary, $V = 0 \Rightarrow p_r = 0 = p_\theta$. From Hamilton's equations, $\dot{p}_\mu = -\frac{1}{2} \left(\partial_\mu g^{rr} p_r^2 + \partial_\mu g^{\theta\theta} p_\theta^2 + \partial_\mu V \right)$. The limit $V \to 0$ leads to $\dot{p}_\mu \to -\frac{1}{2} \, \partial_\mu V$. Hence, photons can only hit the boundary of the allowed region ($V = 0$) perpendicularly. The null geodesic flow only depends on an impact parameter $\eta \equiv L/E$. By fixing η, ones determines the boundary of the forbidden region $V = 0$. Within this setup, we categorized FPOs with the compact notation $X^{n_r \pm}_{n_s}$, where $X = \{O, C\}$, and $\{n_r, n_s\} \in \mathbb{N}_0$:

i) they either reach the boundary [*class O* (open)], or they do not [*class C* (closed)], in which case they loop;

ii) they are either even ($subclass^+$) or odd ($subclass^-$) under the $\mathbb{Z}_2$ reflection symmetry. For odd states a distinct mirror orbit exists;

iii) they cross the equatorial plane ($\theta = \pi/2$) at n_r distinct r values (subclass^{n_r}). Orbits *on* the equatorial plane, such as LRs, have $n_r = 0$ (they never cross it);

iv) They have n_s self-intersection points (subclass$_{n_s}$).

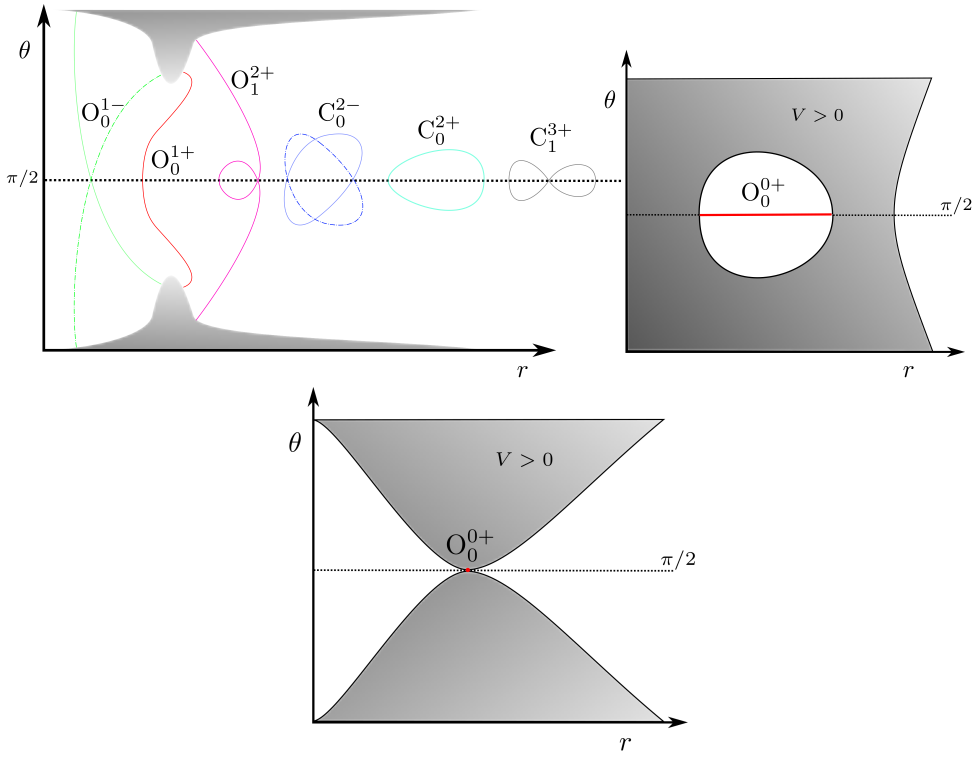


Figure 3.4: Illustration of some FPOs in the (r, θ)-plane and their classification. The grey areas represent forbidden regions with $V > 0$. The left/right panels show a typical unstable LR and a stable planar orbit. Adapted from [11].

Some illustrations of these orbits are given in Fig. 3.4. Typical LRs and more generic planar orbits are type O_0^{0+} (left and right panels). Examples of the latter have been found, *e.g.* in [24]. $\mathbb{Z}_2$ odd orbits, such as O_0^{0-}, exist for instance in the $\mathbb{Z}_2$ Majumdar-Papapetrou dihole [77]. The Kerr FPOs are all of class O_0^{1+}. We have verified class O_1^{2+} and C_0^{2+} exist for rotating Proca stars [22], see Fig. 3.5.

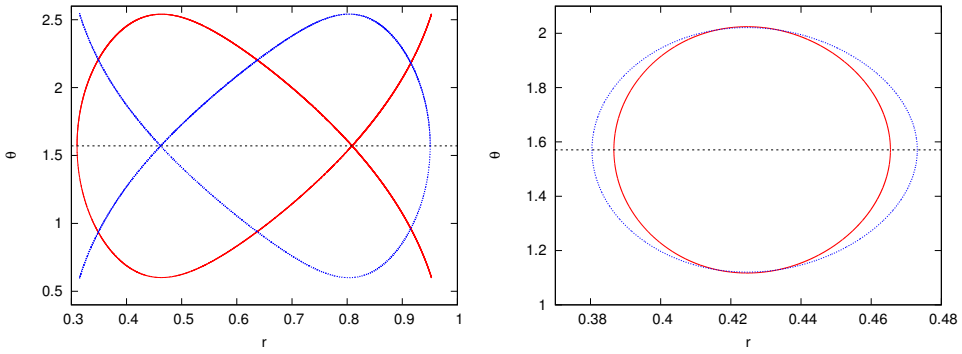


Figure 3.5: Orbits for the rotating PS configuration 8 of Fig. 3.1, represented on the (r, θ). (Left) a pair (shown in different colors) of O_1^{2+} orbits with $\eta = -3\,\mu^{-1}$; (Right) a pair of C_0^{2+} orbits with $\eta = -10.99\,\mu^{-1}$. All of these orbits appear to be dynamically stable. Radial coordinate r shown in $1/\mu$ units.

3.3.2 Stability of FPOs

The stability of FPOs can be analysed with *Poincaré maps* (see *e.g.* [204]). The relevant phase space is the 4-dimensional manifold $\mathbb{M}$, parameterized by $(r, \theta, \dot{r}, \dot{\theta})$. Consider a null geodesic s on $\mathbb{M}$ and let $\mathbb{P}$ be a *Poincaré section*, a submanifold of $\mathbb{M}$, which is assumed to intersect s at multiple points, see Fig. 3.6.

Usually the dimension of $\mathbb{P}$ is taken to be $\dim(\mathbb{M}) - 1 = 3$, but since there is an additional Hamiltonian constrain, we consider $\dim(\mathbb{P})$=2. A *Poincaré map* $f : \mathbb{P} \to \mathbb{P}$, sends a given point of intersection with s to the next intersection point. Parameterising $\mathbb{P}$ by $\mathbf{x} = \{x^1, x^2\}$, the Poincaré map reads $f(\mathbf{x}_n) = \mathbf{x}_{n+1}$. This defines a discrete sequence of the intersection points, indexed by n.

For a FPO, it is always possible to find $\mathbb{P}$ having fixed points $\tilde{\mathbf{x}}$ of this map, at which $f(\tilde{\mathbf{x}}) = \tilde{\mathbf{x}}$. Its stability is determined by the behaviour of f in the neighbourhood of $\tilde{\mathbf{x}}$. Taylor expanding to first order reads

$$f(\mathbf{x}_n) \simeq f(\tilde{\mathbf{x}}) + \nabla f(\tilde{\mathbf{x}}) \cdot \mathbf{y}_n,$$

where $\mathbf{y}_n \equiv \mathbf{x}_n - \tilde{\mathbf{x}}$ is the deviation variable and ∇f is a 2×2 matrix $A_{kj} \equiv (\nabla f^k)_j = \partial_j f^k$.

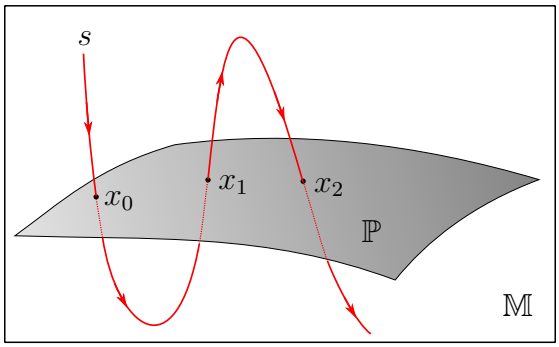


Figure 3.6: Illustration of a Poincaré section $\mathbb{P}$ on a manifold $\mathbb{M}$. Notice that the dimension of $\mathbb{P}$ and $\mathbb{M}$ are actually 2 and 4 respectively. The manifold $\mathbb{M}$ can have as a possible parametrization $(r, \dot{r}, \theta, \dot{\theta})$. A null geodesic s intersects $\mathbb{P}$ at multiple points, forming a sequence of x_i values. The represented case is not a FPO.

Neglecting the higher order terms,

$$\mathbf{y}_{n+1} \simeq \nabla f(\tilde{\mathbf{x}}) \cdot \mathbf{y}_n,$$

such that the N^{th} term of a sequence starting with a deviation $\mathbf{y}_0$ is

$$\mathbf{y}_N \simeq [\nabla f(\tilde{\mathbf{x}})]^N \cdot \mathbf{y}_0 \,.$$

The value of $\mathbf{y}_N$ may diverge depending on the properties of (the matrix) $\nabla f(\tilde{\mathbf{x}})$, and in particular, of the modulus of its eigenvalues Λ_k: if $|\Lambda_k| \leqslant 1$, for all k, the orbit is stable; if $|\Lambda_k| > 1$, for at least one k, the orbit is unstable.

Consider O_0^{1+} orbits and let $\mathbb{P}$ be the equator $\theta = \pi/2$. Using the Hamiltonian constraint, a local patch of $\mathbb{P}$ is parametrized by $\mathbf{x} = (r, \dot{r})$. At the fixed point, $\tilde{\mathbf{x}} = (\tilde{r}, 0)$, only two (symmetric) values of $\dot{\theta}$ are possible. For simplicity, restrict $\mathbb{P}$ to include only the fixed point with $\dot{\theta} \geqslant 0$. We remark that O_0^{1+} actually intersects $\mathbb{P}$ with a symmetric $\dot{\theta}$ before returning to the initial point on $\mathbb{P}$. However, we could then redefine the map $f(x) \to (f \circ f)(x)$, so that $f(\tilde{x}) = \tilde{x}$ without an intermediate point.

Defining $D = \det(A)$ and $T = \mathrm{trace}(A)/2$, the eigenvalues of the 2×2 matrix $A_{kj} \equiv (\nabla f^k)_j = \partial_j f^k$ are provided by $\Lambda_\pm = T \pm \sqrt{T^2 - D}$. For Hamiltonian systems $D = \pm 1$

(see [204]). The examples below have $D = 1$ and fall into one of two cases. If $T^2 > 1$, one of the eigenvalues has modulus larger than unity, and the orbit is unstable. If $T^2 \leqslant 1$, the eigenvalues $\Lambda_\pm = T \pm i\sqrt{1 - T^2}$ have unit modulus, leading to a rotation of the Poincaré map around the fixed point, which is therefore stable. This analysis provides a simple criterion for the stability of the FPO. We remark that $D = -1$ was not found within the cases analysed herein. In such case, the orbit is unstable for $T \neq 0$, and stable for $T = 0$.

3.3.3 Kerr (and Kerr-like) FPOs

A generic Kerr solution has[5] two LRs (see Section 1.1), one for a negative impact parameter, η_-^{LR}, and the other for a positive one, η_+^{LR}. The specific value of $\eta_\pm^{LR}$ depends on the BH spin.

A continuum of FPOs exists with $\eta_-^{LR} < \eta < \eta_+^{LR}$. Each of these is, in BL coordinates, a spherical orbit that crosses the equatorial plane at a given perimetral radius, $r_{\rm Peri}$ (see Section 1.2.1), in between those of the two LRs, and attains a maximal/minimal angular coordinate $\theta_{\rm max}$. Observe that $\theta_{\rm max} = \{0, \pi\}$ for $\eta = 0$, such that $\Delta\theta \equiv |\theta_{\rm max} - \pi/2|$ reaches $\pi/2$. The FPO with $\eta = 0$ is actually the only complete spherical orbit; the remaining ones fail to reach high latitudes - Fig. 3.7 (top panels).

All Kerr FPOs are unstable ($T^2 > 1$). Neighbouring orbits to FPOs either escape to infinity or fall into the BH. Hence, these unstable FPOs determine the edge of the BH shadow - Fig. 3.7 (bottom panel). Rotating BHs in modified gravity (or in GR with reasonable matter contents) have typically small deviations from Kerr, including in their shadows. Thus a similar picture for FPOs holds for many rotating BHs, leading, in particular, to (qualitatively) Kerr-like shadows. Examples exist both in GR and beyond GR [205, 206, 106, 109, 117, 127, 30, 142, 147, 207].

[5] In this section we only consider the region outside the horizon.

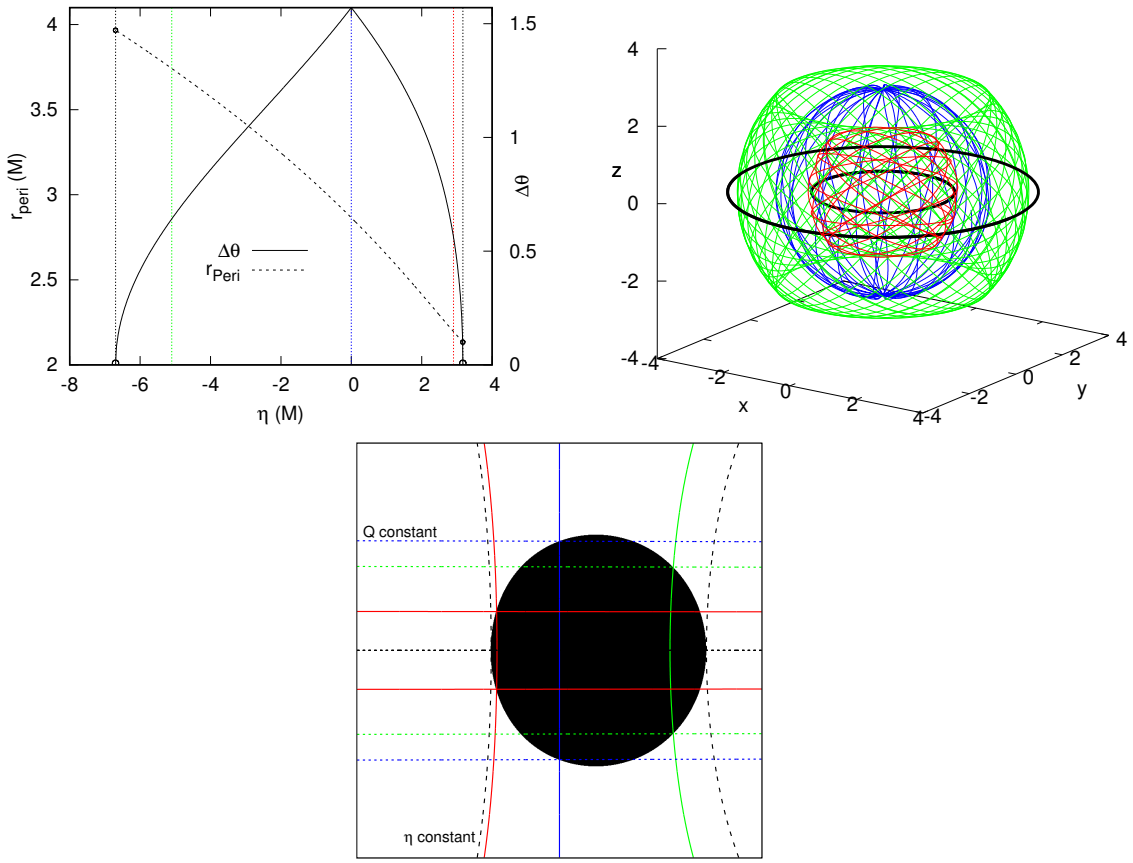


Figure 3.7: Kerr(-like) FPOs and shadow, illustrated for a Kerr BH with dimensionless spin $J/M^2 \simeq 0.820$, $\eta_- = -6.70\,M$, $\eta_+ = 3.17\,M$. (*Top left panel*): $r_{\rm Peri}$ and $\Delta\theta$ for FPOs *vs.* η. Lines with $\eta =$ constant take the values of the LRs or 3 selected FPOs, $\eta = -5.10, 0, 2.90\,M$. (*Top right panel*): Spatial trajectories of these 3 FPOs and 2 LRs, in Cartesian-like coordinates defined from BL coordinates. (*Bottom panel*): BH shadow, in the same observations conditions as Fig 3.8. Almost vertical (solid) lines have $\eta =$ constant and horizontal (dotted) lines have fixed Carter's constant Q, both with the values of the 3 selected FPOs. Observe how the FPOs (η, Q) values correspond to points at the edge of the shadow. The same colours are used in all panels for the same FPOs. Adapted from [11].

3.3.4 Non-Kerr FPOs

Significant non-spherical deformation of the Schwarzschild BH can lead to exotic features in its optical images [208]. For rotating BHs arising in a reasonable GR model with energy conditions abiding matter, non-Kerr-like shadows have been reported [23] for Kerr BHs with scalar hair [12, 13] (see Section 2.1). Here, we illustrate non-Kerrness using its "cousin" model Kerr BHs with Proca hair [16]. In these hairy BHs, the null geodesic flow is non-integrable and chaos occurs for some (sufficiently) hairy BHs [24]. Recent work

suggests the dynamical formation of Kerr BHs with Proca hair [84], justifying a detailed analysis of the theoretical and phenomenological properties of this family of solutions.

Amongst these hairy BHs we have chosen configuration $H8$ of Fig 3.1, which is a sharp and illustrative example of (non-Kerr-like) FPOs, including stable ones. Its lensing produces a *cuspy shadow* – Fig. 3.8. This Kerr BH with Proca hair has ADM mass and angular momentum $(M, J) = (1.075\,\mu^{-1}, 0.948\,\mu^{-2})$ and horizon quantities $(M_H, J_H) = (0.045\,\mu^{-1}, 0.012\,\mu^{-2})$, with the Proca field oscillating with frequency $w = 0.8\,\mu$. The solution's (ADM) quantities, (M, J), match those of the Kerr BH shown in Fig. 3.7. This is a (very) hairy BH with $\sim 96\%$ of the mass and $\sim 99\%$ of the spin stored in the "hair" (Proca field).

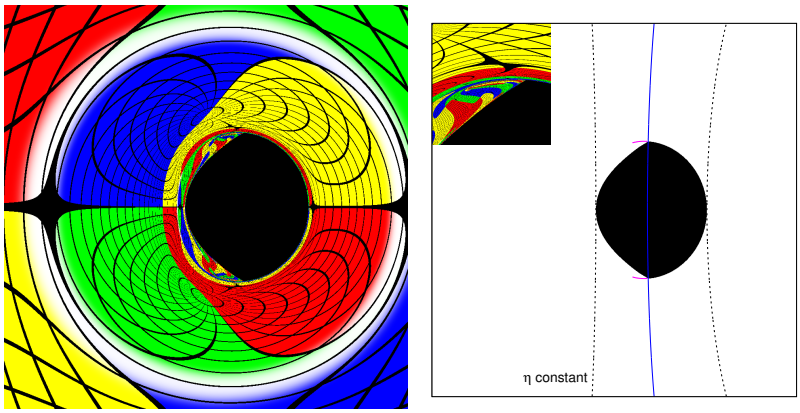


Figure 3.8: (Left panel) Lensing of the hairy BH with a cuspy shadow, obtained with the same setup as in [23]. (Right panel) The cuspy shadow in the same observation conditions as the ones for the Kerr BH [which has the same (M, J)] in Fig. 3.7. Almost vertical lines have constant η and in this case there is no analogue of the Carter's constant. The small (pink) eye lashes correspond to a particular lensing pattern connecting to the cusp, which can be observed in the inset. Adapted from [11].

The salient feature of the cuspy shadow is its non-smooth edge. This feature, which can also occur for some Kerr BHs with scalar hair, is a consequence of the FPOs of this solution, as can be observed by analysing the $r_{\rm Peri}$ and $\Delta\theta$ for these FPOs, in terms of the impact parameter η – Fig. 3.9 (left panel).

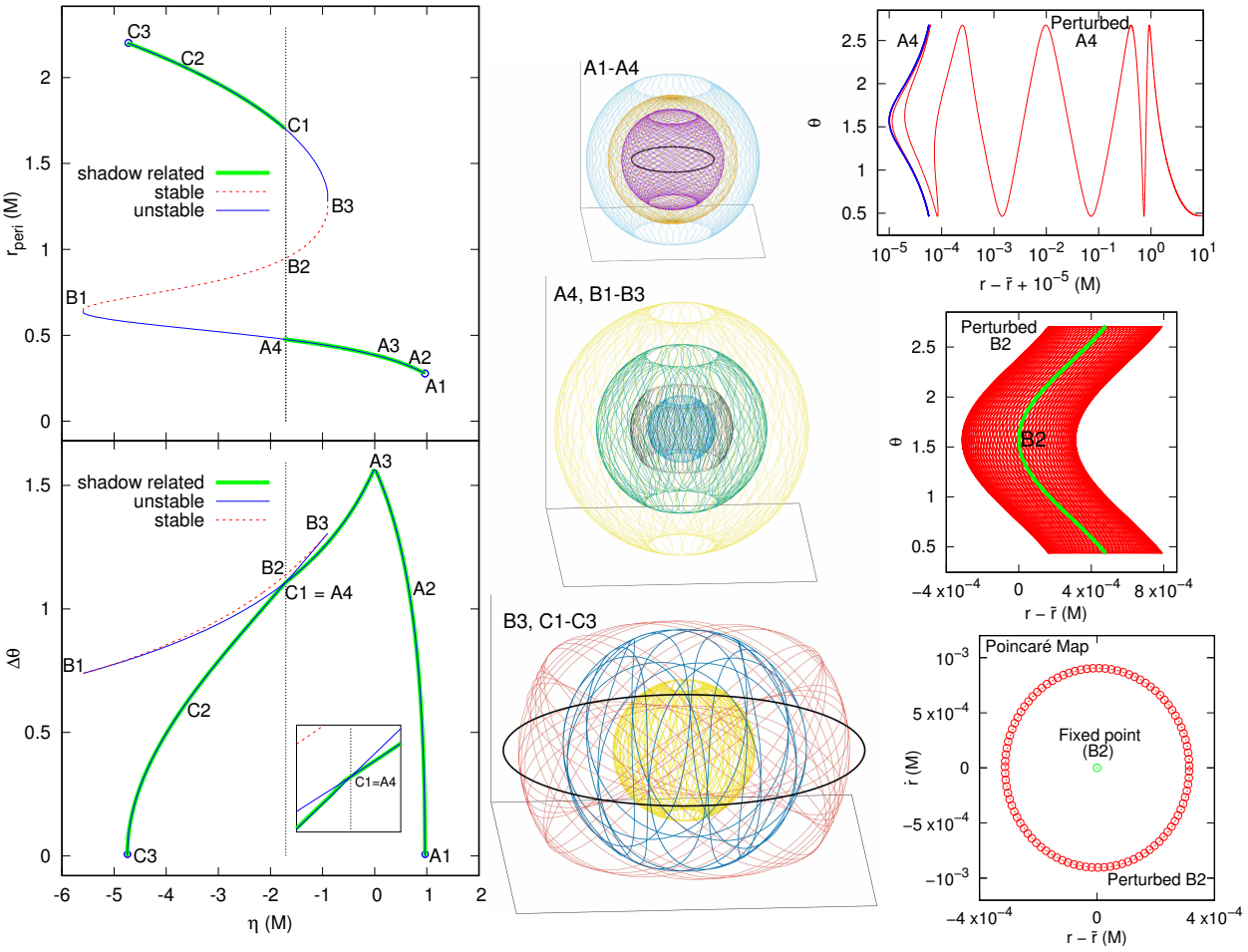


Figure 3.9: Non-Kerr(-like) FPOs, illustrated for the hairy BH described in the text. (Left panel) $r_{\rm Peri}$ and $\Delta\theta$ for FPOs *vs.* η. We selected 10 FPOs (A1-A4,B1-B3,C1-C3), including the two LRs. The line $\eta \simeq -1.71M$ takes the value at which the cusp in the shadow occurs – Fig. 3.8. (Middle panel) Spatial trajectories of these 10 FPOs, in Cartesian coordinates defined from the spheroidal coordinates in [16]. The A4 (blue) and B3 orbits (yellow), at the intersection between stable and unstable branches are repeated to convey a sense of scale. (Right panel) One unstable [stable] FPO of the group A (top) [B (middle)] and a neighbouring perturbed orbit which diverges from [oscillates around] the FPO, together with the Poincaré map (on $\theta = \pi/2$) of B2, showing rotation about the fixed point $(r, \dot{r}) = (\tilde{r}, 0)$. Adapted from [11].

Fig. 3.9 (left panel) informs us that, as for Kerr, there are two LRs, for $\eta_{\pm}^{LR} = -4.75; 0.97M$. However, differently from Kerr, these LRs are connected by a continuum of FPOs that can be split into three branches: two unstable (with $T^2 > 1$, that connect to the LRs) and a stable one, with $T^2 \leqslant 1$, in between. A careful analysis of the two unstable branches reveals that only a part of each (green thicker lines) contributes to the edge of the shadow.

The remaining unstable FPOs, as well as the stable FPOs, do not. Since the edge of the shadow on the equatorial plane is determined by the LRs, the FPOs that determine this edge must jump between the two branches. The jump occurs at the FPOs C1 and A4, which have the same $\eta \simeq -1.71M$ and attain the same angular deviation $\Delta\theta$. But there is a discontinuity in the size of these orbits, $r_{\rm Peri}(C1) > r_{\rm Peri}(A4)$, inducing the cusp in the shadow, precisely at $\eta \simeq -1.71M$ (Fig. 3.8, right panel, blue line).

The unstable FPOs that are not associated to the shadow edge can, however, impact on the lensing properties of the spacetime. This is manifest in the *eye lashes* depicted in Fig. 3.8 (right panel, pink lines) which are associated to FPOs between C1 and B3, and form a clear lensing pattern (inset): a *ghost shadow edge* from that branch of unstable FPOs. Finally, if any photon bound orbit induces a spacetime non-linear instability [26, 27], such instabilities would be missed by analysing solely LRs. Indeed, this example illustrates that non-planar stable FPOs may exist *without* planar ones (LRs).

FPOs are the generic counterpart of LRs in a stationary, axisymmetric spacetime (see [77, 209] for other discussions on extension of LRs). The illustrations herein show that FPOs can have a richer structure than in Kerr, and are instrumental in understanding BH shadows, lensing properties and spacetime stability. Thus, general FPOs can yield spacetime information beyond the scope of LRs. An extension of this concept, for generic spacetimes without any isometries, such as dynamical BH binaries, would be of interest.

Chapter 4

Black Hole mimickers

The dawn of the era of gravitational-wave astronomy [4, 5, 6] promises to deliver detailed information about the nature of very compact objects in the Universe. The standard paradigm is that these are either BHs or neutron stars, but one cannot exclude, *a priori*, the possibility that other compact objects, of an even more exotic nature, may hide in the Cosmos.

The true nature of astrophysical black hole (BH) candidates has been a central question in relativistic astrophysics for decades. The observational elusiveness of their defining property – the existence of an event horizon –, allows the possibility that they may, in reality, be some sort of exotic *horizonless* compact objects, whose phenomenology is sufficiently similar to that of BHs, so that current observations are unable to distinguish these two types of objects.

In this context, the recently opened Gravitational-Wave (GW) window to the Cosmos [4, 5, 6], offers a particularly well suited channel to probe the nature of compact objects. Yet, it has been recently emphasised that observational degeneracy may still remain in this channel [9]. The correspondence between a BH's natural oscillation frequencies (so called quasi-normal modes [210]) and light ring (LR) vibrations [200, 211, 212], implies that compact objects with a LR – henceforth *ultra-compact objects* (UCOs) – but that possess no event horizon can mimic the initial part of the ringdown GW signal of

perturbed BHs. Later parts of the ringdown signal may have signatures of the true nature of the object (through the so called *echos* [213, 214]), but the corresponding lower *signal to noise ratio* challenges clean detections of this part of the signal, at least in the near future – see [215, 216, 217, 218, 219] for recent discussions.

Is there, consequently, a real risk of observationally mistaking UCOs by BHs and vice-versa, with current and near future gravitational-wave measurements? To address this important question, one should start by revisiting the theoretical foundations of concrete UCOs models. Even though many variants of horizonless UCOs have been proposed in the literature, either as stationary solutions of well-defined models or as more speculative possibilities (see *e.g.* [220, 18, 221, 222, 223, 22]), they generically suffer from the absence of a plausible formation scenario. An exception, in this respect, are bosonic stars. (Scalar) BSs in particular, have been shown in spherical symmetry to form through a process of gravitational collapse, due to an efficient cooling mechanism [224]. Moreover, boson stars are known to become UCOs, in parts of their domain of existence [23] (see Chapter 2).

In the first part of this chapter, we shall take spherically symmetric scalar boson stars, as well as their vector cousins, dubbed *Proca stars* [22], collectively referred to as *bosonic stars*, as a reference example of horizonless UCOs that are a proof of concept of BH mimickers that are dynamically possible through known physics. In order to assess their quality as BH mimickers one can perform the following inquiry: when in the UCO regime, does *all their LR associated phenomenology* mimic that of a Schwarzschild BH?

This analysis reveals that bosonic stars, both the scalar and the vector ones, fail to pass this test. Firstly, the same LR that would allow them to vibrate as BHs do, gives rise to a quite distinct pattern of light lensing from standard BH shadows. In a sense, the LR associated electromagnetic channel phenomenology raises the degeneracy of the GW channel phenomenology. Secondly, and more importantly, bosonic stars only become UCOs in a regime wherein they are also perturbatively unstable. Thus, the same perturbations that could make them vibrate as a BH will actually induce their gravitational

collapse into one; fully non-linear simulations show that this is a fast process, and a horizon forms within a few light-crossing times [25]. All together, these results emphasise the difficulty, at least in spherical symmetry, in constructing a reasonable dynamical model of horizonless UCOs whose phenomenology can mimic that of a BH, in all its aspects.

In the second part of the chapter, we discuss a theorem based on the topological charge of LRs; this result implies that horizonless UCOs must possess a stable LR within generic and reasonable assumptions, and the existence of the latter could induce a spacetime instability. This would make such BH mimickers unviable as an alternative to BHs, whenever these instabilities occur on astrophysically short time scales.

4.1 Ultra-compact bosonic stars

The ultra-compact bosonic stars we shall be considering in this chapter are solutions of Einstein's gravity minimally coupled with a spin-s field, with $s = \{0, 1\}$. The scalar case was first discussed in [225, 226] and it is reviewed in [18], whereas the vector case was first discussed in [22] (see also [13, 16]). We shall keep a similar notation as the one used in Chapters 2-3. However, we shall now focus in spherically symmetric solutions, which have the azimuthal harmonic index $m = 0$. They are obtained using the line element

$$ds^2 = -N(r)\sigma^2(r)dt^2 + \frac{dr^2}{N(r)} + r^2(d\theta^2 + \sin^2\theta d\varphi^2) \ , \tag{4.1}$$

where $N(r) \equiv 1 - 2\overline{m}(r)/r$, $\overline{m}(r), \sigma(r)$ are radial functions and $\{r, \theta, \varphi\}$ correspond to Schwarzschild-type coordinates. In particular the radial coordinate r is the geometrically meaningful *areal radius*, meaning that the proper area of a 2-sphere (r, t =constant) is $4\pi r^2$ (this coincides with the perimetral radius of Section 1.2.1). The Einstein-matter equations are solved, numerically, with appropriate boundary conditions. The explicit form of these equations and boundary conditions, together with some examples of profiles of the matter and metric functions can be found in [227] (see also [22] for the Proca case).

In Fig. 4.1 we exhibit various properties of the scalar (left columns) and vector (right

columns) bosonic stars which are relevant for our study. The top panels show the domain of existence of the solutions in an ADM mass, M, *vs.* a bosonic field frequency, w, diagram. Regardless of the spin, the solutions form a characteristic spiralling curve, starting from the Newtonian regime (as $w \to \mu$) wherein the bosonic stars tend to become dilute and weakly relativistic. Following the spiral from this Newtonian limit, the ADM mass reaches a maximum at some frequency. These maximal mass and corresponding frequency are, in units with $\mu = 1$, $(w_{\rm max}, M_{\rm max}) = (0.853, 0.633)$ for the scalar case and $(w_{\rm max}, M_{\rm max}) = (0.875, 1.058)$ for the vector case. Perturbation theory computations for both the scalar [228, 229] and vector cases [22] have shown that at this point in the spiral an unstable mode develops.

More relativistic solutions become perturbatively unstable with different possible fates [230, 231]. Further following the spiral, one finds several backbendings, each defining the end of a *branch*. As it can be seen in the inset of the top panels, the solution at which a LR is first seen (marked by a green square – see [23, 24, 11] for quantitative details) occurs in the third (fourth) branch for the scalar (vector) case, corresponding to $(w_{\rm LR}, M_{\rm LR}) = (0.8424, 0.383)$ for the scalar case and $(w_{\rm LR}, M_{\rm LR}) = (0.8880, 0.573)$ for the vector case. These are highly relativistic solutions, with redshift factors approaching those of an event horizon towards the centre of the solutions. In each case, we have highlighted three solutions, denoted 1-3, in the insets of the top panels of Fig. 4.1, corresponding to the solutions we shall analyse below in more detail.

The top panels of Fig. 4.1 also show the Noether charge of the solutions, Q (see *e.g.* [227] for quantitative expressions), corresponding to a locally conserved charge associated with the global $U(1)$ symmetry of each family of solutions. The ratio Q/M, in units with $\mu = 1$, provides a criterion for stability: $Q/M < 1$ implies excess energy and hence instability against fission into unbound bosonic particles. The point at which, in both cases, solutions have excess (rather than binding) energy occurs close to the minimum frequency, and thus already in the region of perturbative instability.

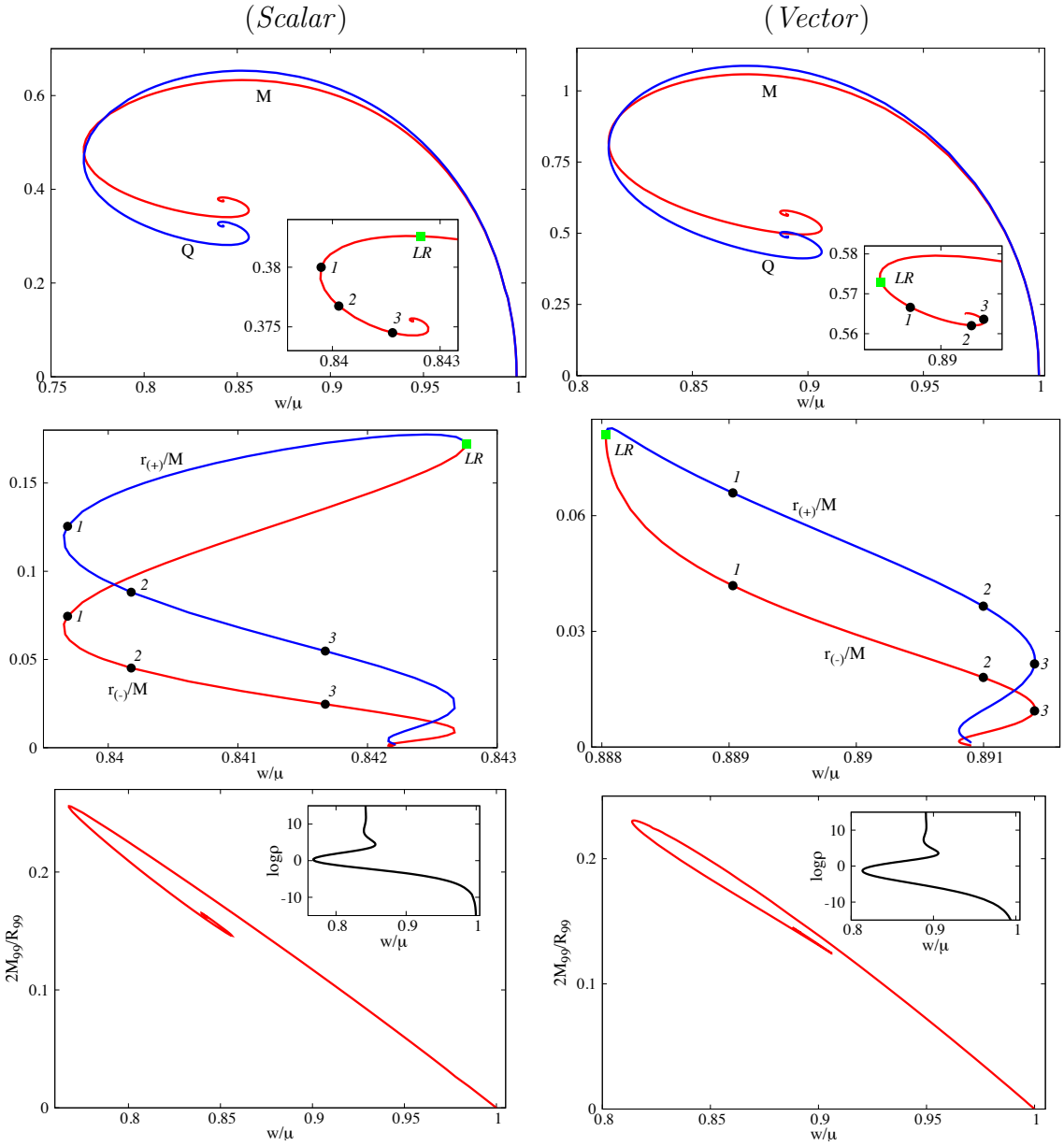


Figure 4.1: (Top panels) Domain of existence of scalar boson stars (left) and Proca stars (right) in an ADM mass (M)/Noether charge (Q) *vs.* field frequency, w/μ, diagram. The green square marks the first solution with a LR. The three highlighted points correspond to the configurations we have analysed in detail, in each case. (Middle panels) Areal radius of the inner r_- and outer r_+ LRs, normalised to the ADM mass, as a function of w, in the region where LRs appear. (Bottom panels) Compactness of the scalar boson stars (left) and Proca stars (right), as measured by $2M_{99}/R_{99}$ (see main text). The inset shows the (log of the) central density. Observe that ρ can get extremely large in the central region, although the solutions will not get more compact, as measured by $2M_{99}/R_{99}$. Adapted from [25].

The middle panels in Fig. 4.1 exhibit the value of the areal radius of each LR, in units of the ADM mass, and its variation along the ultra-compact bosonic star solutions. When the LR first appears in the spiral representing the family of bosonic star solutions it is actually *degenerate*. This solution marks the beginning of the ultra-compact bosonic stars. Deeper into the centre of the spiral, the bosonic stars have two LRs; in fact, generically, smooth ultra-compact objects have an even number of (non-degenerate) LRs [10], as discussed in Section 4.2. The outermost one (with radial coordinate $r_{(+)}$, blue line) always corresponds to an unstable photon orbit; the innermost (with radial coordinate $r_{(-)}$, red line) always corresponds to a stable orbit [10].

As the figure shows, the two radial coordinates start to bifurcate from the first ultra-compact solution, but then converge again, towards the centre of the spiral. Interestingly, the areal radius of the LRs is much smaller than that of a Schwarzschild BH, for which $r/M = 3$. This is associated with the fact these solutions are not constant-density stars, having a much denser central region (inset of bottom panels of Fig. 4.1). The three chosen solutions are also highlighted in these plots, and the corresponding LRs areal radii are given in next table:

Model	w/μ	$\mu M_{\rm ADM}$	$\mu^2 Q$	$r_{(-)}/M$	$r_{(+)}/M$
BS1	0.8397	0.3800	0.3274	0.028	0.048
BS2	0.8402	0.3767	0.3235	0.017	0.033
BS3	0.8417	0.3745	0.3209	0.009	0.020
PS1	0.8890	0.5666	0.4899	0.024	0.037
PS2	0.8911	0.5621	0.4849	0.009	0.019
PS3	0.8914	0.5636	0.4866	0.004	0.010

The bottom panel in Fig. 4.1 show a measure of the compactness of the bosonic stars. Since these stars have no hard surface, several measures of compactness are possible. In view of their exponential fall-off of the matter density, following, *e.g.* [232, 13], we have defined compactness as the ratio of the Schwarzschild radius for 99% of the mass, denoted

$2M_{99}$, to the areal radius that contains such mass, R_{99}. This quantity would be unity for a Schwarzschild BH.

Here we see that the compactness increases from the Newtonian limit until the first back bending, but it decreases along the second branch. Then it increases along the third branch. Such compactness is not a monotonic function along the spiral and indeed the ultra-compact solutions – in the sense of possessing a LR – are not the most compact ones, according to this definition. On the other hand, the central value of the energy density (see *e.g.* [227] for quantitative expressions) is indeed a monotonically increasing function along the spiral, as shown in the inset of these plots. This behaviour, together with the location of the LRs, show that for non-constant density stars, like these bosonic stars, a global measure of compactness, such as $2M_{99}/R_{99}$, may be misleading, as the star may have a considerably denser central region, which is ultra-compact, whereas the star as a whole is not.

4.1.1 Lensing of Ultra-Compact Bosonic Stars

LRs are bound planar photon orbits (see [11] and Section 3 for a general discussion of bound photon orbits). Their existence around a compact object implies strong lensing effects. For the Schwarzschild BH, the LR occurs at an areal radius $r = 3M$ and it is an *unstable* photon orbit. Thus, scattering photons with an impact parameter ($\eta = L/E$, where E, L are the photon's energy and angular momentum, respectively) larger than (in modulus) that of the LR, η_{LR}, return to spatial infinity; but, when η is close to η_{LR}, $|\eta| \gtrsim |\eta_{LR}|$, the scattering angle can be arbitrarily large, in the sense that the photon may circumnavigate the BH an arbitrary number of times before bouncing back to infinity. If $|\eta| < |\eta_{LR}|$, on the other hand, the photon will end up falling into the BH. Thus the LR, defines an absorption cross section for light, the *BH shadow* [44, 197]. This is a timely observable, due to ongoing observations of two supermassive BHs candidates M87* and Sgr A* at horizon scales by the Event Horizon Telescope [199, 118, 1, 2, 3].

In Fig. 4.2 (left panel) the BH shadow and lensing due to a Schwarzschild BH is shown.

The setup is the one introduced in [72] and used in [23, 24, 11], wherein the numerical ray-tracing method is also described (see 1.4). In a nutshell, light emanates from a far away celestial sphere $\mathcal{N}$ that is divided into four quadrants, each painted with one colour (yellow, blue, green red). Black constant latitude and longitude lines are also drawn in the light-emitting celestial sphere. The observer is placed off-centre, within the celestial sphere at some areal radius r_o. Directly in front of the observer, there is a point in the celestial sphere where the four quadrants meet, which is painted in white and blurred. The Schwarzschild BH is placed at the centre of the celestial sphere $\mathcal{N}$.

The left panel of Fig. 4.2 has a few distinctive features. The white circle is the lensing, due to the BH, of the celestial sphere's white dot, which would be right in front of the observer if the BH would not be in the line of sight. It is an *Einstein ring* [35] – see [36] for an historical account of the prediction of multiple images of a source due to gravitational lensing. The black central disk is the BH shadow, whose edge corresponds to photons that skim the LR. In between this edge and the Einstein ring there are infinitely many copies of the celestial sphere, that accumulate in the neighbourhood of the shadow's edge, in a self-similar structure [72]. In the image only two of these copies are clearly visible.

The right panel of Fig. 4.2 shows the lensing pattern due to a bosonic star, model PS2, under similar observation conditions, *i.e.* and observer placed at the same r_o and the BH replaced by the star at the centre of the celestial sphere (see Section 1.4). Since the g_{tt} component of the metric is very close to zero within the star region, the numerical integration of the null geodesics is quite demanding. This issue can be tamed by performing a conformal transformation to a spacetime with less extreme redshift factor, since such transformation leaves invariant null geodesic paths. The is an efficient procedure. We have checked different conformal transformations lead to the same image, validating the method. A particularly reliable choice is the conformal transformation $d\widetilde{s}^2 = ds^2/\sigma^k$, with $k = 1.5$, where $d\widetilde{s}^2$ is the line element of the new metric.

Comparing the left and right panels of Fig. 4.2, leads to two main conclusions. Firstly,

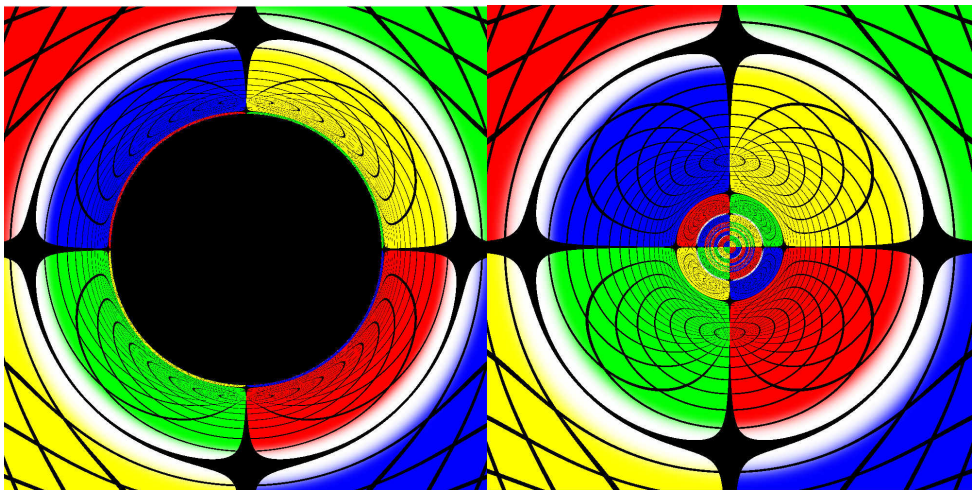


Figure 4.2: Lensing and shadow of a Schwarzschild BH (left panel) and a comparable bosonic star (right panel, model PS2), in similar observation conditions, for which the observer is set at $r_o = 15M$. The Einstein ring has a similar dimension (white lensed region), but the strongly lensed region – shadow edge of the BH *vs.* central rings for the star – is much smaller for the star. Adapted from [25].

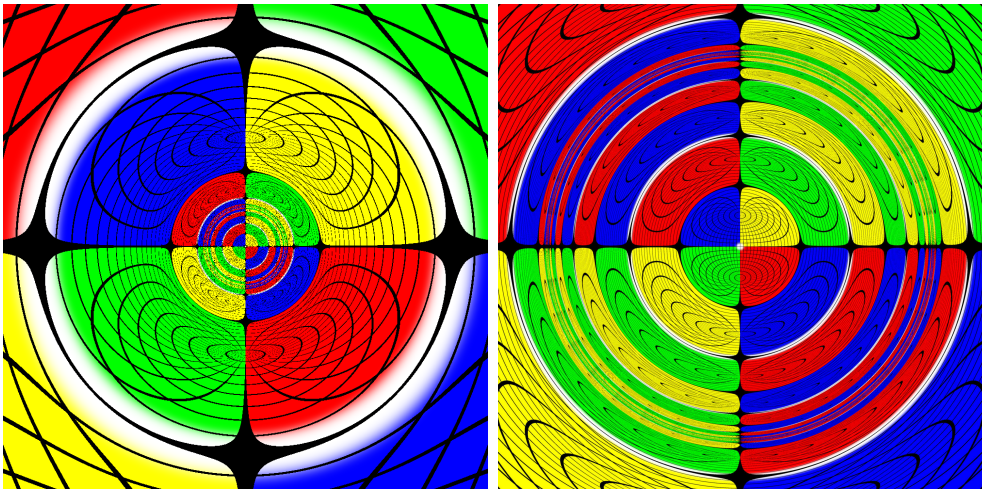


Figure 4.3: Lensing by the boson star model BS1 (left panel) and a zoom around the strong lensing region (right panel). Adapted from [25].

the Einstein ring has a similar dimension. Since there is only one scale for either solution – the total mass – similar observation conditions imply the lensing is due to objects with the same total mass. This explains the same overall (weak) light bending that originates the Einstein ring. Secondly, the strong lensing region, which is due to photons with $\eta \sim \eta_{LR}$, is smaller for the star. This is a consequence of the smaller LRs, see the previous section: for ultra-compact bosonic stars they occur at an areal radius $\ll 3M$.

The lensing for the six selected models of ultra-compact bosonic stars is qualitatively similar. In Fig. 4.3 (left panel), we exhibit the one for model BS1, under similar observation conditions $r_o = 15M$ as the one for PS2 shown in the right panel of Fig. 4.2. As expected the Einstein ring has a similar scale, but the strong lensing region is smaller for the Proca star, which is, qualitatively, in agreement with its smaller (outer) LR. It is important to emphasise, however, that the angular size in the image is determined by the LR's impact parameter, and not by its areal radius [30] (see also Chapter 5).

The right panel of Fig. 4.3 shows a zoom of the left panel, around its central region. The circles, which are Einstein rings, are the lensing images of either the celestial sphere point in front of the observer (white circles) or the one behind the observer (black circles). These two types of circles alternate and appear to accumulate at a given angular radius. This can be confirmed in the right image of Fig. 1.11 (main panel) – shown in the Introduction – which displays the initial angle (which one can regard as the radial coordinate in the lensing images) *vs*. the scattering angle, *i.e*. the final angle in the celestial sphere for PS2.

The scattering angle is here taken to be zero at the white dot of the celestial sphere (directly on the observer's line of sight, if the geometry were flat). Hence, multiples of 2π signal the formation of a white circle in the image, which can be seen by the horizontal dashed lines in the right panel of Fig. 1.11. The peak on the plot is the signature of the unstable LR. Had this been a BH, instead of a bosonic star, the left part of the peak would not exist, as it would correspond to the shadow. The region in between each consecutive black and a white circles in Fig. 4.3, contains a copy-image of the full celestial sphere. As familiar from particle physics/quantum mechanics, the outermost (unstable) LR, which is a bound state, appears as a pole in the scattering amplitude.

The scattering angle divergence near the LR is logarithmic. This allows us to write the impact parameter of the Einstein ring of order k, corresponding to a scattering angle

of $2\pi k$ as

$$\eta_{\rm ER}^{(k)} = \eta_{\rm LR} + be^{-2\pi k/a} \ , \tag{4.2}$$

where a, b are constants, the value of which depends on the LR being approached with values of η above or below $\eta_{\rm LR}$. The right image of Fig. 1.11 (inset) shows this relation is a good approximation to the numerical values, even for the lowest order Einstein rings.

Whereas the LR is not emphasised in the plots in Figs. 4.2 and 4.3, it stands out if instead we plot the *time delay function*. This function is defined as the variation of the coordinate time t, in units of M, required for the photon geodesic emanating from a particular pixel to reach a corresponding point on the celestial sphere [24]. This is a good diagnosis of the LR since photon trajectories that skim the LR take much longer to return to spatial infinity. In the left image of Fig. 1.11 the time delay for model PS2 is portrayed as a heat map with the corresponding scale on the right of the image indicating the variation of the coordinate time (in units of M) for each photon to travel from the camera to the celestial sphere. The LR clearly stands out (compare with Fig. 4.2, right panel).

The left image of Fig. 1.11 shows that UCOs like bosonic stars, made up dark matter that only affect light through the spacetime geometry, have a ring-like darker region, rather than a disk-like shadow. Of course, it is possible that in a more realistic astrophysical environment, with an accretion disk light source, the whole central region becomes an effective shadow, see [126]. Likely, this depends on the accretion modelling and, in any case, this effective shadow will be considerably smaller than that of a comparable Schwarzschild BH.

Thus, an ultra-compact bosonic star and a Schwarzschild BH with the same mass, observed at a similar distance, will be distinguishable. That is, even if the lensing of the bosonic star produces an effective disk-like shadow, due to the blurring of the annulus-like strong lensing region, this disk is considerably smaller than that of the shadow of the comparable Schwarzschild BH ($e.g \sim 6$ times smaller for model PS2). Thus, it seems that even if the existence of a LR for a horizonless object can mimic a part of its GW

relaxation signal, it does not mimic (simultaneously), its electromagnetic phenomenology.

Finally, we would like to emphasise that the UCOs we have considered actually possess two LRs. The phenomenology described herein is associated with the outermost unstable one. But the existence of an innermost stable one also may have important dynamical consequences, in particular with respect to the spacetime stability [26, 27]. It has been recently proven [10] that for generic horizonless UCOs forming smoothly from incomplete gravitational collapse, and within physically reasonable models, this stable LR is always present, and therefore it may trigger an instability. This again challenges the possibility of physically realistic horizonless UCOs in the Universe. This result is now discussed in the next section.

4.2 Light Ring stability in UCOs

Could the LIGO events be sourced by horizonless UCOs rather than BHs? In this section we show that UCO mergers are unlikely within a physically reasonable dynamical framework. We consider the possibility that horizonless UCOs form from the gravitational collapse of unknown forms of matter that can withstand collapse into a BH. Assuming cosmic censorship [42] and causality, such UCOs are smooth and topologically trivial [81]. For such UCOs we prove that LRs always come in pairs, one being a saddle point and the other a local extremum of an effective potential. The local extremum might be either stable or unstable, but Einstein's equations imply that instability is only possible if the UCO violates the null energy condition. Thus, UCOs formed through the collapse of reasonable (albeit exotic) matter *must have a stable LR*.

It has been argued that spacetimes with a stable LR are nonlinearly unstable [26, 27] (see also Section 4.3). Unless these instabilities operate on time scales much longer than a Hubble time, this result implies that smooth, physically reasonable UCOs are generically unstable, and therefore that these objects are unfit as sensible observational alternatives to BHs.

Various sorts of exotic compact objects have been discussed in the literature, some of which may become sufficiently compact to possess LRs. These include boson [18] and Proca stars [22], gravastars [233], superspinars [223] and wormholes [220]. Most of these models, however, are incomplete, in the sense that no dynamical formation mechanism is known. As previously mentioned, Boson stars are an exception in this regard, because they have been shown to form dynamically (at least in spherical symmetry) from a process of gravitational collapse and cooling [224]. It is unclear whether collapse can produce ultracompact, rotating boson stars: in fact, recent numerical simulations suggest that it may not be possible to produce rotating boson stars from boson star mergers [234].

Still, we take spherically symmetric simulations with gravitational cooling as a plausibility argument that some UCOs could form dynamically from classical (incomplete) gravitational collapse, starting from an approximately flat spacetime. The collapse stalls before the formation of an event horizon or high-curvature region, but the resulting compactness allows for LRs. Assuming causality, classical dynamical formation from an approximately flat spacetime implies, via a theorem of Geroch [81], that the resulting spacetime is topologically trivial, so that the discussion does not apply (*e.g.*) to wormholes.

Once equilibrium is attained, we assume that the horizonless UCO is described by a 4-dimensional, stationary and axisymmetric geometry that is asymptotically flat. As before, we use quasi-isotropic coordinates (t, r, θ, φ), adapted to the commuting azimuthal $(\partial/\partial\varphi)$ and stationarity $(\partial/\partial t)$ Killing vectors. We further assume that the metric is invariant under the simultaneous reflection $t \to -t$ and $\varphi \to -\varphi$. The metric functions are assumed to be everywhere smooth (apart from standard spherical coordinate singularities). No event horizon exists, and *no* reflection symmetry $\mathbb{Z}_2$ with respect to an equatorial plane $\theta = \pi/2$ is required. Gauge freedom is used to set $g_{r\theta} = 0$, $g_{rr} > 0$ and $g_{\theta\theta} > 0$. To prevent closed time-like curves we require $g_{\varphi\varphi} > 0$. Here and until otherwise specified we do not make assumptions on the field equations, so that the results apply to any metric theory of gravity in which photons follow null geodesics.

The Hamiltonian $\mathcal{H} = \frac{1}{2} g^{\mu\nu} p_\mu \, p_\nu = 0$ determines the null geodesic flow, where p_μ denotes the photon's 4-momentum. A LR is a null geodesic with a tangent vector field that is always a linear combination of (only) the Killing vectors ∂_t and ∂_φ. One can introduce a 2D potential $V(r, \theta)$ that at a LR satisfies the conditions (details were discussed in Section 1.5.2):

$$V = \nabla V = 0 \, . \tag{4.3}$$

The projection of a LR orbit on the configuration space (r, θ) will be simply a point, not necessarily on the equatorial plane. Moreover, a LR will be stable (unstable) along a direction x^α if $\partial_\alpha^2 V$ is positive (negative).

The "potential" V has the shortcoming of depending on the photon's parameters $\{E, L\}$. By factorization, everywhere regular potential functions $H_\pm(r, \theta)$ can be introduced [24, 11], which are independent of the orbital parameters $\{E, L\}$ and depend only on the spacetime metric:

$$H_\pm(r, \theta) \equiv \frac{-g_{t\varphi} \pm \sqrt{D}}{g_{\varphi\varphi}} \, , \tag{4.4}$$

The LR conditions, $V = \nabla V = 0$ translate, for the potentials $H_\pm$, into the sole requirement of a *critical point*: $\nabla H_\pm = 0$. To infer the stability of a LR one considers the second derivatives of $H_\pm$. In particular, at a LR:

$$\partial_\mu^2 V = \pm \left(\frac{2L^2}{\sqrt{D}} \right) \partial_\mu^2 H_\pm \, . \tag{4.5}$$

Thus, the signs of $\partial_\mu^2 V$ and $\pm \partial_\mu^2 H_\pm$ coincide. A LR can be either a local extremum of $H_\pm$ or a saddle point. A saddle point has two proper directions with opposite stability properties, determined as the eigenvectors of the Hessian matrix at the LR; at a local extremum, both directions have the same stability properties. In particular, if both directions are stable the LR is stable, otherwise it is globally unstable.

4.2.1 LRs come in pairs

We will now show that under the dynamical formation scenario we have described above, LRs of an UCO always come in pairs, with one being a saddle point and the other a local extremum of $H_\pm$. The result relies on a simple topological argument.

Consider the vector fields $\mathbf{v}_\pm$, with components $v^i_\pm = \partial^i H_\pm$, where $i \in \{r, \theta\}$. Let X be a compact, simply connected region of the (r, θ) plane. Both X and $\mathbf{v}_\pm$ are 2-dimensional. The fields $\mathbf{v}_\pm$ are *maps* from X to 2D-spaces $Y_\pm$, parameterised by the components of $v^i_\pm$. In particular, a point in X where $\mathbf{v}_\pm$ vanishes – a critical point of $H_\pm$, that describes a LR – is mapped to the origin of $Y_\pm$.

For maps between manifolds such as the ones above, one can define a topological quantity, called the *Brouwer degree* of the map (see e.g. [78, 79]), that is invariant under continuous deformations of the map. Consider two compact, connected and orientable manifolds X, Y of equal dimension and a continuous map $\mathbf{f} : X \to Y$.

If $\mathbf{y}_0 \in Y$ is a regular value of $\mathbf{f}$, then the set $f^{-1}(\mathbf{y}_0) = \{\mathbf{x}_1, \mathbf{x}_2, \cdots\}$ has a finite number of points, with $\mathbf{x}_n \in X$, such that $f(\mathbf{x}_n) = \mathbf{y}_0$, and the Jacobian $J_n = \det(\partial \mathbf{f}/\partial \mathbf{x}_n) \neq 0$. The sign of J_n embodies how the vector basis in X projects into the basis in Y, and thus if the map is orientation-preserving or orientation-reversing. The Brouwer degree of the map $\mathbf{f}$ with respect to $\mathbf{y}_0 \in Y$ is given by $\deg(\mathbf{f}) = \sum_n \text{sign}(J_n)$. The central property of this quantity is that it does not depend on the actual choice of the regular value $\mathbf{y}_0$, but it is rather a topological property of the map itself. Moreover, it is invariant under homotopies, i.e. continuous deformations of the mapping.

To apply this tool to our setup, we take the map $\mathbf{f}$ to be either of the vector fields $\mathbf{v}_\pm$; thus the maps have components $f^i_\pm = v^i_\pm = \partial^i H_\pm$. We choose the origin of Y as our reference point $y^i_0 = \{0, 0\}$. Then the degree of $\mathbf{f}_\pm$ becomes:

$$\deg(\mathbf{f}_\pm) = \sum_n \text{sign}\left[\det\left(\partial_j \partial^i H_\pm\right)\right]_{\mathbf{x}_n}, \tag{4.6}$$

where $\det\left(\partial_j \partial^i H_\pm\right) = g^{rr} g^{\theta\theta}\left[\partial_r^2 H_\pm \partial_\theta^2 H_\pm - [\partial_{r\theta}^2 H_\pm]^2\right]$ has sign 1 (-1) for a local extremum (saddle point). Thus, we assign a *topological charge* $w \equiv \mathrm{sign}(J_n)$ to each point in X where $\mathbf{v}_\pm$ vanishes, corresponding to a LR, and sum over all contributions to get the Brouwer degree of $\mathbf{v}_\pm$. We remark that in order to use equation (4.6), all LRs must be non-degenerate, *i.e.* the value of $\mathrm{sign}(J_n)$ is well defined; in particular the metric must be at least second order differentiable. To simplify our discussion, by default we shall consider smooth spacetimes, which is a stronger (albeit reasonable) condition. In this respect, the smoothness requirement could be relaxed.

The key point is now that the degree will be preserved under a continuous deformation of $\mathbf{v}_\pm$, like what we have assumed will occur as the result of the process of (incomplete) gravitational collapse. In the initial stages of the collapse our spacetime is almost flat, and is not yet sufficiently compact to possess LRs. Thus taking X to be a (r, θ) domain that practically covers all of spacetime (except for an open region around spatial infinity and the rotation axis, which can be made recedingly small), we have $w = 0$: no points with $\mathbf{v}_\pm = 0$ exist (see left panel of Fig. 1.7 for an illustrative example).

After the end of the collapse, the $\mathbf{v}_\pm$ functions are deformed and LRs arise. However, due to the topological triviality of the final spacetime we can deform the $\mathbf{v}_\pm$ functions back to their initial configurations prior to collapse. This can be done provided that the contribution from boundary[1] of X does not change, which will be for the case described here. As a consequence, the total w after collapse must still vanish. It follows that saddle points and local extrema of $H_\pm$ must form in pairs under a continuous deformation of the metric functions (right panel of Fig. 1.7). Therefore LRs must come in pairs for the horizonless UCO, with one being a local extremum of $H_\pm$ and the other a saddle point. In fact, the argument applies to any spacetime that can be continuously deformed into flat spacetime, while keeping metric smoothness and the boundary conditions of the domain X. A complementary approach using contour integrals, which the reader might find more intuitive, can be found in the end of the Chapter (see Section 4.4).

[1]The issue of the boundary might be eliminated altogether by patching together different copies of X in order to construct a surface with toroidal topology and without a boundary.

4.2.2 LRs in Spherical Symmetry

So far, we have established that a smooth UCO spacetime must have at least two LRs, one of them being a local extremum of the potential, but we have not yet clarified if this extremum is a stable or an unstable LR. We will first address this question for spherically symmetric spacetimes. In this simple case we can show that such LRs are *always stable*, without further assumptions.

If the UCO spacetime is spherically symmetric, the metric can be reduced to the form:

$$ds^2 = -N(r)dt^2 + \frac{1}{g(r)}dr^2 + r^2(d\theta^2 + \sin^2\theta d\varphi^2) \ . \tag{4.7}$$

The functions $H_\pm$ are explicitly given in terms of the metric functions by $H_\pm = \pm\sqrt{N}/(r\sin\theta)$. Due to symmetry, we can restrict our analysis to the equatorial plane $\theta = \pi/2$ without loss of generality; if LRs exist, they can be analyzed on this plane. The derivatives of $H_\pm$ along θ on the equatorial plane are

$$\partial_\theta H_\pm = \mp\frac{\sqrt{N}}{r}\frac{\cos\theta}{\sin^2\theta} = 0, \tag{4.8}$$

$$\partial_\theta^2 H_\pm = \pm\frac{\sqrt{N}}{r}\left(\frac{1+\cos^2\theta}{\sin^3\theta}\right). \tag{4.9}$$

We can then conclude that $\pm\partial_\theta^2 H_\pm > 0 \Rightarrow \partial_\theta^2 V > 0$. This implies that the effective potential is *always* stable along θ.

Recall that for each LR pair that is created, one LR is a local extremum of $H_\pm$, whereas the other is a saddle point. Since both LRs are stable along the θ direction, in a spherically symmetric spacetime the local extremum of $H_\pm$ must be a globally stable LR.

4.2.3 LRs in Axisymmetry

We now turn to the generic case of axi-symmetry (and stationarity). So far, the arguments have made quantitative use of test photon dynamics but *not* of spacetime dynamics, making them independent on the equations of motion. In order to assess, in the generic

axisymmetric case, if the LR that extremizes $H_\pm$ is a local maximum or minimum of V, we will assume Einstein's field equations (in geometrized units): $G^{\mu\nu} = 8\pi\, T^{\mu\nu}$. If the energy-momentum tensor $T^{\mu\nu}$ satisfies, at every point on the spacetime, the *null energy condition*

$$\rho \equiv T^{\mu\nu}\, p_\mu\, p_\nu \geqslant 0 \tag{4.10}$$

for any null vector p^μ (i.e. $p_\mu\, p^\mu = 0$), it follows that the LR that extremizes $H_\pm$ is a local *minimum* of V, and hence globally stable.

To establish this result we will restrict p_μ, from all the possible null vectors, to be the 4-momentum of a null geodesic. Moreover, we will restrict the computation of ρ to the location of a LR orbit. It will be convenient to split the spacetime coordinates into two sets: $x^\mu = \{x^a, x^i\}$, where $\{x^a\} = (t, \varphi)$ and $\{x^i\} = (r, \theta)$. We will use Greek indices for the full range of spacetime coordinates, early latin indices (a, b, c, d) for the Killing coordinates (t, φ) and middle alphabet latin indices (i, j, k) for the nontrivial directions (r, θ). With this notation, we note the following properties. In general, $\partial_a g_{\mu\nu} = 0$, $g_{ai} = 0$ and $p_a =$ constant. Moreover, *specifically at LRs*, $p_i = 0$ and $V = p_a\, p^a = 0$.

Next, we wish to compute the derivatives of V and compare them with different geometrical quantities *at LRs*. It will be useful to bear in mind that the metric $g_{\mu\nu}$ is block-diagonal in the $\{x^a\}$ and $\{x^i\}$ parts. Hence, e.g., $g^{ab} g_{b\mu} = \delta^a_\mu$. We start by computing the first derivatives of the potential V:

$$\partial^a V = 0\ , \qquad \partial^i V = -p^a p^b \partial^i g_{ab}\ . \tag{4.11}$$

Looking at the Christoffel symbols Γ^μ_{ab} one then obtains:

$$\frac{1}{2}\partial^\mu V = \Gamma^\mu_{ab} p^a p^b\ . \tag{4.12}$$

Observe that this expression is nontrivial only for $\mu = i$. We now need the second

derivatives of V. A slightly lengthier computation shows that

$$p^a p^b \partial_i \Gamma^i_{ab} = \frac{1}{2}\partial_i \partial^i V - 2\mathcal{B} \ , \tag{4.13}$$

where $\mathcal{B} \equiv \left(g_{ab} p_c p_d g^{ij} \partial_i g^{ac} \partial_j g^{bd}\right)/2$. Now we invoke Einstein's field equations to write ρ, defined in Eq. (4.10), as:

$$8\pi\rho = \left(R^{\mu\nu} - \frac{1}{2} g^{\mu\nu} R\right) p_\mu p_\nu = R_{\mu\nu}\, p^\mu\, p^\nu \ . \tag{4.14}$$

Equivalently, expanding the Ricci tensor, we have at a LR:

$$8\pi\rho = p^a p^b \Big(\partial_i \Gamma^i_{ab} - \Gamma^\mu_{a\nu}\Gamma^\nu_{b\mu}\Big) \ . \tag{4.15}$$

An expression for the first term on the right hand side is provided by Eq. (4.13). Concerning the second term, it can be re-expressed, at a LR, as:

$$p^a p^b\, \Gamma^\mu_{a\nu}\Gamma^\nu_{b\mu} = -\mathcal{B} \ . \tag{4.16}$$

Plugging Eqs. (4.16) and (4.13) into Eq. (4.15) yields

$$8\pi\rho = \frac{1}{2}\partial_i \partial^i V - \mathcal{B} \ . \tag{4.17}$$

We will now show that $\mathcal{B} = 0$ at a LR. Since p_a =const. we can rewrite $\mathcal{B} = g_{ab}\partial^i\left(p^a\right)\partial_i\left(p^b\right)/2$, or more explicitly:

$$\begin{aligned} 2\mathcal{B} = {} & g^{rr}\left\{g_{tt}\left(\partial_r \dot{t}\right)^2 + 2g_{t\varphi}\left(\partial_r \dot{t}\right)\left(\partial_r \dot{\varphi}\right) + g_{\varphi\varphi}\left(\partial_r \dot{\varphi}\right)^2\right\} \\ & + g^{\theta\theta}\left\{g_{tt}\left(\partial_\theta \dot{t}\right)^2 + 2g_{t\varphi}\left(\partial_\theta \dot{t}\right)\left(\partial_\theta \dot{\varphi}\right) + g_{\varphi\varphi}\left(\partial_\theta \dot{\varphi}\right)^2\right\} \ . \end{aligned} \tag{4.18}$$

The "trick" is now to write $\partial_i \dot{\varphi}$ as a function of $\partial_i \dot{t}$. Since $V = p_a p^a = -E\dot{t} + L\dot{\varphi}$, we have $\partial_i V = -E\partial_i \dot{t} + L\partial_i \dot{\varphi}$. At a LR $\partial_i V = 0$, and thus $\partial_i \dot{\varphi} = (E/L)\,\partial_i \dot{t}$. Returning to $\mathcal{B}$,

Eq. (4.18) becomes:

$$2\mathcal{B} = \left[g^{rr} \left(\partial_r \dot{t}\right)^2 + g^{\theta\theta} \left(\partial_\theta \dot{t}\right)^2 \right] \left[g_{tt} + 2 g_{t\varphi} \frac{E}{L} + g_{\varphi\varphi} \frac{E^2}{L^2} \right] . \tag{4.19}$$

By comparing with Eq. (1.34) we see that the last factor is proportional to V, and so it vanishes at a LR. From (4.17) we therefore conclude that, at a LR:

$$\rho \equiv T^{\mu\nu} p_\mu p_\nu = \frac{1}{16\pi} \partial_i \partial^i V \ . \tag{4.20}$$

This elegant and compact result informs us that the trace of the Hessian matrix of V at a LR determines whether the null energy condition is violated or not. Explicitly, at a LR, $\partial_i \partial^i V = g^{rr} \partial_r^2 V + g^{\theta\theta} \partial_\theta^2 V$. Since $g^{rr} > 0$ and $g^{\theta\theta} > 0$, if $\partial_r^2 V$ and $\partial_\theta^2 V$ are both negative (positive) then the null energy condition is violated (satisfied).

We could also consider extensions of Einstein's theory whose field equations may be written as $G^{\mu\nu} = 8\pi\, T^{\mu\nu}_{\rm eff}$, where $T^{\mu\nu}_{\rm eff}$ is an *effective* energy momentum tensor. Then, trivially, a similar result applies, but now the Null Energy Condition (NEC) is stated in terms of this tensor: $T^{\mu\nu}_{\rm eff}\, p_\mu\, p_\nu \geqslant 0$, with $p_\mu\, p^\mu = 0$.

Discussion

It has long been suggested that "BH mimickers" – horizonless ultra-compact objects of a mysterious nature and composition – could exist in Nature. Detailed observations of celestial BH candidates in electromagnetic or gravitational radiation are expected to provide clear smoking guns to distinguish concrete models of BH mimickers from "ordinary" BHs.

GWs are one of the cleanest and most pristine observables to investigate the true nature of BH candidates, in particular in the wake of the first detections by LIGO. Recent intriguing arguments imply that UCOs could mimic ordinary BHs even in the GW channel. The potential similarity between these exotic UCOs and BHs originates from the shared feature that a LR exists, together with the realization that the most distinctive

GW signature of a perturbed BH (its ringdown radiation) is initially dominated by the vibrations of this LR.

No observational evidence exists, as yet, for UCOs; but scientific open mindedness requires considering all theoretical possibilities which are not observationally excluded. If one is willing to seriously contemplate the existence of such horizonless UCOs as BH mimickers, however, one should consider them in all of their physical aspects, starting with plausible formation scenarios. Here we conservatively assumed that UCOs form from the classical (albeit incomplete) gravitational collapse of some yet unknown form of matter.

This fairly unspecific assumption, together with the assumptions that the UCO is smooth and causal, led us to a compelling conclusion: if the UCO has the necessary LR to mimic a BH's ringdown, it must also have at least another LR. If the UCO is spherically symmetric, the second LR is necessarily stable, without any further requirements. In the more general (and realistic) case where the UCO is axisymmetric, the LR is stable unless the matter collapsing to form the UCO violates the null energy condition. These results apply to a smooth UCO spacetime that can be continuously deformed into Minkowski spacetime (while preserving smoothness and boundary conditions). The impact of non-trivial topology is briefly discussed in Appendix B.

These generic conclusions are in agreement with UCOs studied in the literature. For instance, explicit examples where boson stars become UCOs have been considered in [23, 24, 11]: in all these cases the matter obeys the null energy condition, and indeed LRs always emerge in pairs, with one of them being stable. Consider for instance the contour lines of the effective potentials in Fig 2.4 – 2.6. There is a degenerate case in which the two LRs coincide [80].

Note that the null energy condition is relevant in a central result of general relativity, namely Penrose's singularity theorem [41]. This theorem strengthens the result: as a byproduct of Penrose's singularity theorem, there is no need to assume that our ultra-

compact object is horizonless. If a trapped surface were to form, the singularity theorem would imply the formation of a singularity[2] in the future evolution of the spacetime. Thus, together with the null energy condition, our assumption of smoothness *implies* that the UCOs we consider are horizonless.

The existence of a stable LR allows electromagnetic or gravitational radiation to pile up in its neighbourhood. This radiation may not decay fast enough, potentially triggering a nonlinear spacetime instability [26, 27]. If such instabilities are generic, UCO candidates formed from classical gravitational collapse must have astrophysically long instability time scales in order to be considered as serious alternatives to the BH paradigm. The calculation of instability time scales in nonlinear evolutions of UCOs will require numerical work that is beyond the scope of this work. A brief discussion on the connection between spacetime instability and stable trapping can be found in the next section, based on the works by Keir [26] and Benomio [235].

4.3 Spacetime instability and stable trapping

The Einstein field equations are a complicated set of coupled non-linear partial differential equations, which determine the evolution of the spacetime metric. In suitable gauge, the field equations for the metric $g_{\mu\nu}$ can be written as [26]:

$$\Box_g g_{\mu\nu} = \mathcal{N}(g, \partial g) + T_{\mu\nu}, \tag{4.21}$$

where $\mathcal{N}(g, \partial g)$ includes non-linear terms, $T_{\mu\nu}$ is the energy-momentum tensor and $\Box_g$ is the Laplace-Beltrami operator on the fixed Lorenzian background metric g.

A major problem in General Relativity is determining the stability of a given stationary spacetime, *i.e.* whether the evolution of a perturbed initial spacetime data is not significantly different from the unperturbed version. A stability analysis at the linear level can typically be performed by linearizing the metric field equations around a given

[2]Actually it guarantees geodesic incompleteness.

stationary spacetime solution. However, this approach clearly has limitations, since *linear* stability does not imply *non-linear* stability, which takes into account the non-linear character of the equations of motion.

Rigorously proving that a given spacetime is non-linearly stable is usually an incredibly difficult task, and so it should come as no surprise that very few results are actually available in the literature. In this respect, a notable exception is the result that the Minkowski spacetime is non-linearly stable, as shown by Christodoulou and Klainerman [236, 237]. More recent examples are the discussion of the non-linear stability of the Schwarzschild spacetime under axially symmetric polarized perturbations [238], and also the full global non-linear stability of the Kerr–de Sitter family of black holes [239]. However, even in the absence of a formal argument, attempts can still be made to learn something about the possible stability of a spacetime, even if they only provide an indication about the latter. This section contains a very brief overview over this topic, in which we closely follow two papers, respectively by J. Keir [26] and G. Benomio [235].

In the quest to address the stability of a spacetime, a usual starting point is the analysis of a linear wave equation, with the metric background fixed. This linear wave works as a proxy for a metric perturbation, where some of the insights might carried over to the full non-linear problem. A relevant question is then whether these waves dissipate (or decay) quickly enough, since non-linearities could lead to a pile up of enough perturbations within a small region to induce a back-reaction on the spacetime. However, as a word of caution, one should take special care when attempting to reach a conclusion about the spacetime stability by starting from such a wave analysis.

Indeed, for vacuum, linearization of eq. (4.21) reduces to a linear wave equation for a scalar perturbation of the metric. However, outside vacuum, the same wave equation can become coupled to matter fields, and we might expect a qualitatively different behaviour. Fortunately, some metric perturbations can decouple from some matter degrees of freedom, with an example being "axial perturbations" (or w-modes) in spherical symmetry.

Then, one may hope that the conclusions obtained from a linear wave analysis can still be applied, up to some degree, to metric perturbations.

In his paper [26], Keir analyses a linear wave equation for the scalar field ϕ, in the background of a static spherically symmetric spacetime:

$$\Box_g \phi + \phi F(r) = 0, \tag{4.22}$$

where $F(r)$ is a positive arbitrary function of the (areal) radial coordinate r. In order to analyse how ϕ decays, is is useful to introduce a positive definite quantity E_ϕ which provides an estimate for the perturbation strength at a given time. The latter appears in the context of the so called "energy methods", that can provide a robust framework to deal with both linear and nonlinear problems. There are multiple possible versions for these "energies" (most of which not conserved), that can be applied within the same analysis. A precise formulation of these quantities is beyond the scope of this text, and the interested reader is directed to the appropriate literature on the subject. Usually the "energy" E_ϕ at time t is defined as an integrated quantity of the following form:

$$E_\phi(t) \sim \int_{\Sigma_t} d^3x \sqrt{\gamma}\ \mathcal{E}(\phi, \partial^k \phi),$$

where $\mathcal{E}$ is a positive "energy"density that depends on ϕ and its derivatives up to order k (higher-order energies have $k > 1$). The integration is taken over the spatial hypersurface Σ_t (labeled by t) with induced metric γ; the time coordinate t is defined in terms of a future directed time-like Killing vector field ∂_t, with the family of spatial hypersurfaces Σ_t foliating the spacetime.

The integrated quantity E_ϕ is useful to define wave decay. For smooth, compactly supported initial data ($t = 0$), we will consider uniform decay statements of the form:

$$E_\phi(t) \leqslant C\delta(t)\, E_\phi(0),$$

where $C > 0$ is a constant. The (positive) function $\delta(t)$ sets the decay rate, with $\delta(t) \to 0$ as $t \to \infty$. The word *uniform* is crucial here: we are interested in statements that must hold for any solution ϕ and for any $t > 0$. We emphasize that the current discussion is not formal, where for instance we have omitted the order k used for E_ϕ (which is not always the same), for the sake of simplicity.

An important point in our discussion is establishing bounds for the uniform decay rate. Specifically, a given uniform decay $\delta(t)$ is said to be a *lower bound* if there is no other uniform decay $\delta^*(t)$ with a faster decay rate, *i.e.* $\delta(t)$ is *sharp*:

$$\nexists \quad \delta^*(t) : \qquad \delta^*(t) < \delta(t), \qquad \forall\ t > 0.$$

Similarly, one could also define an upper bound for the uniform decay rate. However, concerning the non-linear problem, what is most relevant is the *lower bound*. If this lower bound is polynomial $\delta(t) \sim 1/t^2$ (which is often regarded as a *fast* decay), then it might be possible to prove stability for the non-linear problem, since a sufficiently strong decay at the linear level is usually required. For that purpose, a decay faster than $\sim 1/t$ will typically be sufficiently fast. In contrast, logarithmic decay $\delta(t) \sim 1/\log^2 t$ is not enough to apply conventional methods that are used to prove non-linear stability, which strongly suggests the existence of a *non-linear instability*. Although this is naturally *not a proof* that such an instability exists, we can expect generic non-linearities to induce one. However, as a word of caution, the non-linearities in Einstein field equations are not of the most generic type, and so it might be possible that the full non-linear system is still stable, although this may be unlikely [26].

The lower bound $\delta(t)$ is spacetime dependent, and in particular it depends on whether trapped null geodesics exist. This is hardly surprising, since high frequency components of ϕ approximately propagate along null geodesics, and the existence of trapped null geodesics can clearly create an obstruction to fast decay.

In the case of *unstable* trapping (*e.g.* photon sphere in Schwarzschild) it is possible to overcome this obstruction by considering a higher order "energy" E_ϕ. Such a procedure

ultimately leads to a polynomial decay as a lower bound.

In contrast, *stable* trapping of null geodesics creates an obstruction to fast decay which cannot be prevented with a similar approach. This will be the case for Kerr-AdS spacetime, where null geodesics can become trapped between some finite radius and the AdS boundary, leading to a logarithmic decay as a lower bound [240, 241]. It is worth mentioning that Kerr-AdS is conjectured to be dynamically unstable [241], which is consistent with our previous remarks of a possible (non-linear) instability. Also for an AdS type boundary, one can further make the observation that the Einstein-massless Vlasov system in AdS with spherical symmetry was recently shown to be non-linearly unstable [242].

We are now in a position to state Keir's main result, concerning linear wave solutions to equation (4.22): *for a static and spherically symmetric spacetime with stable trapping of null geodesics, the lower bound for the uniform decay of linear waves is logarithmic*:

$$E_\phi(t) \leqslant \frac{C}{[\log(2+t)]^2}\, E_\phi(0).$$

Remarkably, this results neither depends on the asymptotic behaviour of the spacetime, nor its topology. In its derivation, a technique is applied which depends on the construction of approximate solutions $\widetilde{\phi}$ to the wave equation (4.22), dubbed *quasi-modes*:

$$\Box_g \widetilde{\phi} + \widetilde{\phi}\, F(r) = \mathbb{E}_{rr}(\widetilde{\phi}),$$

where $\mathbb{E}_{rr}(\widetilde{\phi})$ is the approximation error. Quasi-modes mainly rely on the local geometry, since by construction they are localized around stably trapped null geodesics. This accounts for the local (rather than global) character of Keir's result. The lower bound for the decay is relatively simple to determine once the quasi-modes are constructed, and it can be associated to how the error $\mathbb{E}_{rr}$ decays with time. The most challenging part of the argument is actually proving that such quasi-modes with suitably small errors $\mathbb{E}_{rr}$ exist.

We would like to stress that Keir's result *does not* claim that perturbations have to decay in time; it only establishes that an uniform decay rate faster than a logarithmic one is not possible. For instance, a proof of decay would typically involve an upper bound for the decay function $\delta(t)$, which generically requires knowledge of the spacetime structure, *i.e.* it is a global rather than a local problem [26].

Since this is a subtle point, we further contrast the difference between the lower bound and the decay rate of individual (quasi-normal) modes in the context of linear stability. In particular, all such individual modes with smooth initial data may decay faster than logarithmically. However, given any faster decay rate, one can find a smooth solution ϕ which decays slower than this rate, since it is not possible to establish a uniform bound on decay of linear perturbations that is *faster* than logarithmic. And it is precisely *uniform* bounds that are relevant when considering the non-linear problem, as individual modes will typically not capture the main features of the system.

As a final remark, the non-linear instability which might be induced by the existence of stable trapped geodesics is associated to high frequency perturbations. Furthermore, this instability should not be apparent when analysing spherically symmetric perturbations in spherical symmetry, or even at the level of any individual mode. Moreover, due to its non-linear nature, it is not trivial to anticipate the timescale on which this spacetime instability might develop.

4.4 Topological charges via contour integrals

This section gives some extra details on the connection between the topological charge, computed using contour integrals, and Light Rings. The reader might find this discussion more intuitive than the one discussed in Section 4.2.1. The main focus here is to discuss the mathematical method itself, and so we will try to keep the discussion more general for the moment.

Consider a 2D manifold $(\mathbb{M}, g_{\mu\nu})$ parameterized by an orthogonal coordinate chart (x, y), with $g_{xx} > 0$, $g_{yy} > 0$ and $g_{xy} = 0$. If there is a real function $H(x, y) : \mathbb{M} \to \mathbb{R}$, at least *first* order differentiable, one can connect a topological charge to each *critical point* $\nabla H = 0$. We define (v_x, v_y) as:

$$v_x \equiv \frac{1}{\sqrt{g_{xx}}} \partial_x H, \qquad v_y \equiv \frac{1}{\sqrt{g_{yy}}} \partial_y H.$$

The critical points $\partial_\mu H = 0$ correspond then to $\{v_x, v_y\} = 0 \iff v = 0$. In addition, these quantities satisfy a Cartesian-like normalization:

$$\partial^\mu H \, \partial_\mu H = \frac{(\partial_x H)^2}{g_{xx}} + \frac{(\partial_y H)^2}{g_{yy}} = v_x^2 + v_y^2 \equiv v^2.$$

One can thus introduce an angle Ω:

$$v_x = v \cos \Omega, \qquad v_y = v \sin \Omega,$$

which by differentiation leads to

$$d\Omega = \frac{1}{v^2} \left(v_x \, dv_y - v_y \, dv_x \right).$$

Consider a closed curve C_λ on $\mathbb{M}$, that is piecewise smooth, positive oriented, and parameterized by $\lambda \in \mathbb{R}$. For convenience, lets us further define $\mathcal{M}$ as the 2D region enclosed by C_λ. After a full circulation along C_λ, the value of Ω is the same up to $2\pi w$, where $w \in \mathbb{Z}$. Hence:

$$w = \frac{1}{2\pi} \oint_{C_\lambda} \dot{\Omega} \, d\lambda = \frac{1}{2\pi} \oint_{C_\lambda} \frac{1}{v^2} \left(v_x \dot{v_y} - v_y \dot{v_x} \right) d\lambda,$$

where the dot denotes differentiation with respect to λ. The interpretation of w is as follows.

Each point $\mathcal{P} : (x, y)$ in $\mathbb{M}$ can be mapped to a point $\widetilde{\mathcal{P}} : \{v_x, v_y\}$ in a new (auxiliary)

space $\widetilde{\mathbb{M}}$ according to the value of $\{v_x, v_y\}$ on $\mathcal{P}$. Hence, the curve C_λ is projected to a curve $\widetilde{C}_\lambda$ in $\widetilde{\mathbb{M}}$ (see Fig. 4.4). The quantity w is then simply the winding number of $\widetilde{C}_\lambda$ around the origin ($v = 0$) of $\widetilde{\mathbb{M}}$. We remark that the orientation sense of $\widetilde{C}_\lambda$ depends on the specific profile of the field $\{v_x, v_y\}$ on $\mathbb{M}$ (see for example Fig. 4.5).

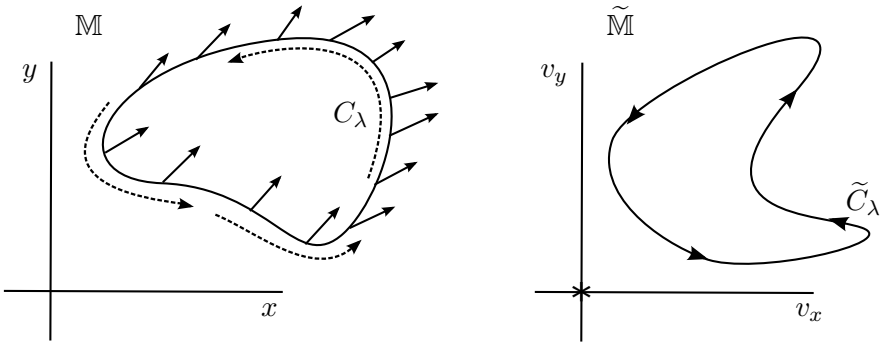


Figure 4.4: (*Left:*) illustration of the contour C_λ on $\mathbb{M}$ with positive (counter-clockwise) orientation; the vectors represent $\{v_x, v_y\}$ at each point. (*Right:*) illustration of the contour $\widetilde{C}_\lambda$ on $\widetilde{\mathbb{M}}$, with orientation depending on the field $\{v_x, v_y\}$ on $\mathbb{M}$. For the particular case here illustrated, $w = 0$.

The winding number w of a closed curve, around a given point O, is an integer that represents the total number of times that curve travels counter-clockwise around the point O. In particular, w depends on the orientation of the curve, and is negative if the curve travels around O clockwise after a full revolution.

The winding number w has a topological character: if one deforms continuously the contour C_λ, the value of w can only change if a critical point $(x, y) : v = 0$ is crossed by the contour at some stage; this would correspond to the intersection of the origin by $\widetilde{C}_\lambda$ in $\widetilde{\mathbb{M}}$, and thus to a change in the winding number. Similarly, we can define the continuous map $\boldsymbol{f} : C_\lambda \to \Omega$ between manifolds of dimension 1, and compute its Brouwer degree. This also leads to a topological invariant under continuous deformations of $\boldsymbol{f}$.

Decomposition of w as a sum

The value of w only changes when a critical point is intersected by C_λ during a continuous deformation of the latter. By deforming the curve C_λ without intersecting any critical

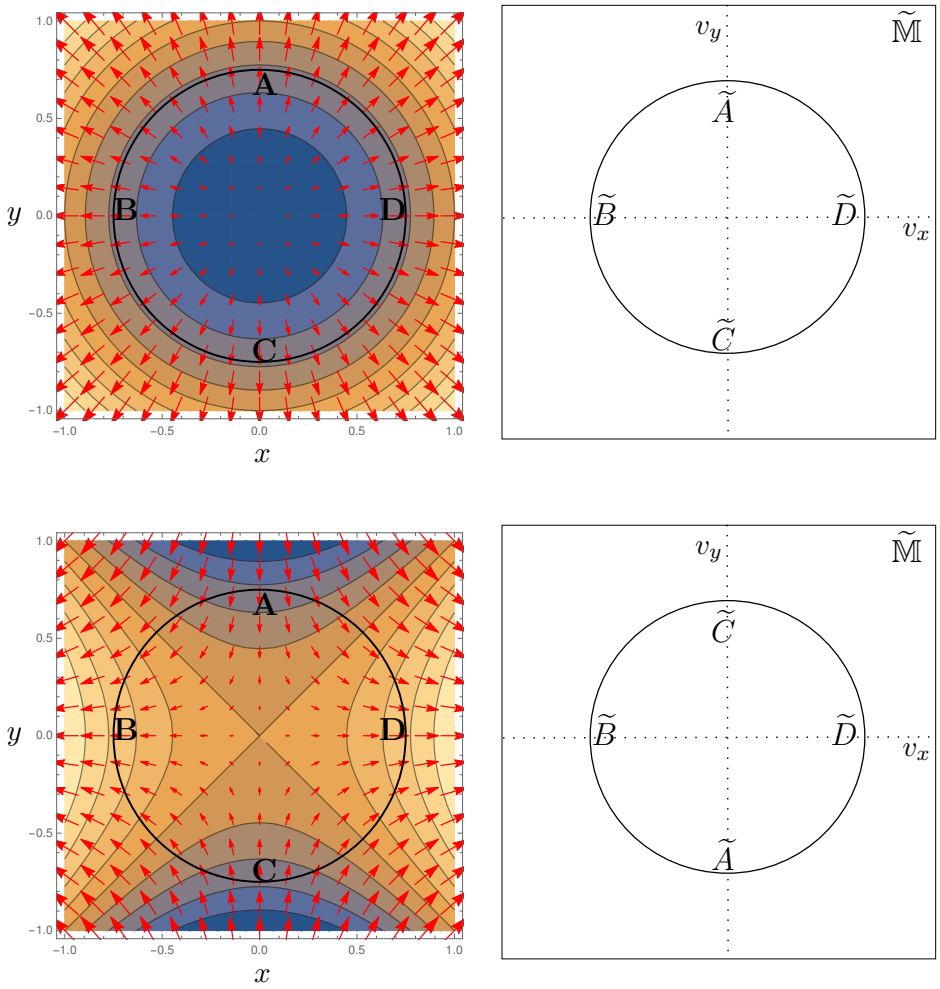


Figure 4.5: *(Left column:)* Gradient and contour lines around a critical point of a function $H(x, y)$, with $g_{xx} = g_{yy} = 1$ for simplicity. A curve C_λ (black), encircling the critical point, contains four points $A \to D$. *(Right column:)* Both this curve and points are mapped to $\widetilde{\mathbb{M}}$ according to the gradient components. As it is made clear by the sequence of points $\widetilde{A} \to \widetilde{D}$, the orientation of the curve in $\widetilde{\mathbb{M}}$ is the same as (or opposite to) C_λ when the critical point is a local maximum (saddle point) in the top (bottom) row.

point, the value of w is preserved. Under such a deformation, we can squeeze and pinch C_λ as illustrated in Fig. 4.6 in order to encircle a particular critical point $\mathcal{P}_*$, until the curve C_λ intersects itself. After this pinching procedure, the curve C_λ can be naturally separated into two components: C_λ^* around $\mathcal{P}_*$, and the remainder C_λ^{rest}.

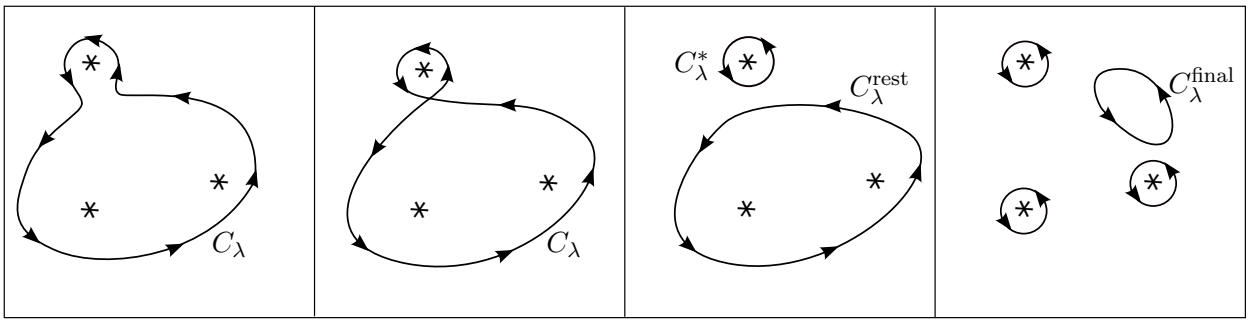


Figure 4.6: (*From left to right:*) The contour C_λ is deformed into two components: C_λ^* and C_λ^{rest}. The section C_λ^* encircles a critical point, here depicted as an asterisk ($*$). *(Last panel)*: This procedure can be repeated recursively over all critical points, with the remaining contour C_λ^{final} giving a vanishing contribution.

The contour integration then separates as:

$$\begin{aligned} w &= \frac{1}{2\pi}\oint_{C_\lambda^*} \dot{\Omega}\, d\lambda + \frac{1}{2\pi}\oint_{C_\lambda^{\text{rest}}} \dot{\Omega}\, d\lambda \\ &= w_* + w_{\text{rest}} \end{aligned}$$

Since the contour C_λ^* can be made arbitrarily small without intersecting the critical point, it is fair to define w^* as the topological charge of that specific critical point.

If the region $\mathcal{M}$ inside C_λ is *simply connected* (*i.e.* no-holes), then this procedure can be repeated recursively over all critical points inside C_λ^{rest}. The remaining contour C_λ^{final} can then be shrunk to a single point (see last panel in Fig. 4.6), with a vanishing contribution to the integration. Thus:

$$w = \sum_i \left(w_*\right)_i ,$$

where the sum goes over all the critical points inside (the initial contour) C_λ. The total w is hence the sum of the individual topological charges of each critical point.

4.4.1 Non-degenerate critical points

In this section we will focus on a single contour C_λ^* arbitrarily close to a single critical point $\mathcal{P}_* : (x_o, y_o)$. In order to simplify notation, we will shift the coordinates' origin to

$\mathcal{P}_*$, *i.e.* $(x - x_o, y - y_o) \to (x, y)$, as well as relabelling $C^*_\lambda \to C_\lambda$ and $w_* \to w$.
If the function $H(x, y)$ is at least *second* order differentiable, we can make the following expansion:

$$v_\mu = A_{\mu\nu}\, x^\nu + \mathcal{O}([x^\nu]^2), \qquad \text{where} \quad A_{\mu\nu} \equiv \partial_\nu v_\mu|_{(0,0)}\,.$$

In these notes we will only consider critical points with $\det(A) \neq 0$, which we now define as *non-degenerate*. Critical points that are *degenerate*, *i.e.* with $\det(A) = 0$, would require a different analysis.

Since w is a topological invariant, let us choose the following parameterization for the local contour C_λ:

$$x(\lambda) = \frac{v}{\det A}\Big(A_{22}\cos\lambda - \epsilon\, A_{12}\sin\lambda\Big),$$

$$y(\lambda) = \frac{v}{\det A}\Big(\epsilon\, A_{11}\sin\lambda - A_{21}\cos\lambda\Big),$$

where $\epsilon \equiv \text{sign}\,(\det A)$ and $\lambda \in [0, 2\pi[$. We remark that the curve C_λ only repeats itself after the full period 2π. However, let us first show that C_λ is endowed with a positive orientation, as required by its definition.

Define $\Theta \equiv x\dot{y} - y\dot{x}$. Taking our choice for $\{x(\lambda), y(\lambda)\}$, one can explicitly show that $\Theta = \epsilon\, v^2\,(\det A)^{-1} = v^2\,|\det A|^{-1} > 0$. Then, by Green's theorem:

$$\oint_{\partial\mathcal{M}^+} (x dy - y dx) = 2\int_{\mathcal{M}} dx\, dy > 0,$$

where the contour integral is taken on the boundary of $\mathcal{M}$ in the positive sense (counter-clockwise), here denoted as $\partial\mathcal{M}^+$. One can further write:

$$\oint_{\partial\mathcal{M}^+} (x dy - y dx) = \oint_{\partial\mathcal{M}^+} \Theta\, d\lambda = \frac{v^2}{|\det A|}\oint_{\partial\mathcal{M}^+} d\lambda > 0 \implies \oint_{\partial\mathcal{M}^+} d\lambda > 0.$$

Thus, the parameterization λ endows C_λ with a positive circulation sense, as required.

Solving $\{v_x, v_y\}$ to first order yields:

$$\begin{pmatrix} v_x \\ v_y \end{pmatrix} \simeq \begin{pmatrix} A_{11} & A_{12} \\ A_{21} & A_{22} \end{pmatrix} \begin{pmatrix} x \\ y \end{pmatrix} \simeq v \begin{pmatrix} \cos\lambda \\ \epsilon \sin\lambda \end{pmatrix},$$

which defines the curve $\widetilde{C_\lambda} : \{v_x(\lambda), v_y(\lambda)\}$ in $\widetilde{\mathbb{M}}$. We remark that ϵ only changes the orientation of this curve. Explicit computation of w then leads to:

$$\begin{aligned} w &= \frac{1}{2\pi} \oint_{C_\lambda} \frac{1}{v^2} \left(v_x \dot{v_y} - v_y \dot{v_x}\right) d\lambda = \frac{1}{2\pi} \oint_{C_\lambda} \epsilon \, d\lambda = \frac{\epsilon}{2\pi} \int_0^{2\pi} d\lambda \\ &= \mathrm{sign}\Big(\mathrm{det} A\Big). \end{aligned}$$

This result can be expressed in terms of the second derivatives of $H(x, y)$. For instance:

$$\partial_\nu v_\mu = \frac{1}{\sqrt{g_{\mu\mu}}} \partial^2_{\mu\nu} H \; + \; (\partial_\mu H)\, \partial_\nu \big(g_{\mu\nu}^{-1/2}\big)\,, \qquad (\text{no } \mu \text{ sum}),$$

where $\{\mu, \nu\} \in \{x, y\}$. Since around the critical point one has $\partial_\mu H = 0$:

$$A_{\mu\nu} = \left(\frac{1}{\sqrt{g_{\mu\mu}}} \partial^2_{\mu\nu} H \right)\Big|_{(0,0)}, \qquad \mathrm{det} A = \frac{1}{\sqrt{g}} \mathrm{det}\left(\partial^2_{\mu\nu} H\right),$$

where g is the determinant of metric, and $\det\left(\partial^2_{\mu\nu} H\right)$ is the determinant of the Hessian matrix of $H(x, y)$ at the critical point. This then implies:

$$w = \mathrm{sign}\Big(\mathrm{det} A\Big) = \mathrm{sign}\Big(\det\left[\partial^2_{\mu\nu} H\right]\Big).$$

Therefore, a local maximum or minimum of H gives rise to $w = +1$, whereas a saddle point of H yields $w = -1$.

In summary, given that C_λ does not intersect any critical points, if the region $\mathcal{M}$ is simply connected and all critical points are non-degenerate, then the (total) topological charge w is given by:

$$w = \sum_i \mathrm{sign}\Big(\det\left[\partial^2_{\mu\nu} H\right]\Big)\Big|_{i_*},$$

where the sum is over all critical points inside C_λ. As a word of caution, this expression is

invalid if degenerate critical points exist inside C_λ. Still, as long as critical points form a *countable* set, their intrinsic topological charges w_* continue to be well defined; however, they could be inexpressible in terms of the determinant of the corresponding Hessian matrix. Some might find the discussion of topological charges in this section vaguely resembling the more familiar computation of contour integrals in the complex plane. This connection is explored in Appendix A.

4.4.2 Application of contour integrals to UCOs

As an application of the contour integration, we now return to the UCO discussion of Section 4.2.1, but now taking a contour C_λ in the (r, θ) configuration space, as illustrated in Fig. 4.7. These images display the contour lines of the effective potential around Rotating Boson Stars, already shown in Fig. 2.4 and 2.5; we have now added a dashed (red) line representing a possible contour C_λ.

Starting with a horizonless UCO spacetime, *e.g.* the top panel of Fig. 4.7, we can deform continuously the metric functions back to Minkowski spacetime while keeping at least second order differentiability, assuming that the UCO is topologically trivial. We remark than we can keep all existing LRs always inside C_λ: the latter can be me made to approach the poles $\theta = \{0, \pi\}$, the origin $R = 0$ and spatial infinity[3] $R = 1$, without intersecting any of these limits. Since LRs cannot exist at the axis, by suitably deforming C_λ all LRs can be placed inside the contour. The result of the corresponding contour integration will then be a topological invariant w.

By deforming the UCO back into flat spacetime one reaches the conclusion that $w = 0$, since the latter does not contain any LRs. This is illustrated by Fig. 4.7: as we move to the bottom panel from the top one the LRs disappear, as we are actually *approaching* flat spacetime by moving clockwise along the RBS spiral (see Fig. 2.2). Although the bottom panel of Fig. 4.7 is not Minkowski, the profile of the contour lines are not (qualitatively) too different from the flat case. We recall that the effective potential is not flat for

[3]We recall that R is a compactified radial coordinate with $r_H = 0$, defined in Section 2.2.

Minkowski spacetime (see equation 2.19). As in the discussion of Section 4.2.1, the result that the total w vanishes allows us to conclude that LRs appear in pairs for horizonless UCOS.

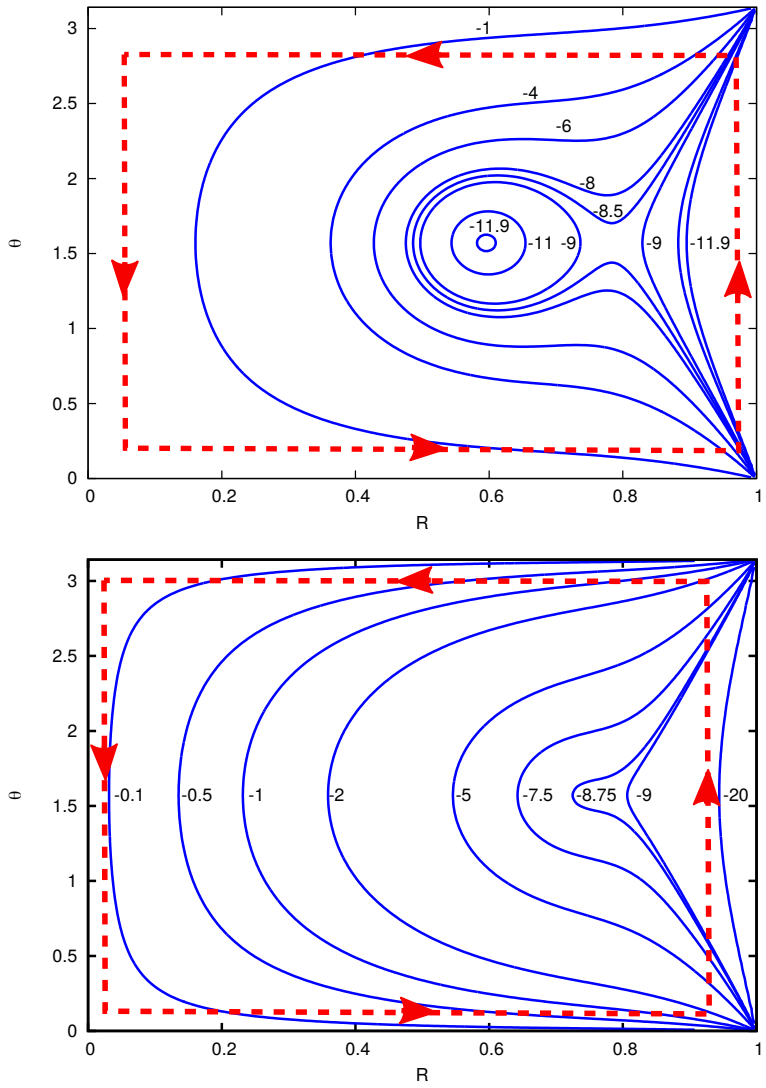


Figure 4.7: These images display the contour lines of the effective potential h_+ around Rotating Boson Stars, already shown in Fig. 2.4 and 2.5; we have now added a dashed (red) line representing a possible contour C_λ. This contour can be made to approach the edges of the diagram in order to include any LR in the domain. The LRs appear as critical points of the potential.

Chapter 5

BHs beyond General Relativity

Ultraviolet theoretical inconsistencies of Einstein's General Relativity, such as its non-renormalizability [243, 244, 245] and the existence of singularities, have since long motivated the suggestion that higher curvature corrections should be taken into account, in an improved theory of gravity (see *e.g.* [246]).

Inclusion of a finite set of such higher curvature corrections, however, generically leads to runaway modes (Ostrogradsky instabilities [28]) in the classical theory and a breakdown of unitarity due to ghosts, in the quantum theory. These undesirable properties can be simply diagnosed, at the level of the classic field equations, by the presence of third order time (and consequently also space, by covariance) derivatives. A natural way around this problem is to require a self-consistent model, obtained as a truncation of the higher curvature expansion, to yield a set of field equations without such higher order derivatives.

Lovelock [29] first established, for vacuum gravity, what are the allowed curvature combinations so that the field equations have no higher than second order time derivatives. It turns out that, in a Lagrangian, these combinations are simply the Euler densities, particular scalar polynomial combinations of the curvature tensors of order n. Since the n^{th} Euler density is a topological invariant in spacetime dimension $D = 2n$ and yields a non-dynamical contribution to the action in dimensions $D \leqslant 2n$, an immediate corollary is that, in $D = 4$ vacuum gravity, the most general Lovelock theory is a combination of

the 0^{th} and 1^{st} Euler density, or in other words, General Relativity with a cosmological constant. The 2^{nd} Euler density, known as the Gauss-Bonnet (GB) combination, is a topological invariant in $D = 4$ and does not contribute to the dynamical equations of motion if included in the action.

There is, however, a simple and natural way to make the GB combination dynamical in a $D = 4$ theory: couple it to a dynamical scalar field. This is actually a model that emerges naturally in string theory [92] (see also [93] for a discussion on this point), where the scalar field is the dilaton, and can be considered as a simple effective model to investigate the consequences of higher curvature corrections in $D = 4$ gravity. The corresponding model takes the name of Einstein-dilaton-Gauss-Bonnet (EdGB) theory and is described by the action (5.1) in Section 5.1 below.

Black holes (BHs) in EdGB theory were first shown to exist, in spherical symmetry, by Kanti et al. [93], wherein they were obtained numerically. These solutions, which moreover are perturbatively stable along their main branch [94], are asymptotically flat, regular on and outside an event horizon, and describe a horizon surrounded by a non-trivial dilaton profile. They circumvent some well-known no (real) scalar hair theorems, namely those by Bekenstein [247, 248] (see [14] for a recent review), due to the non minimal coupling of the dilaton to the geometry and the fact that if one associates some *effective matter* with the GB term, then this represents *exotic matter*, violating the typical energy conditions.

One manifestation of this *effective exotic matter* is that the BH solutions have regions of negative energy density outside the horizon. Another manifestation is that there is a minimal mass for BHs, determined by the GB coupling. We remark that the scalar hair of this BHs has no-independent conserved charge, thus being called *secondary*. See, *e.g.* [95, 96, 97, 98, 99] for further discussions of these spherically symmetric solutions and some charged generalizations.[1]

[1]BH solutions of a closely related Horndeski model can be found in [249, 250].

Rotating BHs in EdGB theory were found, fully non-linearly in [100, 101] (see also [102, 103, 104, 105] for perturbative studies). A minimal mass depending on the GB coupling still exists for these rotating solutions and, as a novel physical feature, some (small) violations of the Kerr bound in terms of ADM quantities are observed. Again, regions with negative energy density exist outside the horizon.

In this Chapter, we discuss how the dGB term impacts on one particular observable feature of a BH: its shadow [197]. Over the last few years there has been a renewed theoretical interest in this old concept, first discussed for the Kerr BH by Bardeen [44], mainly due to the prospect of obtaining an image at horizon scales of the supermassive BH candidates residing respectively in the centre of the M87 galaxy and in our galactic center [118, 1, 2, 3]. In particular, in [23, 169, 24], the shadows of a type of hairy BHs that connect continuously to Kerr, within General Relativity and with matter obeying all energy conditions, called Kerr BHs with scalar hair [12, 161, 13], have been studied (see Chapter 2).

It has been pointed out that, generically, the shadows of these hairy BHs are smaller than those of a comparable Kerr BH, *i.e.* a vacuum rotating BH with the same total mass and angular momentum. A possible interpretation of this qualitative behaviour is the following: the total mass (and angular momentum) of the hairy BHs is now partly stored in the scalar field outside the horizon; in particular the existence of some energy outside the region of unstable spherical photon orbits, also referred to as photon region [117], implies that less energy exists inside this region and hence the Light Rings should be smaller (within an appropriate measure) as compared to their vacuum counterparts and consequently so should be the shadows.

The above interpretation raises an interesting question in relation to the BHs in EdGB theory. Since these have negative energy densities outside the horizon, how do these regions of *effective exotic matter* impact on their shadows? In particular could there be a negative energy contribution outside the photon region that is sufficiently large to

increase the shadow size with respect to a vacuum counterpart? We remark that for other non-vacuum solutions with physical matter, *i.e.* obeying all energy conditions, the size of the shadow typically decreases with respect to the size of a comparable vacuum Kerr BH – see *e.g.* [251] for electrically charged BHs. However, larger shadows have also been observed, *e.g.*, in extended Chern-Simons gravity [206] or brane world BHs [106] which possess *effective exotic matter*, similarly to EdGB. Nevertheless, we shall see that for EdGB the shadows are always smaller with respect to the vacuum case, with the maximal deviation being of the order of only a few percent. For some work on BH shadows in different models see [23, 252, 253, 117, 206, 106, 254, 123, 208, 77, 142, 138, 53, 109], and in particular [145] for perturbative EdGB BHs.

5.1 The EdGB model and solutions

We consider the Einstein-dilaton-Gauss-Bonnet (EdGB) model, described by the following action:

$$S = \frac{1}{16\pi}\int d^4x\sqrt{-g}\left[R - \frac{1}{2}(\partial_\mu\phi)^2 + \alpha e^{-\gamma\phi}R^2_{\rm GB}\right], \tag{5.1}$$

where ϕ is the dilaton field, α is a parameter with units (length)^2 and $R^2_{\rm GB} = R_{\mu\nu\rho\sigma}R^{\mu\nu\rho\sigma} - 4R_{\mu\nu}R^{\mu\nu} + R^2$ is the GB combination. Also, γ is an input parameter of the theory[2], with most of the studies assuming $\gamma = 1$. Both γ and ϕ are dimensionless. As in the previous chapters, we shall use geometric units $c = G = 1$. Varying the action (5.1) with respect to $g_{\mu\nu}$, we obtain[3] the Einstein equations $G_{\mu\nu} = T^{(\rm eff)}_{\mu\nu}$, where $G_{\mu\nu}$ is the standard Einstein tensor and the effective energy-momentum tensor reads

$$T^{(\rm eff)}_{\mu\nu} \equiv \frac{1}{2}\left[\nabla_\mu\phi\nabla_\nu\phi - \frac{1}{2}g_{\mu\nu}(\nabla\phi)^2\right] - \alpha e^{-\gamma\phi}T^{(\rm GBd)}_{\mu\nu}\ , \tag{5.2}$$

where the full expression for $T^{(\rm GBd)}_{\mu\nu}$ can be found in [101]. Varying the action (5.1) with respect to the dilaton field, on the other hand, yields the scalar equation of motion, which

[2]Since the system possesses the symmetry $\gamma \to -\gamma$, $\phi \to -\phi$, it is enough to consider strictly positive values of γ. Furthermore, in order to have a non-trivial coupling to the dilaton field, $\gamma \neq 0$.

[3]In this chapter we follow the conventions in Ref. [255].

reads:

$$\Box\phi = \alpha\gamma e^{-\gamma\phi} R^2_{\rm GB} \ . \tag{5.3}$$

The EdGB model possesses BH and wormhole [256] solutions, but no particle-like solitonic configurations are known (for a review, see the recent work [257]), although the coupling to matter leads, *e.g.*, to neutron stars [258, 259]. Note that in contrast to the GR case, all EdGB solutions (with $\alpha \neq 0$) have been obtained numerically.

In terms of the spherical-like coordinates $\{r,\ \theta,\ \varphi\}$, all known EdGB solutions possess at least two Killing vectors $\zeta = \partial/\partial t$ and $\xi = \partial/\partial\varphi$ (where t is the time coordinate), together with circularity. Then a generic metric ansatz can be written as

$$ds^2 = g_{rr}dr^2 + g_{\theta\theta}d\theta^2 + g_{\varphi\varphi}d\varphi^2 + 2g_{\varphi t}d\varphi dt + g_{tt}dt^2 \ , \tag{5.4}$$

where $g_{\mu\nu}$ and the scalar ϕ are functions of (r, θ). Moreover, we can set $\phi(\infty) = 0$ without any loss of generality (any other choice would correspond to a rescaling of the radial coordinate in (5.4) [101]). The ADM (Arnowitt-Deser-Misner) mass M and angular momentum J are read off, as usual, from the asymptotic expansion

$$g_{tt} = -1 + \frac{2M}{r} + \ldots, \quad g_{\varphi t} = -\frac{2J}{r}\sin^2\theta + \ldots \ . \tag{5.5}$$

One can also define a global dilaton measure D from the asymptotic expansion of the scalar field, $\phi = -D/r + \ldots$ which however is not an independent quantity, since the dilaton field does not qualify as primary hair [93], [101].

5.1.1 The static EdGB black holes

Consider for the moment the static, spherically symmetric solutions ($J = 0$). Close to the event horizon, these solutions possess an approximate expression as a power series in $r - r_H$, where r_H is the radial coordinate of the horizon. In particular, in Schwarzschild coordinates one finds $\phi(r) = \phi_H + \phi_1(r - r_H) + \ldots$, where ϕ_1 satisfies a quadratic equation

(see *e.g.* [93, 95, 96, 101]). Since the scalar field is real, the discriminant of the quadratic equation is required to be positive, yielding the condition:

$$1 - 96\alpha^2\gamma^2 \frac{e^{-2\gamma\phi_H}}{A_H^2/(16\pi^2)} \geq 0, \tag{5.6}$$

where A_H is the event horizon area. Eventually, this condition will be violated after some *limiting solution* is reached, beyond which solutions cease to exist in the parameter space. For a given γ, all solutions can be obtained continuously in the parameter space. When appropriately scaled they form a line, starting from the smooth GR limit ($\phi \to 0$ as $\alpha \to 0$), and ending at the limiting solution. The existence of the latter places a lower bound on the BH horizon radius. It actually also implies the existence of a lower bound on the BH mass. In particular, as discussed in [93, 102], the static EdGB solutions with $\gamma = 1$ are limited to the parameter range $0 \leq \alpha/M^2 \lesssim 0.1728$. A rather similar behaviour holds[4] for $\gamma \neq 1$.

Solutions no longer exist if the ratio α/M^2 is larger than a critical value, which decreases with increasing γ. The configuration at this maximal value is dubbed the *critical solution*, which needs not to coincide with the limiting solution. In particular, for large enough γ, the solution line can be extended backwards in α/M^2, into a "secondary branch", after the critical configuration is reached [255]; this secondary branch eventually terminates at the limiting solution.

Some of these features can be seen in an (α, D)-diagram of solutions with different γ, as shown in Figure 5.1 (left). In particular, notice how for sufficiently large γ values it is possible to have two different values of D/M for the same α/M^2, which indicates the presence of two branches. According to arguments from catastrophe theory, the stability should change at the critical solution, so that the solutions along the secondary branch will be unstable [95].

[4]Note that solutions seem to exist for any nonzero value of γ.

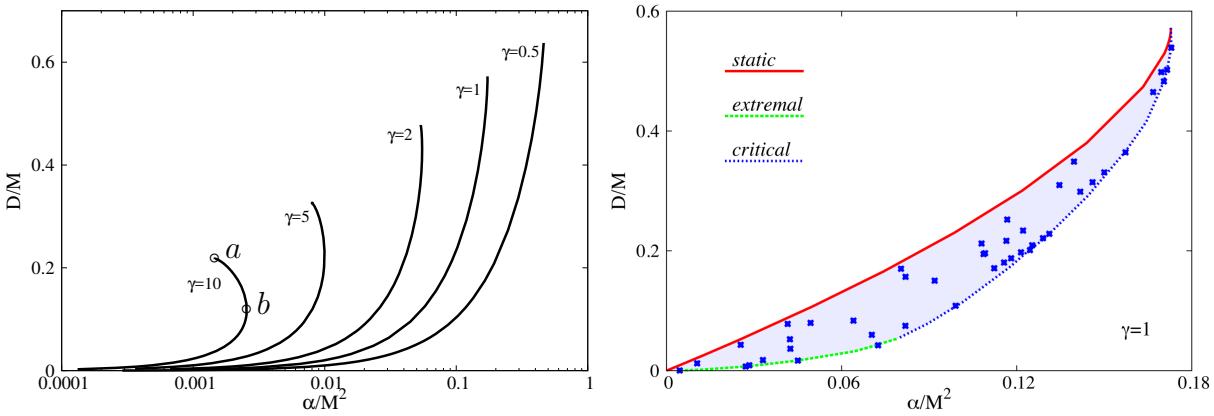


Figure 5.1: (Left) Domain of existence of static EdGB BHs in a D/M vs. α/M^2 diagram with several values of γ. The points a and b depict the limiting and critical solutions respectively for $\gamma = 10$. (Right) Domain of existence of spinning solutions with $\gamma = 1$. The set of considered (spinning) solutions in Fig. 5.3 and Fig. 5.4 are shown here as highlighted points. Adapted from [30].

5.1.2 The spinning EdGB black holes

Spherically symmetric BHs typically possess spinning generalizations. However, so far only the $\gamma = 1$ case has been explored in the literature. These BHs were first obtained at the fully non-linear level in [100] (see also [102, 103, 104, 105] for perturbative results). Similar to the GR case, these BHs possess a $\mathbb{Z}_2$ symmetry along the equatorial plane ($\theta = \pi/2$) and are obtained by solving the field equations $G_{\mu\nu} = T^{(\text{eff})}_{\mu\nu}$ and (5.3) subject to appropriate boundary conditions that are detailed in [101].

The domain of existence of EdGB BHs is bounded by four sets of solutions: *i*) the set of static (*i.e.* spherically symmetric) EdGB BHs with $J = 0$; *ii*) the set of extremal (*i.e.*, zero temperature) EdGB BHs; *iii*) the set of critical solutions; and *iv*) the set of GR solutions – the Kerr/Schwarzschild BHs with $\alpha = 0$. In Fig. 5.3 and Fig. 5.4 (left panel) the boundary line displayed includes the sets *ii*) and *iii*).

The general critical solutions are the rotating generalization of the static case, while the extremal set does not appear to be regular on the horizon [30]. Moreover, the mass of the EdGB rotating BHs is always bounded from below, whereas the angular momentum can (slightly) exceed the Kerr bound, which is given by $J \leqslant M^2$. Further details on

these aspects together with various plots of the domain of existence are found in [101]. Here we give the domain of existence in (α, D)-variables (Fig. 5.1 right panel) and in (α, J)-variables (Fig. 5.3).

5.2 Shadows of EdGB BHs

As it is well described in the literature, the Kerr spacetime supports unstable photon orbits with a fixed Boyer-Lindquist radial coordinate, *i.e.*, the photon region [44, 66]. A subset of the latter is restricted to the equatorial plane ($\theta = \pi/2$), and comprises two independent circular photon orbits with opposite rotation senses, dubbed *Light Rings* (LRs) (see Section 1.1). Such orbits are not unique to the Kerr spacetime and have an intrinsic relation to the BH shadow.

In particular, unstable Light Rings embody a threshold of stability between equatorial null geodesics that scatter to infinity and ones that plunge into the BH. Consequently, LRs account for the shadow edge in observations restricted to the equatorial plane's line of sight (provided both exist). As discussed in Section 2.1, the LR positions can be obtained by analysing the following condition:

$$\nabla h_{\pm} = 0, \quad \text{with} \quad h_{\pm} = \frac{-g_{t\varphi} \pm \sqrt{g_{t\varphi}^2 - g_{tt} g_{\varphi\varphi}}}{g_{tt}}. \tag{5.7}$$

As in the Kerr case, all LRs for EdGB BHs will lay on the equatorial plane. Curiously, although the EdGB BHs discussed in this chapter are fully non-linear solutions (rather than perturbations of Kerr), the light ring qualitative structure still appears to be very similar to Kerr. However, notice that for other families of solutions this is not always the case. For instance, multiple LRs can appear for BHs with scalar hair, some of which are stable [24] (see Chapter 2).

Assuming that a suitable light source is present to provide contrast, a BH casts a black region in an observer's sky: the BH shadow. Although some characteristics are observer

dependent [169], the size and shape of the shadow are essentially a manifestation of the spacetime properties close to the BH, depending for instance on the light ring characteristics. Consequently, instructive physics can be inferred from such observations.

Consider the dummy shadow in Fig. 5.2, represented in the observation image of an observer. Image coordinates (x, y) are used, where the x-axis is defined to be parallel to

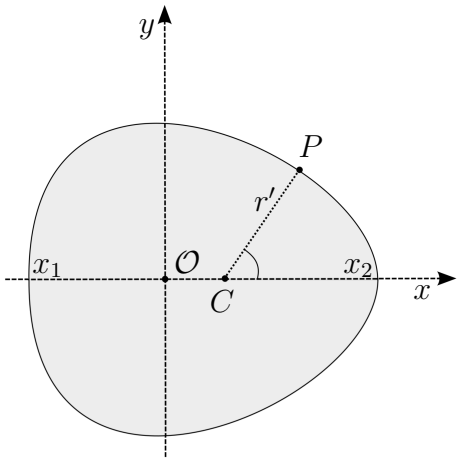


Figure 5.2: Representation of a BH shadow in the (x, y) observation image of the observer. Adapted from [30].

the azimuthal Killing vector $\xi = \partial/\partial\varphi$ at the observer's position (see Section 1.2.1). The origin $(0, 0)$ of this coordinate system, defined as point $\mathcal{O}$ in Fig. 5.2, corresponds to the direction pointing towards the center of the BH, $-\partial/\partial r$, (from the reader into the paper).

The point C in the figure, taken to be the center of the shadow, is such that its abscissa is given by $x_C = (x_{\max}+x_{\min})/2$, where $x_{\max}$ and $x_{\min}$ are respectively the maximum and minimum abscissae of the shadow's edge. If the observer is in the equatorial plane $(\theta = \pi/2)$, which will be assumed throughout the chapter, then the shadow inherits along the x-axis the spacetime reflection symmetry, giving $y_C = 0$. Since the points C and $\mathcal{O}$ need not to coincide, a specific feature of a shadow is the displacement x_C between the shadow and the center of the observation image $\mathcal{O}$.

A generic point P on the shadow's edge is at a distance r' from C, which is defined

as $r' \equiv \sqrt{{y_P}^2 + (x_P - x_C)^2}$. Given the line element[5] $ds^2 = dx^2 + dy^2$, the perimeter $\mathcal{P}$ of the shadow, its average radius $\bar{r}$ and the deviation from sphericity σ_r are defined by:

$$\oint ds \equiv \mathcal{P}, \qquad \bar{r} \equiv \frac{1}{\mathcal{P}} \oint r' \, ds, \qquad \sigma_r = \sqrt{\frac{1}{\mathcal{P}} \oint \left(1 - \frac{r'}{\bar{r}}\right)^2 ds}. \tag{5.8}$$

All these parameters are expressed in units of the ADM mass M. In some cases, it is possible to compare the shadow parameters of a given EdGB solution with the ones from a Kerr BH with the same ADM mass M and angular momentum J. Hence, let us also define the relative deviations to the Kerr case[6]:

$$\delta_r = \frac{\bar{r} - \bar{r}_{\rm kerr}}{\bar{r}_{\rm kerr}}, \qquad \delta_\sigma = \frac{\sigma_r - \sigma_{\rm kerr}}{\sigma_{\rm kerr}}, \qquad \delta_{x_C} = \frac{x_C - x_{C\,\rm kerr}}{x_{C\,\rm kerr}}. \tag{5.9}$$

5.2.1 Shadows of rotating EdGB BHs

Due to the existence of a hidden constant of motion - the Carter constant - the edge of the Kerr shadow can be obtained in a closed analytical form [44, 117, 32] (see section 1.3). However, EdGB BHs are not expected to have such a property, since they all appear to be of Petrov type I [101]. This is consistent with the perturbative results in [104]. As a consequence, in general the shadow of the latter has to be obtained numerically through the standard *backwards ray-tracing* framework [53, 260] (see Section 1.6).

In order to generate a virtual image of the shadow, this method requires propagating null geodesics "backwards in time", where a high frequency approximation is assumed, starting from the observer's position and determining the source of each light ray. Different points in the observation image correspond to different directions in the observer's sky, and hence to different initial conditions of the geodesic equations. The shadow is precisely the set of all those initial conditions which induce geodesics with endpoints on the event horizon, when propagated backwards in time. Since the event horizon is not a

[5] For sufficiently far observers.

[6] An analytical expression for the Kerr shadow, as seen by an observer with zero angular momentum (ZAMO), can be found in Section 1.3.

source of any light (classically), the shadow actually embodies a lack of radiation[7].

The geodesic propagation method described above is necessary to compute most of the shadow edge. However, the points x_1 and x_2 in Fig. 5.2, where the edge intersects the x-axis, can be computed using a highly precise local method. In particular, for an observer in the equatorial plane, Light Rings are the orbits responsible for these intersection points. The impact parameter $\eta = L/E$ will play here a crucial role, where E and L are respectively the photon's energy and axial angular momentum with respect to a static observer at infinity. Moreover, these quantities are constants of geodesic motion, connected to the Killing vectors of the spacetime $\zeta = \partial/\partial t$ and $\xi = \partial/\partial\varphi$. The function $h_\pm$ will now be helpful again, as the value of η in a given light ring orbit is provided simply by $\eta = h_\pm$, computed at that position [24].

The precise relation between the image coordinate x and the impact parameter η depends on the choice for the observer's frame, but also on how x is constructed in terms of observation angles. Following [24, 32], the x coordinate is defined to be directly proportional to an observation angle β along that axis: $x = -\tilde{R}\,\beta$, where the perimetral radius $\tilde{R} \equiv \sqrt{g_{\varphi\varphi}}$ is computed at the observer's position (see Section 1.2.1). By computing the projection of the photon's 4-momentum onto a ZAMO frame [24, 32], the relation $\sin\beta = \eta/(A_0 + \eta\, B_0)$ can be derived (if $y = 0$), where the following quantities are computed at the position of the observer: $A_0 = g_{\varphi\varphi}/\sqrt{D}$, $\quad B_0 = g_{t\varphi}/\sqrt{D}$, with $D \equiv g_{t\varphi}^2 - g_{tt}g_{\varphi\varphi}$. This leads to the relation (with $y = 0$):

$$x = -\tilde{R}\arcsin\left(\frac{\eta}{A_0 + \eta B_0}\right). \tag{5.10}$$

We remark that for a very far away observer ($r \to \infty$) we recover the very simple relation $x = -\eta$. By computing η_1 and η_2 for each of the two Light Rings, we can obtain the shadow radius $\bar{r}_x$ on the x-axis simply with $\bar{r}_x = |x_1 - x_2|/2$, where each x is evaluated from the respective η. Notice that this is a local method, in the sense that it does not require the evolution of a geodesic throughout the spacetime. Hence, obtaining a very

[7]We are implicitly assuming that there is no glowing matter in front of the BH.

precise $\bar{r}_x$ value only depends on knowing η at the Light Rings with sufficiently high accuracy. Furthermore, by comparing this $\bar{r}_x$ value with the one obtained with ray-tracing, we can estimate that the precision of the latter to be $\sim 0.08\%$.

The data of the EdGB shadows, computed with ray-tracing, is represented in Fig. 5.3 and Fig. 5.4, where a dilaton coupling $\gamma = 1$ is assumed. The observer is always placed in the equatorial plane, at a radial coordinate such that $\tilde{R} = \sqrt{g_{\varphi\varphi}} = 15M$.

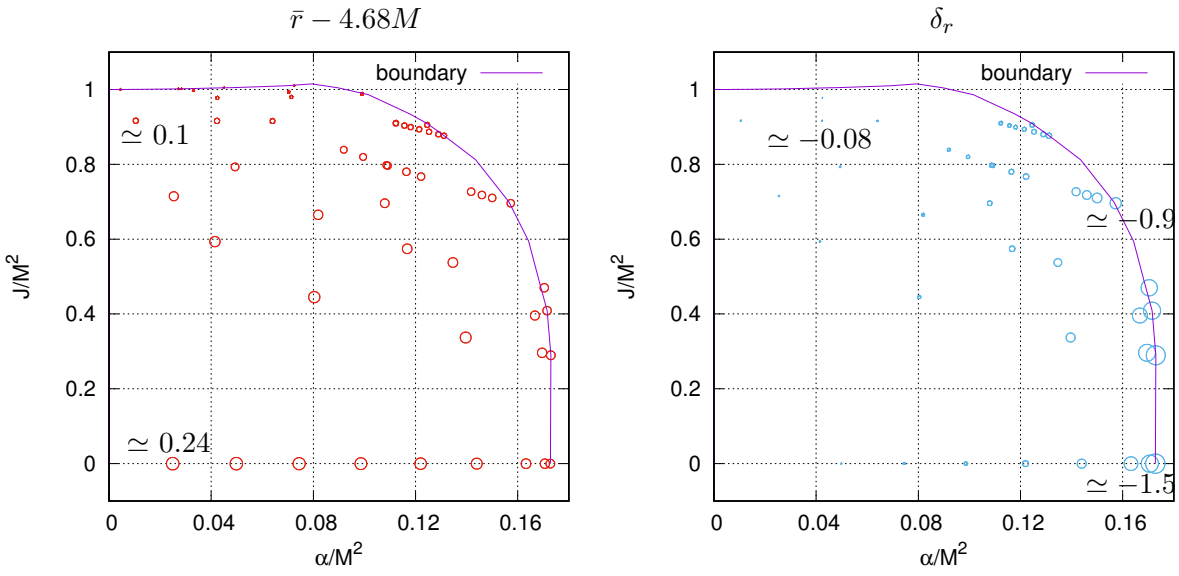


Figure 5.3: Representation of $(\bar{r} - 4.68M)$ (left) and δ_r (right) for EdGB solutions with $\gamma = 1$, in a α/M^2 vs. J/M^2 diagram. Each circle radius is proportional to the quantity represented, with some values also included for reference. All the values of δ_r are negative, with the maximum deviation to Kerr being around $\simeq -1.5\%$. Adapted from [30].

In the left of Fig. 5.3, the size of each circle represents the value of the shadow radius $\bar{r}$ for several EdGB solutions. In order to make the differences across the solution space more apparent, the circle radius is proportional to $\bar{r} - 4.68M$. In other words, a vanishing circle (in this plot only) represents $\bar{r} = 4.68M$. With this depiction, it is clear that - as a rule of thumb - increasing either J or α decreases the shadow size. However, from an observational[8] point of view, it is much more relevant to compare the shadow pre-

[8]For a given BH under observation, the quantities M, J and $\tilde{R}$ are all assumed to be known.

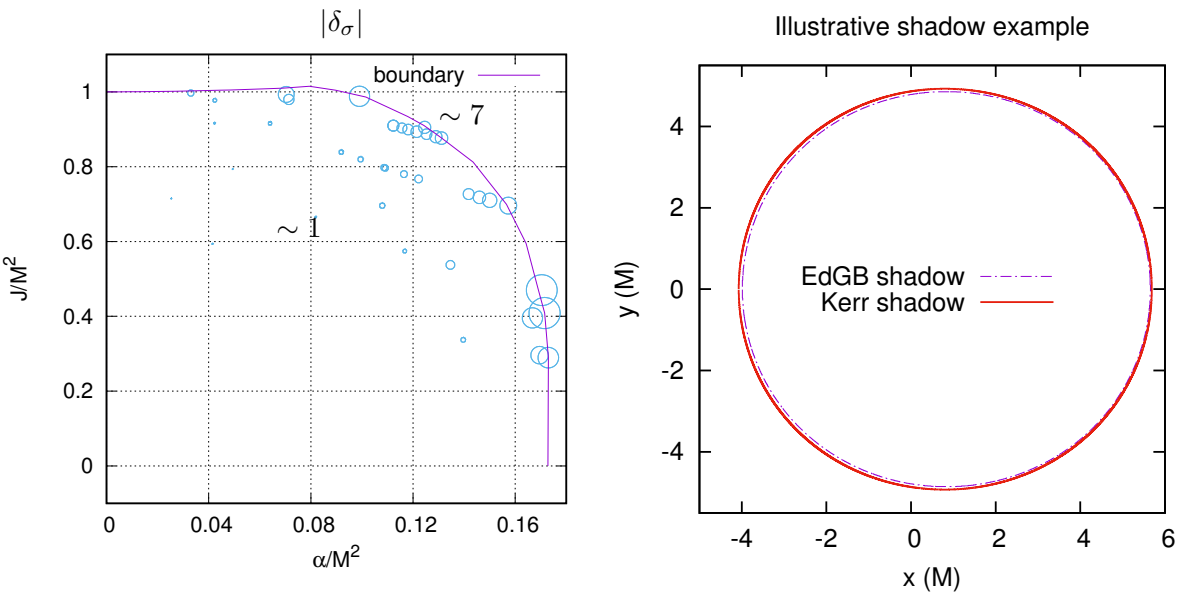


Figure 5.4: (Left) Representation of $|\delta_\sigma|$ for EdGB solutions with $\gamma = 1$, in a α/M^2 vs. J/M^2 diagram. Each circle radius is proportional to the quantity represented, with some values also included for reference. All the values of δ_σ are negative. (Right) Depiction of the shadow edge of a EdGB BH with $\gamma = 1$ and $(\alpha/M^2, J/M^2) \simeq (0.172, 0.41)$, yielding $\bar{r} \simeq 4.85$, $\sigma = 0.3$, $x_C = 0.84$; the radial deviation δ_r with respect to the comparable Kerr case is $\simeq -1.35\%$. The observer is at a perimetral radius $15M$. Adapted from [30].

diction of an EdGB model with the one of a comparable[9] Kerr BH with the same M and J.

In particular, on the right of Fig. 5.3 the relative differences of the shadow size δ_r with respect to Kerr is represented in a circle plot. All deviations are negative, with the largest ones (in absolute) around $\simeq -1.5\%$. As (another) rule of thumb, increasing α/M^2 appears to lead to larger radial deviations from Kerr. In particular, the spherically symmetric EdGB line ($J = 0$) includes some of the largest $|\delta_r|$ values. As a side note, the data represented by the smallest circles in the right of Fig. 5.3 correspond to deviations around $\sim 0.08\%$, which is about the estimated numerical accuracy.

For completeness, the deviations[10] of σ_r with respect to Kerr are represented in the left of Fig. 5.4. Curiously, all values of δ_σ are negative, which means that EdGB shadows are

[9] The shadows are comparable if M, J and the observation distance $\tilde{R} = \sqrt{g_{\varphi\varphi}}$ are the same.
[10] Additional measures of EdGB shadow shapes are possible, but they resemble closely Kerr ones.

more "circular" than the corresponding Kerr case. Hence, the GB term appears to soften the spin deformations that exist on the Kerr shadows. Moreover, notice how the largest $|\delta_\sigma|$ values can be found close to the critical boundary in solution space. Additionally, the deviations δ_{x_C} can be both positive and negative, although a plot for this quantity is not shown.

In order to display an illustrative shadow case, in the right of Fig. 5.4 we have the representation of a EdGB shadow edge in the observation image, together with the comparable Kerr one. Although the difference between the curves is barely visible, amounting to a variation of only $\simeq -1.35\%$ in the shadow size, the case here depicted has one of the largest values of $|\delta_r|$ for $\gamma = 1$. Such an example reinforces the idea that shadow observations are very unlikely to constrain EdGB BH models in the near future.

5.2.2 Shadows of static EdGB BHs

Until this point we discussed only the shadows of EdGB solutions for dilatonic coupling $\gamma = 1$. Repeating the above analysis for other values of γ would be rather cumbersome. Nevertheless, as discussed in the previous subsection, some of the largest $\bar{r}$ deviations occur within the static case. Therefore this can be considered as an incentive to explore other values of γ, while restricting ourselves to $J = 0$. This will provide some insight on the effect of the γ parameter without much more effort.

For the static case ($J = 0$) the shadow is a circle due to the spherical symmetry of the spacetime. Using this property, we have $\bar{r} = \bar{r}_x$, which allows us to use the high precision method described before, thus obtaining the shadow edge without having to resort to any ray-tracing. Notice that in this case σ_r and x_C are both zero due to the spherical symmetry.

The radial deviations δ_r of static EdGB shadows with respect to those of a comparable Schwarzschild BH are represented in Fig. 5.5, for different γ values. The data suggests a scenario where for a fixed value of α/M^2 the deviations on the stable branches are larger

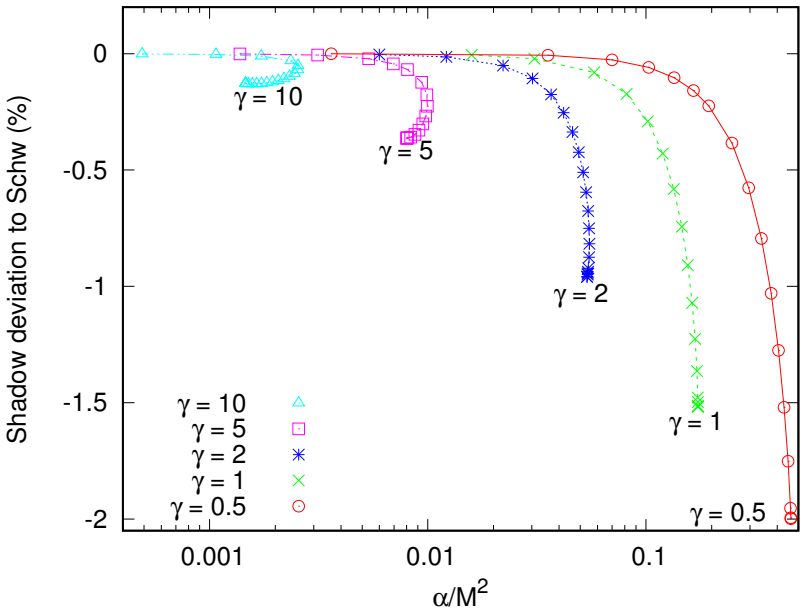


Figure 5.5: Representation of δ_r for static EdGB BHs, computed with respect to the Schwarzschild case. Data for different γ values is displayed as a function of α/M^2. All deviations are negative. The displayed lines only interpolate the numerical data, with colors red, green, blue, pink and light blue respectively for $\gamma = \{0.5, 1, 2, 5, 10\}$. The observer's perimetral radius was set at $15M$. Adapted from [30].

if we increase γ; however, after entering the domain of the secondary (unstable) branches, γ has to decrease in order to yield larger deviations. Furthermore, for a given γ, the maximum deviation always appears to occur at the limiting solution, with this maximal deviation being larger for smaller γ values. For instance, $\gamma = 0.5$ can lead to shadows $\simeq 2\%$ smaller than for Schwarzschild, whereas for $\gamma = 1$ all deviations are below 1.5%.

Discussion

The shadows of the analysed EdGB BHs are always smaller than the comparable Kerr one. However, the deviations observed are always smaller (in modulus) than a few percent ($\sim 1\%$). Since such differences are below the resolution of current observation capabilities ($\sim 10\%$ see [3, 261]), it is unlikely that in the near future any shadow measurement can exclude or restrict EdGB models. Nevertheless, the present study was not exhaustive; it leaves, for instance, studies for different inclinations and distances as future work. Since

EdGB theory possesses unusual features such as *effective exotic matter*, it might come as a surprise that there are no significant effects at the level of the shadow.

However, this *effective exotic matter* is concentrated close to the horizon, such that there is no negative energy contribution outside the photon region that could significantly affect the shadow's size. At the same time any near-horizon odd effects are concealed from a remote observer by the shadow. It may come as another surprise, that the light ring size[11] of EdGB BHs can, for instance, change by as much as $\simeq 4\%$, when considering the static case with $\gamma = 0.5$, and this effect increases with further decreasing γ.

The natural question is then: why are the deviations in the shadow size not larger? For the sake of the argument consider the static case, where it becomes clear that the critical ingredient for the shadow radius is the impact parameter η, and not the light ring size. Naturally, there is a strong correlation between both concepts, but at the end of the day what matters is the value of the impact parameter. This is a point often not clear enough in the literature: a large variation of the light ring size does not have to lead to equally large variations of the shadow radius.

We can equally remark that shadows in a similar cousin model – scalarized BHs in extended scalar-tensor–Gauss-Bonnet – has been recenlty discussed [252]. These solutions reduce to Kerr BHs when the scalar field vanishes. For each value of spin, Scalarized BHs (SBHs) exist in an interval between two critical masses, with the lowest one vanishing in the static limit. Non-uniqueness with Kerr BHs of equal global charges is observed with SBHs being entropically favoured. This suggests that SBHs form dynamically from the spontaneous scalarization of Kerr BHs, which are prone to a scalar-triggered tachyonic instability, below the largest critical mass. Phenomenologically, the introduction of BH spin damps the maximal observable difference between comparable scalarized and vacuum BHs. In the static limit, (perturbatively stable) SBHs can store over 20% of the spacetime energy outside the event horizon; in comparison with Schwarzschild BHs, their geodesic

[11]The perimetral radius $\sqrt{g_{\varphi\varphi}}$ in M units can be used as an invariant measure for the light ring size.

frequency at the ISCO can differ by a factor of 2.5 and deviations in the shadow areal radius may top 40%.

Chapter 6

The Road ahead

As mentioned in the beginning of this work, the true nature of BH candidates that populate the cosmos remains elusive, and scientific open mindedness can certainly help us in this quest. In that matter, it might prove useful to consider different models of compact objects and their associated astrophysical signatures. Due to their connection to observations, the analysis of FPOs in particular might hold one of the keys to test ultra-compact objects in the cosmos.

There are a number of open questions that can be pursued in the near future.

To my knowledge, there is not a generic proof that all BHs must be endowed with a Light Ring. Due to the importance that LRs have for astrophysical observations, it could be of interest to explore this question in the future. The association of a topological charge to LRs might prove useful in this endeavor. One might equally conjecture that by analogy to LRs, a similar topological charge can be associated to FPOs. This might lead to novel results and new types of no-go theorems for black hole mimickers.

Another unsolved issue is the *time scale* of non-linear instabilities that might be associated to stable Light Rings. This point could be addressed numerically, by analysing systems that would only suffer from this instability, and thus disentangling its effects from other causes, such as an ergoregion instability.

In addition, it could be interesting to analyse how FPOs could be generalised to non-stationary or non-axially symmetric spacetimes. As particularly relevant question is then if there is any geometric structure that could be responsible for the shadow edge during a BH merger.

As another possible research direction, with the recent release of the shadow of M87* by the EHT one can attempt to impose constrains on existing models of compact objects. Due to its rich space of solutions, Kerr BHs with scalar hair are a natural candidate for this task. Although some shadows within this family of solutions can be very non Kerr-like (*e.g.* the hammer shadow), those hairy BHs that exist in solution space close to (vacuum) Kerr can display very similar shadows to the latter, and can thus still be consistent with the EHT image within the observation uncertainty. Since the scalar field can work as a proxy for dark matter, this could certainly be a relevant study.

Finally, the generic connection between FPOs and GWs is relatively uncharted. An intriguing possibility is to obtain a simple proxy for the spectrum of quasinormal modes via an inspection of the FPO structure, even when non-separability prevents an analytical approach. This would have direct applications in BH spectroscopy [262].

As a closing remark, with the recent breakthroughs in gravitational wave astrophysics and unveiling of the first BH shadow image, the field of strong gravity has just entered its precision era. One can certainly hope for new and exciting discoveries in the near future. Who knows what might be lurking in the "shadows"?

Bibliography

[1] K. Akiyama et al. First M87 Event Horizon Telescope Results. I. The Shadow of the Supermassive Black Hole. *Astrophys. J.*, 875(1):L1, 2019. doi: 10.3847/2041-8213/ab0ec7.

[2] K. Akiyama et al. First M87 Event Horizon Telescope Results. V. Physical Origin of the Asymmetric Ring. *Astrophys. J.*, 875(1):L5, 2019. doi: 10.3847/2041-8213/ab0f43.

[3] K. Akiyama et al. First M87 Event Horizon Telescope Results. VI. The Shadow and Mass of the Central Black Hole. *Astrophys. J.*, 875(1):L6, 2019. doi: 10.3847/2041-8213/ab1141.

[4] B. P. Abbott et al. Observation of Gravitational Waves from a Binary Black Hole Merger. *Phys. Rev. Lett.*, 116(6):061102, 2016. doi: 10.1103/PhysRevLett.116.061102.

[5] B. P. Abbott et al. GW151226: Observation of Gravitational Waves from a 22-Solar-Mass Binary Black Hole Coalescence. *Phys. Rev. Lett.*, 116(24):241103, 2016. doi: 10.1103/PhysRevLett.116.241103.

[6] B. P. Abbott et al. GW170104: Observation of a 50-Solar-Mass Binary Black Hole Coalescence at Redshift 0.2. *Phys. Rev. Lett.*, 118(22):221101, 2017. doi: 10.1103/PhysRevLett.118.221101.

[7] B. P. Abbott et al. GW170814: A Three-Detector Observation of Gravitational Waves from a Binary Black Hole Coalescence. *Phys. Rev. Lett.*, 119(14):141101, 2017. doi: 10.1103/PhysRevLett.119.141101.

[8] B. P. Abbott et al. GW170608: Observation of a 19-solar-mass Binary Black Hole Coalescence. *Astrophys. J.*, 851(2):L35, 2017. doi: 10.3847/2041-8213/aa9f0c.

[9] V. Cardoso, E. Franzin, and P. Pani. Is the gravitational-wave ringdown a probe of the event horizon? *Phys. Rev. Lett.*, 116(17):171101, 2016. doi: 10.1103/PhysRevLett.117.089902,10.1103/PhysRevLett.116.171101. [Erratum: Phys. Rev. Lett.117,no.8,089902(2016)].

[10] P. V. P. Cunha, E. Berti, and C. A. R. Herdeiro. Light ring stability in ultra-compact objects. *Phys. Rev. Lett.*, 119(25):251102, 2017. doi: 10.1103/PhysRevLett.119.251102.

[11] P. V. P. Cunha, C. A. R. Herdeiro, and E. Radu. Fundamental photon orbits: black hole shadows and spacetime instabilities. *Phys. Rev.*, D96(2):024039, 2017. doi: 10.1103/PhysRevD.96.024039.

[12] C. A. R. Herdeiro and E. Radu. Kerr black holes with scalar hair. *Phys.Rev.Lett.*, 112:221101, 2014. doi: 10.1103/PhysRevLett.112.221101.

[13] C. Herdeiro and E. Radu. Construction and physical properties of Kerr black holes with scalar hair. *Class.Quant.Grav.*, 32(14):144001, 2015. doi: 10.1088/0264-9381/32/14/144001.

[14] C. A. R. Herdeiro and E. Radu. Asymptotically flat black holes with scalar hair: a review. *Int. J. Mod. Phys.*, D24(09):1542014, 2015. doi: 10.1142/S0218271815420146.

[15] C. A. R. Herdeiro and E. Radu. Dynamical Formation of Kerr Black Holes with Synchronized Hair: An Analytic Model. *Phys. Rev. Lett.*, 119(26):261101, 2017. doi: 10.1103/PhysRevLett.119.261101.

[16] C. Herdeiro, E. Radu, and H. Runarsson. Kerr black holes with Proca hair. *Class. Quant. Grav.*, 33(15):154001, 2016. doi: 10.1088/0264-9381/33/15/154001.

[17] S. Yoshida and Y. Eriguchi. Rotating boson stars in general relativity. *Phys.Rev.*, D56:762–771, 1997. doi: 10.1103/PhysRevD.56.762.

[18] F. Schunck and E. Mielke. General relativistic boson stars. *Class.Quant.Grav.*, 20: R301–R356, 2003. doi: 10.1088/0264-9381/20/20/201.

[19] F. E. Schunck and E. W. Mielke. Rotating boson star as an effective mass torus in general relativity. *Phys.Lett.*, A249:389–394, 1998. doi: 10.1016/S0375-9601(98)00778-6.

[20] B. Kleihaus, J. Kunz, and M. List. Rotating boson stars and Q-balls. *Phys.Rev.*, D72:064002, 2005. doi: 10.1103/PhysRevD.72.064002.

[21] S. L. Liebling and C. Palenzuela. Dynamical Boson Stars. *Living Rev.Rel.*, 15:6, 2012.

[22] R. Brito, V. Cardoso, C. A. R. Herdeiro, and E. Radu. Proca stars: Gravitating Bose-Einstein condensates of massive spin 1 particles. *Phys. Lett.*, B752:291–295, 2016. doi: 10.1016/j.physletb.2015.11.051.

[23] P. V. P. Cunha, C. A. R. Herdeiro, E. Radu, and H. F. Runarsson. Shadows of Kerr black holes with scalar hair. *Phys. Rev. Lett.*, 115(21):211102, 2015. doi: 10.1103/PhysRevLett.115.211102.

[24] P. V. P. Cunha, J. Grover, C. Herdeiro, E. Radu, H. Runarsson, and A. Wittig. Chaotic lensing around boson stars and Kerr black holes with scalar hair. *Phys. Rev.*, D94(10):104023, 2016. doi: 10.1103/PhysRevD.94.104023.

[25] P. V. P. Cunha, J. A. Font, C. Herdeiro, E. Radu, N. Sanchis-Gual, and M. Zilhão. Lensing and dynamics of ultracompact bosonic stars. *Phys. Rev.*, D96(10):104040, 2017. doi: 10.1103/PhysRevD.96.104040.

[26] J. Keir. Slowly decaying waves on spherically symmetric spacetimes and ultracompact neutron stars. *Class. Quant. Grav.*, 33(13):135009, 2016. doi: 10.1088/0264-9381/33/13/135009.

[27] V. Cardoso, L. C. B. Crispino, C. F. B. Macedo, H. Okawa, and P. Pani. Light rings as observational evidence for event horizons: long-lived modes, ergoregions

and nonlinear instabilities of ultracompact objects. *Phys. Rev.*, D90(4):044069, 2014. doi: 10.1103/PhysRevD.90.044069.

[28] M. Ostrogradsky. Mémoires sur les équations différentielles, relatives au problème des isopérimètres. *Mem. Acad. St. Petersbourg*, 6(4):385–517, 1850.

[29] D. Lovelock. The Einstein tensor and its generalizations. *J. Math. Phys.*, 12:498–501, 1971. doi: 10.1063/1.1665613.

[30] P. V. P. Cunha, C. A. R. Herdeiro, B. Kleihaus, J. Kunz, and E. Radu. Shadows of Einstein-dilaton-Gauss-Bonnet black holes. *Phys. Lett.*, B768:373–379, 2017. doi: 10.1016/j.physletb.2017.03.020.

[31] P. V. P. Cunha and C. A. R. Herdeiro. Shadows and strong gravitational lensing: a brief review. *Gen. Rel. Grav.*, 50(4):42, 2018. doi: 10.1007/s10714-018-2361-9.

[32] P. V. P. Cunha, C. A. R. Herdeiro, E. Radu, and H. F. Runarsson. Shadows of Kerr black holes with and without scalar hair. In *3rd Amazonian Symposium on Physics and 5th NRHEP Network Meeting is approaching: Celebrating 100 Years of General Relativity Belem, Brazil, September 28-October 2, 2015*, 2016. URL `http://inspirehep.net/record/1465816/files/arXiv:1605.08293.pdf`.

[33] A. Eddington. *Space, Time and Gravitation*. Cambridge University Press, 1920.

[34] O. Chwolson. Über eine mögliche Form fiktiver Doppelsterne. *Astron. Nachr.*, 221: 329, 1924.

[35] A. Einstein. Lens-Like Action of a Star by the Deviation of Light in the Gravitational Field. *Science*, 84:506–507, 1936. doi: 10.1126/science.84.2188.506.

[36] J. Renn, T. Sauer, and J. Stachel. The origin of gravitational lensing: a postscript to Einstein's 1936 Science paper. *Science*, 275:184–186, Jan. 1997. doi: 10.1126/science.275.5297.184.

[37] M. Schmidt. 3C 273 : A Star-Like Object with Large Red-Shift. *Nature*, 197:1040, Mar. 1963. doi: 10.1038/1971040a0.

[38] D. Walsh, R. F. Carswell, and R. J. Weymann. 0957 + 561 A, B - Twin quasistellar objects or gravitational lens. *Nature*, 279:381–384, May 1979. doi: 10.1038/279381a0.

[39] http://wwwstaff.ari.uni-heidelberg.de/mitarbeiter/cfaure/cosmos/info.html.

[40] N. Inada, M. Oguri, B. Pindor, J. F. Hennawi, K. Chiu, W. Zheng, S.-I. Ichikawa, M. D. Gregg, R. H. Becker, Y. Suto, M. A. Strauss, E. L. Turner, C. R. Keeton, J. Annis, F. J. Castander, D. J. Eisenstein, J. A. Frieman, M. Fukugita, J. E. Gunn, D. E. Johnston, S. M. Kent, R. C. Nichol, G. T. Richards, H.-W. Rix, E. S. Sheldon, N. A. Bahcall, J. Brinkmann, Ž. Ivezić, D. Q. Lamb, T. A. McKay, D. P. Schneider, and D. G. York. A gravitationally lensed quasar with quadruple images separated by 14.62arcseconds. *Nature*, 426:810–812, Dec. 2003.

[41] R. Penrose. Gravitational collapse and space-time singularities. *Phys. Rev. Lett.*, 14:57–59, 1965. doi: 10.1103/PhysRevLett.14.57.

[42] R. Penrose. Gravitational collapse: The role of general relativity. *Riv. Nuovo Cim.*, 1:252–276, 1969. [Gen. Rel. Grav.34,1141(2002)].

[43] A. E. Broderick, T. Johannsen, A. Loeb, and D. Psaltis. Testing the No-Hair Theorem with Event Horizon Telescope Observations of Sagittarius A*. *Astrophys.J.*, 784:7, 2014. doi: 10.1088/0004-637X/784/1/7.

[44] J. M. Bardeen. Timelike and null geodesics in the Kerr metric. In C. Dewitt and B. S. Dewitt, editors, *Black Holes (Les Astres Occlus)*, pages 215–239, 1973.

[45] J. L. Synge. The escape of photons from gravitationally intense stars. *Monthly Notices of the Royal Astronomical Society*, 131(3):463–466, 1966. doi: 10.1093/mnras/131.3.463. URL `+http://dx.doi.org/10.1093/mnras/131.3.463`.

[46] V. Perlick and O. Yu. Tsupko. Light propagation in a plasma on Kerr spacetime: Separation of the Hamilton-Jacobi equation and calculation of the shadow. *Phys. Rev.*, D95(10):104003, 2017. doi: 10.1103/PhysRevD.95.104003.

[47] D. O. Muhleman, R. D. Ekers, and E. B. Fomalont. Radio Interferometric Test of the General Relativistic Light Bending Near the Sun. *Phys. Rev. Lett.*, 24:1377–1380, 1970. doi: 10.1103/PhysRevLett.24.1377.

[48] V. Perlick. *Ray Optics, Fermat's Principle, and Applications to General Relativity.* Lecture Notes in Physics Monographs. Springer, 2000. ISBN 9783540668985. URL `https://books.google.pt/books?id=Un3my55rV6YC`.

[49] O. Yu. Tsupko and G. S. Bisnovatyi-Kogan. Gravitational lensing in plasma: Relativistic images at homogeneous plasma. *Phys. Rev.*, D87(12):124009, 2013. doi: 10.1103/PhysRevD.87.124009.

[50] G. S. Bisnovatyi-Kogan and O. Yu. Tsupko. Gravitational Lensing in Plasmic Medium. 2015. doi: 10.1134/S1063780X15070016. [Plasma Phys. Rep.41,562(2015)].

[51] A. Abdujabbarov, B. Juraev, B. Ahmedov, and Z. Stuchlík. Shadow of rotating wormhole in plasma environment. *Astrophys. Space Sci.*, 361(7):226, 2016. doi: 10.1007/s10509-016-2818-9.

[52] A. Abdujabbarov, B. Toshmatov, Z. Stuchlík, and B. Ahmedov. Shadow of the rotating black hole with quintessential energy in the presence of plasma. *Int. J. Mod. Phys.*, D26(06):1750051, 2016. doi: 10.1142/S0218271817500511.

[53] T. Johannsen. Photon Rings around Kerr and Kerr-like Black Holes. *Astrophys.J.*, 777:170, 2013. doi: 10.1088/0004-637X/777/2/170.

[54] V. P. Frolov and A. Zelnikov. *Introduction to black hole physics.* OUP Oxford, 2011.

[55] V. P. Frolov and I. D. Novikov, editors. *Black hole physics: Basic concepts and new developments.* 1998.

[56] A. Riazuelo. Seeing relativity-I: Ray tracing in a Schwarzschild metric to explore the maximal analytic extension of the metric and making a proper rendering of the stars. *Int. J. Mod. Phys.*, D28(02):1950042, 2018. doi: 10.1142/S0218271819500421.

[57] R. P. Kerr. Gravitational field of a spinning mass as an example of algebraically special metrics. *Phys.Rev.Lett.*, 11:237–238, 1963. doi: 10.1103/PhysRevLett.11.237.

[58] D. Robinson. Four decades of black holes uniqueness theorems. In D. Wiltshire, M. Visser, and S. M. Scott, editors, *The Kerr Spacetime: Rotating Black Holes in General Relativity*. Cambridge University Press, 2009.

[59] P. T. Chrusciel, J. L. Costa, and M. Heusler. Stationary Black Holes: Uniqueness and Beyond. *Living Rev.Rel.*, 15:7, 2012.

[60] M. Heusler. Stationary black holes: Uniqueness and beyond. *Living Rev.Rel.*, 1:6, 1998.

[61] J. L. Jaramillo and E. Gourgoulhon. Mass and Angular Momentum in General Relativity. *Fundam. Theor. Phys.*, 162:87–124, 2011. doi: 10.1007/978-90-481-3015-3_4. [,87(2010)].

[62] H. Stephani, D. Kramer, M. A. H. MacCallum, C. Hoenselaers, and E. Herlt. *Exact solutions of Einstein's field equations*. Cambridge Monographs on Mathematical Physics. Cambridge Univ. Press, Cambridge, 2003. ISBN 9780521467025, 0521467020, 9780511059179, 9780521467025. doi: 10.1017/CBO9780511535185. URL `http://www.cambridge.org/uk/catalogue/catalogue.asp?isbn=0521461367`.

[63] B. Carter. Global structure of the Kerr family of gravitational fields. *Phys. Rev.*, 174:1559–1571, 1968. doi: 10.1103/PhysRev.174.1559.

[64] D. C. Wilkins. Bound Geodesics in the Kerr Metric. *Phys. Rev.*, D5:814–822, 1972. doi: 10.1103/PhysRevD.5.814.

[65] M. Demianski and M. Francaviglia. Type-D space-times with a Killing tensor. *Journal of Physics A Mathematical General*, 14:173–179, Jan. 1981. doi: 10.1088/0305-4470/14/1/017.

[66] E. Teo. Spherical photon orbits around a kerr black hole. *General Relativity and Gravitation*, 35(11):1909–1926, 2003.

[67] S. Chandrasekhar. *The Mathematical Theory of Black Holes*. Oxford classic texts in the physical sciences. Clarendon Press, 1998. ISBN 9780198503705. URL `http://books.google.pt/books?id=3aoongEACAAJ`.

[68] R. W. D. Nickalls. Viète, descartes and the cubic equation. *The Mathematical Gazette*, 90(518):203–208, 2006. doi: 10.1017/S0025557200179598.

[69] R. W. Nickalls. A new approach to solving the cubic: Cardan's solution revealed. *The Mathematical Gazette*, 77(480):354–359, 1993.

[70] A. F. Zakharov, F. De Paolis, G. Ingrosso, and A. A. Nucita. Measuring the black hole parameters in the galactic center with RADIOASTRON. *New Astron.*, 10: 479–489, 2005. doi: 10.1016/j.newast.2005.02.007.

[71] V. Perlick. Gravitational lensing from a spacetime perspective. *Living Rev. Rel.*, 7: 9, 2004.

[72] A. Bohn, W. Throwe, F. Hébert, K. Henriksson, D. Bunandar, et al. What does a binary black hole merger look like? *Class.Quant.Grav.*, 32(6):065002, 2015. doi: 10.1088/0264-9381/32/6/065002.

[73] P. Grandclément. Light rings and light points of boson stars. *Phys. Rev.*, D95(8): 084011, 2017. doi: 10.1103/PhysRevD.95.084011.

[74] R. Arnowitt, S. Deser, and C. W. Misner. Dynamical structure and definition of energy in general relativity. *Phys. Rev.*, 116:1322–1330, Dec 1959. doi: 10.1103/PhysRev.116.1322. URL `https://link.aps.org/doi/10.1103/PhysRev.116.1322`.

[75] J. M. Bardeen, W. H. Press, and S. A. Teukolsky. Rotating black holes: Locally nonrotating frames, energy extraction, and scalar synchrotron radiation. *Astrophys.J.*, 178:347, 1972. doi: 10.1086/151796.

[76] J. Grover and A. Wittig. Black Hole Shadows and Invariant Phase Space Structures. *Phys. Rev.*, D96(2):024045, 2017. doi: 10.1103/PhysRevD.96.024045.

[77] J. Shipley and S. R. Dolan. Binary black hole shadows, chaotic scattering and the Cantor set. *Class. Quant. Grav.*, 33(17):175001, 2016. doi: 10.1088/0264-9381/33/17/175001.

[78] *Topology and Geometry in Physics*, pages edited by E. Bick and F. D. Steffen (Springer, Berlin, Heidelberg, 2005).

[79] G. L. Naber. *Topology, geometry, and gauge fields*. Springer, New York, 2000.

[80] S. Hod. On the number of light rings in curved spacetimes of ultra-compact objects. *Phys. Lett.*, B776:1–4, 2018. doi: 10.1016/j.physletb.2017.11.021.

[81] R. P. Geroch. Topology in general relativity. *J. Math. Phys.*, 8:782–786, 1967. doi: 10.1063/1.1705276.

[82] V. A. Rubakov. The Null Energy Condition and its violation. *Phys. Usp.*, 57:128–142, 2014. doi: 10.3367/UFNe.0184.201402b.0137. [Usp. Fiz. Nauk184,no.2,137(2014)].

[83] S. R. Dolan and J. O. Shipley. Stable photon orbits in stationary axisymmetric electrovacuum spacetimes. *Phys. Rev.*, D94(4):044038, 2016. doi: 10.1103/PhysRevD.94.044038.

[84] W. E. East and F. Pretorius. Superradiant Instability and Backreaction of Massive Vector Fields around Kerr Black Holes. *Phys. Rev. Lett.*, 119(4):041101, 2017. doi: 10.1103/PhysRevLett.119.041101.

[85] S. Hod. Stationary Scalar Clouds Around Rotating Black Holes. *Phys.Rev.*, D86: 104026, 2012. doi: 10.1103/PhysRevD.86.129902,10.1103/PhysRevD.86.104026.

[86] S. Hod. Stationary resonances of rapidly-rotating Kerr black holes. *The European Physical Journal C 73,*, 2378, 2013.

[87] M. Wang, S. Chen, and J. Jing. Shadow casted by a Konoplya-Zhidenko rotating non-Kerr black hole. *JCAP*, 1710(10):051, 2017. doi: 10.1088/1475-7516/2017/10/051.

[88] J. José and E. Saletan. *Classical Dynamics: A Contemporary Approach*. Cambridge University Press, 1998. ISBN 9780521636360. URL `https://books.google.pt/books?id=Eql9dRQDgvQC`.

[89] S. B. Pikel'Ner. Book Review: Ya. B. Zel'dovich and I. D. Novikov. The theory of gravitation and stellar evolution. *Soviet Astronomy*, 17:562, Feb. 1974.

[90] S. Schneider and V. Perlick. The shadow of a collapsing dark star. *Gen. Rel. Grav.*, 50(6):58, 2018. doi: 10.1007/s10714-018-2379-z.

[91] S. Chakraborty and S. SenGupta. Strong gravitational lensing — A probe for extra dimensions and Kalb-Ramond field. *JCAP*, 1707(07):045, 2017. doi: 10.1088/1475-7516/2017/07/045.

[92] B. Zwiebach. Curvature Squared Terms and String Theories. *Phys. Lett.*, 156B: 315–317, 1985. doi: 10.1016/0370-2693(85)91616-8.

[93] P. Kanti, N. E. Mavromatos, J. Rizos, K. Tamvakis, and E. Winstanley. Dilatonic black holes in higher curvature string gravity. *Phys. Rev.*, D54:5049–5058, 1996. doi: 10.1103/PhysRevD.54.5049.

[94] P. Kanti, N. E. Mavromatos, J. Rizos, K. Tamvakis, and E. Winstanley. Dilatonic black holes in higher curvature string gravity. 2: Linear stability. *Phys. Rev.*, D57: 6255–6264, 1998. doi: 10.1103/PhysRevD.57.6255.

[95] T. Torii, H. Yajima, and K.-i. Maeda. Dilatonic black holes with Gauss-Bonnet term. *Phys. Rev.*, D55:739–753, 1997. doi: 10.1103/PhysRevD.55.739.

[96] S. O. Alexeev and M. V. Pomazanov. Black hole solutions with dilatonic hair in higher curvature gravity. *Phys. Rev.*, D55:2110–2118, 1997. doi: 10.1103/PhysRevD.55.2110.

[97] M. Melis and S. Mignemi. Global properties of charged dilatonic Gauss-Bonnet black holes. *Phys. Rev.*, D73:083010, 2006. doi: 10.1103/PhysRevD.73.083010.

[98] C.-M. Chen, D. V. Gal'tsov, and D. G. Orlov. Extremal black holes in D=4 Gauss-Bonnet gravity. *Phys. Rev.*, D75:084030, 2007. doi: 10.1103/PhysRevD.75.084030.

[99] C.-M. Chen, D. V. Gal'tsov, and D. G. Orlov. Extremal dyonic black holes in D=4 Gauss-Bonnet gravity. *Phys. Rev.*, D78:104013, 2008. doi: 10.1103/PhysRevD.78.104013.

[100] B. Kleihaus, J. Kunz, and E. Radu. Rotating Black Holes in Dilatonic Einstein-Gauss-Bonnet Theory. *Phys. Rev. Lett.*, 106:151104, 2011. doi: 10.1103/PhysRevLett.106.151104.

[101] B. Kleihaus, J. Kunz, S. Mojica, and E. Radu. Spinning black holes in Einstein–Gauss-Bonnet–dilaton theory: Nonperturbative solutions. *Phys. Rev.*, D93 (4):044047, 2016. doi: 10.1103/PhysRevD.93.044047.

[102] P. Pani and V. Cardoso. Are black holes in alternative theories serious astrophysical candidates? The Case for Einstein-Dilaton-Gauss-Bonnet black holes. *Phys. Rev.*, D79:084031, 2009. doi: 10.1103/PhysRevD.79.084031.

[103] P. Pani, C. F. B. Macedo, L. C. B. Crispino, and V. Cardoso. Slowly rotating black holes in alternative theories of gravity. *Phys. Rev.*, D84:087501, 2011. doi: 10.1103/PhysRevD.84.087501.

[104] D. Ayzenberg and N. Yunes. Slowly-Rotating Black Holes in Einstein-Dilaton-Gauss-Bonnet Gravity: Quadratic Order in Spin Solutions. *Phys. Rev.*, D90:044066, 2014. doi: 10.1103/PhysRevD.91.069905,10.1103/PhysRevD.90.044066. [Erratum: Phys. Rev.D91,no.6,069905(2015)].

[105] A. Maselli, P. Pani, L. Gualtieri, and V. Ferrari. Rotating black holes in Einstein-Dilaton-Gauss-Bonnet gravity with finite coupling. *Phys. Rev.*, D92(8):083014, 2015. doi: 10.1103/PhysRevD.92.083014.

[106] L. Amarilla and E. F. Eiroa. Shadow of a rotating braneworld black hole. *Phys. Rev.*, D85:064019, 2012. doi: 10.1103/PhysRevD.85.064019.

[107] A. Yumoto, D. Nitta, T. Chiba, and N. Sugiyama. Shadows of Multi-Black Holes: Analytic Exploration. *Phys. Rev.*, D86:103001, 2012. doi: 10.1103/PhysRevD.86.103001.

[108] A. Abdujabbarov, F. Atamurotov, Y. Kucukakca, B. Ahmedov, and U. Camci. Shadow of Kerr-Taub-NUT black hole. *Astrophys. Space Sci.*, 344:429–435, 2013. doi: 10.1007/s10509-012-1337-6.

[109] L. Amarilla and E. F. Eiroa. Shadow of a Kaluza-Klein rotating dilaton black hole. *Phys. Rev.*, D87(4):044057, 2013. doi: 10.1103/PhysRevD.87.044057.

[110] P. G. Nedkova, V. K. Tinchev, and S. S. Yazadjiev. Shadow of a rotating traversable wormhole. *Phys. Rev.*, D88(12):124019, 2013. doi: 10.1103/PhysRevD.88.124019.

[111] F. Atamurotov, A. Abdujabbarov, and B. Ahmedov. Shadow of rotating Hořava-Lifshitz black hole. *Astrophys. Space Sci.*, 348:179–188, 2013. doi: 10.1007/s10509-013-1548-5.

[112] F. Atamurotov, A. Abdujabbarov, and B. Ahmedov. Shadow of rotating non-Kerr black hole. *Phys. Rev.*, D88(6):064004, 2013. doi: 10.1103/PhysRevD.88.064004.

[113] Z. Li and C. Bambi. Measuring the Kerr spin parameter of regular black holes from their shadow. *JCAP*, 1401:041, 2014. doi: 10.1088/1475-7516/2014/01/041.

[114] V. K. Tinchev and S. S. Yazadjiev. Possible imprints of cosmic strings in the shadows of galactic black holes. *Int. J. Mod. Phys.*, D23:1450060, 2014. doi: 10.1142/S0218271814500606.

[115] S.-W. Wei and Y.-X. Liu. Observing the shadow of Einstein-Maxwell-Dilaton-Axion black hole. *JCAP*, 1311:063, 2013. doi: 10.1088/1475-7516/2013/11/063.

[116] N. Tsukamoto, Z. Li, and C. Bambi. Constraining the spin and the deformation parameters from the black hole shadow. *JCAP*, 1406:043, 2014. doi: 10.1088/1475-7516/2014/06/043.

[117] A. Grenzebach, V. Perlick, and C. Lammerzahl. Photon Regions and Shadows of Kerr-Newman-NUT Black Holes with a Cosmological Constant. *Phys. Rev.*, D89 (12):124004, 2014. doi: 10.1103/PhysRevD.89.124004.

[118] R.-S. Lu, A. E. Broderick, F. Baron, J. D. Monnier, V. L. Fish, S. S. Doeleman, and V. Pankratius. Imaging the Supermassive Black Hole Shadow and Jet Base of M87 with the Event Horizon Telescope. *Astrophys. J.*, 788:120, 2014. doi: 10.1088/0004-637X/788/2/120.

[119] U. Papnoi, F. Atamurotov, S. G. Ghosh, and B. Ahmedov. Shadow of five-dimensional rotating Myers-Perry black hole. *Phys. Rev.*, D90(2):024073, 2014. doi: 10.1103/PhysRevD.90.024073.

[120] N. Sakai, H. Saida, and T. Tamaki. Gravastar Shadows. *Phys. Rev.*, D90(10): 104013, 2014. doi: 10.1103/PhysRevD.90.104013.

[121] D. Psaltis, F. Ozel, C.-K. Chan, and D. P. Marrone. A General Relativistic Null Hypothesis Test with Event Horizon Telescope Observations of the black-hole shadow in Sgr A*. *Astrophys. J.*, 814(2):115, 2015. doi: 10.1088/0004-637X/814/2/115.

[122] S.-W. Wei, P. Cheng, Y. Zhong, and X.-N. Zhou. Shadow of noncommutative geometry inspired black hole. *JCAP*, 1508(08):004, 2015. doi: 10.1088/1475-7516/2015/08/004.

[123] S. Abdolrahimi, R. B. Mann, and C. Tzounis. Distorted Local Shadows. *Phys. Rev.*, D91(8):084052, 2015. doi: 10.1103/PhysRevD.91.084052.

[124] J. W. Moffat. Modified Gravity Black Holes and their Observable Shadows. *Eur. Phys. J.*, C75(3):130, 2015. doi: 10.1140/epjc/s10052-015-3352-6.

[125] A. Grenzebach. Aberrational Effects for Shadows of Black Holes. *Fund. Theor. Phys.*, 179:823–832, 2015. doi: 10.1007/978-3-319-18335-0_25.

[126] F. H. Vincent, Z. Meliani, P. Grandclement, E. Gourgoulhon, and O. Straub. Imaging a boson star at the Galactic center. *Class. Quant. Grav.*, 33(10):105015, 2016. doi: 10.1088/0264-9381/33/10/105015.

[127] A. Grenzebach, V. Perlick, and C. Lämmerzahl. Photon Regions and Shadows of Accelerated Black Holes. *Int. J. Mod. Phys.*, D24(09):1542024, 2015. doi: 10.1142/S0218271815420249.

[128] A. A. Abdujabbarov, L. Rezzolla, and B. J. Ahmedov. A coordinate-independent characterization of a black hole shadow. *Mon. Not. Roy. Astron. Soc.*, 454(3):2423–2435, 2015. doi: 10.1093/mnras/stv2079.

[129] N. Ortiz, O. Sarbach, and T. Zannias. Shadow of a naked singularity. *Phys. Rev.*, D92(4):044035, 2015. doi: 10.1103/PhysRevD.92.044035.

[130] M. Ghasemi-Nodehi, Z. Li, and C. Bambi. Shadows of CPR black holes and tests of the Kerr metric. *Eur. Phys. J.*, C75:315, 2015. doi: 10.1140/epjc/s10052-015-3539-x.

[131] T. Ohgami and N. Sakai. Wormhole shadows. *Phys. Rev.*, D91(12):124020, 2015. doi: 10.1103/PhysRevD.91.124020.

[132] F. Atamurotov, S. G. Ghosh, and B. Ahmedov. Horizon structure of rotating Einstein–Born–Infeld black holes and shadow. *Eur. Phys. J.*, C76(5):273, 2016. doi: 10.1140/epjc/s10052-016-4122-9.

[133] V. Perlick, O. Yu. Tsupko, and G. S. Bisnovatyi-Kogan. Influence of a plasma on the shadow of a spherically symmetric black hole. *Phys. Rev.*, D92(10):104031, 2015. doi: 10.1103/PhysRevD.92.104031.

[134] C. Bambi. Testing the Kerr Paradigm with the Black Hole Shadow. In *14th Marcel Grossmann Meeting on General Relativity on Recent Developments in Theoretical and Experimental General Relativity, Astrophysics, and Relativistic Field Theories (MG14) Rome, Italy, July 12-18, 2015*, 2015. URL `http://inspirehep.net/record/1383867/files/arXiv:1507.05257.pdf`.

[135] F. Atamurotov and B. Ahmedov. Optical properties of black hole in the presence of plasma: shadow. *Phys. Rev.*, D92:084005, 2015. doi: 10.1103/PhysRevD.92.084005.

[136] L. Yang and Z. Li. Shadow of a dressed black hole and determination of spin and viewing angle. *Int. J. Mod. Phys.*, D25(02):1650026, 2015. doi: 10.1142/S0218271816500267.

[137] V. K. Tinchev. The Shadow of Generalized Kerr Black Holes with Exotic Matter. *Chin. J. Phys.*, 53:110113, 2015. doi: 10.6122/CJP.20150810.

[138] M. Amir and S. G. Ghosh. Shapes of rotating nonsingular black hole shadows. *Phys. Rev.*, D94(2):024054, 2016. doi: 10.1103/PhysRevD.94.024054.

[139] P. V. P. Cunha, C. A. R. Herdeiro, and M. J. Rodriguez. Shadows of Exact Binary Black Holes. *Phys. Rev.*, D98(4):044053, 2018. doi: 10.1103/PhysRevD.98.044053.

[140] P. V. P. Cunha, C. A. R. Herdeiro, and M. J. Rodriguez. Does the black hole shadow probe the event horizon geometry? *Phys. Rev.*, D97(8):084020, 2018. doi: 10.1103/PhysRevD.97.084020.

[141] T. Johannsen, A. E. Broderick, P. M. Plewa, S. Chatzopoulos, S. S. Doeleman, F. Eisenhauer, V. L. Fish, R. Genzel, O. Gerhard, and M. D. Johnson. Testing General Relativity with the Shadow Size of Sgr A*. *Phys. Rev. Lett.*, 116(3):031101, 2016. doi: 10.1103/PhysRevLett.116.031101.

[142] A. Abdujabbarov, M. Amir, B. Ahmedov, and S. G. Ghosh. Shadow of rotating regular black holes. *Phys. Rev.*, D93(10):104004, 2016. doi: 10.1103/PhysRevD.93.104004.

[143] Y. Huang, S. Chen, and J. Jing. Double shadow of a regular phantom black hole as photons couple to the Weyl tensor. *Eur. Phys. J.*, C76(11):594, 2016. doi: 10.1140/epjc/s10052-016-4442-9.

[144] S. Dastan, R. Saffari, and S. Soroushfar. Shadow of a Charged Rotating Black Hole in $f(R)$ Gravity. arXiv:1606.06994, 2016.

[145] Z. Younsi, A. Zhidenko, L. Rezzolla, R. Konoplya, and Y. Mizuno. New method for shadow calculations: Application to parametrized axisymmetric black holes. *Phys. Rev.*, D94(8):084025, 2016. doi: 10.1103/PhysRevD.94.084025.

[146] T. Ohgami and N. Sakai. Wormhole shadows in rotating dust. *Phys. Rev.*, D94(6): 064071, 2016. doi: 10.1103/PhysRevD.94.064071.

[147] J. R. Mureika and G. U. Varieschi. Black hole shadows in fourth-order conformal Weyl gravity. *Can. J. Phys.*, 95(12):1299–1306, 2017. doi: 10.1139/cjp-2017-0241.

[148] M. Sharif and S. Iftikhar. Shadow of a Charged Rotating Non-Commutative Black Hole. *Eur. Phys. J.*, C76(11):630, 2016. doi: 10.1140/epjc/s10052-016-4472-3.

[149] O. Yu. Tsupko. Analytical calculation of black hole spin using deformation of the shadow. *Phys. Rev.*, D95(10):104058, 2017. doi: 10.1103/PhysRevD.95.104058.

[150] G. Bisnovatyi-Kogan and O. Tsupko. Gravitational Lensing in Presence of Plasma: Strong Lens Systems, Black Hole Lensing and Shadow. *Universe*, 3(3):57, 2017. doi: 10.3390/universe3030057.

[151] M. Amir, B. P. Singh, and S. G. Ghosh. Shadows of rotating five-dimensional charged EMCS black holes. *Eur. Phys. J.*, C78(5):399, 2018. doi: 10.1140/epjc/s10052-018-5872-3.

[152] A. Alhamzawi. Observing the shadow of modified gravity black hole. *Int. J. Mod. Phys.*, D26(14):1750156, 2017. doi: 10.1142/S0218271817501565.

[153] N. Tsukamoto. Black hole shadow in an asymptotically-flat, stationary, and axisymmetric spacetime: The Kerr-Newman and rotating regular black holes. *Phys. Rev.*, D97(6):064021, 2018. doi: 10.1103/PhysRevD.97.064021.

[154] M. Mars, C. F. Paganini, and M. A. Oancea. The fingerprints of black holes-shadows and their degeneracies. *Class. Quant. Grav.*, 35(2):025005, 2018. doi: 10.1088/1361-6382/aa97ff.

[155] M. Wang, S. Chen, and J. Jing. Shadows of Bonnor black dihole by chaotic lensing. *Phys. Rev.*, D97(6):064029, 2018. doi: 10.1103/PhysRevD.97.064029.

[156] B. P. Singh. Rotating charge black holes shadow in quintessence. arXiv:1711.02898, 2017.

[157] E. F. Eiroa and C. M. Sendra. Shadow cast by rotating braneworld black holes with a cosmological constant. *Eur. Phys. J.*, C78(2):91, 2018. doi: 10.1140/epjc/s10052-018-5586-6.

[158] T. Johannsen and D. Psaltis. Testing the No-Hair Theorem with Observations in the Electromagnetic Spectrum: II. Black-Hole Images. *Astrophys. J.*, 718:446–454, 2010. doi: 10.1088/0004-637X/718/1/446.

[159] S. Chatrchyan et al. Observation of a New Boson at a Mass of 125 GeV with the CMS Experiment at the LHC. *Phys. Lett.*, B716:30–61, 2012. doi: 10.1016/j.physletb.2012.08.021.

[160] G. Aad et al. Observation of a new particle in the search for the Standard Model Higgs boson with the ATLAS detector at the LHC. *Phys. Lett.*, B716:1–29, 2012. doi: 10.1016/j.physletb.2012.08.020.

[161] C. A. R. Herdeiro and E. Radu. A new spin on black hole hair. *Int. J. Mod. Phys.*, D23(12):1442014, 2014. doi: 10.1142/S0218271814420140.

[162] C. Herdeiro and E. Radu. Ergosurfaces for Kerr black holes with scalar hair. *Phys. Rev.*, D89(12):124018, 2014. doi: 10.1103/PhysRevD.89.124018.

[163] Y. Brihaye, C. Herdeiro, and E. Radu. Myers–Perry black holes with scalar hair and a mass gap. *Phys. Lett.*, B739:1–7, 2014. doi: 10.1016/j.physletb.2014.10.019.

[164] C. Herdeiro, J. Kunz, E. Radu, and B. Subagyo. Myers–Perry black holes with scalar hair and a mass gap: Unequal spins. *Phys. Lett.*, B748:30–36, 2015. doi: 10.1016/j.physletb.2015.06.059.

[165] B. Kleihaus, J. Kunz, and S. Yazadjiev. Scalarized Hairy Black Holes. *Phys. Lett.*, B744:406–412, 2015. doi: 10.1016/j.physletb.2015.04.014.

[166] C. A. R. Herdeiro, E. Radu, and H. Rúnarsson. Kerr black holes with self-interacting scalar hair: hairier but not heavier. *Phys. Rev.*, D92(8):084059, 2015. doi: 10.1103/PhysRevD.92.084059.

[167] C. A. R. Herdeiro, E. Radu, and H. F. Rúnarsson. Spinning boson stars and Kerr black holes with scalar hair: the effect of self-interactions. *Int. J. Mod. Phys.*, D25 (09):1641014, 2016. doi: 10.1142/S0218271816410145.

[168] Y. Brihaye, C. Herdeiro, and E. Radu. Inside black holes with synchronized hair. *Phys. Lett.*, B760:279–287, 2016. doi: 10.1016/j.physletb.2016.06.078.

[169] F. H. Vincent, E. Gourgoulhon, C. Herdeiro, and E. Radu. Astrophysical imaging of Kerr black holes with scalar hair. *Phys. Rev.*, D94(8):084045, 2016. doi: 10.1103/PhysRevD.94.084045.

[170] Y. Ni, M. Zhou, A. Cardenas-Avendano, C. Bambi, C. A. R. Herdeiro, and E. Radu. Iron Kα line of Kerr black holes with scalar hair. *JCAP*, 1607(07):049, 2016. doi: 10.1088/1475-7516/2016/07/049.

[171] J. F. M. Delgado, C. A. R. Herdeiro, and E. Radu. Violations of the Kerr and Reissner-Nordström bounds: Horizon versus asymptotic quantities. *Phys. Rev.*, D94(2):024006, 2016. doi: 10.1103/PhysRevD.94.024006.

[172] J. F. M. Delgado, C. A. R. Herdeiro, E. Radu, and H. Runarsson. Kerr–Newman black holes with scalar hair. *Phys. Lett.*, B761:234–241, 2016. doi: 10.1016/j.physletb.2016.08.032.

[173] O. J. Dias, G. T. Horowitz, and J. E. Santos. Black holes with only one Killing field. *JHEP*, 1107:115, 2011. doi: 10.1007/JHEP07(2011)115.

[174] C. P. Dettmann, N. E. Frankel, and N. J. Cornish. Fractal basins and chaotic trajectories in multi - black hole space-times. *Phys. Rev.*, D50:R618–R621, 1994. doi: 10.1103/PhysRevD.50.R618.

[175] U. Yurtsever. Geometry of chaos in the two center problem in general relativity. *Phys. Rev.*, D52:3176–3183, 1995. doi: 10.1103/PhysRevD.52.3176.

[176] C. P. Dettmann, N. E. Frankel, and N. J. Cornish. Chaos and fractals around black holes. *Fractals*, 3:161, 1995. doi: 10.1142/S0218348X9500014X.

[177] N. J. Cornish and G. W. Gibbons. The Tale of two centers. *Class. Quant. Grav.*, 14:1865–1881, 1997. doi: 10.1088/0264-9381/14/7/020.

[178] Y. Sota, S. Suzuki, and K.-i. Maeda. Chaos in static axisymmetric space-times. 1: Vacuum case. *Class. Quant. Grav.*, 13:1241–1260, 1996. doi: 10.1088/0264-9381/13/5/034.

[179] A. P. S. de Moura and P. S. Letelier. Chaos and fractals in geodesic motions around a nonrotating black hole with an external halo. *Phys. Rev.*, E61:6506–6516, 2000. doi: 10.1103/PhysRevE.61.6506.

[180] A. P. S. de Moura and P. S. Letelier. Scattering map for two black holes. *Phys. Rev.*, E62:4784–4791, 2000. doi: 10.1103/PhysRevE.62.4784.

[181] W. Hanan and E. Radu. Chaotic motion in multi-black hole spacetimes and holographic screens. *Mod. Phys. Lett.*, A22:399–406, 2007. doi: 10.1142/S0217732307022815.

[182] D. Alonso, A. Ruiz, and M. Sanchez-Hernandez. Escape of photons from two fixed extreme Reissner-Nordstrom black holes. *Phys. Rev.*, D78:104024, 2008. doi: 10.1103/PhysRevD.78.104024.

[183] A. Daza, J. O. Shipley, S. R. Dolan, and M. A. F. Sanjuán. Wada structures in a binary black hole system. *Phys. Rev.*, D98(8):084050, 2018. doi: 10.1103/PhysRevD.98.084050.

[184] M. A. Almeida, I. C. Moreira, and H. Yoshida. On the nonintegrability of the Stormer problem. *Journal of Physics A Mathematical General*, 25:L227–L230, Mar. 1992. doi: 10.1088/0305-4470/25/5/003.

[185] A. J. Maciejewski and M. Przybylska. Non-integrability of the three-body problem. *Celestial Mechanics and Dynamical Astronomy*, 110:17–30, May 2011. doi: 10.1007/s10569-010-9333-z.

[186] A. Saa and R. Venegeroles. Chaos around the superposition of a black hole and a thin disk. *Phys. Lett.*, A259:201–206, 1999. doi: 10.1016/S0375-9601(99)00447-8.

[187] O. Semerak and P. Sukova. Free motion around black holes with discs or rings: between integrability and chaos - I. *Mon. Not. Roy. Astron. Soc.*, 404:545–574, 2010. doi: 10.1111/j.1365-2966.2009.16003.x.

[188] . http://gravitation.web.ua.pt/index.php?q=node/416.

[189] W. Hasse and V. Perlick. A Morse-theoretical analysis of gravitational lensing by a Kerr-Newman black hole. *J. Math. Phys.*, 47:042503, 2006. doi: 10.1063/1.2188209.

[190] M. Heusler. No hair theorems and black holes with hair. *Helv. Phys. Acta*, 69: 501–528, 1996.

[191] J. A. Wheeler. Geons. *Phys. Rev.*, 97:511–536, 1955. doi: 10.1103/PhysRev.97.511.

[192] I. Salazar Landea and F. García. Charged Proca Stars. *Phys. Rev.*, D94(10):104006, 2016. doi: 10.1103/PhysRevD.94.104006.

[193] M. Duarte and R. Brito. Asymptotically anti-de Sitter Proca Stars. *Phys. Rev.*, D94(6):064055, 2016. doi: 10.1103/PhysRevD.94.064055.

[194] J. D. Bekenstein. Nonexistence of baryon number for static black holes. *Phys. Rev.*, D5:1239–1246, 1972. doi: 10.1103/PhysRevD.5.1239.

[195] J. D. Bekenstein. Nonexistence of baryon number for black holes. ii. *Phys. Rev.*, D5:2403–2412, 1972. doi: 10.1103/PhysRevD.5.2403.

[196] . http://gravitation.web.ua.pt/index.php?q=node/515.

[197] H. Falcke, F. Melia, and E. Agol. Viewing the shadow of the black hole at the galactic center. *Astrophys.J.*, 528:L13, 2000. doi: 10.1086/312423.

[198] A. E. Broderick and A. Loeb. Imaging optically-thin hotspots near the black hole horizon of Sgr A* at radio and near-infrared wavelengths. *MNRAS*, 367:905–916, Apr. 2006. doi: 10.1111/j.1365-2966.2006.10152.x.

[199] S. Doeleman, E. Agol, D. Backer, F. Baganoff, G. C. Bower, A. Broderick, A. Fabian, V. Fish, C. Gammie, P. Ho, M. Honman, T. Krichbaum, A. Loeb, D. Marrone,

M. Reid, A. Rogers, I. Shapiro, P. Strittmatter, R. Tilanus, J. Weintroub, A. Whitney, M. Wright, and L. Ziurys. Imaging an Event Horizon: submm-VLBI of a Super Massive Black Hole. In *astro2010: The Astronomy and Astrophysics Decadal Survey*, volume 2010 of *ArXiv Astrophysics e-prints*, page 68, 2009.

[200] C. J. Goebel. Comments on the "vibrations" of a Black Hole. *Astrophys. J.*, 172: L95, Mar. 1972. doi: 10.1086/180898.

[201] G. Khanna and R. H. Price. Black hole ringing, quasinormal modes, and light rings. *Phys. Rev. D*, 95:081501, Apr 2017. doi: 10.1103/PhysRevD.95.081501. URL `https://link.aps.org/doi/10.1103/PhysRevD.95.081501`.

[202] M. A. Abramowicz. Black holes and the centrifugal force paradox. *Scientific American*, 268:26–31, Mar. 1993.

[203] V. Cardoso, A. S. Miranda, E. Berti, H. Witek, and V. T. Zanchin. Geodesic stability, lyapunov exponents, and quasinormal modes. *Physical Review D*, 79(6): 064016, 2009.

[204] J. V. José and E. Saletan. *Classical Dynamics: A Contemporary Approach*. Cambridge University Press, Cambridge, 1998.

[205] A. de Vries. The apparent shape of a rotating charged black hole, closed photon orbits and the bifurcation set A_4. *Classical and Quantum Gravity*, 17:123–144, Jan. 2000. doi: 10.1088/0264-9381/17/1/309.

[206] L. Amarilla, E. F. Eiroa, and G. Giribet. Null geodesics and shadow of a rotating black hole in extended Chern-Simons modified gravity. *Phys. Rev.*, D81:124045, 2010. doi: 10.1103/PhysRevD.81.124045.

[207] S. Dastan, R. Saffari, and S. Soroushfar. Shadow of a Kerr-Sen dilaton-axion Black Hole. arXiv:1610.09477, 2016.

[208] S. Abdolrahimi, R. B. Mann, and C. Tzounis. Double Images from a Single Black Hole. *Phys. Rev.*, D92:124011, 2015. doi: 10.1103/PhysRevD.92.124011.

[209] H. Yoshino, K. Izumi, T. Shiromizu, and Y. Tomikawa. Extension of photon surfaces and their area: Static and stationary spacetimes. *PTEP*, 2017(6):063E01, 2017. doi: 10.1093/ptep/ptx072.

[210] E. Berti, V. Cardoso, and A. O. Starinets. Quasinormal modes of black holes and black branes. *Class. Quant. Grav.*, 26:163001, 2009. doi: 10.1088/0264-9381/26/16/163001.

[211] V. Cardoso, A. S. Miranda, E. Berti, H. Witek, and V. T. Zanchin. Geodesic stability, Lyapunov exponents and quasinormal modes. *Phys. Rev.*, D79:064016, 2009. doi: 10.1103/PhysRevD.79.064016.

[212] G. Khanna and R. H. Price. Black Hole Ringing, Quasinormal Modes, and Light Rings. *Phys. Rev.*, D95(8):081501, 2017. doi: 10.1103/PhysRevD.95.081501.

[213] V. Cardoso, S. Hopper, C. F. B. Macedo, C. Palenzuela, and P. Pani. Gravitational-wave signatures of exotic compact objects and of quantum corrections at the horizon scale. *Phys. Rev.*, D94(8):084031, 2016. doi: 10.1103/PhysRevD.94.084031.

[214] V. Cardoso and P. Pani. The observational evidence for horizons: from echoes to precision gravitational-wave physics. arXiv:1707.03021, 2017.

[215] J. Abedi, H. Dykaar, and N. Afshordi. Echoes from the Abyss: Tentative evidence for Planck-scale structure at black hole horizons. *Phys. Rev.*, D96(8):082004, 2017. doi: 10.1103/PhysRevD.96.082004.

[216] G. Ashton, O. Birnholtz, M. Cabero, C. Capano, T. Dent, B. Krishnan, G. D. Meadors, A. B. Nielsen, A. Nitz, and J. Westerweck. Comments on: "Echoes from the abyss: Evidence for Planck-scale structure at black hole horizons". arXiv:1612.05625, 2016.

[217] R. H. Price and G. Khanna. Gravitational wave sources: reflections and echoes. *Class. Quant. Grav.*, 34(22):225005, 2017. doi: 10.1088/1361-6382/aa8f29.

[218] H. Nakano, N. Sago, H. Tagoshi, and T. Tanaka. Black hole ringdown echoes and howls. *PTEP*, 2017(7):071E01, 2017. doi: 10.1093/ptep/ptx093.

[219] Z. Mark, A. Zimmerman, S. M. Du, and Y. Chen. A recipe for echoes from exotic compact objects. *Phys. Rev.*, D96(8):084002, 2017. doi: 10.1103/PhysRevD.96.084002.

[220] M. Visser. *Lorentzian wormholes: From Einstein to Hawking.* 1995. ISBN 1563966530, 9781563966538.

[221] S. D. Mathur. The Fuzzball proposal for black holes: An Elementary review. *Fortsch. Phys.*, 53:793–827, 2005. doi: 10.1002/prop.200410203.

[222] P. O. Mazur and E. Mottola. Gravitational vacuum condensate stars. *Proc. Nat. Acad. Sci.*, 101:9545–9550, 2004. doi: 10.1073/pnas.0402717101.

[223] E. G. Gimon and P. Horava. Astrophysical violations of the Kerr bound as a possible signature of string theory. *Phys. Lett.*, B672:299–302, 2009. doi: 10.1016/j.physletb.2009.01.026.

[224] E. Seidel and W.-M. Suen. Formation of solitonic stars through gravitational cooling. *Phys. Rev. Lett.*, 72:2516–2519, 1994. doi: 10.1103/PhysRevLett.72.2516.

[225] D. J. Kaup. Klein-Gordon Geon. *Phys. Rev.*, 172:1331–1342, 1968. doi: 10.1103/PhysRev.172.1331.

[226] R. Ruffini and S. Bonazzola. Systems of selfgravitating particles in general relativity and the concept of an equation of state. *Phys. Rev.*, 187:1767–1783, 1969. doi: 10.1103/PhysRev.187.1767.

[227] C. A. R. Herdeiro, A. M. Pombo, and E. Radu. Asymptotically flat scalar, Dirac and Proca stars: discrete vs. continuous families of solutions. *Phys. Lett.*, B773:654–662, 2017. doi: 10.1016/j.physletb.2017.09.036.

[228] M. Gleiser and R. Watkins. Gravitational Stability of Scalar Matter. *Nucl. Phys.*, B319:733–746, 1989. doi: 10.1016/0550-3213(89)90627-5.

[229] T. D. Lee and Y. Pang. Stability of Mini - Boson Stars. *Nucl. Phys.*, B315:477, 1989. doi: 10.1016/0550-3213(89)90365-9. [,129(1988)].

[230] E. Seidel and W.-M. Suen. Dynamical Evolution of Boson Stars. 1. Perturbing the Ground State. *Phys. Rev.*, D42:384–403, 1990. doi: 10.1103/PhysRevD.42.384.

[231] N. Sanchis-Gual, C. Herdeiro, E. Radu, J. C. Degollado, and J. A. Font. Numerical evolutions of spherical Proca stars. *Phys. Rev.*, D95(10):104028, 2017. doi: 10.1103/PhysRevD.95.104028.

[232] P. Amaro-Seoane, J. Barranco, A. Bernal, and L. Rezzolla. Constraining scalar fields with stellar kinematics and collisional dark matter. *JCAP*, 1011:002, 2010. doi: 10.1088/1475-7516/2010/11/002.

[233] P. O. Mazur and E. Mottola. Gravitational condensate stars: An alternative to black holes. arXiv:gr-qc/0109035, 2001.

[234] M. Bezares, C. Palenzuela, and C. Bona. Final fate of compact boson star mergers. *Phys. Rev.*, D95(12):124005, 2017. doi: 10.1103/PhysRevD.95.124005.

[235] G. Benomio. The Stable Trapping Phenomenon for Black Strings and Black Rings and its Obstructions on the Decay of Linear Waves. arXiv:1809.07795, 2018.

[236] D. Christodoulou and S. Klainerman. The Global nonlinear stability of the Minkowski space. Published in Princeton University Press, Princeton, 1993.

[237] H. Lindblad and I. Rodnianski. The Global stability of the Minkowski space-time in harmonic gauge. arXiv:math/0411109, 2004.

[238] S. Klainerman and J. Szeftel. Global Nonlinear Stability of Schwarzschild Spacetime under Polarized Perturbations. arXiv:1711.07597, 2017.

[239] P. Hintz and A. Vasy. The global non-linear stability of the Kerr-de Sitter family of black holes. arXiv:1606.04014, 2016.

[240] G. Holzegel. On the massive wave equation on slowly rotating Kerr-AdS spacetimes. *Commun. Math. Phys.*, 294:169–197, 2010. doi: 10.1007/s00220-009-0935-9.

[241] G. Holzegel and J. Smulevici. Decay properties of Klein-Gordon fields on Kerr-AdS spacetimes. *Commun. Pure Appl. Math.*, 66:1751–1802, 2013. doi: 10.1002/cpa.21470.

[242] G. Moschidis. A proof of the instability of AdS for the Einstein–massless Vlasov system. arXiv:1812.04268, 2018.

[243] G. 't Hooft and M. J. G. Veltman. One loop divergencies in the theory of gravitation. *Ann. Inst. H. Poincare Phys. Theor.*, A20:69–94, 1974.

[244] S. Deser and P. van Nieuwenhuizen. One Loop Divergences of Quantized Einstein-Maxwell Fields. *Phys. Rev.*, D10:401, 1974. doi: 10.1103/PhysRevD.10.401.

[245] S. Deser, H.-S. Tsao, and P. van Nieuwenhuizen. One Loop Divergences of the Einstein Yang-Mills System. *Phys. Rev.*, D10:3337, 1974. doi: 10.1103/PhysRevD.10.3337.

[246] K. S. Stelle. Renormalization of Higher Derivative Quantum Gravity. *Phys. Rev.*, D16:953–969, 1977. doi: 10.1103/PhysRevD.16.953.

[247] J. D. Bekenstein. Transcendence of the law of baryon-number conservation in black hole physics. *Phys. Rev. Lett.*, 28:452–455, 1972. doi: 10.1103/PhysRevLett.28.452.

[248] J. D. Bekenstein. Novel "no-scalar-hair" theorem for black holes. *Phys. Rev.*, D51 (12):R6608, 1995. doi: 10.1103/PhysRevD.51.R6608.

[249] T. P. Sotiriou and S.-Y. Zhou. Black hole hair in generalized scalar-tensor gravity. *Phys. Rev. Lett.*, 112:251102, 2014. doi: 10.1103/PhysRevLett.112.251102.

[250] T. P. Sotiriou and S.-Y. Zhou. Black hole hair in generalized scalar-tensor gravity: An explicit example. *Phys. Rev.*, D90:124063, 2014. doi: 10.1103/PhysRevD.90.124063.

[251] R. Takahashi. Black hole shadows of charged spinning black holes. *Publ. Astron. Soc. Jap.*, 57:273, 2005. doi: 10.1093/pasj/57.2.273.

[252] P. V. P. Cunha, C. A. R. Herdeiro, and E. Radu. Spontaneously scalarised Kerr black holes. *Phys. Rev. Lett.*, 123(1):011101, 2019. doi: 10.1103/PhysRevLett.123.011101.

[253] P. V. P. Cunha, C. A. R. Herdeiro, and E. Radu. Isolated black holes without $\mathbb{Z}_2$ isometry. *Phys. Rev.*, D98(10):104060, 2018. doi: 10.1103/PhysRevD.98.104060.

[254] D. A. Tretyakova and T. M. Adyev. Horndeski/Galileon black hole shadows. arXiv:1610.07300, 2016.

[255] Z.-K. Guo, N. Ohta, and T. Torii. Black Holes in the Dilatonic Einstein-Gauss-Bonnet Theory in Various Dimensions. I. Asymptotically Flat Black Holes. *Prog. Theor. Phys.*, 120:581–607, 2008. doi: 10.1143/PTP.120.581.

[256] P. Kanti, B. Kleihaus, and J. Kunz. Wormholes in Dilatonic Einstein-Gauss-Bonnet Theory. *Phys. Rev. Lett.*, 107:271101, 2011. doi: 10.1103/PhysRevLett.107.271101.

[257] J. L. Blázquez-Salcedo et al. Black holes in Einstein-Gauss-Bonnet-dilaton theory. *IAU Symp.*, 324:265–272, 2016. doi: 10.1017/S1743921316012965.

[258] P. Pani, E. Berti, V. Cardoso, and J. Read. Compact stars in alternative theories of gravity. Einstein-Dilaton-Gauss-Bonnet gravity. *Phys. Rev.*, D84:104035, 2011. doi: 10.1103/PhysRevD.84.104035.

[259] B. Kleihaus, J. Kunz, S. Mojica, and M. Zagermann. Rapidly Rotating Neutron Stars in Dilatonic Einstein-Gauss-Bonnet Theory. *Phys. Rev.*, D93(6):064077, 2016. doi: 10.1103/PhysRevD.93.064077.

[260] D. Psaltis and T. Johannsen. A Ray-Tracing Algorithm for Spinning Compact Object Spacetimes with Arbitrary Quadrupole Moments. I. Quasi-Kerr Black Holes. *Astrophys. J.*, 745:1, 2012. doi: 10.1088/0004-637X/745/1/1.

[261] T. Johannsen, C. Wang, A. E. Broderick, S. S. Doeleman, V. L. Fish, A. Loeb, and D. Psaltis. Testing General Relativity with Accretion-Flow Imaging of Sgr A*. *Phys. Rev. Lett.*, 117(9):091101, 2016. doi: 10.1103/PhysRevLett.117.091101.

[262] E. Berti, A. Sesana, E. Barausse, V. Cardoso, and K. Belczynski. Spectroscopy of Kerr black holes with Earth- and space-based interferometers. *Phys. Rev. Lett.*, 117 (10):101102, 2016. doi: 10.1103/PhysRevLett.117.101102.

[263] L. V. Ahlfors. *An Introduction to the Theory of Analytic Functions of One Complex Variable*. McGraw-Hill, 1979.

[264] H. G. Ellis. Ether flow through a drainhole - a particle model in general relativity. *J. Math. Phys.*, 14:104–118, 1973. doi: 10.1063/1.1666161.

[265] O. James, E. von Tunzelmann, P. Franklin, and K. S. Thorne. Visualizing Interstellar's Wormhole. *Am. J. Phys.*, 83:486, 2015. doi: 10.1119/1.4916949.

Appendix A

Connection to integrations in the Complex plane

Some might find the discussion of topological charges in Section 4.4 vaguely resembling the more familiar computation of contour integrals in the complex plane, which likewise is determined by special points inside the contour (the poles). Could there be any connection between both cases? As we will now illustrate with the Argument Principle, indeed there can be a similar underlying mechanism, which is an indication of a much deeper topological structure at play in both cases.

Consider a piecewise smooth, positive oriented, closed contour C in the complex plane, which is contractible to a point and that also avoids both poles and zeros of a meromorphic[1] function $f(z)$. Then the *Argument Principle* states that [263]:

$$\oint_C dz\, \frac{f'(z)}{f(z)} = 2\pi i(n_o - n_P), \tag{A.1}$$

where n_o and n_P are respectively the number of zeros and poles of $f(z)$ inside C (accounting for multiplicity), where $f'(z)$ denotes the derivative of $f(z)$ with respect to the argument. This result can have several applications: for example it can be used to prove the *Fundamental Theorem of Algebra*[2], whereas numerically it can be helpful as a tool

[1] A complex differentiable function defined in an open set, except at some isolated points: the *poles*.

[2] Every non-zero, single-variable, degree n polynomial has exactly n complex roots (with multiplicity).

to count the zeros of a function, *e.g.* Riemann's zeta function $\zeta(z)$ along the critical line $\Re(z) = 1/2$ in order to test the Riemann's hypothesis[3].

As it will become clear, a continuous deformation of C leaves the contour integration invariant, unless C intersects either a pole or a zero of $f(z)$. In order to simplify the analysis, we now make the curious observation that the zeros of the inverse function $F(z) = 1/f(z)$ are the poles of f (and vice-versa)[4], and that replacing $f \to -F$ leaves the integrand invariant, since

$$\frac{F'(z)}{F(z)} = -\frac{f'(z)}{f(z)}.$$

With no loss in generality, we may then restrict our attention to the zeros of $f(z)$, since the poles of $f(z)$ will entail a similar contribution, albeit with a minus sign. Writing $f(z) = re^{i\Omega}$, the contour integral separates into:

$$\oint_C dz\, \frac{f'(z)}{f(z)} = \oint_C \left(\frac{dr}{r} + i\, d\Omega \right) = i \oint_C d\Omega = 2\pi i w, \qquad w \in \mathbb{Z}, \tag{A.2}$$

In a similar spirit to Section 4.4, we now define a map $z \to f(z)$ from the complex plane $\mathbb{C}$ to itself, thus projecting the curve C to a new curve $\widetilde{C}$. Just as before, the integer quantity w has the nice interpretation of the winding number of the projected curve $\widetilde{C}$ around the origin ($r = 0$). For completeness, what remains to be determined is the variation of w when C crosses a zero, say $z = z_o$. Considering that this zero has a multiplicity $n \in \mathbb{N}$, then close to that zero $f(z) \simeq (z - z_o)^n\, f_o(z)$, where $f_o(z_o) \neq 0$. Taking a local contour C^* in the close neighborhood of z_o to determine its contribution (see Fig. 4.6):

$$\oint_{C^*} dz\, \frac{f'(z)}{f(z)} = \oint_{C^*} dz\, \frac{n}{(z - z_o)} + \oint_{C^*} dz\, \frac{f_o'}{f_o} = 2\pi i n.$$

Hence, a zero with multiplicity n contributes $2\pi i n$ to w; similarly a pole of $f(z)$ with multiplicity $k \in \mathbb{N}$ will give a contribution $-2\pi i k$. By combining all zeros and poles inside C we recover the result in equation (A.1).

[3]This conjecture states that all the non-trivial zeros of $\zeta(z)$ lie on the critical line $1/2 + i\lambda$, with $\lambda \in \mathbb{R}$.
[4]Meromorphic functions can be expressed as a ratio between two complex differentiable functions.

As a concrete example, take $f(z) = (z^k - 1)/z$, which has a pole at $z = 0$ and $k \in \mathbb{N}$ zeros on the circle $|z| = 1$. Taking the contour C as a circle with radius r, centered at the origin of the complex plane, one then has:

$$\oint_C dz \, \frac{f'(z)}{f(z)} = -2\pi i + k\pi i \Big(1 + \text{sign}\,[r - 1] \Big).$$

As expected, this gives $(2\pi i)(-1)$ if $r < 1$ and yields $(k - 1)(2\pi i)$ if $r > 1$.

Appendix B

Horizonless UCOs with non-trivial topology

In Section 4.2 we have considered horizonless ultra-compact objects (UCOs) described by spacetimes that are topologically trivial, because they can be *continuously* deformed into *flat* space (Minkowski), while keeping smoothness and the boundary conditions around the axis and spatial infinity. Light Rings (LRs) do not exist in Minkowski spacetime, and so the total LR topological charge w is zero. Since w is preserved under such continuous deformations, one can conclude that the end state UCO formed via gravitational collapse also has $w = 0$.

If instead we start with a spacetime that is topologically nontrivial, we cannot deform it continuously into flat spacetime while fixing the boundary conditions, and so the total w can be different from zero. As a specific example of a topologically non trivial spacetime, consider the Ellis wormhole [264, 265], with metric:

$$ds^2 = -dt^2 + dr^2 + (r^2 + a^2)d\Omega^2,$$

where $a \neq 0$ is a constant. The effective potential is given by $H_\pm(r, \theta) = \pm(\sin\theta\sqrt{r^2 + a^2})^{-1}$. Due to spherical symmetry, we can limit attention to the equatorial plane ($\theta = \pi/2$). In this case there is only one LR at $r = 0$, and it is unstable (a saddle point of $H_\pm$). In

clear contrast to the topologically trivial case, the total w is now $w = -1$. Any spacetime that can be continuously deformed into the Ellis wormhole (including spacetimes with rotation), while keeping smoothness and boundary conditions, has $w = -1$.

The creation of any *additional* LRs via continuous spacetime deformations still occurs in pairs. However, by dropping topological triviality, a single (non-degenerate) unstable LR can exist and the theorem fails. In this sense, wormholes can be BH alternatives, as discussed for instance in [9]. Topological non-triviality, however, requires new physics, since gravitational collapse is not expected to change the topology of spacelike sections unless causality is violated [81].

Appendix C

List of publications

- [23]: *"Shadows of Kerr black holes with scalar hair "*, Phys. Rev. Lett. **115** (2015) no.21, 211102, Pedro V. P. Cunha, Carlos A. R. Herdeiro, Eugen Radu, Helgi F. Runarsson; arXiv:1509.00021, 176 citations; PRL cover image

- [10]: *"Light-Ring Stability for Ultracompact Objects"*, Phys. Rev. Lett. **119** (2017) no.25, 251102 , Pedro V.P. Cunha, Emanuele Berti, Carlos A.R. Herdeiro; arXiv:1708.04211

- [252]: *"Spontaneously scalarised Kerr black holes "*, Phys. Rev. Lett. **123** (2019) no.1, 011101 , Pedro V. P. Cunha, Carlos A. R. Herdeiro, Eugen Radu; arXiv:1904.09997; PRL cover image

- [253]: *"Isolated black holes without $\mathbb{Z}_2$ isometry"*, Phys.Rev. D **98** (2018) no.10, 104060 , Pedro V.P. Cunha, Carlos A.R. Herdeiro, Eugen Radu, arXiv:1808.06692

- [139]: *"Shadows of Exact Binary Black Holes "*, Phys. Rev. D **98** (2018) no.4, 044053, Pedro V.P. Cunha, Carlos A.R. Herdeiro, Maria J. Rodriguez, arXiv:1805.03798

- [140]: *"Does the black hole shadow probe the event horizon geometry?"*, Phys. Rev. D **97** (2018) no.8, 084020, Pedro V.P. Cunha, Carlos A.R. Herdeiro, Maria J. Rodriguez, arXiv:1802.02675

- [31]: *"Shadows and strong gravitational lensing: a brief review"*, Gen.Rel.Grav. **50** (2018) no.4, 42, Pedro V. P. Cunha, Carlos A. R. Herdeiro; **(Editor's choice)**, arXiv:1801.00860

- [25]: *"Lensing and dynamics of ultracompact bosonic stars"*, Phys. Rev. D **96** (2017) no.10, 104040, Pedro V.P. Cunha, José A. Font, Carlos Herdeiro, Eugen Radu, Nicolas Sanchis-Gual, M. Zilhäo, arXiv:1709.06118

- [11]: *"Fundamental photon orbits: black hole shadows and spacetime instabilities"*, Phys.Rev.D **96** (2017) no.2, 024039, Pedro V.P. Cunha, Carlos A.R. Herdeiro, Eugen Radu, arXiv:1705.05461

- [30]: *"Shadows of Einstein–dilaton–Gauss–Bonnet black holes"*, Phys. Lett. B **768** (2017) 373-379, Pedro V.P. Cunha, Carlos A. R. Herdeiro, Burkhard Kleihaus, Jutta Kunz, Eugen Radu, arXiv:1701.00079

- [24]: *"Chaotic lensing around boson stars and Kerr black holes with scalar hair"*, Phys.Rev.D **94** (2016) no.10, 104023, P.V.P. Cunha, J. Grover, C. Herdeiro, E. Radu, H. Runarsson, A. Wittig, arXiv:1609.01340

- [32]: *"Shadows of Kerr black holes with and without scalar hair "*, Int.J.Mod.Phys. D25 (2016) no.09, 1641021, Pedro V. P. Cunha, Carlos A. R. Herdeiro, Eugen Radu, Helgi F. Runarsson, arXiv:1605.08293